

**Pre-clinical *in vivo* studies of parenteral drug delivery systems
using non-invasive multispectral fluorescence imaging**

Dissertation

zur Erlangung des
Doktorgrades der Naturwissenschaften (Dr. rer. nat.)

der

Naturwissenschaftlichen Fakultät I – Biowissenschaften –

der Martin-Luther-Universität
Halle-Wittenberg,

vorgelegt

von Herrn Dipl. Pharm. Andreas Schädlich

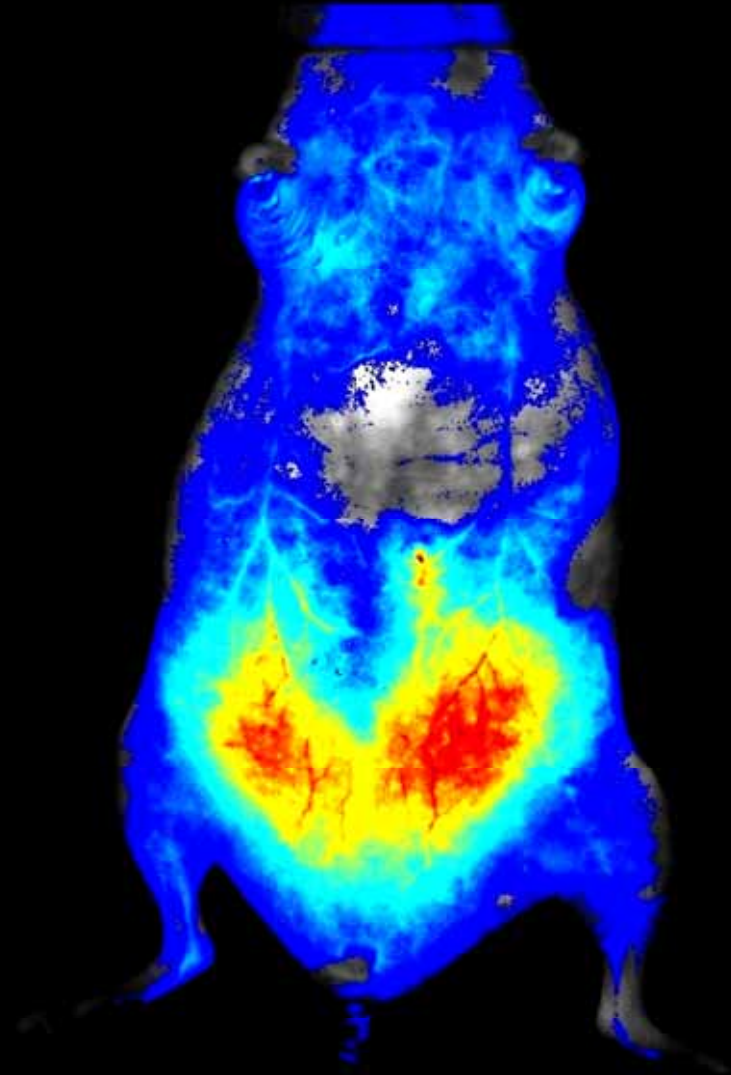
geb. am 16. Mai 1980 in Schlema

Gutachter

1. Prof. Dr. rer. nat. habil. Karsten Mäder
2. Prof. Dr. rer. nat. habil. Jörg Kreßler
3. Prof. Dr. rer. nat. habil. Achim Göpferich

Datum der öffentlichen Verteidigung: 05.12.2013

DAS SCHÖNSTE, WAS WIR ENTDECKEN KÖNNEN,
IST DAS GEHEIMNISVOLLE.



THE MOST BEAUTIFUL THING WE CAN EXPERIENCE IS THE MYSTERIOUS.
IT IS THE SOURCE OF ALL TRUE ART AND ALL SCIENCE.
HE TO WHOM THIS EMOTION IS A STRANGER, WHO CAN NO LONGER PAUSE
TO WONDER AND STAND RAPT IN AWE, IS AS GOOD AS DEAD: HIS EYES ARE CLOSED.

ALBERT EINSTEIN (1879 - 1955)

Contents

Chapter I: Introduction	1
A <i>Pre-clinical imaging in pharmaceutical research</i>	1
A 1. <i>The role of pre-clinical studies in drug development</i>	1
A 2. <i>The importance of pre-clinical studies to research the in vivo behavior of APIs</i>	2
A 3. <i>Imaging systems used for pre-clinical studies</i>	2
A 4. <i>Potential application areas of pre-clinical fluorescence imaging</i>	4
B <i>Research objectives</i>	9
C <i>Basic principles</i>	12
C 1. <i>Fundamentals of fluorescence imaging</i>	12
C 1.1. <i>Overall principles of optical imaging</i>	12
C 1.2. <i>Principles of fluorescence</i>	14
C 1.3. <i>Dyes applicable for fluorescence imaging</i>	15
C 1.4. <i>Intrinsic limitations of in vivo optical imaging</i>	19
C 1.5. <i>Challenges when using in vivo imaging</i>	20
C 1.6. <i>Measurement systems for optical in vivo imaging</i>	21
C 2. <i>The Maestro in vivo imaging system</i>	22
C 2.1. <i>Instrumentation</i>	22
C 2.2. <i>Measurement fundamentals</i>	23
C 2.3. <i>Acquisition of multispectral fluorescence images</i>	24
C 2.4. <i>Spectral unmixing and auto-fluorescence removal</i>	26
C 2.5. <i>Analyses of measurement files</i>	28
Chapter II: Results of pre-clinical in vivo studies of polymers	31
D <i>Long-term in vivo biodistribution studies of i.p. injected high molecular weight PVA</i>	31
D 1. <i>Summary</i>	31

Chapter III: Results of pre-clinical in vivo studies of nanoparticles	34
<i>E In vivo characterization of nanocarriers and their potential capability in cancer therapies.....</i>	34
<i>E 1. Summary.....</i>	34
<i>F Investigating the potential toxicity risk of nanocarriers</i>	37
<i>F 1. Summary.....</i>	37
Chapter IV: Results of pre-clinical in vivo studies of in situ forming implants	39
<i>G Long-term in vivo pH measurements of in situ forming PLGA implants</i>	39
<i>G 1. Summary.....</i>	39
Chapter V: Results of alternative application fields of fluorescence imaging	41
<i>H Monitoring internal pH gradients in swelling multi-layer tablets.....</i>	41
<i>H 1. Summary.....</i>	41
<i>I Monitoring temperature distributions in tablets - caused by the tableting process.....</i>	43
<i>I 1. Summary.....</i>	43
<i>J In vivo and ex vivo characterization of nanocapsules</i>	44
<i>J 1. Summary.....</i>	44
<i>K Monitoring the in vivo efficiency of rhBMP-2 loaded microparticles</i>	45
<i>K 1. Summary.....</i>	45
Chapter VI: Fluorescence pre-clinical imaging – an overall discussion of results	46
<i>L Potential capabilities and limitations of pre-clinical fluorescence imaging</i>	46
<i>M Major limitations of pre-clinical fluorescence imaging studies.....</i>	47
<i>N Major challenges of pre-clinical fluorescence imaging studies.....</i>	48
<i>N 1. The choice of the correct dye.....</i>	48
<i>N 2. Quantification – an impossible challenge in pre-clinical in vivo experiments?</i>	50
Chapter VII: Summary and future perspectives	54
<i>O Summary.....</i>	54
<i>P Future perspectives.....</i>	60
<i>Q German summary.....</i>	61

Bibliography 68

Supplemental material 83

(a) Investigation of the in vivo fate of a water soluble polymer

- (I) *Noninvasive in vivo monitoring of the biofate of 195 kDa poly(vinyl alcohol) by multispectral fluorescence imaging.*
- (II) *In-vivo studies on intraperitoneally administrated poly(vinyl alcohol).*
- (III) *Tracking the in vivo fate of high molar mass poly(vinyl alcohol) using multispectral fluorescence in vivo imaging.*

(b) Characterization of nanocarriers and their potential usage in cancer therapy

- (IV) *How stealthy are PEG-PLA nanoparticles? An NIR in vivo study combined with detailed size measurements.*
- (V) *Tumor accumulation of NIR fluorescent PEG PLA nanoparticles: impact of particle size and human xenograft tumor model.*
- (VI) *Accumulation of nanocarriers in the ovary: A neglected toxicity risk?*

(c) Characterization of in situ forming implants for potential controlled API release

- (VII) *Long-term in vivo pH measurements of in situ forming PLGA implants using multispectral fluorescence imaging.*

(d) Investigating alternative application fields of fluorescence imaging

- (VIII) *Monitoring of internal pH gradients within multi-layer tablets by optical methods and EPR imaging.*

Annex

<i>Acknowledgements</i>	I
<i>Publication list</i>	III
<i>Curriculum vitae</i>	VII
<i>Declaration of the self-contribution of research articles</i>	VIII
<i>Selbstständigkeitserklärung</i>	XI

Abbreviations

AF4	-	Asymmetrical Flow Field Flow Fractionation
API	-	Active Pharmaceutical Ingredient
BCS	-	Biopharmaceutical Classification System
BMP	-	Bone Morphogenetic Protein
CCD	-	Charged-Coupled Device
Cri	-	Cambridge research & instrumentation
CT	-	x-ray Computed Tomography
Cy	-	Cyanine
Da	-	Dalton
Di	-	Dialkylcarbocyanine
DNA	-	DeoxyriboNucleic Acid
DOT	-	Diffuse Optical Tomography
E _{max}	-	Emission maximum
EPR	-	Electron Paramagnetic Resonance (in German ESR)
ESR	-	Elektronenspinresonanz (in English EPR)
FDA	-	U.S. Food and Drug Administration
FITC	-	Fluorescein IsoThioCyanate
FMT	-	Fluorescence-Mediated Tomography
<i>i.m.</i>	-	<i>intramuscular</i>
<i>i.p.</i>	-	<i>intraperitoneal</i>
<i>i.v.</i>	-	<i>intravenous</i>
IR	-	InfraRed
LED	-	Light-Emitting Diode
MALLS	-	MultiAngle Laser Light Scattering
MPS	-	Mononuclear Phagocytic System
MRI	-	Magnetic Resonance Imaging
NIR	-	Near InfraRed
NR	-	Nile Red
OPT	-	Optical Projection Tomography
PCS	-	Photon Correlation Spectroscopy
PDI	-	PolyDispersity Index
PEG	-	PolyEthylene Glycol
PET	-	Positron Emission Tomography

PLA	-	PolyLactic Acid
PLGA	-	Poly(Lactic-Co-Glycolic) Acid
PVA	-	Poly(Vinyl Alcohol)
QD	-	Quantum Dots
RGB	-	Red-Green-Blue
rh	-	recombinant human
RNA	-	RiboNucleic Acid
ROI	-	Region Of Interest
s.c.	-	<i>subcutaneous</i>
SNARF	-	SemiNAphthoRhodaFluor
SPECT	-	Single Photon Emission Computed Tomography
TEM	-	Transmission Electron Microscopy
TMR	-	TetraMethylRhodamine
VIS	-	VISible

Preface

This dissertation is prepared as a cumulative PhD Thesis. The results of the pre-clinical *in vivo* studies of parenteral drug delivery systems using non-invasive multispectral fluorescence imaging are discussed in several publications. Those are already published or submitted for publication. They contain the results obtained during my research in the Pharmaceutical Technology Group (Faculty of Pharmacy) at the Martin Luther University Halle-Wittenberg, Germany. The PhD Thesis was prepared under the supervision of Professor Dr. rer. nat. habil. Karsten Mäder.

The respective chapters within this dissertation are supposed to be a summary of the corresponding publications [1-8] which can be found in the 'Supplemental Material' section of this dissertation.

Namely, this cumulative PhD Thesis consists of the following research articles which are grouped into four research topics (a-d):

(a) Investigation of the *in vivo* fate of a water soluble polymer

- (I) **Schädlich, A.**, Naolou, T., Amado, E., Schöps, R., Kressler, J., Mäder, K., (2011) Noninvasive *in vivo* monitoring of the biofate of 195 kDa poly(vinyl alcohol) by multispectral fluorescence imaging. *Biomacromolecules* 12 (10): 3674-3683. [1]
- (II) Jiang, Y., **Schädlich, A.**, Amado, E., Weis, C., Odermatt, E., Mäder, K., Kressler, J., (2010) In-vivo studies on *intraperitoneally* administrated poly(vinyl alcohol). *Journal of Biomedical Materials Research Part B-Applied Biomaterials* 93B (1): 275-284. [2]
- (III) **Schädlich, A.**, Jiang, Y., Kressler, J., Mäder, K., (2010) Tracking the *in vivo* fate of high molar mass poly(vinyl alcohol) using multispectral fluorescence *in vivo* imaging. *Scientifically Speaking News (Controlled Release Society)* 27 (2): 15-16 (**Cover Story**). [3]

(b) Characterization of nanocarriers and their potential usage in cancer therapy

- (IV) Schädlich, A.,** Rose, C., Kuntsche, J., Caysa, H., Mueller, T., Göpferich, A., Mäder, K., (2011) How stealthy are PEG-PLA nanoparticles? An NIR *in vivo* study combined with detailed size measurements. *Pharmaceutical Research* 28: 1995-2007. [4]
- (V) Schädlich, A.,** Caysa, H., Mueller, T., Tenambergen, F., Rose, C., Göpferich, A., Kuntsche, J., Mäder, K., (2011) Tumor accumulation of NIR fluorescent PEG PLA nanoparticles: impact of particle size and human xenograft tumor model. *ACS Nano* 5 (11): 8710-8720. [5]
- (VI) Schädlich, A.,** Hoffmann, S., Mueller, T., Caysa, H., Rose, C., Göpferich, A., Li, J., Kuntsche, J., Mäder, K., (2012) Accumulation of nanocarriers in the ovary: A neglected toxicity risk? *Journal of Controlled Release* 160 (1): 105-112 (**Cover Story**). [6]

(c) Characterization of *in situ* forming implants for potential controlled API release

- (VII) Schädlich, A.,** Kempe, S., Mäder, K., (2013) Long-term *in vivo* pH measurements of *in situ* forming PLGA implants using multispectral fluorescence imaging. Submitted to *Journal of Controlled Release* (**under peer-review**) [7].

(d) Investigating alternative application fields of fluorescence imaging

- (VIII) Eisenächer, F., Schädlich, A.,** Mäder, K., (2011) Monitoring of internal pH gradients within multi-layer tablets by optical methods and EPR imaging. *International Journal of Pharmaceutics* 417 (1-2): 204-215. [8]

Chapter I: Introduction

A Pre-clinical imaging in pharmaceutical research

A 1. The role of pre-clinical studies in drug development

The process of discovering, producing and launching new active pharmaceutical ingredients (API) is expensive and time-consuming. Several development and testing phases must be passed through, until a new pharmaceutical product is allowed to be sold on the market to treat human diseases. Thereby, many of the original promising APIs fail and never get the marketing authorization.

However, before a new API can be registered as a medicinal product, it has to be tested for its safety and efficacy in cells, animals and humans. Pre-clinical studies in animals must be conducted in order to test the pharmacology, pharmacokinetic and toxicology effects. Those are related to the API but also mainly influenced by the route of administration and the drug delivery system. As the drug formulation has a major effect on the effectiveness of the API they are often already explored within the first pre-clinical animal experiments. If these pre-clinical tests were promising three extensive and cost-intensive clinical phase studies in humans have to be followed. They sometimes lasting over a decade before the new tested API possibly reach the marketing authorization application step and consequently the market. In average this long and expensive undertaking requires often more than \$800 million per new molecular entity while the development takes about 10 years to 13 years before a new drug is available on the market [9-11]. Thereby 58 % of the total costs and half of the development period are apportionable to clinical studies [10]. Within this long undertaking pre-clinical studies are milestones. As much information as possible have to be gathered based on performed animal studies in order to make the right decisions regarding the prospects of the API afterwards. However, studies in animals are complex. To use a new technique for pre-clinical studies it has to be evaluated in detail using various drug delivery systems prior it can be commonly applied in drug discovery research.

A 2. The importance of pre-clinical studies to research the *in vivo* behavior of APIs

More and more new APIs have increased potency and selectivity in their effects but do also have concomitant challenging physical properties, like high molecular masses and increased hydrophobic characteristics [12; 13]. To simply classify new APIs, the Biopharmaceutical Classification System (BCS) has become an important tool since it was introduced in 1995 [14]. Most of the new APIs can be assigned to BCS class II or IV based on their poor water solubility. Due to this property, the galenics of the API is very crucial and the formulation itself gets a pivotal influence.

Knowing the complex *in vivo* behavior of the galenic formulations is important for the improvement of the drug development process. The galenic has a major influence to the therapeutic effect of an API and is essential for the future success of clinical studies. However, the API behavior in the formulation as well as the release of the API is often hardly predictable *in vitro*. This complexity demands more and more pre-clinical *in vivo* tests which increases the development costs. To reduce ethical problematic and cost-intensive pre-clinical animal experiments, new drug candidates and also the formulation approaches with the desired best pharmacological properties for further application have to be identified as early as possible.

In addition, the effectiveness of the pharmaceutical development and the prediction expressiveness of *in vitro* experiments must be increased just as well as the informative values of pre-clinical *in vivo* studies. However, even the ideal API for the respective target from a biological perspective is of little value if it is not transported to the desired site of action in the body. Therefore, the API biodistribution research is very crucial and should be conducted in complex *in vivo* surroundings. The *in vivo* imaging technique has the capability to assess the *in vivo* fate and allows answering target biological questions in early pre-clinical trials. The results can increase the efficiency of potential API candidate selection by providing earlier, more predictive information about potential *in vivo* behavior in humans.

A 3. Imaging systems used for pre-clinical studies

Several anatomical and functional imaging systems for humans have been developed over the past 30 years, including X-ray Computed Tomography (CT), Magnetic Resonance Imaging (MRI), Positron Emission Tomography (PET) and Single Photon Emission Computed Tomography (SPECT) [15-17]. Based on their imaging modality each of these systems is used for different indications. For example

CT can visualize bone tissue and with use of certain contrast agents soft tissues. MRI offers the highest spatial resolution and best soft tissue imaging. Functional imaging methods like PET and SPECT represent high resolution and high sensitivity in nuclear functional methodologies. The PET method requires the use of isotopes and tracer molecules. But the number of isotopes which are available to be incorporated to characterize drug delivery systems is limited. SPECT, on the other hand, offers easier access to isotopes which are also suitable for the labeling of biologicals like peptides and antibodies. These techniques have an important impact to the development and therapy in modern human clinical medicine but they are very expensive in acquisition and servicing [15]. Therefore, these techniques are normally reserved to a restricted number of patients and are often not used for extensive pre-clinical tests. Hence, the interest in the affordable and powerful imaging systems for small animal models has highly increased over the last 10 years [18; 19].

An overview of available pre-clinical imaging techniques to be used for the imaging of small animals is shown in Figure 1. Due to the limitations of some techniques nowadays also combinations of two different measurement approaches within one imaging system are available on the market.

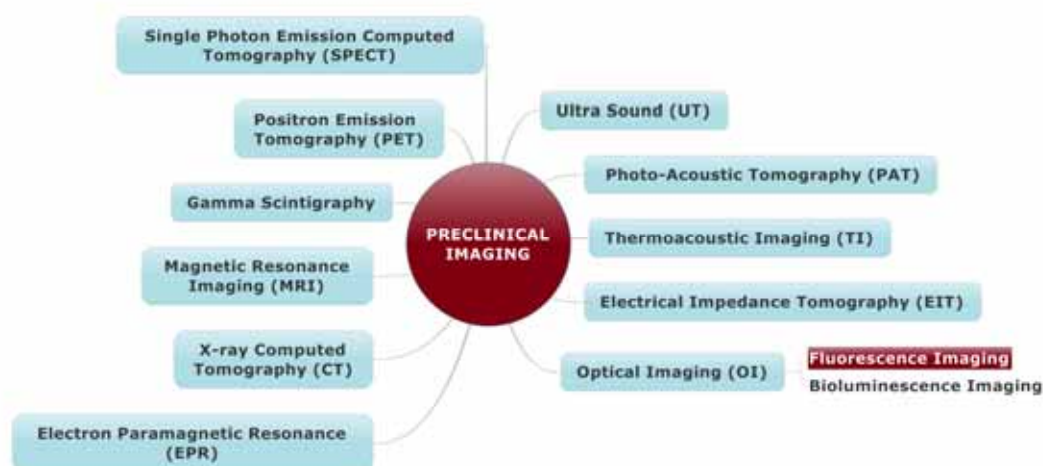


Figure 1: Overview of imaging techniques applied in pre-clinical studies.

Fluorescence imaging is characterized by short measurement times and a broad variety of application fields due to hundreds of available fluorescence dyes with varied physicochemical and light emitting properties. Compared to CT, MRI, PET and SPECT the equipment is relatively inexpensive. Altogether this enables optical imaging and especially fluorescence imaging to be a powerful multifunctional tool for molecular *in vivo* imaging [20-22]. But there is an incomplete understanding of the

actual fundamental capabilities and limitations of fluorescence *in vivo* imaging (Figure 2). Thus, this imaging technique has not yet reached a state of routine use in pre-clinical and clinical studies [23].

The purpose of this research was to identify application possibilities as well as of constraints when using fluorescence imaging in the drug delivery research field in order to improve pre-clinical studies in future. Thereby, the *in vivo* behavior of different parenteral drug carrier systems should be researched in detail. The research was focused on key issues required for the pre-clinical characterization of parenteral formulations like the feasibility of measuring *in vivo* compound distribution, accumulation and elimination processes as well as release profiles of incorporated dyes and measuring the pH *in vivo*. In addition a variety of topics (illustrated in Figure 2) had to be evaluated.

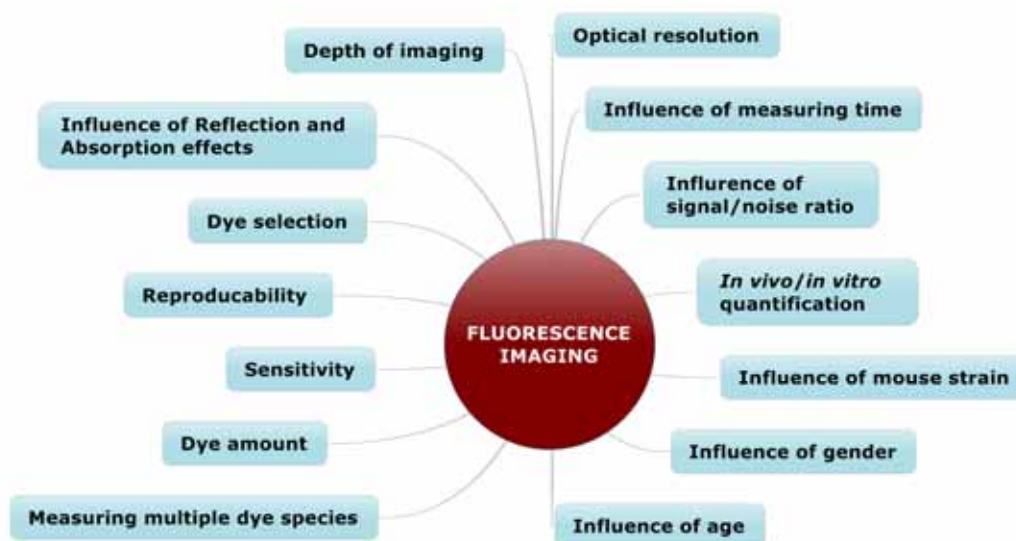


Figure 2: Variety of topics to be researched when using fluorescence imaging in pre-clinical experiments.

A 4. Potential application areas of pre-clinical fluorescence imaging

To explore the fluorescence imaging extensively, three different parenteral drug delivery systems, (a) water soluble polymer conjugates (publication I - III), (b) nanocarriers (publication IV - VI) and (c) *in situ* forming implants (publication VII), with expected complex *in vivo* behaviors were chosen and injected via three different administration routes: (a) *intraperitoneal (i.p.)*, (b) *intravenously (i.v.)* and (c)

subcutaneously (s.c.) [1-7]. The gained knowledge from the performed pre-clinical *in vivo* studies should enable to identify also (d) alternative application fields for fluorescence imaging within the pharmaceutical research field (publication VIII) [8].

(a) Investigation of the *in vivo* fate of a water soluble polymer

The knowledge about the *in vivo* distribution pathway of polymers is essential for their further administration in humans. A high molecular weight (195 kDa) poly(vinyl alcohol), PVA was chosen to track body distribution, accumulation and elimination processes of polymers using pre-clinical imaging. The PVA polymer is relatively inert in body fluids. PVA formulations are approved by the Food and Drug Administration (FDA) and are already used in various pharmaceutical and biomedical applications [24]. PVA is further applied in biotechnology and food chemistry [24-28]. Due to its excellent film-forming, emulsifying and adhesive characteristics, PVA hydro-gels are researched for accelerating wound healing and preventing postoperative adhesions [29-33]. It is already known that high molecular weight PVA remains at least 7 to 10 days at the abdominal wall when the gel is applied over the wound field [34]. The first *in vivo* studies indicated an elimination of PVA via the kidneys despite the high molecular weight [34]. However the detailed *in vivo* fate after *i.p.* application as well the possible long-term PVA accumulations were still unexplored. It should be investigated if fluorescence imaging can be used for *in vivo* and additional *ex vivo* studies to identify the complex *in vivo* fate of PVA. In addition the requirements concerning the choice of dyes, the measurement parameters and possible dye quantification *in vivo* and also *ex vivo* should be investigated.

(b) Characterization of nanocarriers and their potential usage in cancer therapy

In anticancer therapies commonly used chemotherapeutic agents are known to be generally distributed non-specifically in the body. Thereby, they simultaneously affect both cancerous- and normal, healthy cells. However, they are therapeutically inefficient if the API is not able to access its site of action. Nanocarriers can enhance the intracellular concentration of drugs in cancer cells while avoiding toxicity in healthy cells [35; 36]. Nanocarriers like quantum dots (QD) are already used for the fluorescence tissue imaging [37-39]. Nevertheless QDs are criticized for their high production costs, potential *in vivo* toxicity depending on used materials as well as their surface properties [40] and also their limited drug loading capacities. Nanoparticles can be classified into nanocapsules and nanospheres. Compared to QDs they enable an extended drug loading. Nanocapsules are colloidal-sized and

consist of an external polymer layer and an inner core serving as a reservoir that normally represents an oily or aqueous phase which is able to encapsulate the drug molecules [41-45]. Nanospheres can be described as a matrix-type, solid, colloidal particle in which the drug molecules are molecularly dispersed, dissolved, entrapped, chemically bound or adsorbed to the constituent polymer matrix [46; 47]. The industrial development of both types of nanocarriers is amongst others limited by stability problems of their suspensions [48]. Sedimentation and aggregation processes of the nanocarriers occur very slowly due to mixing tendencies of diffusion and convection of the nanometer sized particles [49]. However, after several months of storage in aqueous environment, aggregation can occur next to microbiological growth, hydrolysis of the polymer and drug leakage [49-51]. Freeze drying can avoid this but it is challenging in the case of nanocapsules which can often not be lyophilized due to low stability properties. As result of their vesicular character they tend to collapse during the procedure [51]. Nanospheres can more easily be transferred into the dry state and are stable over months [52]. This increases their potential use in future medicinal therapies. Therefore, nanospheres were chosen within this research as a model nanocarrier system to investigate the size dependent *in vivo* fate as well as size related tumor accumulation characteristics using pre-clinical fluorescence imaging. In this work the nanospheres are to be further referred as nanoparticles.

Poly(lactic acid) (PLA) and poly(lactic-co-glycolic) acid (PLGA) are well known hydrophobic polymer matrices, which are good suitable for the incorporation of poorly-water soluble APIs. Both are approved by the FDA in several market products for parenteral application and are frequently used for the purpose of nanoparticle production [53]. PLA is the more hydrophobic polymer and therefore best suitable as biodegradable and biocompatible one which allows the reproducible production of homogeneous nanoparticles [53]. Besides the size also surface properties of nanoparticles play an important role for their *in vivo* fate. It is well established that hydrophilic surfaces, (e.g. achieved by polymer modification with polyethylene glycol, PEG) reduces opsonisation and through it an uptake by the mononuclear phagocytic system (MPS) [54; 55]. Such PEG shells also provide a sterical stabilization of the particles in aqueous systems [56]. Based on this knowledge, PEG-PLA block polymers were synthesized in the group of Prof. Dr. habil. A. Göpferich in Regensburg and were used for the production of defined, stable and nontoxic nanoparticles varying in size [52]. It is well known that body distribution, elimination processes and pathways as well as tumor accumulation behavior of nanoparticles

are strongly particle size dependent [55; 57-62]. But there is a lack of knowledge about the exact size dependent *in vivo* behavior and the tumor accumulation capability of nanoparticles. Based on published *in vivo* studies, with polydispersities of nanocarriers between 0.2 and 0.5 [63-65], statements about particle size dependencies are doubtful. An overlapping of particle sizing can be presumed due to the broad distributions of particle sizes.

To study the *in vivo* biodistribution and the tumor accumulation particularly, considering potential size dependencies, comprehensive *in vitro* characterizations are a prerequisite to ensure the use of well-defined nanoparticles with narrow sized distributions. Size characterizations and stability studies of nanoparticle dispersions, together with detailed dye suitability studies must be prefixed within this research topic before statements regarding pre-clinical *in vivo* studies can be made. To investigate biodistribution *in vivo*, calculation methods to quantify and compare several nanoparticle batches based on detected fluorescence intensities have to be established. This is hampered by different absorption, scattering and auto-fluorescence effects of miscellaneous tissues. It is also influenced by the properties of the used dye, the light emission spectra as well as the stability and the quenching effects of the dye. Furthermore, the emission position in the body plays a crucial role. These influencing factors have to be considered in detail when using fluorescence imaging for nanocarrier characterization in pre-clinical studies in future.

Based on the obtained knowledge detailed pre-clinical tumor accumulation studies should be followed within this research to identify in which extend quantifications and size dependent predictions of the tumor accumulation behavior of nanoparticles can be made using fluorescence imaging.

(c) Characterization of *in situ* forming implants for potential controlled API release

In situ forming drug delivery systems are innovative formulation types which facilitate a controlled release of APIs over days up to months. They can easily be injected by a syringe into the target site. Among plenty of investigated synthetic and natural polymers, biodegradable PLA and PLGA polymers are most widespread used for the implant preparation. The popularity is based on the fact that these polymers are well characterized and provide an excellent safety and biocompatibility record [66-68]. PLGA for instance, has already been applied in some commercially available parenteral applied controlled releasing products like Eligard, Sandostatin LAR, Lupron Depot, Decapeptyl SR, Suprecur MP, Risperdal Consta and Atridox [69-72].

However, the formulation and release of proteins and peptides as well as of pH dependent poorly water soluble drugs appeared to be very difficult when PLGA systems are used. The degradation products of PLGA are acidic in nature [73]. This can cause protein instabilities, changes in API solubility and API decomposition during manufacturing, storage and application processes [68; 73-75]. Accelerated polymer degradation prior to API release could occur due to low pH values. *In vitro* experiments with PLGA microspheres showed that during incubation under physiologic conditions the pH value in the microspheres can drop from pH 7.4 to values around pH 3 [76; 77]. Although, the pH behavior of PLGA systems is intensively researched *in vitro*, only very few *in vivo* data is available [78]. Under *in vivo* conditions complex factors like perfusion, body liquids, enzymes, elimination processes may also strongly influence the pH in PLGA implants. Until now, the possibilities of fluorescence pH measurements are restricted to confocal microscopy studies measuring for example the microclimate in microspheres [77; 79]. These measurement principles are not by default transferable to the *in vivo* studies and are limited to the skin surface [80]. However, measurements of pH values in *in vivo* studies using non-invasive fluorescence imaging is hampered by a multitude of influencing factors like auto-fluorescence of skin, lack of capable dyes with sufficient quantum yields, wavelength dependent light absorption, intensity variations, possible bleaching and many others. Those factors have to be thoroughly characterized *in vitro* and *ex vivo* prior to *in vivo* measurements.

(d) Investigating alternative application fields of fluorescence imaging

This work was focused on the research of the *in vivo* behavior of PVA, nanoparticles and *in situ* forming PLGA implants. Nevertheless, the obtained knowledge should also be used to characterize other drug delivery systems. Therefore, cooperation projects to transfer established measurement and analyzing techniques to other comparable and also alternative formulation systems were initiated within this research project.

B Research objectives

Due to fast growing market demands for complex APIs like peptides, monoclonal antibodies and highly lipophilic drugs, parenteral applications have attracted increasing scientific and commercial attention over the last decade. Therewith, also the need of parenteral controlled delivery formulations and of targeted carriers arose. While pre-clinical animal studies and clinical studies in humans are ethnic problematic, time and cost-intensive, *in vitro* characterization techniques often not yield in predictable *in vivo* results. This makes it necessary to establish reliable pre-clinical methods to research complex *in vivo* behaviors. New pre-clinical non-invasive fluorescence imaging systems were launched in the early twenty-first century. But there is a lack of data available in which extension that technique can be applied to characterize parenteral formulations *in vivo*.

The current work focuses on the *in vivo* and *ex vivo* characterization of parenteral formulations by multispectral fluorescence imaging. Key measurements within these studies are exemplarily shown in Figure 3.

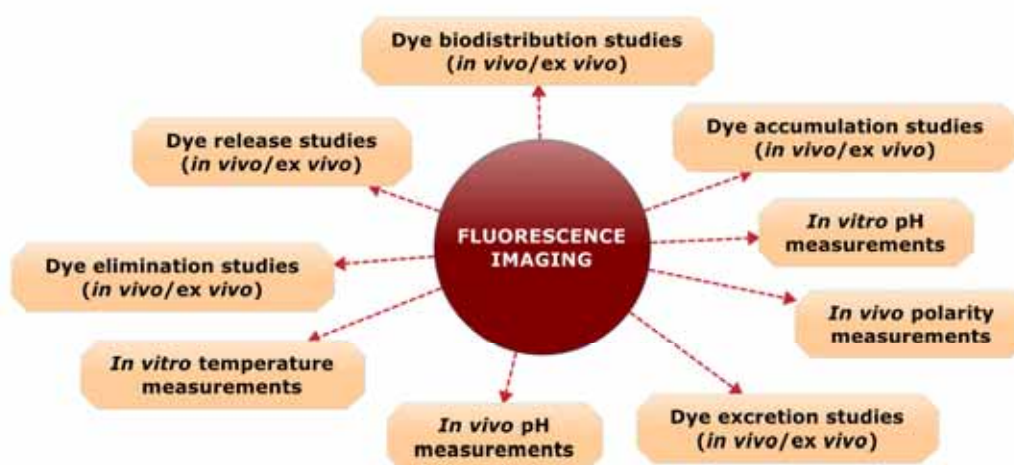


Figure 3: Overview chart of key measurement issues within the current work while using fluorescence imaging.

Briefly, the research objectives of the present cumulative thesis were focused on the use of non-invasive, multispectral fluorescence imaging in pre-clinical *in vivo* studies as an analytical tool for the investigation of:

(a) Investigation of the *in vivo* fate of a water soluble polymer

- Researching the *in vivo* fate of poly(vinyl alcohol) with focus on the accumulation as well as of elimination processes.
- Investigating analyzing methods for the characterization of release profiles and of gender specific variations

(b) Characterization of nanocarriers and their potential usage in cancer therapy

- Exploring methods for size dependent *in vivo* distribution, accumulation and elimination studies of PEG-PLA nanoparticles.
- Researching the size dependent *in vivo* tumor accumulation using NIR fluorescent PEG-PLA nanoparticles and fluorescent tumor xenografts.
- Studying the potential *in vivo* toxicity of nanocarriers.

(c) Characterization of *in situ* forming implants for potential controlled API release

- Investigating *in vivo* measurement approaches to detect microclimate pH values inside *in situ* forming PLGA implants.

(d) Investigating alternative application fields of fluorescence imaging

Transfer the obtained fluorescence imaging method and analyzing knowledge to other formulation systems and pharmaceutical technology research fields.

- Monitoring of internal pH gradients in swelling multi-layer tablets.
- Monitoring of temperature distributions in tablets during tableting process.
- Measurement of the *in vivo* biodistribution of nanocapsules.

The appropriate characterization of parenteral formulations using fluorescence imaging is highly challenging. In order to obtain and discuss meaningful *in vivo* results complementary *in vivo*, *ex vivo* and *in vitro* measurement methods were applied (Figure 4). Detailed analytical *in vitro* measurements were additionally performed prior the *in vivo* application of the drug delivery systems to ensure the required pharmaceutical quality (Figure 4).

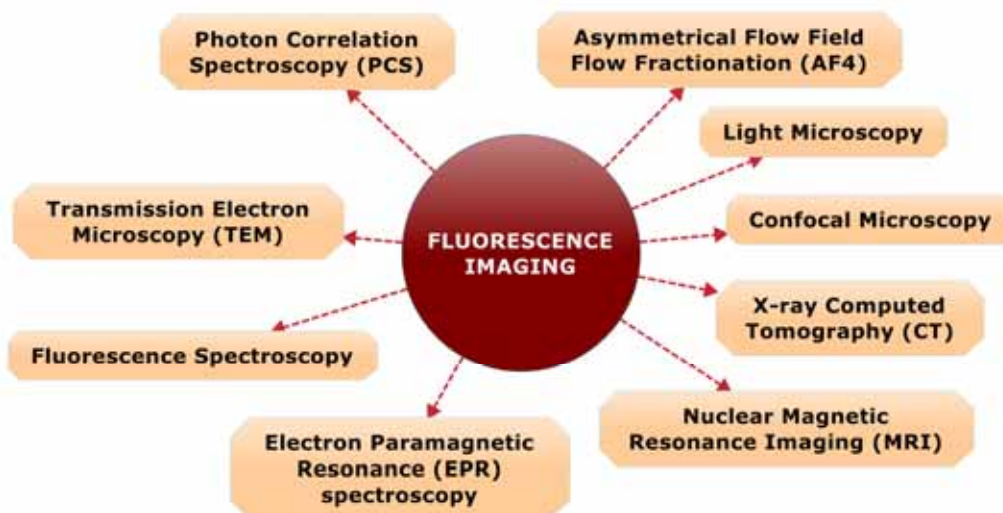


Figure 4: Overview chart of complementary *in vivo*, *ex vivo* and *in vitro* measurement methods applied for the characterization of drug delivery systems.

C Basic principles

C 1. Fundamentals of fluorescence imaging

C 1.1. Overall principles of optical imaging

Clinical imaging systems for humans, like MRI, CT, PET and SPECT are primarily used for displaying anatomical, physiological, and metabolic parameters [15-17]. Additionally first smaller, experimental imaging systems have been developed which allow to research also cellular and molecular levels *in vivo* non-invasively in animals [81-83]. Optical imaging is the most often used single pre-clinical imaging modality followed by MRI and PET [84]. Currently, various optical imaging systems are available on the market. They differ in spatial resolution, sensitivity, for image generation expended energy and in resulting penetration measurement depths [23; 85; 86]. The properties are mainly influenced by the used electromagnetic spectrum. The spectra ranges of selected techniques are shown in Figure 5.

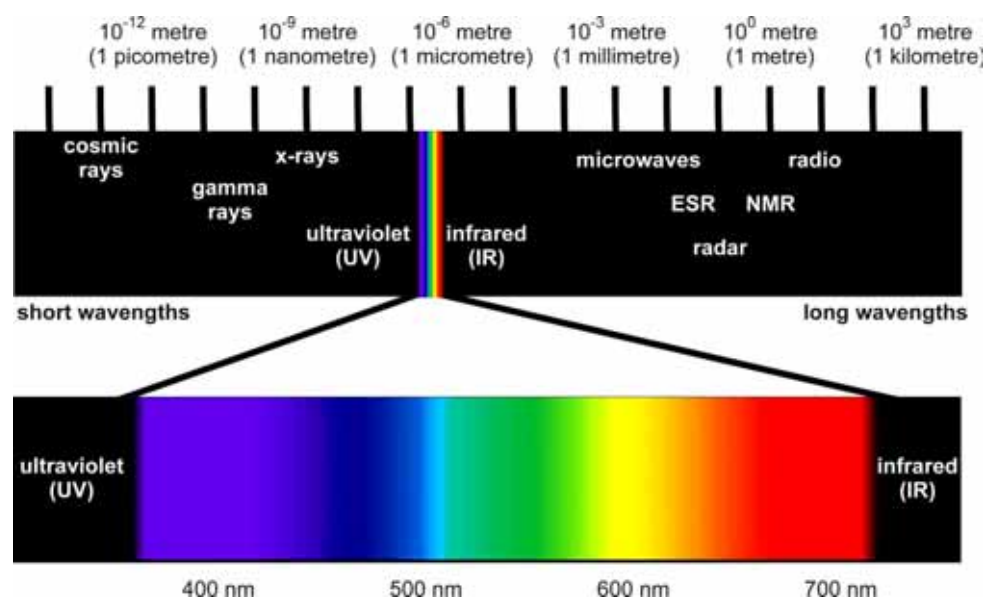


Figure 5: Electromagnetic spectra and respective application techniques. Figure adapted according to Hüttmann and Lönig [87].

Optical imaging systems use light in the wavelength range between 400 nm and 900 nm. Compared to other diagnostic techniques like traditional X-ray CT scans, non-ionic radiation is used. Limitations of the optical imaging technique are mainly caused by the low penetration depth of light into body tissues [88; 89]. Visible (VIS) light like used for endoscopy is routinely used to examine tissue surfaces. The

imaging of deeper tissues ($>500 \mu\text{m}$) requires NIR light [88; 90; 91] which has much better penetration efficiency.

Hemoglobin, oxyhemoglobin and water are the major absorbers of visible light in biological tissues [92]. These three components have the lowest absorption coefficient between 650 nm and 900 nm (Figure 6).

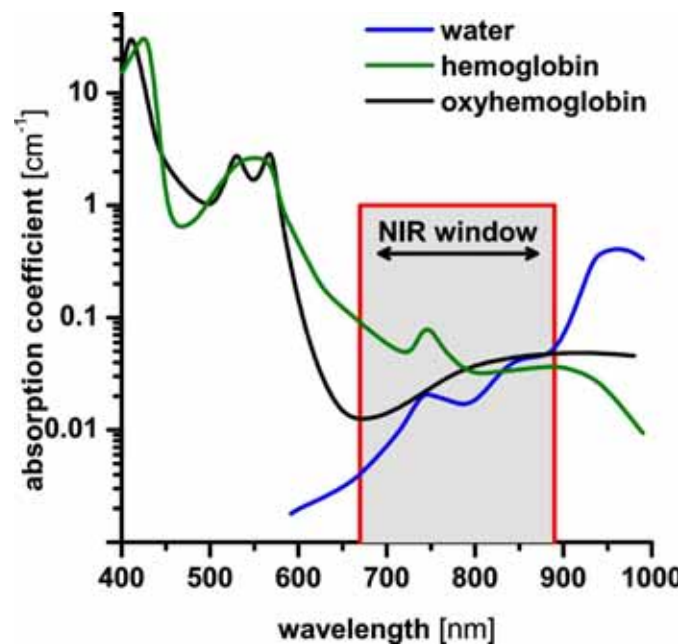


Figure 6: Absorption spectra of the 3 major biological light absorbers (water, hemoglobin, oxyhemoglobin). Within the NIR window the light absorption is minimal. Therewith, NIR light can be used for measurements in deeper body tissues. Figure adapted according to Weissleder et. al [90].

This low absorption rate enables NIR fluorescence light to pass easily through body tissues. In the case of optical measurements the use of NIR light enables also to reduce the influence of disturbing background signals and consequently to achieve better signal to noise ratios. Therefore, this bandwidth is called the diagnostic- or NIR-window and is more and more utilized for *in vivo* fluorescence imaging.

C 1.2. Principles of fluorescence

Optical fluorescence strongly depends on the properties of the used fluorophore, the corresponding characteristics of excited and emitted light and on the surrounding properties (pH, polarity, etc). Three fundamental processes of the fluorophore can be considered after it is excited by a quantum of specific energy from the excitation light [93; 94]:

- Absorption of light energy, associated with an electron transfer to an excited state,
- Emission of radiation associated with relaxation and
- Non-radiative relaxation within and from the excited state.

A typical possibility to illustrate these electronic processes is the Jablonski diagram, shown in Figure 7.

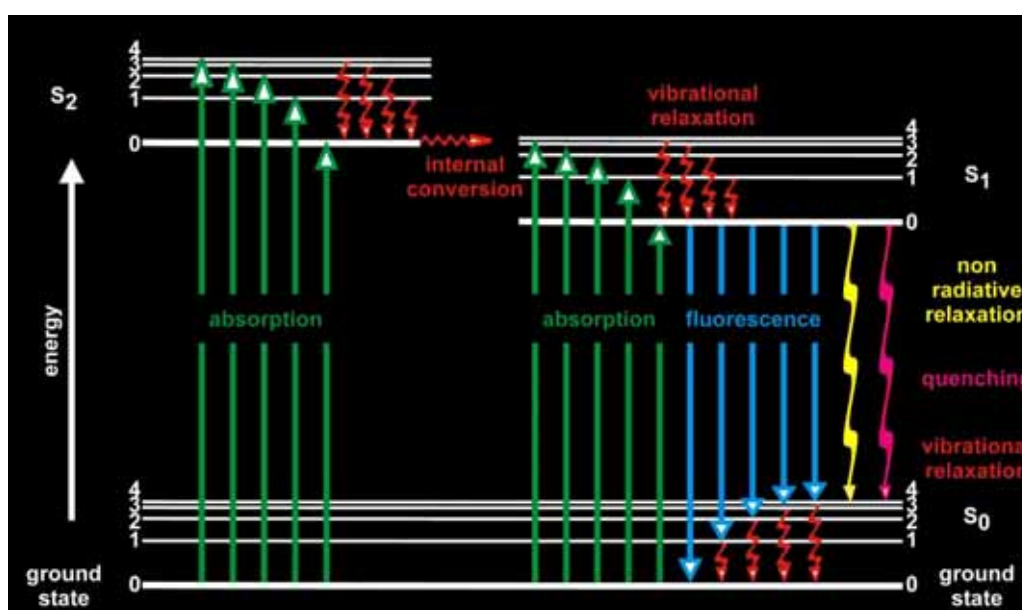


Figure 7: Jablonski diagram, illustrating energy processes. Figure adapted according to Lakowicz [95].

The singlet ground state S_0 , in addition to the first S_1 and second S_2 excited singlet states are displayed in Figure 7 as a stack of horizontal lines. The thicker lines represent electronic energy levels, while the thinner ones denote the various vibrational energy states. The absorption of light occurs approximately in femtoseconds by what the fluorophore is usually excited from the ground state (S_0) to higher vibrational levels of the first (S_1) or second (S_2) singlet energy states.

The transferred energies (excitation and emission) are measured in terms of quanta and are expressed by the Planck's Law:

$$E = h \cdot \nu = \frac{h \cdot c}{\lambda}$$

where E is the energy, h is the Planck's constant, ν and λ are the frequency and the wavelength of the incoming photon respectively, and c is the speed of light. The Planck's Law dictates that the radiation energy of an absorbed photon is directly proportional to the frequency and inversely proportional to the wavelength. The efficiency of the fluorescence process is normally specified by the fluorescence quantum yield, as the ratio of the emitted and absorbed number of photons. Immediately after absorption of a photon, several processes may occur with varying probabilities. The most likely is the relaxation to the lowest vibrational energy level of the first excited state ($S_1 = 0$), known as vibrational relaxation (loss of energy without light emission). Due to the loss of energy during this step, there is always a shift from higher to lower energies and the emission wavelength is bathochromic shifted. This phenomenon was first observed by the British scientist, George G. Stokes and was therefore termed Stokes' shift [95].

If the relaxation from the lowest S_1 level is accompanied by an emission of a photon, the process is called fluorescence. This circular process of excitation and further emission can be repeated for most fluorophores many hundreds to thousands of times before the highly reactive excited state molecule is photobleached. The time, to the destruction of the fluorophore and the loss of further fluorescence, is one quality parameter of a fluorescence dye. In the case of fluorescein isothiocyanate (FITC) the molecule can undergo approximately 35,000 excitation and relaxation cycles before the molecule no longer responds to incident illumination [96].

C 1.3. Dyes applicable for fluorescence imaging

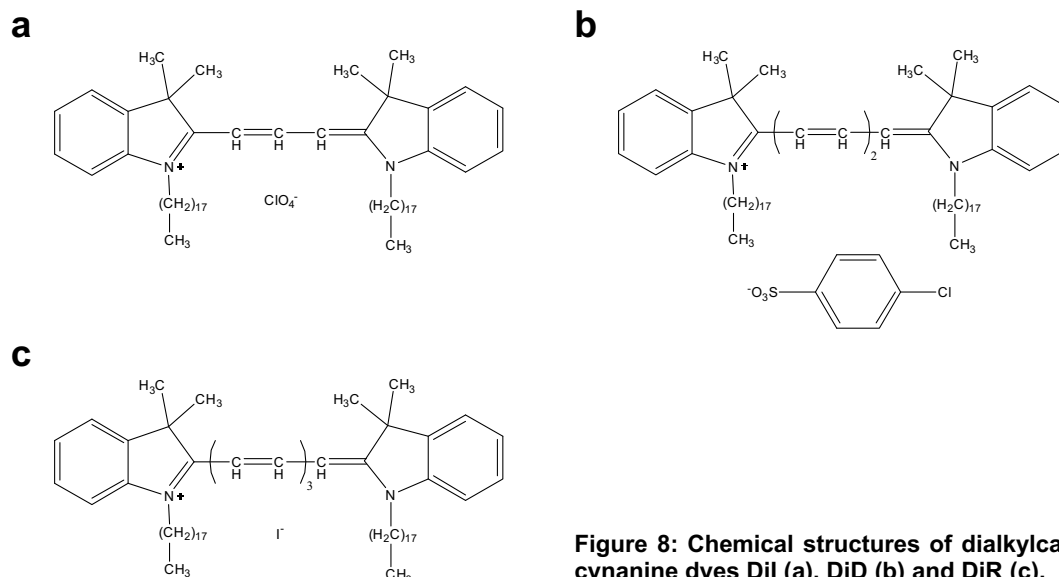
The ability of different molecules as well as of few proteins to emit photons, after their excitation with light requires conjugated systems and delocalized electrons. Unflexible systems are preferred, due to constrained relaxation and thus increased fluorescence [97]. Diversified targeted [98-100], non-targeted [101] as well as of activatable fluorochromes [99; 102; 103], fluorescent proteins [104-106] and bioluminescent probes [107; 108] are commercially available. Depending on the chemical structure, those dyes can be excited with light of specific wavelengths (within VIS or NIR bandwidths). They have different properties and therewith specific capabilities.

Photobleaching should be considered as one characteristic property, especially when dyes are excited with high energy lasers as it can be the case in confocal microscopy studies. Dyes used for *in vivo* fluorescence imaging should have a combination of various other properties like high fluorescence quantum yields in the desired wavelength spectrum, sharp and characteristic emission spectra, sufficient biological stability to permit unimpaired image acquisition, and solubility in the respective environment. Also the chemical stability, the dye/protein binding ratio *in vivo* and specific targeting abilities have to be considered. Among numerous of organic fluorophores there are some often used particular dye classes like the polymethine dyes (e.g. cyanines, hemicyanines and benzopyrillium dyes), xanthene dyes (e.g. fluoresceins and rhodamines), oxazine dyes (nile blue) and oxazone derivatives like nile red (NR) [109-111].

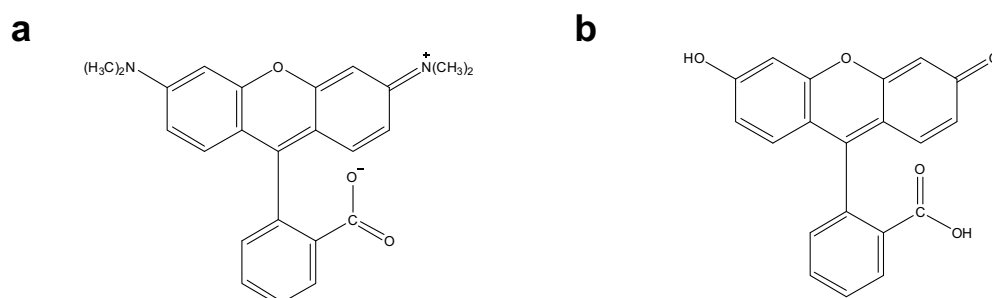
Altogether there are hundreds of fluorescent dyes available on the market. Also dyes with several reactive groups for direct protein or polymer labeling can be purchased. Most of the fluorescence dyes were synthesized to be used for fluorescence microscopy especially to visualize for example cellular structures and cell components. Dyes which are suitable for the *in vivo* characterization of parenteral formulations must emit fluorescence light at least above 500 nm. Light which is emitted at lower emission wavelengths would be absorbed by the body tissue nearly completely and could not or only hardly be detected by non-invasive optical imaging. A small, representative selection of dyes which is highly interesting for fluorescence imaging within this research topics is described briefly in the following.

Cyanine dyes are capable to cover the whole light spectrum from visible to far NIR wavelengths. The spectral properties of cyanines (e.g. Alexa Fluor dyes, Cy5, Cy7) and especially of dialkylcarbocyanine dyes (e.g. DiI, DiD, DiR) are mainly independent from the lengths of the alkyl chains. The fluorescence emission of the dialkylcarbocyanine dyes is mainly influenced by the heteroatoms in the terminal ring systems and the length of the connecting bridges (Figure 8). They are characterized to have very high extinction coefficients but rather moderate fluorescence quantum yields (30 % compared to xanthene dyes) and comparable short excited state lifetimes in lipid environments [110; 112]. Dialkylcarbocyanine dyes are nearly insoluble in water (log P values between 17.4 [113; 114] and 20 [115]) and they are weakly fluorescent in aqueous surroundings [116]. Compared to other lipophilic dyes like Cy5 the photobleaching rate of dialkylcarbocyanine dyes after 100 h excitation (<2 % in methanol solutions and 10 % when loaded to lipid carriers) is highly reduced and attests them ideally properties for *in vivo* applications

[117]. For *in vivo* imaging often used dialkylcarbocyanine dyes with corresponding fluorescence emission wavelengths are (according to the synonym of the distributor invitrogen): DiI: emission maximum (Emax) at 565 nm, DiD Emax at 665 nm and DiR with an Emax at 780 nm.



Compared to cyanine dyes, xanthene stains like fluorescein and rhodamine (Figure 9) are not available with fluorescence emissions far beyond 700 nm [110]. However, they exhibit extremely high quantum yields and are very good water soluble. Corresponding log P values are given to be between -2.4 and 2.8 [114; 115; 118]. Due to the hydrophilic properties, next to fluorescence emissions at around 540 nm, rhodamine can easily be used to stain hydrophilic drug carrier systems like gels or implants which allow making predictions of future hydrophilic drug releases [119; 120].



Fluorescein and many of its derivatives (the second xanthene dye family) have a pH-dependent fluorescence. Both, the phenol and the carboxylic acid, functional groups of fluorescein are almost totally ionized in aqueous solutions above pH 9. An

acidification of the di-anion, protonates the phenol (pK_a about 6.4) first, yielding in the mono-anion. Both are fluorescent and can be used for pH dependent fluorescence measurements. However, the fluorescence emission spectrum is dominated by the dianion by what the wavelengths and the shapes of the emission spectra are relatively pH independent. Only the fluorescence intensity is reduced at acidic pH values. Based on fluorescein derivatives were synthesized by Molecular Probes (now invitrogen): SNARF-1 ($pK_a \approx 7.5$) and SNARF-4F ($pK_a \approx 6.4$), shown in Figure 10 [121; 122].

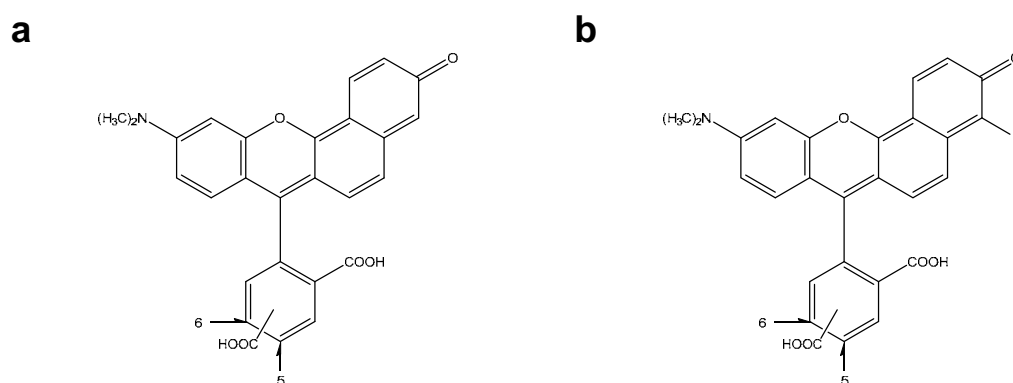


Figure 10: Chemical structures of 5-(and-6)-carboxy SNARF-1 (a) and SNARF-4F 5-(and-6)-carboxylic acid (b).

These seminaphtho dyes are structurally not equivalent and exhibit dissimilar spectral properties [111]. The emission spectrum undergoes pH-dependent wavelength shifts. This allows the analysis of two emission maxima: typically at about 580 nm and at 640 nm and permits intensity independent pH detections at least *in vitro* for SNARF-4F between pH 5 and 7 [77; 79; 123].

Nile red (NR), an oxazone derivate is another often used dye (Figure 11). The log P value of NR is reported to be between rhodamine and that of cyanine dyes (3.8 [124] - 5.1 [125]). NR is a solvatochromic dye. The emission spectra vary in shape, position, and intensity with the polarity of the surrounding solvent [126]. The emitted light is shifted to shorter wavelengths with decreasing solvent polarities and the fluorescence is quenched nearly completely in aqueous media [127].

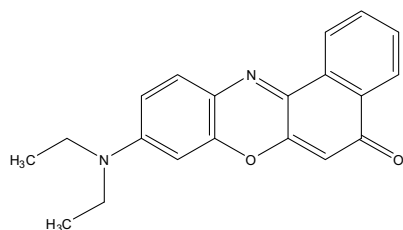


Figure 11: Chemical structure of Nile red.

C 1.4. Intrinsic limitations of *in vivo* optical imaging

The multitude of fluorescence dyes with a large variety of properties and the ability to measure different native parameters like absorption, scattering, emission or spectral characteristics [128] might suggest an easy and wide use of fluorescence *in vivo* imaging. However, there are several intrinsic limitations when using fluorescence imaging. The spectrum of light which is passing tissues often varies by biochemical events. Emitted photons, detected by the imager, undergo multiple scattering events on their way through the body tissues [91; 128; 129]. Next to hemoglobin, oxyhemoglobin and water as the major absorbers, other tissue components can absorb light too such as:

- Small molecules like sugars, fatty acids, amino acids and nucleotides;
- Macromolecules like proteins, phospholipids, ribonucleic acid (RNA) deoxyribonucleic acid (DNA) and polysaccharides;
- As well as structures like organelles and cell membranes.

The general absorption occurs especially in the VIS wavelength range and is at least one order of magnitude less pronounced in the above discussed NIR window. Pelt as well as organs, which are highly supplied with blood like liver, spleen and kidneys absorb fluorescence excitation and emission light below 650 nm nearly completely.

In the VIS wavelength range both, the limited ability of excitation light to penetrate into the skin (Figure 12, green spot) as well as the limited capability of light emitted from a fluorophore to pass the skin surface (Figure 12, yellow spot) hamper the *in vivo* use of fluorescence dyes emitting in the VIS range.

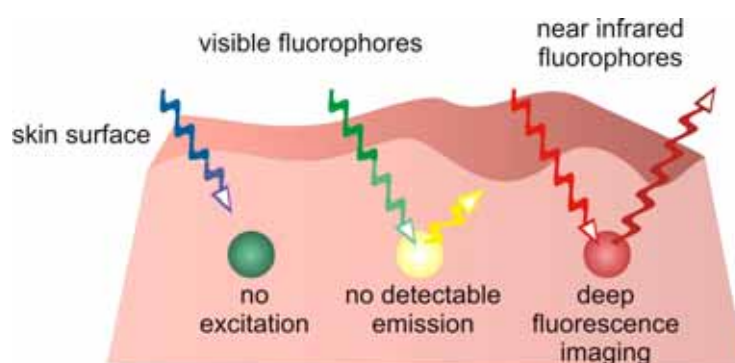


Figure 12: Schematic illustration of excitation and emission processes using visible (green and yellow) and NIR (dark red) light for deep fluorescence imaging. Figure adapted according to Shuhendler [91].

Due to the reduced absorption in the NIR range, NIR dyes are capable of deep tissue penetration. Multiple elastic scattering effects of photons are the main mechanism of light propagation of NIR light in body tissues [130]. By this phenomenon, NIR light transport within tissue can be modeled as a simple isotropic diffusing process [131]. Therefore, an exact localization of the emitting fluorescence light source beyond the surface becomes challenging. Depending on the depth of the fluorescent targets, structures obtained in the measurement images getting more and more blurred.

Another consequence of this light scattering is an alteration of the intrinsic fluorescence emission spectra during the way through body tissues [128; 132]. This effect depends on optical properties of the tissue, the depth of the fluorophore, and is additionally influenced by the geometry and the wavelength of the light irradiation. In consequence the shape and the peak position of the detected fluorescence spectra may vary depending on the structure and the path lengths through the tissue [92; 133; 134]. Emission spectra of NIR dyes are very smooth and have no detail information like characteristic peaks. Also spectral shifts are not as good detectable as it is possible for fluorophores, emitting in the VIS band width. Dyes with emissions below 650 nm have higher quantum yields and more characteristic spectral shapes. Variations in the emission peaks are more easily detectable.

C 1.5. Challenges when using *in vivo* imaging

The auto-fluorescence of various other molecules in the animal feed and in different body tissues is next to the absorption and scattering effects another main limiting factor. Collagen, elastin, flavins, NADH, porphyrins, pyridoxine, tryptophan as well as chlorophyll, a component of animal fodder for instance are well known as auto-fluorescence molecules [135; 136].

These natural fluorophores emit light usually at lower VIS wavelengths. Their influence on far-red and NIR fluorescence imaging is often negligible. To circumvent that fodder influences measurements, special non-fluorescent chow can be used.

Auto-fluorescence resulting from the body tissues is mainly initiated by the pelt and the skin of the mice. This may substantially overlay emitted fluorescence light. To sensitively track dyes *in vivo*, hair above the measurement regions should be removed completely. This can be performed only for smaller skin areas, whereas shaving is inefficient and depilation with foam or cream requires additional narcosis, results in skin irritation, and increases the risk of cooling out. However, also for small regions these strategies are insufficient for long-term measurements as the hair grow

fast. Therefore, the use of nude, hairless mice like SKH1-*Hr^{hr}* or NU-Foxn1^{*nu*} is preferred for comprehensive fluorescence *in vivo* measurements.

All factors mentioned above hamper the *in vivo* imaging. To increase the selectivity and the sensitivity of detecting fluorescence dyes *in vivo*, additional imaging and analyzing techniques were commercially developed. Some *in vivo* fluorescence imaging systems reduce auto-fluorescence influences by special spectral un-mixing techniques. This enables to perform certain corrections of the undesired auto-fluorescence signals [137]. Other measurement factors like imperfect filtering, different light sources as well as of different analyzing software influence the outcome of *in vivo* measurements too. Even though all fluorescence *in vivo* imaging systems are rapid, painless and harmless to the animals, they are distinguished by the differences in sensitivity, handling, evaluation possibilities as well as by the functionalities in removing auto-fluorescence and scattering artifacts.

C 1.6. Measurement systems for optical *in vivo* imaging

The development of small animal imaging systems has progressed rapidly over the last 10 years. A wide variety of approaches and components using fluorescent or bioluminescent signals were developed [18; 138-140]. Bioluminescent systems have certain restrictions and are generally used for luciferase genes and with luciferin substrates as reporters [141]. These systems are promising but limited to special areas of application and therefore will not be further discussed in the current work.

Fluorescence based imaging systems require an external light source to excite the fluorophores. In the last 5 years, the Maestro imaging system and more than 5 other pre-clinical imaging systems were launched to the market [23]. This emphasizes the wide range of approaches and capabilities. All these systems are either reflectance mode based (light source and detectors are located on the same side of the tissue) or transmission mode based, which is constructed like a transmittance light microscope [130].

Another main differentiating characteristic of these imagers is the light source itself. Broad beam imagers are based on xenon, tungsten or halogen lamps. Other source systems are either LED- or laser-based [23]. Systems with broad beam light sources are simple, relatively inexpensive, provide rapid acquisition and can be applied for various dyes. The excitation wavelength for each respective dye can normally be adjusted using special light filters. Broad beam systems are generally configured in the reflectance mode. However, this increases the light scattering effects. Fluorescence emissions of fluorophores are overlaid by non-specific auto-

fluorescence signals. This requires the effective filtering of excitation as well as of emission light. But those systems allow measuring a large variety of VIS and NIR dyes.

In the beginning of this work, the newly launched fluorescence imager: Maestro *in vivo* fluorescence imaging system from Cambridge Research & Instrumentation (Cri), United States (now PerkinElmer (Caliper Life Sciences), United States) was chosen to evaluate the possibilities of fluorescence imaging. The Maestro is a reflectance mode system equipped with a broad beam xenon lamp.

C 2. The Maestro *in vivo* imaging system

C 2.1. Instrumentation

The instrumentation design of the Maestro *in vivo* fluorescence imaging system is shown in Figure 13. The Maestro system is equipped with a 300 Watt Cermax-type, xenon lamp. The lamp emits light in the range between 500 nm and 950 nm. Undesired light can be blocked by one out of six available excitation filter (Figure 13 a, left).

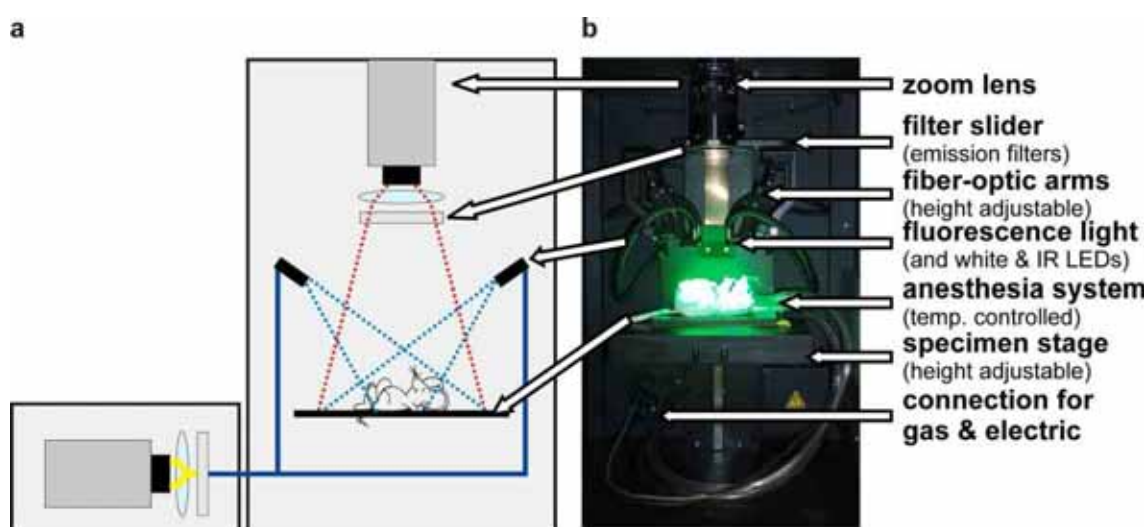


Figure 13: Schematic illustration (a) of the main Maestro *in vivo* imaging components and a photograph (b) of the imaging unit of the Maestro *in vivo* imaging chamber.

The excitation filter specifications for all available Maestro filter sets are given in Table 1. As specified in the table the excitation filters have comparable narrow pass widths. Light beyond the limits is blocked completely. Only light of a certain wavelength range can pass the respective filter and excite the fluorophore. This reduces the amount of auto-fluorescence.

Table 1: Available Maestro filter sets.

Filter set	Excitation filter	Emission filter	Standard acquisition setting
Blue	445 to 490 nm	515 nm	500 to 720 nm, in 10 nm steps
Green	503 to 555 nm	580 nm	550 to 800 nm, in 10 nm steps
Yellow	575 to 605 nm	645 nm	630 to 850 nm, in 10 nm steps
Red	615 to 665 nm	700 nm	680 to 950 nm, in 10 nm steps
Deep red	671 to 705 nm	750 nm	730 to 950 nm, in 10 nm steps
NIR	710 to 760 nm	800 nm	780 to 950 nm, in 10 nm steps

Fiber optics and height adjustable arms ensure that the excitation light (Figure 13 a, blue line) illuminates the object homogeneously. Emitted fluorescence light (Figure 13 a, red dotted line) passes an appropriate long pass emission filter (specified in Table 1) which blocks the excitation light completely. The blocking of light with lower wavelengths by the long pass emission filter minimizes also the amount of auto-fluorescence light that can interfere with the desired specific fluorescence signal.

Afterwards, the emission light passes an objective which includes a downstream tunable solid-state liquid crystal element filter (Figure 13 a, top, specified in Table 1). These liquid crystal element allow to control that only specific wavelengths in predefined intervals can pass the objective (10 nm intervals are by default predefined). By this, only desired wavelengths are detected by the scientific grade charged-coupled device (CCD) light sensor which acquires the measurement images.

C 2.2.Measurement fundamentals

Measurements using the Maestro *in vivo* imaging system are performed in three steps:

- (1) Acquisition of multispectral fluorescence images
- (2) Spectral unmixing and auto-fluorescence removal
- (3) Analyses of measurement files

These three main imaging steps are common for all *in vitro*, *ex vivo* and *in vivo* experiments. An *in vitro* pH measurement was used as an example to discuss the three steps briefly in the following.

This experiment was one of the prerequisites for the *in vivo* pH detection of *in situ* forming implants (see section G Long-term *in vivo* pH measurements of *in situ* forming PLGA implants). Within the experiment, three *Eppendorf* cups filled with

aqueous solutions of different pH values (pH 5, pH 6 and pH 7) were dyed with SNARF-4F. As described above the emission spectrum of this dye undergoes a pH-dependent wave length shift which can be afterwards used for unmixing and analyzing tests. Within the experiment, all three *Eppendorf* cups were imaged simultaneously.

C 2.3.Acquisition of multispectral fluorescence images

The multispectral analyses are based on the principle that all fluorescent molecules have unique emission spectra. If a fluorescent sample is excited, the emitted fluorescence is distributed over a range of wavelengths of varying emission intensities. To ensure the detection of the unique wavelengths, the Maestro software controls a tunable liquid crystal filter and the CCD chip. This allows the automatic acquisition of a set of multispectral images at predefined wavelength intervals. Figure 14 depicts the resulting images. The pictures were acquired with the green filter set between 550 nm and 800 nm and additionally with the yellow filter set between 700 nm and 850 nm using a predefined wavelength interval of 50 nm. All other measurements within this research work were performed with intervals of 2 nm or 10 nm. The start and the end wavelengths were defined in accordance to the respective filter set and the corresponding acquisition settings (compare Table 1). An acquisition in 2 nm steps increased the available spectral information while extending the measurement time. A recording in 10 nm steps accelerated the measurement, which minimizes motion in the *in vivo* records.

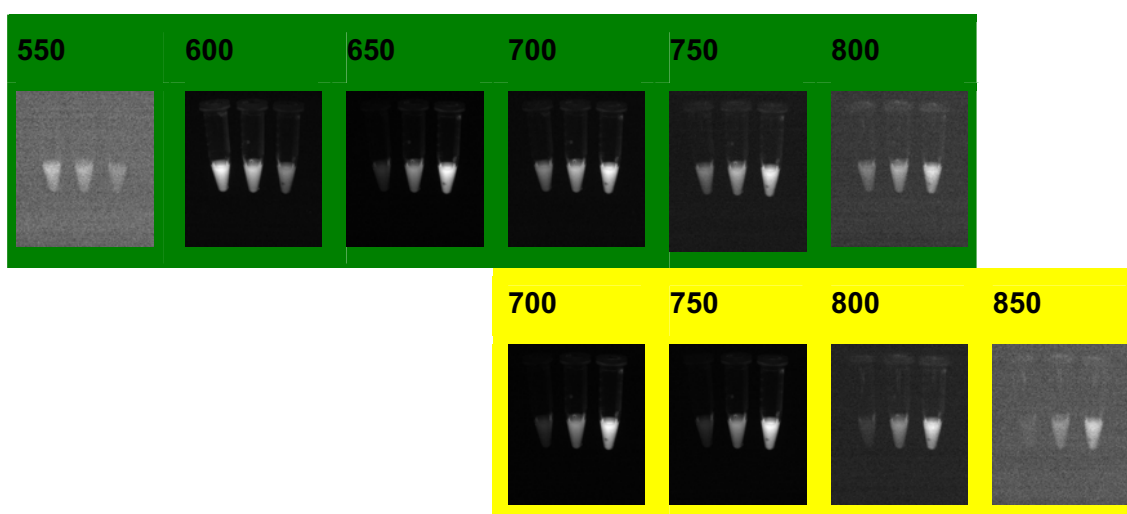


Figure 14: Two grayscale image sets (50 nm steps, top: green filter set, bottom: yellow filter set) of a sample pH measurement (3 *Eppendorf* cups, pH 5, 6 and 7, dyed with SNARF-4F).

The CCD chip records one 12 bit file (intensity values between 0 and 4,096) at each wavelength interval. Images of the files captured in 50 nm intervals are exemplarily shown in Figure 14. As the emission intensity and consequently the signal to noise ratio is normally very low at the beginning and at the end of a measurement set (see also Figure 16), the overall signal intensity for the visualization is amplified to display slight intensity variations. Images are grey with high noise levels. Images at the maximum emission wavelengths have a very high signal to noise ratio. The total signal is not amplified and the images have an excellent contrast ratio. Thus the background is displayed black and the measured emission graduated white. For all pixels in the images there is a corresponding intensity value which is used for the unmixing calculations.

Altogether, each pixel displayed in the image is related to the measured intensity value of the probe at this wavelength.

Intensity values of all images, captured at each defined wavelength interval are stapled to one working file: '*cube*' (Figure 15). The *cube* is displayed as a red-green-blue (RGB) color image. The colors are related to the respective acquisition wavelengths. This facilitates the manual handling in selecting for example a defined region of interest (ROI) without influencing the software analysis.



Figure 15: Image of a Maestro working file: '*cube*'. Within this *cube* all recorded images shown in Figure 14 are stapled. The file is automatically RGB colored which is helpful for the analyzing process.

Each single pixel in the *cube* file contains the intensity information of all images stapled in the *cube* file. The more images were made, the more information is available for each pixel of the *cube*. Based on the intensity values of all single images, the emission spectrum can be extracted for each pixel or group of pixels of the *cube*. This spectrum varies more or less from pixel to pixel and is specific for each respective fluorescent sample.

C 2.4. Spectral unmixing and auto-fluorescence removal

A fluorescence emission spectrum can be extracted manually or automatically by combining the spectral information of a certain group of pixels. This emission spectrum is composed of at least two single spectra: the emission spectra from the dye itself and the background signal. In the case of the imaged *Eppendorf* cups in Figure 15, the spectrum is composed of:

- The SNARF-4F emission spectra (varying depending on the respective pH value in the *Eppendorf* cup) and
- The potential signal of the plastic material of the *Eppendorf* cup itself.

However, also the overlapping of two or more emission spectra can occur. This is for example the case if different dyes are imaged simultaneously or if the spectral shift of a dye due to diversified surrounding properties occurs. Also the spectral change caused by *in vivo* interactions could result in varying spectra.

For further detailed analysis the isolated dye spectrum loaded into a spectral library is needed. Disturbing background signals must be recomputed. Therefore, the Maestro *in vivo* imaging system uses patented algorithms. Those, allow auto-fluorescence removal, spectral unmixing and fluorescence quantification analyses.

Generating the spectral library is a crucial step within the spectral unmixing process. The spectral library is the basis for the analysis of all *cubes* within a series of measurements. Spectral libraries within this research work were mostly be generated manually. Therefore, control samples measured under same conditions as the probes itself were used. Many main prerequisites had to be clarified especially for *in vivo* experiments such as:

- Is the emission spectrum changed by surrounding properties or overlaid by other spectra?
- Are *in vitro* and *in vivo* spectra comparable?
- Does the spectrum depend on the measurement depth?
- Do different body tissues have differentiating auto-fluorescence signals?
- Is the auto-fluorescence depending on the measurement depth of the fluorophore in the body?
- Is the background signal depending on the wavelength of the excitation light?
- Is the spectrum itself and/or the ratio between the dye and the background spectrum exposure time dependent?

For advanced spectral calculations using other software, generated spectral libraries can also be exported. Figure 16 depicts the isolated spectra of the sample *cube* shown in Figure 15.

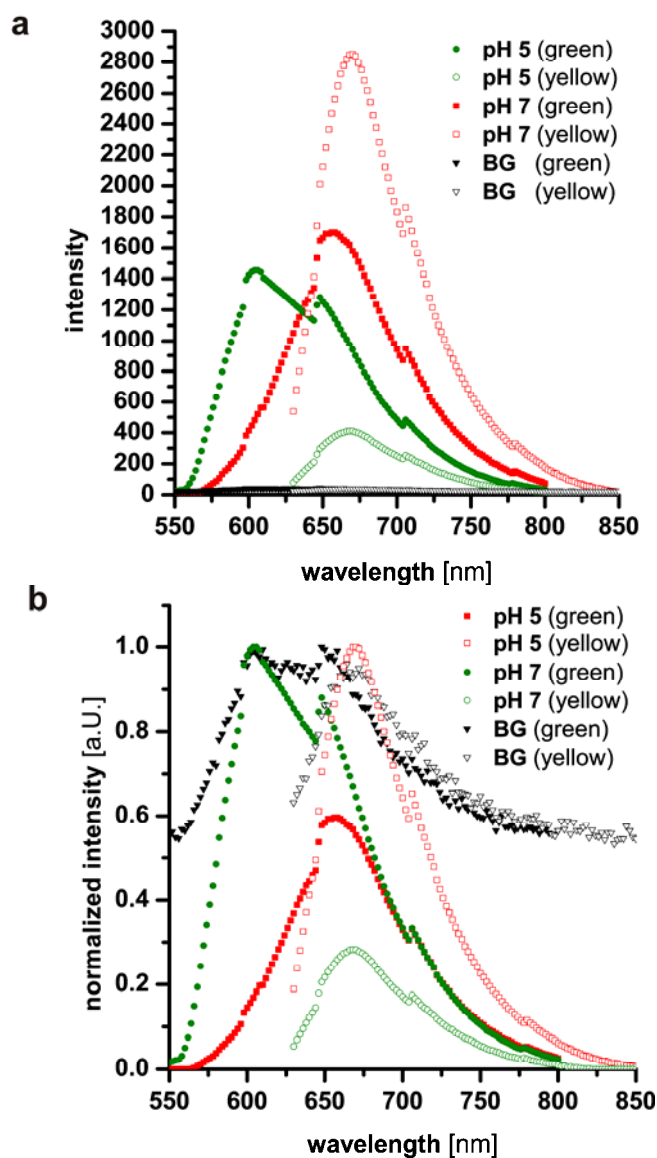


Figure 16: Intensity weighted (a) and to the maximum, normalized intensity (b) graphs of the isolated SNARF-4F emission spectra at pH 5 and pH 7 of the left and right *Eppendorf* cup shown in Figure 15. The background signal was extracted measuring empty plastic *Eppendorf* cups under same conditions. All measurements were performed using two filter sets (green, yellow).

The generated spectra can be used to analyze the *cube* file. This spectral unmixing step is based on mathematical disentanglement of the measured spectra. The Maestro software calculates for each pixel in the *cube* if the pixel is either assignable to the background signal, to the spectral species of the dye or proportionately to both of them. The software has to consider that signals might variably be mixed also with

different, unknown amounts of dyes and auto-fluorescence [142]. Thereby, the software estimates the spectral shape of the putative, pure component based on spectral differences between the background and the dye spectra. By the help of the software the signals can be differentiated and quantitatively unmixed. Even very similar spectra with varying peak emissions of no more than 2 nm to 3 nm can be unmixed reproducibly [137; 143]. In the unmixing analysis, each pixel of the *cube* can be fully, partly or not assigned to a single spectrum of the used respective reference library. Using this data, respective intensity weighted grayscale images are generated for each spectrum of the used spectral library (Figure 17).

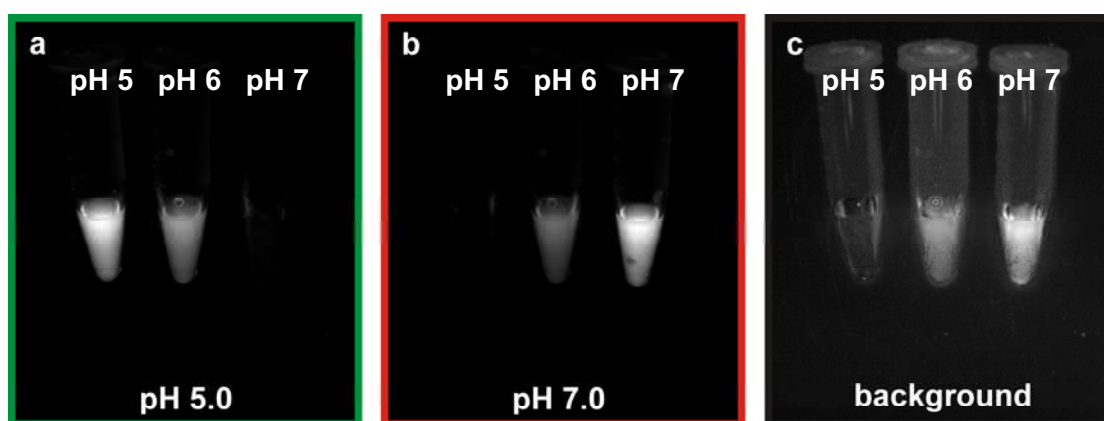


Figure 17: Unmixed grayscale images of the *cube* (Figure 15). Each picture summarizes the pixel information which was assigned to the extracted reference spectra (shown in Figure 16) of pH 5 (a), pH 7 (b) and the background (c).

C 2.5. Analyses of measurement files

Various strategies can be applied for further analyses of the obtained, unmixed grayscale images. The Maestro software enables an advanced image processing for the visualization of the fluorescence allocation as well as of data analysis to determine values like the threshold signal areas [144]. The evaluation of the best and most meaningful analyzing method either image processing and/or data analysis has to be identified in numerous preliminary experiments.

The image processing is based on the obtained individual component grayscale images which are calculated after the unmixing step (Figure 17). Based on the grayscale distribution in the files an incremental jet color profile can be used to generate intensity-weighted images (Figure 18 a and b).

Pixels with maximum intensities are set to dark red and pixels with zero fluorescence to black. In between there is a gradation from red to orange, yellow and then to light

and to dark blue. This allows the visualization of intensity distributions in the respective extracted signal images.

The same principle can be used for a set of chronological sequences of images analyzed with the same reference spectra named as 'compare imaging' function. This enables to analyze multiple grayscale images within a measurement series related to their individual measurement conditions. Time-dependent variations can be displayed independently from varying measurement conditions like different exposure times. Also RGB composite images can be generated based on the unmixed grayscale images. Those RGB images (unmixed composite images) enhance the visual expressiveness of the unmixed grayscale images. Conclusions about the formation of separated signals in the *cube* can be made. Unmixed RGB pictures are generated while allocating respective manually chosen colors to the grayscale spectrum. In Figure 18 c these principles were used exemplarily. Green was assigned to pixels allocated to the pH 5 spectra, red to the pH 7 emission spectra and black to the unmixed background signal.

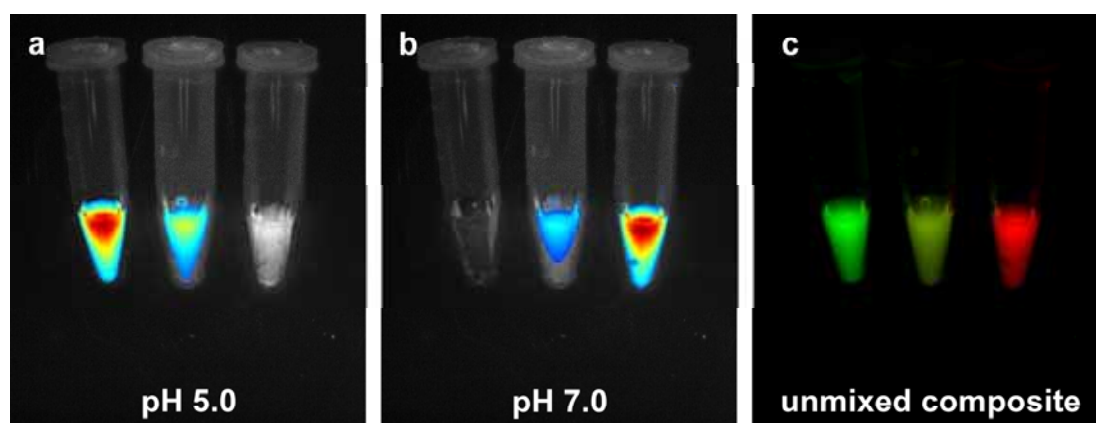


Figure 18: Intensity weighted images (a and b) of the corresponding unmixed grayscale pictures. Unmixed composite image (c) generated in assigning green to pH 5, red to pH 7 and black to the background signal.

Image processing using algorithms of the Maestro software allow the visualization of imaging results. However, the underlying data is quantitative. Intensity information is available for each pixel in an unmixed grayscale image which was allocated to the respective reference spectrum.

Based on this underlying data several parameters can be calculated by the Maestro software for a defined region of interest (ROI):

- Average signal, as the average intensity value of all pixels in the ROI
- Total signal, as the sum of all the pixel intensity values in the ROI
- Total signal related to the exposure time
- Maximum signal, as the maximum pixel intensity value included in the ROI
- Maximum signal related to the exposure time
- Area as the number of pixels or the size of the ROI

For further calculations, these generated data can also be exported to spreadsheets and other analyzing programs like Microsoft Excel.

Altogether the Maestro analyzing software provides a variety of functions which have to be evaluated for each project as well as to each series of measurements, in order to identify the analyzing method with the highest expressiveness for the respective research objective.

Chapter II: Results of pre-clinical in vivo studies of polymers

D Long-term in vivo biodistribution studies of i.p. injected high molecular weight PVA

- (I) **Schädlich, A.**, Naolou, T., Amado, E., Schöps, R., Kressler, J., Mäder, K., (2011) Noninvasive *in vivo* monitoring of the biofate of 195 kDa poly(vinyl alcohol) by multispectral fluorescence imaging. *Biomacromolecules* 12 (10): 3674-3683.
- (II) Jiang, Y., **Schädlich, A.**, Amado, E., Weis, C., Odermatt, E., Mäder, K., Kressler, J., (2010) In-vivo studies on *intraperitoneally* administrated poly(vinyl alcohol). *Journal of Biomedical Materials Research Part B- Applied Biomaterials* 93B (1): 275-284.
- (III) **Schädlich, A.**, Jiang, Y., Kressler, J., Mäder, K., (2010) Tracking the *in vivo* fate of high molar mass poly(vinyl alcohol) using multispectral fluorescence *in vivo* imaging. *Scientifically Speaking News (Controlled Release Society)* 27 (2): 15-16. **(Cover Story)**

D 1. Summary

Long-term *in vivo* studies of *i.p.* administered high molecular weight (195 kDa) PVA were performed to investigate the possibilities and constraints of using the non-invasive fluorescence imaging technique for the characterization of the water soluble polymer PVA [1-3]. To examine the body distribution, accumulation, and elimination processes by means of fluorescence imaging, the polymer had to be labeled with fluorescence dyes. For this purpose, two different dyes, either TMR (a rhodamine dye) or Alexa Fluor 750 (a NIR dye) were covalently bound to the PVA backbone by the group of Prof. Dr. habil. Jörg Kreßler [1; 2]. Both covalent labels were stable *in vivo* and had different spectral and optical properties. Imaging the TMR and the NIR labeled PVA allowed thorough *in vivo* biodistribution studies over several months.

It was observed that after *i.p.* injection into nude mice, the labeled PVA was mainly distributed by passive diffusion processes which were accelerated by the motion of the gastrointestinal tract and also after the PVA uptake into the bloodstream. An imaging of the blood vessels after 24 h confirmed the long-term circulation ability of the water soluble polymer in the bloodstream [3].

Non-invasive fluorescence imaging experiments indicated that PVA is highly accumulated in the different body fat tissues such as abdominal fat, kidney fat and also in fat layers under the skin [1]. Analyzing small spectral variances between the fluorescence emissions of labeled PVA from different body fat tissues, multispectral fluorescence imaging allowed for the first time even to differentiate non-invasively between the accumulations of PVA in different fat tissues. In addition, the PVA accumulations in the fat depots of male and also female mice were quantified over more than 6 months. This enabled calculation of the different release rates for both genders. The respective analysis indicated to a continuous, long-term release of PVA. *Ex vivo* fluorescence imaging studies of both labeled PVA polymer batches and additionally performed confocal microscopy studies confirmed the observed enrichment effect. It has been found that PVA molecules are accumulated in high concentrations between fat cells. Fluorescence imaging of the *in vivo* stable NIR labeled PVA polymer enabled further studies of PVA accumulation, its release and elimination pathways also in deeper body tissues as well as in organs which are highly supplied with blood [1]. High intensity fluorescence signals were detectable in the kidneys for up to 3 days *in vivo*. This confirmed urinary excretion studies which were performed with TMR labeled PVA [2]. Urine samples were collected and *in vitro* imaged by the Maestro imaging system. The amount of excreted PVA decreased over 5 days until the concentration fell below the detection limit of the imager [2]. This confirmed previous PVA studies in rabbits [34]. A slight accumulation of high-molar mass PVA was also detected in the liver in *ex vivo* experiments. This effect could be attributed to the high level of blood supply to the liver causing the preferential transport and accumulation of labeled PVA. Finally, PVA was eliminated from the liver by feces. Nine months after *i.p.* application, the PVA-NIR fluorescence in the liver was below the detection limit. Therewith, a complete elimination of PVA from the organism can be expected [1]. Based on the studies performed the accumulation of PVA molecules in various fat tissues, observed *in vivo* and confirmed *ex vivo*, seems to be non-critical for clinical PVA use. No evidence indicating that PVA could accumulate permanently in body tissues or that it is toxic to cells was found within these studies. The results regarding the *in vivo* release of PVA from fat tissues

Chapter II: Results of pre-clinical in vivo studies of polymers

attested PVA to be potentially suitable for a controlled long-term release of bound drug molecules or proteins. Within these studies it has been shown that fluorescence imaging is very helpful tool for the pre-clinical characterization of the biodistribution and excretion pathways of polymers.

Chapter III: Results of pre-clinical *in vivo* studies of nanoparticles

E In vivo characterization of nanocarriers and their potential capability in cancer therapies

- (IV) **Schädlich, A.**, Rose, C., Kuntsche, J., Caysa, H., Mueller, T., Göpferich, A., Mäder, K., (2011) How stealthy are PEG-PLA nanoparticles? An NIR *in vivo* study combined with detailed size measurements. *Pharmaceutical Research* 28: 1995-2007.
- (V) **Schädlich, A.**, Caysa, H., Mueller, T., Tenambergen, F., Rose, C., Göpferich, A., Kuntsche, J., Mäder, K., (2011) Tumor accumulation of NIR fluorescent PEG PLA nanoparticles: impact of particle size and human xenograft tumor model. *ACS Nano* 5 (11): 8710-8720.

E 1. Summary

It is known that serious side effects occur very often due to nonspecific distributions of chemotherapeutic agents to both cancerous and normal cells. Often this is also the reason why the cancer therapies are terminated. To avoid this, drug carriers are needed to deliver their toxic cargo specific to cancer cells. The particle size distribution of the formulation is one of the key parameters for the nanoparticle accumulation in tumor tissues [59; 61; 62; 145].

To investigate the influence of particle sizes and to research the nanoparticle biodistribution, accumulation and elimination processes in detail, *in vivo* and *ex vivo* fluorescence imaging studies were combined with thorough particle size characterizations [4; 5]. Polyethylene glycol - polylactide acid (PEG-PLA) block copolymers were synthesized in the group of Prof. Dr. Achim Göpferich and were used for the production of defined, stable, and nontoxic NIR dye-loaded nanoparticle batches [52]. PEG with an average molecular weight of 2000 Da was covalently bound to PLA to prolong the estimated *in vivo* circulation time of the NPs [4]. Nanoparticles were lyophilized to assure long-term stability [52]. Performed particle size experiments indicated that even aqueous dispersions, stored at 5 °C were stable

over at least 3 months. Cell toxicity experiments with PEG-PLA NPs showed that they are biocompatible and non-toxic to CHO and L929 cells [4; 52].

To investigate the size dependent *in vivo* fate of PEG-PLA nanoparticle, well-defined batches varying in size were needed. Therefore, asymmetrical field flow fractionation (AF4) coupled with multiangle laser light scattering (MALLS), photon correlation spectroscopy (PCS) and transmission electron microscopy (TEM) were used to determine the particle sizes of produced nanoparticle batches.

The results of AF4/MALLS showed that even in batches with rather low polydispersity indices (e.g. PCS z-average = 166 nm, PDI = 0.13), 10 % of the nanoparticles were smaller than 48 nm (D10) and the same amount of particles was larger than 230 nm (D90) [5]. This confirmed the need to combine different size measurement techniques for detailed particle size characterization as consumption for size-dependent biodistribution studies. For *in vivo* experiments several nanoparticle batches varying in size were produced and characterized [5]. The particle size z-averages of the batches (between 111 nm and 166 nm) are in the size range which is reported to be best suitable for tumor targeting [55].

Initial *in vivo* fluorescence imaging experiments were performed with Nile red (NR) loaded nanoparticles [4]. The results indicated the fast release of the NR dye from the particles and the rapid dye elimination from the bloodstream. The incorporation of the highly hydrophobic NIR dye DiR which is not released from the particles enabled the detection of circulating nanoparticles in the bloodstream for up to 6 h after injection [4]. This time period should be sufficient for the accumulation of nanoparticles in tumor tissues.

The *in vivo* fate of produced NIR nanoparticles was carried out in nude mice using the Maestro *in vivo* fluorescence imaging system [5]. The multispectral fluorescence imaging technique made it possible to follow the *in vivo* fate of the particles non-invasively even in deep tissues over several days. These experiments were combined with detailed fluorescence *ex vivo* imaging studies. The combination of *in vivo* and *ex vivo* imaging appeared to be a promising approach to study nanoparticle accumulation in different tissues and organs. Therefore, a new calculation approach was developed to calculate the total and maximum fluorescence intensities [4]. This enabled the comparison of nanoparticle batches with varying fluorescence intensities and provided the basis for the determination of the influence of varying particle sizes on the *in vivo* fate.

Based on these results tumor accumulation studies were performed in order to investigate the influence of particle sizes to their accumulation potential in tumor

tissues [5]. For this purpose, two human xenograft tumor models with different shapes and growth rates: the colon carcinoma (HT29) and the ovarian carcinoma (A2780) were chosen.

Non-invasive multispectral fluorescence imaging using the Maestro *in vivo* imaging system enabled the simultaneous combination of the visualization of DsRed2 expressing HT29 xenografts and the *in vivo* tracking of NPs [5]. *Ex vivo* imaging together with additional confocal microscopy studies facilitated to reveal also information about the accumulation characteristics of the nanoparticles inside the tumor tissues. The confocal microscopic pictures confirmed the *ex vivo* imaging results. The particles could be detected between fluorescent, DsRed2 expressing cells [5]. *In vivo* studies with HT29 and A2780 tumor bearing mice indicated that nanoparticles accumulated in both tumor models. The *ex vivo* studies furthermore demonstrated that the accumulation pattern mainly differed between both researched tumor models. Nanoparticles enriched primarily in the tumor center in HT29 tumor tissues whereas A2780 showed no centralized nanoparticle accumulation [5].

To investigate the size dependent tumor accumulation ability in both tumor models the respective total and maximum fluorescence intensities over several hours were calculated for three NIR PEG-PLA nanoparticle batches [5]. Two nanoparticle batches (111 nm and 141 nm in diameter) accumulated efficiently in the human xenograft tumor tissues. The highest tumor enrichment was found for the nanoparticle batch with a z-average of 111 nm for the A2780 tumors. Whereas the 141 nm nanoparticles were most accumulated in HT29 tumors [5]. This emphasized the fact that slightly larger nanoparticles (z-average of 141 nm) seems to be beneficial for accumulations in necrotic (HT29) tissue, whereas a slightly smaller size (z-average of 111 nm) was preferable for vascular permeation. Light microscopic studies of thin section slides of tumor tissue confirmed the accumulation in necrotic tissues for HT29 xenografts. Bigger nanoparticles (z-average of 166 nm) were not effective in both xenografts [5]. It can be expected that they are eliminated rapidly by the liver and therewith the accumulation in the tumor tissues was ineffective. Visualizing the nanoparticles and the dyed cells simultaneously in *in vitro* experiments with A2780 and HT29 cell layers using confocal microscopy indicated the ability of the particles to bind to tumor cells.

Based on these experiment results, the combination of extended accurate size determinations with *in vivo* fluorescence imaging technique appeared to be a very promising approach to study the size dependent fate and the tumor accumulation potency of nanoparticles.

F Investigating the potential toxicity risk of nanocarriers

- (VI) **Schädlich, A.**, Hoffmann, S., Mueller, T., Caysa, H., Rose, C., Göpferich, A., Li, J., Kuntsche, J., Mäder, K., (2012) Accumulation of nanocarriers in the ovary: A neglected toxicity risk? *Journal of Controlled Release* 160 (1): 105-112. **(Cover Story)**

F 1. Summary

Many different nanocarrier formulations are already frequently used in modern pharmaceutical therapies or are intensively researched to be used in future for example in anticancer therapies [53; 60; 146]. However, compared to traditionally used drug dosage forms, the application of nano-scaled formulation systems may result in different *in vivo* behaviors and in new potential toxicity risks due to varied physicochemical properties.

Therefore, this research work was besides the characterization of the biodistribution and the tumor accumulation behavior also focused on unusual distribution and accumulation patterns of injected nanocarriers, indicating potential toxicity risks. Within the performed *in vivo* characterizations it was found that used PEG-PLA nanoparticles seems to accumulate in rodent ovaries after *i.v.* administration [6]. The further research was focus to investigate the identified accumulation in ovarian tissues in detail. The effect was confirmed in different mouse species and also in Wistar rats. Numerous additional *in vivo* fluorescence imaging studies were performed while using other nanocarrier systems (nanoparticles, nanocapsules and nanosized lipid emulsions) which were differently composed, including multiple excipients, carrier sizes and surfaces. An accumulation in specific compartments in the rodent ovaries was found for all original and additional researched nanocarriers [6].

All tested nanocarrier batches with diameters between 45 nm and 350 nm accumulated in high concentrations in the ovaries, whereas tested polymers were not accumulated [6]. A comparison of three nanoparticle batches varying in size led to the conclusion that bigger particles seemed to be more accumulated than smaller ones. The accumulation found *in vivo* was further characterized by *ex vivo* fluorescence imaging and confocal microscopy. Based on the size and structures of the accumulation areas identified in the performed experiments, enrichments in tertiary vesicular follicles are possible. However, the nanocarrier accumulation in

cells of the *corpus luteum* seems to be more likely. The *corpus luteum* is formed from the wall of the ruptured follicles after the ovulation. It is described that the rates of tissue growth and angiogenesis in the *corpus luteum* rival those of fast growing tumors [147]. This supports the assumption that the accumulation of the nanocarriers in the *corpus luteum* is related to the enhanced permeability and retention effect known for tumor tissues. By this, nanocarriers have the ability to be retained in tumor tissues which is a highly size dependent effect.

Altogether, this is the first study which comprehensively investigated the accumulation of nanocarriers in the ovaries. Reasons, why the nanocarrier accumulation had not yet attracted attention might be the fact that often male mice or not yet pubescent female mice are used. In addition, the nanocarrier accumulation appears to be restricted only to certain local parts of the ovaries. Thus the overall amount of fluorescence signal from the total ovary tissue was rather small and comparable to other organs and tissues where no nanoparticles accumulated [6]. Usually, in *in vivo* studies the average nanocarrier amounts are related to the organ/tissue weight or to the administered dosages. This information is then used to compare different body compartments. Therefore, the accumulation of nanocarriers in the ovaries might remain unnoticed although it can be concluded based on a small number of other published results which refer to *in vivo* and *ex vivo* studies with different kinds of nanoparticles and liposomes [148-154]. Newly published studies identified also accumulations and/or potential toxicological effects of silver and of titanium dioxide nanoparticles as well as of nanocapsules in rodent ovaries [155-157]. These results confirm the found accumulation of nanocarriers.

It has to be noted that the accumulation of the nanocarriers in the ovaries does not necessarily need to result in a risk for the widespread use of nano-scaled carrier systems in medicine. Especially due to the fact that the accumulation is limited to special regions in the ovaries, the toxic risk for humans might be rather low. However, this effect should be further investigated, particularly in other species and with other nanocarriers, to elucidate the mechanism of the accumulation. Also the chances of these results for a new ovarian targeted therapy should be taken into consideration.

The results strongly emphasize the relevance of early explorative *in vivo* studies in the development of drug delivery systems using sensitive analytical imaging techniques like fluorescence imaging using NIR fluorescence dyes.

Chapter IV: Results of pre-clinical *in vivo* studies of *in situ* forming implants

G Long-term *in vivo* pH measurements of *in situ* forming PLGA implants

(VII) **Schädlich, A.**, Kempe, S., Mäder, K., (2013) Long-term *in vivo* pH measurements of *in situ* forming PLGA implants using multispectral fluorescence imaging. Submitted to Journal of Controlled Release. **(under peer-review)**

G 1. Summary

In the last decade the number of peptides and proteins used for medicinal therapies increased continuously. However, peptide and protein delivery has been a challenge due to their limited stability during preparation, storage and *in vivo* release. They have to be parenteral administered e.g. via *intramuscular (i.m.)* or *s.c.* routes. Several parenteral drug delivery systems like microspheres, solid implants and *in situ* forming implants were developed for peptide delivery to achieve constant therapy levels and to reduce the application frequency [67; 158]. These formulation systems enable a controlled release of incorporated therapeutic agents over several days, weeks up to months and improve the therapy compliance of the patients. Furthermore, these depot formulations minimize the fluctuation of drug plasma levels and therewith undesirable side effects. *In situ* forming implants can be injected with syringes into the target site, where the implant is formed immediately. PLGA is the most widespread polymer used for implants. One of the major concerns using PLGA is its uncontrolled pH drop in those controlled release drug delivery systems which can causing the instability of encapsulated drugs or proteins [76; 77; 159; 160]. Therefore, it is important to measure the microenvironment in PLGA implants and to understand the relationship between pH shift and the implant degradation.

In vitro EPR experiments showed that during incubation under 'physiologic' conditions the pH value can drop from pH 7.4 to values around pH 3 [7]. Due to fluctuating fluorescence intensities in *in vivo* surroundings as well as of the disturbing

auto-fluorescence of mouse tissues dyes with two (pH dependent) emission maxima at longer preferably wavelengths were needed. Only one dye, SNARF-4F (pKa of about 6.4) fulfilled those defined measurement requirements.

Thorough *in vitro* and *ex vivo* fluorescence imaging experiments were performed using the SNARF-4F dye to evaluate the influence of factors like auto-fluorescence of the skin, light absorption, intensity variations, measurement conditions and others. Those tests enabled the development of a method that allows calculating pH values independently from the fluorescence intensity. Therefore, a Boltzmann plot based on more than 40 *ex vivo* measured standard buffer solutions was computed [7]. Additionally visual evaluation of the captured fluorescence imaging measurement files was performed and tested *in vitro*.

All these tests were the basis to non-invasively measure and visualize the microclimate pH (μpH) value of PLGA implants in complex *in vivo* surroundings. In addition, the physically entrapping of the hydrophilic SNARF-4F enabled to measure the release profiles of the dye from the implant. It could be shown that the solvent/non-solvent exchange after injecting the PLGA/PEG 400 solution is very fast. After 1 h about 70 % of the PEG 400 was replaced by body fluids and the implant started to solidify. During the next hours body fluids and remaining PEG 400 were eliminated from the implant. After three days the emission intensity in the implant was smallest as the implant was completely solidified [7].

The μpH measurements revealed that within the first 2 - 3 days the μpH remains constant. Afterwards, the μpH decreased continuously to the lower pH detection limit of pH 5.0. This was found *in vivo* and *ex vivo*. The results are in good accordance with the current knowledge of the implant degradation processes [161].

The subsequent pH increase as well as the continuous dye release from the implant within this phase was measured additionally and visualized in detail. However, the pH drop caused by the PLGA degradation products was observed to be slower *in vivo*.

The results confirm some *in vitro* and *in vivo* EPR experiments and are in accordance with published *in vitro* confocal laser scanning microscopy measurements [78; 79; 159; 162-164]. The experiments showed that *in vitro* pH measurement results are not by implication transferrable for the estimation of *in vivo* behaviors. The obtained results underlined that the evaluated fluorescence imaging method is a non-invasive method which allows the mapping of μpH values *in vivo*.

Chapter V: Results of alternative application fields of fluorescence imaging

H Monitoring internal pH gradients in swelling multi-layer tablets

(VIII) Eisenächer, F., **Schädlich, A.**, Mäder, K., (2011) Monitoring of internal pH gradients within multi-layer tablets by optical methods and EPR imaging. International Journal of Pharmaceutics 417 (1-2): 204-215.

H 1. Summary

The techniques and principles in measuring pH values of *in situ* forming PLGA implants *in vivo* were as well applied for *in vitro* pH measurements in swelling multi-layer tablets. Varying pH values in different section of the human intestine highly influence the release and the uptake of especially ionizable drugs from tablets. The solubility of those drugs highly depends on the surrounding pH value. APIs which are not dissolved completely *in vivo* are normally not able to enter the blood circulation. Thus influencing the microclimate pH (μpH) within solid formulations is used to achieve pH-independent API release profiles.

Fluorescence imaging was used to measure μpH values non-destructive in swelling two-layer tablets [8]. The measured μpH gradients were compared with two other pH measurement techniques: incorporating pH indicator dye and cutting the tablets after different time points as well as with EPR imaging. The obtained results of all three methods were comparable. However the informative value and the research findings were different. Even though the developed principles of calculating pH values using fluorescence imaging were applied, comprehensive pretests had to be performed additionally to evaluate issues like the influence of used excipients, best suitable pH sensitive dye and the finally needed dye concentration.

To get a consistent measurement surface area and to limit the hydration process to one-dimension, the tablets were placed into transparent tubes with the exact size of the tablets. Thus the swelling of the tablets was only possible from the top and the bottom of the tablets [8]. This setup emphasized as the best method to measure the

μpH variation under the current experimental conditions. By means of fluorescence imaging the spatial μpH distribution of the tablet surface could be non-destructively obtained across the swelling process. However inner regions of the tablet were accessible only by cutting the tablet.

The fluorescence imaging results demonstrated that the incorporation of internal buffer substances as well as the nature of used matrix forming excipients strongly influences the μpH .

I Monitoring temperature distributions in tablets - caused by the tableting process

I 1. Summary

It is generally known that changes in temperature can have crucial effects on APIs. The processing and the storage of APIs below or above defined temperatures can cause chemical modification and degradation of the API. It is also known that increased temperatures in different parts of the tablet during the tableting process can lead to polymorph changes of the incorporated API [165]. Different temperature ranges in the tablet can be expected during the tableting process due to the heterogeneity of the pressure distribution [165].

Until now it is unclear if this is caused e.g. by the mechanical pressure, the choice and the humidity of the used excipients or the porosity of the tablet. Therefore, an *in situ* measurement system is needed which would enable to measure the temperature distribution during the tableting process.

To perform temperature burden measurements using fluorescence imaging a temperature sensitive dye had to be found which changes the fluorescence emission spectra at higher temperatures irreversibly. In addition the dye had to be very sensitive so that it can be added in low concentrations to prevent interactions with other excipients. In addition the dye had to change the emission spectra independently from pressure but immediately to changes in temperatures. Permatherm Concentrate Magenta 60° was identified to fulfill all identified requirements [165]. The dye has an irreversible color change between 40 °C and 80 °C. The existence of two emission maxima enabled to calculate the temperature independently from concentration and intensity changes.

Temperature calibration experiments were performed based on comparable principals which were emerged for the *in vivo* and *in situ* pH measurements [165]. Due to limitations of the Maestro software, emission spectra of desired ROI were exported and analyzed manually. The temperature which occurred during the tableting was fivefold determined for six mixtures and for three tableting processes [165]. The results demonstrated that temperature maxima varied depending mostly on used excipients and partly on the applied tableting conditions. It could be demonstrated that not only the used excipients influence the maximum temperatures. Also the specific humidity of the used excipients affected the temperature burden.

J In vivo and ex vivo characterization of nanocapsules

(IX) Li, J., **Schädlich, A.**, Hause, G., Vogel, J., Kuntsche, J., Groth, T., Mäder, K., Pre-clinical *in vivo* studies of oily core PEG-PLGA Nanocapsules using fluorescence imaging. **(in preparation)**

J 1. Summary

Compared to other colloidal carriers nanocapsules have the advantage to be able to incorporate comparable high API amounts. The nanocapsules are composed of a liquid core, which can be loaded with API and a solid shell. The distribution of the nanocapsules *in vivo* as well as their degradation is triggered by the varying composition and the thickness of the shell. It has been reported that hydrophilic polymers (e.g. PEG) on the surface can reduce the opsonisation and thus the uptake by the mononuclear phagocytic system (MPS) [4]. However there is a lack of data available concerning the *in vivo* distribution of nanocapsules and the effect of PEG on the surface of the nanocapsules. Therefore, two very lipophilic fluorescent dyes either DiI or DiR were incorporated into the oily core to characterize the *in vivo* fate of oily nanocapsules with different composed shells by means of fluorescence imaging [166]. This was performed using methods which were established for the *in vivo* and *ex vivo* characterization of nanoparticles [4; 5]. Comparable particle sizes (z-average around 150 nm) were measured for all tested nanocapsule batches [166]. *In vivo* fluorescence imaging results showed that these nanocapsules circulated in the bloodstream for several hours. This confirmed the effectiveness of the PEG surface. The highest nanocapsule concentration was determined in the MPS 24 h after *i.v.* injection. A reduced liver and spleen uptake was observed *in vivo* for batches with increased PEG amounts. *Ex vivo* quantification analysis reconfirmed this result. Additional *ex vivo* confocal microscopic experiments proved the previously found accumulation of polymeric nanocapsules in the ovaries [6; 166].

K Monitoring the in vivo efficiency of rhBMP-2 loaded microparticles

- (X) Lochmann, A., **Schädlich, A.**, Nitzsche, H., Metz, H., Schön, I., Schwarz, E., Mäder, K., Quantitative Monitoring of the *in vivo* Efficiency of rhBMP-2 loaded PLGA and PEG-PLGA Microparticles by means of Optical Imaging, CT and BT-MRI. (in preparation)

K 1. Summary

The Bone Morphogenetic Protein 2 (BMP-2) is important for the development of bone and cartilages. The recombinant human osteogenic protein (rhBMP-2) is used in the United States for the treatment of bone defects. After implantation, the rhBMP-2 protein induces bone formation. However, the protein is quite unstable which requires the administration of high doses. Therewith, the therapies are very expensive by what they are accessible only to a limited number of patients. Research is focused to reduce the rhBMP-2 doses while developing controlled parenteral protein release formulations.

Micro-particulate drug delivery systems which proved to be promising were developed [167]. *In vivo* fluorescence imaging was used to research the biodistribution as well as the pharmacological effect on bone formation. The protein was labeled with Rhodamine B to research the rhBMP-2 delivery [167]. *In vivo* fluorescence imaging was also used for tracking the rhBMP-2 induced calcification progress which is an important parameter of bone formation. Therefore, a NIR fluorescent calcium chelator was *i.v.* injected one day prior the measurements [167]. Comparable principles as used for the detection and visualization of the accumulation of nanoparticles in tumor tissues were used to visualize and quantify the calcification progress as well the distribution of the rhBMP-2. Fluorescence imaging was performed up to 12 weeks after rhBMP-2 application and confirmed the calcification effect for all investigated formulations [167].

Chapter VI: Fluorescence pre-clinical imaging – an overall discussion of results

L Potential capabilities and limitations of pre-clinical fluorescence imaging

The results of this work confirmed that *in vivo* fluorescence imaging is a promising technology for pre-clinical research of parenteral drug delivery systems. Based on the presented current results as well as on the data from literature it is expected that fluorescence imaging will have great impact to future drug development studies [168]. The studies revealed the broad range of potential applications of the method. Fluorescence imaging allowed monitoring and visualizing of body tissues as well as the assessment of molecular biodistribution processes. Results showed that the imaging modality has a high specificity in analyzing different and a high sensitivity in detecting even smallest fluorescence concentrations. This fact is in concordance with the general knowledge about optical imaging [169]. Plenty of open questions related to fundamental capabilities and limitations of fluorescence *in vivo* imaging were raised at the beginning of this research such as:

- What is the optical resolution?
- Does reflection and absorption influence the measurements and what is the maximum depth of imaging?
- Which amount of dye is needed?
- What is the reproducibility of the method?
- Is the reproducibility related to the signal to noise ratio?
- Which dyes can be used and which sensitivity do they have?

Experiments performed emphasized the capabilities and limitations of fluorescence *in vivo* imaging and complemented insufficient knowledge when using the technique as a pre-clinical imaging tool.

M Major limitations of pre-clinical fluorescence imaging studies

It is known that a major limitation of fluorescence imaging is the lack of penetration depth of the light into body tissues [23; 88; 89]. The photon penetration into living tissue is highly dependent on its absorption and scattering properties [170]. Both, the scattering and the absorption of light are primarily related to the intensity and the wavelength of the excitation light and to the emission maxima of the fluorescence dye. This can result in low penetration depths of a few millimeters and thus highly influence the resolution of *in vivo* imaging records. The Maestro *in vivo* imaging system used within the current research is based on reflectance mode measurement principles and equipped with a broad beam xenon lamp. Laser systems can excite dyes to higher energy levels which enhances the underlying organ imaging. However, increased excitation laser power might also result in tissue photo damage. Another limiting factor is that laser systems do only excite certain wavelengths, which limits their use to a small number of special dyes.

As the Maestro imaging system uses a broad beam xenon lamp, the excitation intensity was default and the excitation light is filtered within the range between 445 nm and 760 nm by using six different optical filter sets. Thus, the optimal required wavelength range can be chosen individually for the dye used.

Another variable measurement parameter which mainly influences the measurements is the exposure time setting for each CCD frame. It was shown that lower acquisition exposure times reduced blurriness due to mouse breathing while they required high dye concentrations. Higher exposure times were needed if dye concentrations decreased over time. Simultaneously the noise level increased. Furthermore, it emerged that some experiments required constant exposure times over the whole series of experiments which required extensive evaluations and pretests [2].

N Major challenges of pre-clinical fluorescence imaging studies

N 1. The choice of the correct dye

When choosing appropriate dyes for an experiment, the advantages and disadvantages of different dyes were evaluated based on literature research and pretests. The selection was often hampered by the limited number of dyes for specific measurement issues. Using the Masetro *in vivo* imaging systems enabled due to a broad number of filters and of the multispectral measurement capabilities to measure various different dyes emitting at different wavelength ranges simultaneously.

As an example, this allowed measuring of two dyes emitting at different wavelength ranges within the PVA experiments. Therefore, the dyes TMR (emitting in the VIS range) and the NIR dye Alexa Fluor 750 were utilized. TMR allowed the differentiation of PVA accumulations in various fat tissues. The NIR dye facilitated the characterization of PVA elimination processes e.g. from the liver [1-3] as well as the measurement of the biodistribution in deep located body tissues, or in organs which are highly supplied with blood. NIR fluorophores have higher molar extinction coefficients. NIR light can deep penetrate organs due to considerably low absorption coefficients of tissues in the emitting region between 700 nm and 900 nm [79]. Therefore, the NIR dyes proved to be an optimal choice to study the biodistribution processes of drug delivery systems. NIR dye molecules covalently bound to PVA polymer chains permitted within performed *in vivo* studies imaging depths up to a few centimeters [1; 5; 6]. However, the overall use of NIR dyes was restricted. The numbers of NIR tracer molecules for special demands are either limited or even no NIR dyes are available for special requests e.g. to measure pH values or polarities. NIR dyes have commonly low quantum yields [171]. This required longer exposure times for pre-clinical measurements which increased the signal-to-noise ratio. At the same time, the number of pictures taken per image file had to be reduced, to kept measurement times in acceptable ranges and to avoid blurring of the images caused by mouse breath. Consequently, the lower number of single images reduced the spectral detail information of the emission fluorescence spectrum. Those appeared to be less characteristic [4]. This is enforced by the properties of the light and therewith the mechanism of light propagation in body tissues [130]. After excitation, the emitted

light is isotropically scattered in the tissue [131; 172]. The increased number of scattering events for NIR dyes in tissues reduced detectable information while spectra got smoother. This results in a loss of spectral information depending on the measurement depth [128]. Therefore, the exact localization of the emission light source was hampered.

Knowledge obtained within the PVA studies allowed preselecting dyes for all further *in vivo* studies. In the case of nanoparticle biodistribution studies it could be assumed that VIS dyes would have restricted the studies to analyze surface tissues. Thus NIR dyes had to be chosen to research the biodistribution, accumulation and elimination of nanoparticles in deep tissues and organs.

Also the way of incorporating the dye molecule into the drug delivery system has to be considered while choosing the best suitable one. Generally either physical entrapment or covalent labeling is the preferred technique. Whereas, dyes had to be labeled covalently to research the distribution in case of polymers they could be physically entrapped in nanocarriers.

Covalent labeling normally must be stable in *in vivo* surroundings. In addition it retrieves the risk that physicochemical properties e.g. of the polymer are influenced due to the general high molecular weights of the NIR dyes. Thus, the number of NIR molecules which were labeled to the polymer backbone was reduced to a minimum within PVA studies in order to preserve the properties of the PVA polymer [1].

For nanoparticle characterization NIR dye molecules were physically entrapped. Therefore, very hydrophobic dyes were required. Those cannot diffuse out of the drug delivery system until the carrier is degraded. The dialkylcarbocyanine dye DiR was chosen because of its high lipophilic properties [113-115] by what the dye is insoluble in aqueous media. Therefore a distinct leakage of the dye from the nanoparticles could be excluded [173; 174].

Nanoparticle studies proofed further that the emission spectra of NIR dyes are similar *in vitro* and *in vivo*. The penetration of emitted NIR fluorescence light through living tissue has no influence on the spectral emission profile [4]. Due to the above discussed loss of spectral information in NIR emission ranges, VIS fluorescent dyes were used if the detection of spectral changes was needed to characterize the drug delivery systems regarding physicochemical properties.

The detection of spectral changes was amongst others the basis for pH measurements in *in situ* forming implants as well as for pH and temperature measurements in tablets [4; 7; 8; 165]. Even smallest differences in the emitted fluorescence light spectra could be detected and used for extensive calculations.

However, based on the absorption and scattering properties of the light in the VIS wavelength range the measurements were limited to the near-surface areas. In case of performed *in vivo* pH measurements the detection limit was a few millimeters [7]. Summarized, it can be concluded that the choice of the correct dye depends on plenty individual experimental requirements and has to be considered previously.

N 2. Quantification – an impossible challenge in pre-clinical *in vivo* experiments?

In vitro, the fluorescence intensity is normally proportional to the concentration of the fluorophore and can be influenced e.g. by the spectroscopic properties of the emission light, the scattering effects of light and the technical equipment used. The magnitude of the *in vivo* emitted light strongly depends on a multiplicity of additional influencing factors. Many body components like haemoglobin and water but also chlorophyll in the fodder of the mice influences the emission of the light. Also parameters like the depth of the fluorescence source within the tissue, the density and homogeneity of the tissue itself as well as the absorption of the tissue influence measurements. Planar imaging systems like the Maestro *in vivo* imager which was used in the current work detect the fluorescence response which is projected to the surface of the living objects [175]. Quantification of the fluorophors as it is known from the nuclear medicine (determination of the percentage drug dose per respective organs) is at least not yet possible when fluorescence imaging is applied. In general, semi-quantitative data might be obtained using fluorescence imaging.

Within this research work, several approaches for the Maestro imaging system were investigated in order to emerge strategies allowing comparative semi-quantitative statements of different drug delivery systems.

For instance, pharmacokinetic information like circulation time would allow better interpretation of the effectiveness of polymers and of different sized nanocarrier batches. Detailed pretests were necessary in order to investigate potential analyzes strategies. The techniques known from the intravital microscopy such as the fluorescence intensity measurements in blood capillaries in surface tissue regions [176; 177] were tried to adapt. However, even in the cases when it was possible to visualize blood vessels indicating the circulating polymers and nanoparticles [3; 4], the quantification approaches failed. Fluctuating fluorescence intensities from the blood vessels could not be detected because of the limited resolution of the captured fluorescence images. Also the evaluation of HPLC methods to determine the dye concentration in blood samples failed due the complexity of the disturbing blood

components and the limited blood volume available for analytic measurements.

The combination of different visual analysis and calculation approaches using underlying data was a prerequisite for comprehensive characterization of drug delivery systems. Image analyses were performed for all experiments and allowed the *in vivo* localization of analyzed dyes in the body [1; 3-7]. The visualization possibilities and the compared to other pre-clinical techniques like MRI or CT high resolutions of the images was another benefit of fluorescence imaging. Results like the detection of accumulated dye in the ovaries were only found while using the visualization functions [6]. In combination with *ex vivo* results, studying the biodistribution, accumulation and elimination of processes was feasible. The Maestro imaging system enabled the monitoring of the multiple fluorescence probes for multispectral imaging approaches too [137; 178; 179]. Therewith, the spectral unmixing functionality enabled to visualize tumor tissues and accumulated nanoparticles simultaneously *in vivo* [5]. This facilitated meaningful pre-clinical results while importantly reducing the number of animal experiments.

The same multispectral measurement principles were also the basis for the visualization of changing pH distributions in *in situ* forming implants [7]. The multispectral functionality allowed further the development of an imaging strategy that visualizes the local temperature allocation in tablets which occurred during the tablet pressing process [165].

Another imaging analysis technique used was the compare imaging tool. This analyzing possibility enabled the comparison of different images within a measurement series. Thus individual images taken over time can be correlated even if they have not the same scaling or intensities due to varied bit-depths, exposure times and binnings [180; 181]. Conclusions regarding the biodistribution over time were made based on the visualization results of the intensity differences in the component images [1; 3-5]. The same function enabled the visualization of the dye intensity change over time in an *in situ* forming implant [6]. Therewith, statements regarding the micro-mobility in *in situ* forming implants were possible. The findings indicated the accumulation of degradation products which was in accordance to published EPR results [161; 182].

Other data analyses were based on ROI principles. These were used to extract total and maximum intensities from isolated emission images. Therefore, the underlying data of the unmixed greyscale images were analyzed. The ROI in the size of the whole mouse or in the dimensions of tissues or organs of performed *ex vivo* experiments were used. The total fluorescence intensity, calculated as the sum of all

fluorescent pixels within the ROI were assigned to a reference spectrum [181]. The maximum intensity reflects the intensity value of the pixel, having the highest intensity within the selected ROI. Both, the total and the maximum fluorescence intensities were exposure time weighted. This allowed comparing the data obtained at different exposure times, which was a prerequisite to measure at optimum, automatically defined measurement conditions. Thus the analyses made by means of total and maximum intensity calculations enabled to track the biodistribution of PVA for more than 180 days [3]. Comparative long-term studies between VIS and NIR labelled high molecular weight PVA provided detailed information about the biodistribution processes. The fluorescence emission of TMR was absorbed nearly completely by organs highly supplied with blood. Thus, the TMR signal was only detectable in the surface regions and analyses reflected only the accumulation in s.c. tissues. Due to the better optical penetration properties of NIR light, the accumulation in deeper tissues was investigated while analyzing total and maximum intensities of detected NIR signals. These semi-quantitative analyses underlined the importance to combine the optical properties of different dyes in order to obtain comprehensive pre-clinical information of the drug delivery system being researched.

Further approaches were evaluated to characterize the *in vivo* fate of nanoparticles. As discussed above, resolution limitations of the CCD camera chip restricted the analysis of blood vessels in order to calculate blood half-life times. Therefore, the total signals of the body were measured at different time points. The calculated values reflect the sum of all s.c. dye signals (from blood vessels, upper parts of liver and spleen). They indicated that 50 % of the initially detectable nanoparticles were eliminated in about 45 minutes and about 75 % in 95 minutes after injection [4]. Tumor accumulations as well as nanoparticle enrichments in various tissues and organs were measured using PVA characterization principles. Detailed additional experiments were performed *ex vivo* to exclude interdependencies between the detection of fluorescence signals from overlying body tissues. Reproducible conditions like the arrangement of organs, the positioning in the Maestro imaging system, incident angle of the light, etc. were addressed while performing a different approach. Organs or respective organ parts in case of intestine and liver, were placed into a transparent 24-holes well-plate [4-6]. Performed *ex vivo* imaging results confirmed the nanoparticle accumulation in organs as already detected *in vivo*. The total and the maximum intensity analyses were used for ROIs defined in the sizes of the well-plate holes. The direct comparisons of total intensities proved to be challenging due to the diversity of dye loadings and dye allocation e.g. in different

nanoparticle batches [4]. A new calculation approach was developed as basis for further evaluations of size-dependent tumor accumulation studies with different nanoparticle batches [4]. This allowed recalculating the effects of varying dye loadings reproducible. To exclude the influence of different dye amounts, the *ex vivo* total intensity values were divided through the maximum intensity of the *in vitro* emission spectra of the nanoparticles. The studies proved that same tissues of different batches can be compared. Analyzing the maximum intensity values enabled the comparison of nanoparticle accumulation in organs of different sizes. Therewith, comparative *in vivo* and *ex vivo* analyses of the nanoparticle accumulation in xenograft tumor tissues could be performed [5].

Another novel calculation approach was used for the *in vivo* pH calculations of *in situ* forming implants. To get measurement files with more detailed information multispectral imaging *cube* sets were acquired in 2 nm steps with two different filter sets. Average emission spectra of several ROI were extracted from the measurement *cubes*. The new established calculation approach used three intensity values of the emission curve. This calculation eliminated the influence of both, varying dye concentrations as well as of different exposure times and allowed to calculate *in vivo* pH values reproducible. Furthermore, this approach reduced the influence of disturbing auto-fluorescence.

Altogether, the obtained results proved that the evaluated fluorescence imaging method is useful to semi-quantify fluorescence emissions *in vivo*. Recently developments were published which might enable better quantification of dyes in the future. Those improved systems are based on theoretical models of photon propagation as well as of absorption and scattering processes of the excitation and the emission light in tissues. The underlying mathematical calculations of those fluorescence imaging techniques would provide 3-D information in future. Examples are fluorescence-mediated tomography (FMT), optical projection tomography (OPT) and diffuse optical tomography (DOT) [183]. Those systems might enable the quantification of dyes independently from their depth in the body. First systems were already successfully applied *in vivo* to monitor tumor tissue, vascular volume fractions as well as for the quantification of pulmonary inflammation [184-187]. Meanwhile also prototype diagnostic NIR light applications for humans like mammography, retinal angiography, detecting of rheumatoid arthritis in hands and liver functional testing were developed [110; 188-190]. However, the mathematical models for the analysis and calculation of the optical tissue properties still require many efforts and additional extensive studies until those systems can be used.

Chapter VII: Summary and future perspectives

O Summary

Fluorescence imaging emerged in the early twenty-first century as a potential *in vivo* imaging technique to track fluorescence markers non-invasively. In the drug discovery research field of the pharmaceutical technology this method could allow to follow-up the distribution, accumulation and elimination processes of APIs or drug model substances in living organisms. In addition it is an excellent easy to use method to research physicochemical properties and *in vivo* behaviors of various drug delivery systems. Thus, fluorescence imaging conducted in early pre-clinical phases, could help to understand and optimize drug delivery systems. It is expected that next to the scientific benefit, fluorescence imaging can have also a major economic impact on cost saving due to the higher informative value of earlier and more precise pre-clinical experiments. However, new techniques possess new questions and challenges like: Which pharmaceutical technology research fields can benefit from fluorescence imaging? Which information can be obtained? Which limitations may hamper the application?

The Maestro imaging system as one of the first commercially available pre-clinical fluorescence imagers was launched to the market in the beginning of this research work. There was a lack of data and available knowledge about the application possibilities of this technique in order to characterize parenteral formulations. Therefore, the aim of this work was focused on evaluating *in vivo* and *ex vivo* imaging methods. In addition different analyzing approaches were developed to characterize parenteral formulations. Altogether, novel knowledge and an advanced understanding of the *in vivo* behavior of characterized complex drug carrier systems were provided.

The performed fluorescence imaging studies were focused on three different parenteral drug delivery systems: (a) water soluble polymer conjugates (publications I - III), (b) nanocarriers (publications IV - VI) and (c) *in situ* forming implants (publication VII). These were applied via three different administration routes: (a) *i.p.*, (b) *i.v.*, and (c) *s.c.* [1-7]. In addition the gained information from performed pre-

clinical *in vivo* studies was used to characterize also (d) alternative drug delivery systems (publication VIII) [8].

All *in vivo* experiments were complied in accordance to the animal protection standards as stated in the guideline from the animal care and use committee of Saxony-Anhalt and were officially approved.

(a) Pre-clinical *in vivo* studies of PVA were successfully performed to investigate the long-term *in vivo* fate after *i.p.* injection. PVA was either covalently labeled with the VIS dye TMR (fluorescent in the range of visible light) or with the NIR dye Alexa Fluor 750. Using fluorescence imaging and two in their characteristics completely different dyes allowed performing comprehensive studies of the *in vivo* biodistribution of PVA. New findings are mainly related to the *in vivo* distribution, accumulation and the release from accumulated organs and tissues.

The characteristic emission spectra of TMR and using the unmixing functions of the Maestro imaging systems enabled to visualize the blood vessels due to long circulating PVA molecules. Also the accumulation of PVA in fat tissues has been identified with the use of the imaging system for the first time. Additionally the non-invasive differentiation between the accumulation of PVA in abdominal fat and in s.c. fat tissue has been shown. The amounts of accumulated PVA were analyzed and the further release rates were tracked for more than 6 months. Using different analyzing approaches a distinction between the release in female and in male mice was possible. Further *ex vivo* studies confirmed *in vivo* findings of PVA accumulation in fat tissues. Additional applied confocal microscopy permitted to follow the PVA accumulation up to cellular levels. Thereby, PVA enrichment between fat cells has been verified.

In vivo experiments performed non-invasively with NIR labeled PVA enabled studying the biodistribution of PVA also in deeper tissues and in organs which are highly supplied with blood. The combination of the advantages of both dyes facilitated studying the PVA elimination pathways. During the first days the PVA has been found to be mainly excreted via the urine. In addition, the long-term elimination of PVA was followed in all tissues where PVA was accumulated. Longest, NIR labeled PVA was detectable in the liver. After up to 9 months the concentration dropped below the detection limit. This suggested a complete elimination of water soluble high molecular weight PVA from the body.

A major challenge in performing pre-clinical *in vivo* experiments is to get a maximum of information while reducing the stress for each animal during an experiment as well

as minimizing the total number of animal experiments. The method of fluorescence imaging fulfills these both conditions. Within this research it has been shown that PVA could be non-invasively followed from the point of injection until it has been eliminated from the organism while miscellaneous information was obtained simultaneously. This enabled to reduce the number of terminal animal experiments to a minimum.

(b) Additional pre-clinical *in vivo* studies were conducted to access the *in vivo* fate of nanoparticles, their potential to be used in targeted cancer therapy and possible toxicity risks which may occur during their administration.

Thorough particle size measurement studies were performed in order to justify size-dependent biodistribution conclusions afterwards. Experiments with AF4/MALLS, PCS and TEM showed that particle sizes of all used batches were narrow distributed within predefined size ranges (between 100 nm and 200 nm).

The biodistribution of NIR nanoparticles was followed for several days *in vivo* and verified *ex vivo*. In the bloodstream circulating NIR loaded nanoparticles were detectable *in vivo* for up to 6 hours.

A new *ex vivo* imaging procedure was evaluated to get comparative biodistribution data of nanoparticles in intestine, fat, uterus with ovary, liver, gall bladder, lung, spleen, kidneys and heart. These extensive *ex vivo* studies were performed to enable size dependent justifications of the *in vivo* fate. Based on the data acquired within the research a new calculation method has been developed. This allowed time-dependent comparisons of total and maximum fluorescence intensities of different batches with varying intensities. This approach was a pre-requisite to research the influence of varying particle sizes on the biodistribution and the potential tumor accumulation ability in future.

Nanoparticle biodistribution studies were performed to investigate the potential use in cancer therapy. The use of non-invasive multispectral fluorescence imaging allowed for the first time to combine tumor visualization of DsRed2 expressing HT29 xenografts with simultaneous tracking of the nanoparticle accumulation. In addition size dependent accumulation studies in human colon carcinoma (HT29) and ovarian carcinoma (A2780) xenografts have been performed. The studies showed that all tested nanoparticles were accumulated in both tumor models whereas different sized nanoparticle batches were most effective for HT29 as well as for A2780 xenografts.

Ex vivo studies showed different accumulation pattern. Slightly bigger nanoparticles were most effective and enriched primarily in specific necrotic regions in the tumor

center of HT29 tumors. This was confirmed by confocal microscopy. Nanoparticles were visualized between fluorescent, DsRed2 expressing HT29 cells. Light microscopic studies of thin section slides of tumor tissue confirmed the accumulation in necrotic tissues for HT29 xenografts.

No centralized nanoparticle accumulation was observed for A2780 tumors. Slightly smaller sized nanoparticles were most effective. This led to the conclusion that vascular permeation for A2780 and accumulations in necrotic areas for HT29 were the preferable mechanisms of nanoparticle accumulation.

In vivo experiments identified also high local, punctual enrichments in parts of the ovaries for all tested nanoparticle batches. Within *ex vivo* experiments it has been found that the total fluorescence signals from overall ovarian tissues were rather low compared to other tissues with verifiable nanoparticle accumulation. *Ex vivo* fluorescence imaging and confocal microscopy studies enabled to localize the accumulation. This effect has been confirmed in further experiments in a second mouse species (BALB/c) and in Wistar rats. Same accumulation pattern were found for two other tested nanocarrier systems, for nanocapsules and nano-sized lipid emulsions. It has been concluded that an accumulation of nanocarriers was most likely in the fast-growing *corpus luteum* and is related to the enhanced permeability and retention effect known for tumor tissues.

The presented studies demonstrated that fluorescence imaging allowed investigating the *in vivo* fate of drug delivery formulations while imaging fluorescent tissues at the same time. The experiments can be the basis for future pre-clinical studies to determine pharmacokinetic parameters next to the therapeutic success. The gathered measurement principals allow measuring the nanoparticle biodistribution next to the tumor localization and the detection of changing tumor sizes.

(c) Pre-clinical *in vivo* studies of *in situ* forming implants were performed to characterize both changing pH values and dye release profiles of PLGA implants. Thorough preliminary *in vitro* and *ex vivo* fluorescence imaging experiments have been performed. The effect of external influencing factors like system, components, measurement depths etc. as well of varying measurement conditions (varying exposure times, resolutions, filter settings) were assessed.

A novel non-invasive *in vivo* pH measurement method for fluorescence imaging was established. This allowed for the first time to perform non-invasive measurements and visualizations of the micro pH shift in *in situ* forming PLGA implants. The pH decrease was measured non-invasively for more than 3 weeks and confirmed

ex vivo. The results are in good accordance to other *in vitro* EPR and *in vitro* confocal laser scanning microscopy studies. The comparison of the studies has been shown that the pH change occurred *in vivo* slower than *in vitro*.

Measuring the fluorescence intensity of the dye allowed further analyzing the solvent/non-solvent exchange process during implant solidification and to draw conclusions regarding the mobility of dye molecules in the implant. The physically entrapping of the hydrophilic dye facilitated also to research the release profiles from the implant.

The experiments showed that fluorescence imaging serves as valuable tool for pre-clinical studies. The technique enabled the non-invasive detection of pH values and the characterization of parenteral drug formulations.

(d) The knowledge obtained from the current pre-clinical *in vivo* research studies has been applied to characterize also other non-parenteral drug delivery systems. The conducted *in vivo* pH measuring principles were successfully used to monitor non-destructively pH gradients in swelling multi-layer tablets. As a prerequisite for *in vitro* pH measurements in tablets additional pretests were performed to access the influence of e.g. excipients, different dyes and dye concentrations. Imaging experiments allowed to measure and to visualize the spatial pH distribution in the tablet surface across the swelling process. It has been shown that the incorporation of internal buffer substances and the choice of excipients strongly influenced the pH in the swelling layer. The pH measurement results obtained in the current research were comparable with other performed pH measurement techniques: the EPR spectroscopy and the usage of pH indicator substances. Results showed the respective different potentials of each of the methods.

A comparable approach was used to monitor the temperature distribution in tablets, caused during the tableting process. A dye mixture was identified which changes irreversible the intensity of two emission maxima when exposed to temperatures between 40 °C and 80 °C. Extensive temperature calibration tests were successfully performed. Due to limitations of the Maestro software, a manual Microsoft Excel based procedure for temperature analysis was evaluated. The temperature which occurred during the tableting was five-fold determined for six mixtures and for three tableting processes. The analysis showed that the maximum observed temperature varied depending on used excipients, the humidity of the excipients and to some extent on the applied tableting conditions.

Obtained fluorescence *in vivo* imaging knowledge could also be used to characterize other parenteral drug delivery systems non-invasively *in vivo*. As part of the work also nanocapsules were thorough characterized *in vivo* and *ex vivo*. The established methods were further adopted to study the biodistribution and the *in vivo* efficiency of rhBMP-2 loaded microparticles.

The results of this research work demonstrated the potential applications of the pre-clinical fluorescence *in vivo* imaging method in the pharmaceutical technology research field. It has been shown that this technique offers a comprehensive imaging platform for the characterization and analysis of multiple *in vivo*, *ex vivo* and *in vitro* issues. Applied to small animals *in vivo*, this technique provided superior monitoring and visualization possibilities of drug delivery systems.

The presented new multispectral fluorescence imaging approaches serve as the basis for the characterization of other parenteral drug delivery systems. Thus this work can contribute to the better understanding of *in vivo* biodistribution processes in future.

P Future perspectives

Based on the research findings presented within this cumulative thesis, new scientific questions emerged which should be addressed in future pre-clinical multispectral fluorescence imaging experiments. Briefly, further research should be focused on:

1. Knowledge transfer to characterize other parenteral formulations

- Evaluated fluorescence imaging methods should be applied and broadened to characterize other parenteral formulations regarding their *in vivo* fate.

2. Correlation of nanocarrier *in vivo* characterization and use for cancer treatments

- Further multispectral studies with fluorescent tumor tissues and fluorescent nanocarriers should be carried out simultaneously to investigate the accumulation behavior in more detail.
- For the visualization of metastases in the body of small animals it should be tried to establish xenograft tumor models with fluorescent emissions in the dark red or even NIR wavelength area.
- Size dependent tumor accumulation studies should be extended to other xenograft tumor models in order to get detailed understanding of the relationship between nanocarrier sizes and the tumor accumulation behavior.

3. Research the accumulation of nanocarriers in ovaries

- Detailed investigations on the influence of size, surface structure and surface charge should be performed using various other nanocarrier systems.
- To investigate dye and potential API polarity specific accumulations, other dyes should be incorporated and covalently bound to the nanocarriers.
- The accumulation capabilities of high molar mass polymers which are covalently NIR labeled should be investigated.

4. Implementation of *in vivo* pH measurements

- Visualization and measurement of pH values in tumor tissues should be conducted based on the knowledge obtained.

Q German summary

Anfang des 21. Jahrhundert wurden neue Systeme zur *in vivo* Bildgebung kommerziell verfügbar, die in der Lage sind fluoreszierende Markermoleküle nicht-invasiv und *in vivo* verfolgen zu können. In der pharmazeutischen Technologie könnte sich die Möglichkeit mittels dieser Geräte erschließen, Verteilungs-, Anreicherungs- und Eliminierungsprozesse in lebenden Organismen zu verfolgen sowie physiko-chemische Eigenschaften parenteraler Arzneistoffträgersysteme zu erforschen. Die Fluoreszenzbildgebung könnte damit einen Beitrag dazu leisten in präklinischen Studien Arzneifreisetzungssysteme besser zu charakterisieren um sie anschließend weiter optimieren zu können, bevor sie schließlich am Menschen zur Anwendung kommen. Neben diesem wissenschaftlichen Nutzen kann die Fluoreszenzbildgebung aber auch einen entscheidenden finanziellen Vorteil im Rahmen der klinischen Erprobung bringen. So würde unter anderem Dank der weitaus aussagekräftigeren Ergebnisse die Versuchszahl innerhalb eines Experimentes und auch die Gesamtzahl von Experimenten stark reduziert werden. Um jedoch die Methode zur präklinischen Charakterisierung einzusetzen, müssen im Vorfeld zahlreiche Fragestellungen beantwortet werden. Es ist unter anderem zu klären, in welchen pharmazeutischen/technologischen Forschungsbereichen und für welche Thematiken die Fluoreszenzbildgebung genutzt werden kann. Darüber hinaus müssen aber auch die Grenzen der Anwendung untersucht werden.

Das Maestro Bildgebungssystem ist eines der ersten kommerziell erhältlichen optischen Fluoreszenzbildgebungssysteme. Die Markteinführung erfolgte zu Beginn dieser Promotionsarbeit. Dem geschuldet sind auch die zu dieser Zeit begrenzten Informationen über allgemeine Anwendungsmöglichkeiten. Unklar war auch in wie weit parenterale Formulierungen mit dieser Methode überhaupt charakterisiert werden können. Daher war es das Hauptziel dieser Arbeit, verschiedene *in vivo* und *ex vivo* Messmethoden zu entwickeln und zu evaluieren. Darüber hinaus sollten unterschiedliche Auswertungsansätze erarbeitet werden, um parenterale Arzneistoffträgersysteme charakterisieren zu können und um neue Erkenntnisse über das *in vivo* Verhalten komplexer Trägersysteme zu erhalten.

Hierfür wurden drei parenterale Arzneistoffträgersysteme: **(a)** wasserlösliche Polymere (Publikationen I - III), **(b)** Nanopartikel (Publikationen IV - VI) und **(c)** sich *in situ* bildende Implantate (Publikationen VII) ausgewählt welche auf drei

verschiedenen Applikationsarten injiziert wurden: **(a)** *i.p.*, **(b)** *i.v.* und **(c)** *s.c.*) [1-7]. Es ist bekannt, dass das *in vivo* Verhalten aller drei Systeme sehr komplex ist und damit nur schwer in *in vitro* Experimenten erforscht werden kann. Des Weiteren wurde das in den *in vivo* Studien erlangte Wissen genutzt, um andere Arzneistoffträgersysteme zu charakterisieren **(d)** [8].

Alle Tierversuche innerhalb dieses Forschungsprojektes sind von der Tierschutzkommission des Landes Sachsen - Anhalt genehmigt und unter Beachtung deutscher Tierschutzgesetze durchgeführt worden.

(a) Hochmolekulares, wasserlösliches PVA ist im Rahmen der Arbeit erfolgreich in verschiedenen präklinischen *in vivo* Studien charakterisiert worden. Dabei wurde sowohl die Verteilung, die Anreicherung als auch die Eliminierung zweier unterschiedlich fluoreszenzmarkierter PVA Chargen mittels der Fluoreszenzbildgebung über mehrere Monate hinweg untersucht. Eine Charge wurde kovalent mit dem, im sichtbaren Lichtbereich fluoreszierenden TMR - Molekül markiert, die andere Charge mit, dem im nahen Infrarotbereich (NIR) fluoreszierenden Farbstoff Alexa Fluor 750. Mit beiden markierten Polymerchargen war es möglich die Verteilung des PVA im Körper nach *i.p.* Applikation zu verfolgen. Die charakteristischen Emissionsspektren des TMR - Farbstoffes in Kombination mit den Auswertungsmöglichkeiten des Maestro Imaging Systems erlaubten auf diese Weise über einen Tag die Darstellung von Blutgefäßen. Dies ließ die Schlussfolgerung zu, dass die PVA Moleküle über Stunden im Blutkreislauf zirkulieren. Im Besonderen aber war es erstmalig möglich in nicht-invasiven Messungen nachzuweisen, dass sich PVA im Fettgewebe anreichert. Darüber hinaus konnte zwischen der Anreicherung im visceralen und subkutanen Fettgewebe nicht-invasiv differenziert werden. Dank verschiedener Auswertungsmethoden konnten entsprechend der unterschiedlichen Fettverteilung bei den Geschlechtern, abweichende Freisetzungsprofile für PVA bei männlichen und weiblichen Mäusen nachgewiesen und über mehr als 6 Monate hinweg verfolgt werden. *Ex vivo* Messungen bestätigten die in den zuvor durchgeführten *in vivo* Experimenten gefundene Anreicherung im Fettgewebe. Ergänzende Untersuchungen mittels der Konfokalmikroskopie erlaubten die PVA Anreicherung bis auf zelluläre Ebene zu verfolgen. So konnte nachgewiesen werden, dass sich das PVA Polymer zwischen den Fettzellen anreichert.

Das Emissionsspektrum des NIR - Farbstoffes ist im Vergleich zum TMR - Spektrum weniger charakteristisch, so dass aus den aufgenommenen Bilddateien weit weniger spektrale Informationen abgeleitet werden konnten. Während der Durchführung von

in vivo Experimenten mit dem NIR - gelabelten PVA konnte aber Dank der Emission im NIR Bereich die Verteilung der PVA Moleküle in tiefer liegenden Geweben sowie in stark durchbluteten Organen nicht-invasiv verfolgt werden. Die Vorteile beider Farbstoffe konnten ebenfalls zur Untersuchung von Ausscheidungsprozessen genutzt werden. In den ersten Tagen wird PVA demnach hauptsächlich mit dem Urin ausgeschieden was eine bereits publizierte ESR Studie an Kaninchen bestätigt [34]. Weiterhin wurde mit der NIR markierten PVA - Charge die Eliminierung des Polymers aus jenen Geweben verfolgt, in denen sich das Polymer anreicherte. Am Längsten war der NIR Farbstoff in der Leber detektierbar. Aber auch hier fiel die Intensität des Farbstoffes nach bis zu 9 Monaten unter die Detektionsgrenze. Daraus ließ sich ableiten, dass das hochmolekulare PVA über die Zeit wohl vollständig aus dem Körper ausgeschieden wird.

Mittels der Fluoreszenzbildgebung und der Untersuchung zweier in ihren spektralen Eigenschaften völlig unterschiedlicher Farbstoffe war es möglich, umfangreiche Untersuchungen hinsichtlich des *in vivo* Verteilungsverhaltens von PVA durchzuführen. Daraus ergaben sich neue Erkenntnisse bezüglich der *in vivo* Verteilung des Polymers, sowie dessen Anreicherung und Freisetzung aus Organen und Geweben.

Eine große Herausforderung präklinischer Studien ist es, bei kleinstmöglicher Tierversuchszahl und mit einer minimalen Belastung für die Tiere möglichst viele Erkenntnisse zu erhalten. In den PVA Studien konnte gezeigt werden, dass mit Hilfe der Fluoreszenzbildgebung genau dieses erreicht werden kann. PVA konnte nicht-invasiv ohne große Belastung der Versuchstiere vom Punkt der Injektion an bis hin zur Eliminierung aus dem Körper verfolgt werden. Gleichzeitig konnte eine Vielzahl weiterer Informationen aus den Messergebnissen abgeleitet werden. Schließlich war es auch möglich die Zahl terminaler Experimente auf ein Minimum zu reduzieren.

(b) Weiterhin wurden präklinische Studien durchgeführt, die die Verteilung von Nanopartikeln im Körper untersuchen, um schließlich Rückschlüsse bezüglich der Anwendbarkeit der hergestellten Partikel in der Tumorthherapie ziehen zu können. Außerdem sollte herausgefunden werden ob eine potentielle Toxizität von ihnen ausgehen könnte. Um nun auf Basis der durchgeführten Fluoreszenzmessungen größenabhängige Aussagen treffen zu können, sind vor Studienbeginn umfassende Partikelgrößenmessungen durchgeführt worden. Die AF4/MALLS, PCS und TEM Messungen bestätigten, dass die Partikelgrößen aller gemessenen Chargen eng

verteilt und die mittleren Partikelgrößen im Größenbereich zwischen 100 nm und 200 nm lagen. Die Verteilung der intravenös applizierten Nanopartikel im Blut konnte mit Hilfe des inkorporierten NIR - Farbstoffes über 6 Stunden verfolgt werden. Diese lange Zirkulationszeit wurde durch Oberflächenmodifizierung mit PEG - Ketten erreicht, wodurch die Oberfläche der Partikel eine bürtsenartige Struktur erhält. Die Partikel sind damit nach außen hin abgeschirmt - eine Maßnahme um die Phagozytose der Partikel erheblich zu verringern. Die weitere Verteilung der Partikel im Körper wurde über mehrere Tage *in vivo* nicht-invasiv mittels des Maestro Bildgebungssystems verfolgt. Die erhaltenen Ergebnisse konnten durch *ex vivo* Experimente bestätigt werden. Um vergleichende quantitative Aussagen über die Menge der in Geweben und Organen angereicherten Menge von Nanopartikeln treffen zu können wurde eine neue Methode zur Auswertung erarbeitet. Diese ermöglicht es totale und maximale Fluoreszenzmissionssignale von Chargen unterschiedlicher Partikelgrößen und mit unterschiedlichen Intensitäten miteinander zu vergleichen. Dies war eine Grundvoraussetzung, um den Einfluss der Partikelgröße auf das *in vivo* Verhalten und auf die Fähigkeit der Anreicherung im Tumorgewebe zu untersuchen. Zur Gewinnung größenabhängiger Aussagen über die *in vivo* Verteilung der Nanopartikel im Organismus wurden die maximalen und totalen Intensitäten des Darmes, des Fettgewebes, des Uterus zusammen mit den Ovarien, der Leber, der Gallenblase, der Lunge, der Milz, der Nieren und des Herzens zeitabhängig für verschiedene Chargen bestimmt und entsprechende Rückschlüsse diskutiert.

In den durchgeführten *in vivo* - sowie in *ex vivo* - Experimenten wurde festgestellt, dass das Gesamtfluoreszenzsignal in den Ovariengewebe verglichen zu anderen Gewebestrukturen und Organen mit nachgewiesener Nanopartikelanreicherung sehr gering ist. Allerdings konnte mittels der Fluoreszenzbildgebung auch gezeigt werden, dass es bei allen Nanopartikelchargen zu einer hohen, punktförmigen, lokalen Anreicherung in einem bestimmten Areal der Ovarien kommt. Dieser Effekt der Anreicherung wurde in einem weiteren Mausstamm sowie in Wistar Ratten und auch unter Verwendung anderer Nanoträgersysteme (Nanokapseln und parenterale Fettemulsion) bestätigt. Dank intensiver *ex vivo* Studien und verschiedener konfokalmikroskopischer Experimente war es möglich, die Anreicherung genauer lokalisieren zu können. Basierend auf den gewonnenen Ergebnissen kann eine Anreicherung von nanopartikelären Systemen im schnell wachsenden *Corpus Luteum* angenommen werden. Dies könnte mit einer erhöhten Durchlässigkeit und dem Rückhaltevermögen, wie es auch für Tumorgewebe bekannt ist, erklärt werden. Die

erhaltenen Ergebnisse sind im Rahmen dieser kumulativen Forschungsarbeit erstmalig detailliert untersucht und intensiv diskutiert worden.

Bezug nehmend auf die mit Nanopartikeln durchgeführten *in vivo* Verteilungsstudien, wurden weitere Experimente geplant, um ihren zukünftigen Einsatz in Tumorthérapien zu untersuchen. So gelang es erstmalig die nicht-invasive, multispektrale Fluoreszenzbildgebung zu nutzen, um die Anreicherung NIR-fluoreszierender Nanopartikel in ebenfalls fluoreszierenden DsRed2 exprimierenden Xenograft Tumorgewebe zu untersuchen. Zusätzlich wurde die größenabhängige Anreicherung in humanen kolorektalen Karzinomen (HT29) und in Ovarialkarzinomen (A2780) in Mäusen mittels der *in vivo* und *ex vivo* Fluoreszenzbildgebung und eines neu entwickelten Auswertungsansatzes erforscht. Die Studienergebnisse zeigten, dass sich die applizierten Nanopartikel erfolgreich in beiden Tumormodellen anreicherten. Dabei waren bei beiden Tumormodellen (HT29 und A2780) jeweils unterschiedliche Chargen mit Nanopartikeln verschiedener Größe am Effektivsten. Außerdem zeigten *ex vivo*-Studien, dass sich die Nanopartikel in den oben genannten Modellen auch in unterschiedlichen Bereichen des Tumorgewebes unterschiedlich stark anreichern. Nanopartikel mit einer durchschnittlichen Partikelgröße (PCS z-average) von 141 nm reicherten sich in HT29 Tumorgewebe vor allem in Regionen im Inneren des Tumorgewebes am Stärksten an. Dies konnte ebenfalls in konfokalmikroskopischen Experimenten bestätigt werden. So kann vermutet werden, dass sich die Nanopartikel zwischen den fluoreszierenden, DsRed2 exprimierenden HT29 Tumorzellen anreichern. Lichtmikroskopische Aufnahmen bestätigten für das HT29 Tumormodell eine Akkumulation in zentral gelegenen, nekrotischen Tumorgewebeteilen. Keine zentralisierte Anreicherung wurde bei A2780 Tumoren gefunden. Jedoch konnten in A2780 Tumorgewebe im Besonderen Nanopartikel der Charge mit den kleinsten Partikeln (PCS z-average von 111 nm) detektiert werden. Hieraus ließ sich ableiten, dass sich Nanopartikel bevorzugt durch vaskuläre Permeation in A2780 Tumoren anreichern, während sie in HT29 Tumoren hauptsächlich in nekrotischen Gebieten akkumulieren.

Zusammenfassend kann festgestellt werden, dass es mittels der Fluoreszenzbildgebung möglich ist *in vivo* Verteilungsprozesse von Arzneistoffformulierungen darzustellen. Damit ist es in zukünftigen präklinischen Studien möglich die Pharmakokinetik und den Therapieerfolg, also beispielsweise die Reduktion der Tumorgröße, gleichzeitig zu bestimmen.

(c) Präklinische Studien mit *in situ* Gel bildenden Implantaten wurden durchgeführt, um den unkontrollierten pH Abfall in und die Freisetzung eines Farbstoffes aus PLGA - Implantaten *in vivo* zu untersuchen. Dafür sind auch umfangreiche *in vitro* - und *ex vivo* - Vortests durchgeführt worden, in denen die Auswirkungen externer Einflussfaktoren und schwankender Messparameter auf die Messergebnisse untersucht wurden. Diese Ergebnisse waren maßgeblich, um eine neue nicht-invasive Methode zur *in vivo* pH Wert Messung zu entwickeln. Damit war es erstmals möglich gleichzeitig den pH Wert *in vivo* zu messen, ihn zu visualisieren und die Langzeit pH Wertveränderung nicht-invasiv verfolgen zu können. Der gemessene pH Abfall wurde in *ex vivo* Experimenten bestätigt und ist in guter Übereinstimmung mit *in vitro* ESR - Experimenten sowie mit publizierten konfokalmikroskopischen *in vitro* Ergebnissen. Außerdem konnte gezeigt werden, dass der pH Abfall *in vivo* langsamer abläuft als es in *in vitro* Experimenten beobachtet wurde. Darüber hinaus erlaubte die Messung der Fluoreszenzintensität, Rückschlüsse auf das Freisetzungsprofil des Farbstoffes und der Molekülmobilität im Implantat zu ziehen.

Die Ergebnisse zeigen, dass die Fluoreszenzbildgebung in präklinischen Studien auch zur Beantwortung analytischer Fragestellungen wie der nicht-invasiven Bestimmung des pH Wertes und zur Charakterisierung von parenteralen Arzneistoffformulierungen genutzt werden kann.

(d) Weiterhin konnte, dass in den präklinischen *in vivo* Studien erlangte Wissen auf die Charakterisierung anderer Arzneistoffformulierungen sowie auch auf die Untersuchung weiterer pharmazeutisch - technologische Fragestellungen übertragen werden.

So sind die entwickelten *in vivo* pH - Messprinzipien erfolgreich genutzt und erweitert worden, um zerstörungsfrei pH Gradienten in quellenden Mehrschichttabletten zu messen. Hierzu war jedoch eine Vielzahl zusätzlicher Vortests notwendig. Unter anderem waren der Einfluss von Tablettenhilfsstoffen zu ermitteln, aber auch die Wahl eines geeigneten Fluoreszenzfarbstoffes, sowie die Bestimmung seiner optimalen Konzentration. In den Experimenten mittels Fluoreszenzbildgebung konnten die pH Werte ermittelt und die räumlichen pH - Verteilungen an der Oberfläche über die Zeit des Quellprozesses visualisiert werden. Die Ergebnisse zeigten, dass das Hinzufügen von Puffersubstanzen und die Wahl der Hilfsstoffe einen großen Einfluss auf den pH Wert hat. Im Weiteren waren die erzielten pH Messergebnisse mit zwei anderen pH Messmethoden der ESR Spektroskopie und

der optischen Charakterisierung mittels pH Indikatoren vergleichbar. Dabei wies jede der genutzten Methoden unterschiedliche Vor- und Nachteile auf und leistete zur Beantwortung verschiedener Fragestellungen einen wichtigen Beitrag.

Ein ähnlicher Ansatz wurde verfolgt, um Rückschlüsse auf die Temperatur in Tabletten ziehen zu können, die durch den Pressvorgang im Inneren entsteht. Hierfür konnte eine Fluoreszenzfarbstoffmischung gefunden werden, die zwei Fluoreszenzmaxima besitzt welche ihre jeweiligen Emissionsintensitäten irreversibel zwischen 40 °C und 80 °C in Abhängigkeit der ausgesetzten Temperatur verändern. Umfangreiche Temperaturkalibrierungen wurden erfolgreich durchgeführt. Da die Maestro Software für derartige Auswertungen nur begrenzte Möglichkeiten bietet, wurde eine Microsoft Excel basierte Analysemethode entwickelt. Die bei der Tablettierung entstehenden Temperaturen wurden jeweils fünffach für sechs verschiedene Hilfsstoffmischungen und für drei verschiedene Tablettierprozesse bestimmt. Insgesamt zeigten die Auswertungen, dass die maximal entstehende Temperatur abhängig ist von den jeweils eingesetzten Hilfsstoffen, ihrer Feuchte und teilweise von den Tablettierbedingungen.

Die entwickelten Methoden und Techniken konnten aber auch genutzt werden, um andere parenteral applizierbare Formulierungen *in vivo* zu charakterisieren. So war es beispielsweise möglich das Verhalten und die Wirksamkeit von rhBMP-2 beladenen Mikropartikeln zu untersuchen. Außerdem konnten auf Basis der entwickelten Methoden verschiedene Nanokapselchargen erfolgreich *in vivo* und auch *ex vivo* charakterisiert werden.

Die im Zusammenhang mit der vorliegenden Arbeit erlangten Ergebnisse zeigen die Vielzahl möglicher Anwendungsgebiete für die Fluoreszenzbildgebung speziell im Rahmen präklinischer *in vivo* Studien. Die Erkenntnisse unterstreichen, dass die Fluoreszenzbildgebung sehr gut für die Charakterisierung und Analyse verschiedenster *in vivo*, *ex vivo* und *in vitro* Systeme im Bereich der pharmazeutischen Technologie herangezogen werden kann. Die Fluoreszenzbildgebung bietet speziell für die Verwendung an Kleintieren im Rahmen präklinischer Untersuchungen hervorragende Möglichkeiten Arzneistoffträgersysteme *in vivo* untersuchen und Prozesse *in vivo* visualisieren zu können. Im Rahmen dieser Studien aufgezeigte Messmethoden können die Grundlage sein für die Charakterisierung anderer parenteraler Arzneiträgersysteme. Damit kann die vorliegende Arbeit schließlich dazu beitragen *in vivo* Prozesse in Zukunft besser untersuchen und damit auch besser verstehen zu können.

Bibliography

- [1] Schädlich, A., Naolou, T., Amado, E., Schöps, R., Kressler, J., Mäder, K., (2011) Noninvasive in Vivo Monitoring of the Biofate of 195 kDa Poly(vinyl alcohol) by Multispectral Fluorescence Imaging. *Biomacromolecules*, 12 (10): 3674-3683.
- [2] Jiang, Y., Schädlich, A., Amado, E., Weis, C., Odermatt, E., Mäder, K., Kressler, J., (2010) In-vivo studies on intraperitoneally administrated poly(vinyl alcohol). *Journal of Biomedical Materials Research Part B-Applied Biomaterials*, 93B (1): 275-284.
- [3] Schädlich, A., Jiang, Y., Kressler, J., Mäder, K., (2010) Tracking the in vivo fate of high molar mass poly (vinyl alcohol) using multispectral fluorescence in vivo imaging. *Scientifically Speaking News (Controlled Release Society)*, 27 (2): 15-16.
- [4] Schädlich, A., Rose, C., Kuntsche, J., Caysa, H., Mueller, T., Göpferich, A., Mäder, K., (2011) How Stealthy are PEG-PLA Nanoparticles? An NIR In Vivo Study Combined with Detailed Size Measurements. *Pharmaceutical Research*, 28: 1995-2007.
- [5] Schädlich, A., Caysa, H., Mueller, T., Tenamberg, F., Rose, C., Göpferich, A., Kuntsche, J., Mäder, K., (2011) Tumor Accumulation of NIR Fluorescent PEG PLA Nanoparticles: Impact of Particle Size and Human Xenograft Tumor Model. *Acs Nano*, 5 (11): 8710-8720.
- [6] Schädlich, A., Hoffmann, S., Mueller, T., Caysa, H., Rose, C., Göpferich, A., Li, J., Kuntsche, J., Mäder, K., (2012) Accumulation of nanocarriers in the ovary: A neglected toxicity risk? *Journal of Controlled Release*, 160 (1): 105-112.
- [7] Schädlich, A., Kempe, S., Mäder, K., (2013) Long-term in vivo pH measurements of in situ forming PLGA implants using multispectral fluorescence imaging. *Submitted to Journal of Controlled Release*, under peer-review.
- [8] Eisenächer, F., Schädlich, A., Mäder, K., (2011) Monitoring of internal pH gradients within multi-layer tablets by optical methods and EPR imaging. *International Journal of Pharmaceutics*, 417 (1-2): 204-215.
- [9] Adams, C.P., Brantner, V.V., (2006) Estimating the cost of new drug development: Is it really \$802 million? *Health Affairs*, 25 (2): 420-428.
- [10] Dimasi, J.A., Hansen, R.W., Grabowski, H.G., (2003) The price of innovation: new estimates of drug development costs. *Journal of Health Economics*, 22 (2): 151-185.

Bibliography:

- [11] Beckmann, N., (2006) *In Vivo MR Techniques in Drug Discovery and Development*. Book, Taylor & Francis Group, New York.
- [12] Lipinski, C.A., Lombardo, F., Dominy, B.W., Feeney, P.J., (1997) Experimental and computational approaches to estimate solubility and permeability in drug discovery and development settings. *Advanced Drug Delivery Reviews*, 23 (1-3): 3-25.
- [13] Milne, G., (2003) Pharmaceutical productivity — the imperative for new paradigms. *Annual Reports in Medicinal Chemistry*, 38: 383-396.
- [14] Lindenberg, M., Kopp, S., Dressman, J.B., (2004) Classification of orally administered drugs on the World Health Organization Model list of Essential Medicines according to the biopharmaceutics classification system. *European Journal of Pharmaceutics and Biopharmaceutics*, 58 (2): 265-278.
- [15] Reiser, M., Semmler, W., Hricak, H., (2008) *Magnetic Resonance Tomography*. Book, 3rd, Springer Verlag Berlin, Heidelberg.
- [16] Eastman, G., Wald, C., Crossin, J., (2006) *Getting started in clinical radiology: from image to diagnosis*. Book, Georg Thieme Verlag, Stuttgart.
- [17] Moonen, C. Bandettini, P., (2000) *Functional MRI*. Book, Springer-Verlag, Heidelberg.
- [18] Kiessling, F. Pichler, B., (2011) *Small Animal Imaging*. Book, Springer-Verlag Berlin, Heidelberg.
- [19] Weissleder, R., Pittet, M.J., (2008) Imaging in the era of molecular oncology. *Nature*, 452 (7187): 580-589.
- [20] Oppelt, A., (2005) *Imaging systems for medical diagnostics*. Book, Publicis Corporate Publishing, Erlangen.
- [21] Kumar, C., (2007) *Nanomaterials for cancer diagnosis*. Book, WILEY-VCH Verlag GmbH & Co. KGaA, Weinheim.
- [22] Weissleder, R., Ross, B., Rehemtulla, A., Gambhir, S., (2010) *Molecular Imaging: Principles and Practice*. Book, 1, People's Medical Publishing House - USA.
- [23] Leblond, F., Davis, S.C., Valdes, P.A., Pogue, B.W., (2010) Pre-clinical whole-body fluorescence imaging: Review of instruments, methods and applications. *Journal of Photochemistry and Photobiology B-Biology*, 98 (1): 77-94.
- [24] Yao, R.S., You, Q.D., Liu, P.J., Xu, Y.F., (2009) Synthesis and pH-Induced Phase Transition Behavior of PAA/PVA Nanogels in Aqueous Media. *Journal of Applied Polymer Science*, 111 (1): 358-362.

Bibliography:

- [25] Peppas, N.A., Hilt, J.Z., Khademhosseini, A., Langer, R., (2006) Hydrogels in biology and medicine: From molecular principles to bionanotechnology. *Advanced Materials*, 18 (11): 1345-1360.
- [26] Noguchi, T., Yamamuro, T., Oka, M., Kumar, P., Kotoura, Y., Hyon, S.H., Ikada, Y., (1991) Poly(Vinyl Alcohol) Hydrogel As An Artificial Articular-Cartilage - Evaluation of Biocompatibility. *Journal of Applied Biomaterials*, 2 (2): 101-107.
- [27] Paradossi, G., Cavalieri, F., Chiessi, E., (2003) Poly(vinyl alcohol) as versatile biomaterial for potential biomedical applications. *Journal of Materials Science-Materials in Medicine*, 14 (8): 687-691.
- [28] Grosova, Z., Rosenberg, M., Rebroš, M., Sipocz, M., Sedlackova, B., (2008) Entrapment of beta-galactosidase in polyvinylalcohol hydrogel. *Biotechnology Letters*, 30 (4): 763-767.
- [29] Kokabi, M., Sirousazar, M., Hassan, Z.M., (2007) PVA-clay nanocomposite hydrogels for wound dressing. *European Polymer Journal*, 43 (3): 773-781.
- [30] Metwally, M., Cheong, Y., Li, T.C., (2008) A review of techniques for adhesion prevention after gynaecological surgery. *Current Opinion in Obstetrics & Gynecology*, 20 (4): 345-352.
- [31] Lang, R.A., Gruntzig, P.M., Weisgerber, C., Weis, C., Odermatt, E.K., Kirschner, M.H., (2007) Polyvinyl alcohol gel prevents abdominal adhesion formation in a rabbit model. *Fertility and Sterility*, 88: 1180-1186.
- [32] Sliker, J.C., Ditzel, M., Harlaar, J.J., Mulder, I.M., Deerenberg, E.B., Bastiaansen-Jenniskens, Y.M., Kleinrensink, G.J.J., Jeekel, J., Lange, J.F., (2012) Effects of New Anti-Adhesion Polyvinyl Alcohol Gel on Healing of Colon Anastomoses in Rats. *Surgical Infections*, 13 (6): 396-400.
- [33] Deerenberg, E.B., Mulder, I.M., Ditzel, M., Sliker, J.C., Bemelman, W.A., Jeekel, J., Lange, J.F., (2012) Polyvinyl Alcohol Hydrogel Decreases Formation of Adhesions in a Rat Model of Peritonitis. *Surgical Infections*, 13 (5): 321-325.
- [34] Besheer, A., Mäder, K., Kaiser, S., Kressler, J., Weis, C., Odermatt, E.K., (2007) Tracking the urinary excretion of high molar mass poly(vinyl alcohol). *Journal of Biomedical Materials Research Part B-Applied Biomaterials*, 82B (2): 383-389.
- [35] Maeda, H., (2001) The enhanced permeability and retention (EPR) effect in tumor vasculature: The key role of tumor-selective macromolecular drug targeting. *Advances in Enzyme Regulation*, 41: 189-207.
- [36] Allen, T.M., (2002) Ligand-targeted therapeutics in anticancer therapy. *Nature Reviews Cancer*, 2 (10): 750-763.

Bibliography:

- [37] Hezinger, A.F.E., Tessmar, J., Göpferich, A., (2008) Polymer coating of quantum dots - A powerful tool toward diagnostics and sensorics. *European Journal of Pharmaceutics and Biopharmaceutics*, 68 (1): 138-152.
- [38] Medintz, I.L., Uyeda, H.T., Goldman, E.R., Mattoussi, H., (2005) Quantum dot bioconjugates for imaging, labelling and sensing. *Nature Materials*, 4 (6): 435-446.
- [39] Smith, A.M., Duan, H.W., Mohs, A.M., Nie, S.M., (2008) Bioconjugated quantum dots for in vivo molecular and cellular imaging. *Advanced Drug Delivery Reviews*, 60 (11): 1226-1240.
- [40] Derfus, A.M., Chan, W.C.W., Bhatia, S.N., (2004) Probing the cytotoxicity of semiconductor quantum dots. *Nano Letters*, 4 (1): 11-18.
- [41] Liu, K.H., Chen, S.Y., Liu, D.M., Liu, T.Y., (2008) Self-assembled hollow nanocapsule from amphiphatic carboxymethyl-hexanoyl chitosan as drug carrier. *Macromolecules*, 41 (17): 6511-6516.
- [42] Rube, A., Mäder, K., (2005) Electron Spin Resonance Study on the Dynamics of Polymeric Nanocapsules. *Journal of Biomedical Nanotechnology*, 1 (2): 208-213.
- [43] Barratt, G., (2003) Colloidal drug carriers: achievements and perspectives. *Cellular and Molecular Life Sciences*, 60 (1): 21-37.
- [44] Shen, Y.Q., Jin, E.L., Zhang, B., Murphy, C.J., Sui, M.H., Zhao, J., Wang, J.Q., Tang, J.B., Fan, M.H., Van Kirk, E., Murdoch, W.J., (2010) Prodrugs Forming High Drug Loading Multifunctional Nanocapsules for Intracellular Cancer Drug Delivery. *Journal of the American Chemical Society*, 132 (12): 4259-4265.
- [45] Allard, E., Passirani, C., Garcion, E., Pigeon, P., Vessieres, A., Jaouen, G., Benoit, J.P., (2008) Lipid nanocapsules loaded with an organometallic tamoxifen derivative as a novel drug-carrier system for experimental malignant gliomas. *Journal of Controlled Release*, 130 (2): 146-153.
- [46] Gref, R., Domb, A., Quellec, P., Blunk, T., Muller, R.H., Verbavatz, J.M., Langer, R., (1995) The Controlled Intravenous Delivery of Drugs Using Peg-Coated Sterically Stabilized Nanospheres. *Advanced Drug Delivery Reviews*, 16 (2-3): 215-233.
- [47] Soppimath, K.S., Aminabhavi, T.M., Kulkarni, A.R., Rudzinski, W.E., (2001) Biodegradable polymeric nanoparticles as drug delivery devices. *Journal of Controlled Release*, 70 (1-2): 1-20.
- [48] Saez, A., Guzman, M., Molpeceres, J., Aberturas, M.R., (2000) Freeze-drying of polycaprolactone and poly(D,L-lactic-glycolic) nanoparticles induce minor particle size changes affecting the oral pharmacokinetics of loaded drugs. *European Journal of Pharmaceutics and Biopharmaceutics*, 50 (3): 379-387.

Bibliography:

- [49] Magenheimer, B., Benita, S., (1991) Nanoparticle characterization: a comprehensive physicochemical approach. *S. T. P. Pharma sciences*, 1 (4): 221-241.
- [50] Allemann, E., Gurny, R., Doelker, E., (1993) Drug-Loaded Nanoparticles - Preparation Methods and Drug Targeting Issues. *European Journal of Pharmaceutics and Biopharmaceutics*, 39 (5): 173-191.
- [51] Chasteigner, S., Fessi, H., Cave, G., Devissaguet, J.P., Puisieux, F., (1995) Gastrointestinal Tolerance Study of A Freeze-Dried Oral Dosage Form of Indomethacin-Loaded Nanocapsules. *Sciences et Techniques Pharmaceutiques (STP) Pharma Sciences*, 5 (3): 242-246.
- [52] Rose, C., (2010) Particulate systems for Fluorescence Imaging and Drug Delivery. PhD Thesis, University of Regensburg.
- [53] Feng, S.S., (2006) New-concept chemotherapy by nanoparticles of biodegradable polymers: where are we now? *Nanomedicine*, 1 (3): 297-309.
- [54] Dunn, S.E., Coombes, A.G.A., Garnett, M.C., Davis, S.S., Davies, M.C., Illum, L., (1997) In vitro cell interaction and in vivo biodistribution of poly(lactide-co-glycolide) nanospheres surface modified by poloxamer and poloxamine copolymers. *Journal of Controlled Release*, 44 (1): 65-76.
- [55] Storm, G., Belliot, S.O., Daemen, T., Lasic, D.D., (1995) Surface Modification of Nanoparticles to Oppose Uptake by the Mononuclear Phagocyte System. *Advanced Drug Delivery Reviews*, 17 (1): 31-48.
- [56] Kwon, G.S., Kataoka, K., (1995) Block-Copolymer Micelles As Long-Circulating Drug Vehicles. *Advanced Drug Delivery Reviews*, 16 (2-3): 295-309.
- [57] Maeda, H., Bharate, G.Y., Daruwalla, J., (2009) Polymeric drugs for efficient tumor-targeted drug delivery based on EPR-effect. *European Journal of Pharmaceutics and Biopharmaceutics*, 71 (3): 409-419.
- [58] Maeda, H., (2010) Tumor-Selective Delivery of Macromolecular Drugs via the EPR Effect: Background and Future Prospects. *Bioconjugate Chemistry*, 21 (5): 797-802.
- [59] Moghimi, S.M., Porter, C.J.H., Muir, I.S., Illum, L., Davis, S.S., (1991) Non-Phagocytic Uptake of Intravenously Injected Microspheres in Rat Spleen - Influence of Particle-Size and Hydrophilic Coating. *Biochemical and Biophysical Research Communications*, 177 (2): 861-866.
- [60] Moghimi, S.M., (1995) Mechanisms of Splenic Clearance of Blood-Cells and Particles - Towards Development of New Splenotropic Agents. *Advanced Drug Delivery Reviews*, 17 (1): 103-115.
- [61] Moghimi, S.M., Hunter, A.C., Murray, J.C., (2001) Long-circulating and target-specific nanoparticles: Theory to practice. *Pharmacological Reviews*, 53 (2): 283-318.

Bibliography:

- [62] Yuan, F., Dellian, M., Fukumura, D., Leunig, M., Berk, D.A., Torchilin, V.P., Jain, R.K., (1995) Vascular-Permeability in A Human Tumor Xenograft - Molecular-Size Dependence and Cutoff Size. *Cancer Research*, 55 (17): 3752-3756.
- [63] Gaumet, M., Vargas, A., Gurny, R., Delie, F., (2008) Nanoparticles for drug delivery: The need for precision in reporting particle size parameters. *European Journal of Pharmaceutics and Biopharmaceutics*, 69 (1): 1-9.
- [64] Avgoustakis, K., Beletsi, A., Panagi, Z., Klepetsanis, P., Livaniou, E., Evangelatos, G., Ithakissios, D.S., (2003) Effect of copolymer composition on the physicochemical characteristics, in vitro stability, and biodistribution of PLGA-mPEG nanoparticles. *International Journal of Pharmaceutics*, 259 (1-2): 115-127.
- [65] Beletsi, A., Panagi, Z., Avgoustakis, K., (2005) Biodistribution properties of nanoparticles based on mixtures of PLGA with PLGA-PEG diblock copolymers. *International Journal of Pharmaceutics*, 298 (1): 233-241.
- [66] Gombotz, W.R., Pettit, D.K., (1995) Biodegradable Polymers for Protein and Peptide Drug-Delivery. *Bioconjugate Chemistry*, 6 (4): 332-351.
- [67] Schwendeman, S.P., (2002) Recent advances in the stabilization of proteins encapsulated in injectable PLGA delivery systems. *Critical Reviews in Therapeutic Drug Carrier Systems*, 19 (1): 73-98.
- [68] van de Weert, M., Hennink, W.E., Jiskoot, W., (2000) Protein instability in poly(lactic-co-glycolic acid) microparticles. *Pharmaceutical Research*, 17 (10): 1159-1167.
- [69] Steinberg, D., Friedman, M., (1999) Dental drug-delivery devices: Local and sustained-release applications. *Critical Reviews in Therapeutic Drug Carrier Systems*, 16 (5): 425-459.
- [70] Sartor, O., (2003) Eligard: Leuprolide acetate in a novel sustained-release delivery system. *Urology*, 61 (2A): 25-31.
- [71] Okada, H., Inoue, Y., Heya, T., Ueno, H., Ogawa, Y., Toguchi, H., (1991) Pharmacokinetics of Once-A-Month Injectable Microspheres of Leuprolide Acetate. *Pharmaceutical Research*, 8 (6): 787-791.
- [72] Wischke, C., Schwendeman, S.P., (2008) Principles of encapsulating hydrophobic drugs in PLA/PLGA microparticles. *International Journal of Pharmaceutics*, 364 (2): 298-327.
- [73] Houchin, M.L., Topp, E.M., (2008) Chemical degradation of peptides and proteins in PLGA: A review of reactions and mechanisms. *Journal of Pharmaceutical Sciences*, 97 (7): 2395-2404.

Bibliography:

- [74] Perez, C., Castellanos, I.J., Costantino, H.R., Al-Azzam, W., Griebenow, K., (2002) Recent trends in stabilizing protein structure upon encapsulation and release from bioerodible polymers. *Journal of Pharmacy and Pharmacology*, 54 (3): 301-313.
- [75] Sinha, V.R., Trehan, A., (2003) Biodegradable microspheres for protein delivery. *Journal of Controlled Release*, 90 (3): 261-280.
- [76] Lu, W.Q., Park, T.G., (1995) In-Vitro Release Profiles of Eristostatin from Biodegradable Polymeric Microspheres - Protein Aggregation Problem. *Biotechnology Progress*, 11 (2): 224-227.
- [77] Ding, A.G., Schwendeman, S.P., (2008) Acidic Microclimate pH Distribution in PLGA Microspheres Monitored by Confocal Laser Scanning Microscopy. *Pharmaceutical Research*, 25 (9): 2041-2052.
- [78] Mäder, K., Gallez, B., Liu, K.J., Swartz, H.M., (1996) Non-invasive in vivo characterization of release processes in biodegradable polymers by low-frequency electron paramagnetic resonance spectroscopy. *Biomaterials*, 17 (4): 457-461.
- [79] Li, L., Schwendeman, S.P., (2005) Mapping neutral microclimate pH in PLGA microspheres. *Journal of Controlled Release*, 101 (1-3): 163-173.
- [80] Gatenby, R.A., Gawlinski, E.T., Gmitro, A.F., Kaylor, B., Gillies, R.J., (2006) Acid-mediated tumor invasion: a multidisciplinary study. *Cancer Research*, 66 (10): 5216-5223.
- [81] Weissleder, R., (2002) Scaling down imaging: Molecular mapping of cancer in mice. *Nature Reviews Cancer*, 2 (1): 11-18.
- [82] Rudin, M., Weissleder, R., (2003) Molecular imaging in drug discovery and development. *Nature Reviews Drug Discovery*, 2 (2): 123-131.
- [83] Massoud, T.F., Gambhir, S.S., (2003) Molecular imaging in living subjects: seeing fundamental biological processes in a new light. *Genes & Development*, 17 (5): 545-580.
- [84] HTStec, (2011) In Vivo Preclinical Imaging Trends 2011. Book, HTStec Ltd, Cambridge, UK.
- [85] Hebden, J.C., Arridge, S.R., Delpy, D.T., (1997) Optical imaging in medicine: I. Experimental techniques. *Physics in Medicine and Biology*, 42 (5): 825-840.
- [86] Cassidy, P.J., Radda, G.K., (2005) Molecular imaging perspectives. *Journal of the Royal Society Interface*, 2 (3): 133-144.
- [87] Hüttmann, G. Lönig, M., (2007) Physikalische Grundlagen optischer Technologien. Book, *Der Gynäkologe*, 5, 332-337.
- [88] Weissleder, R., Ntziachristos, V., (2003) Shedding light onto live molecular targets. *Nature Medicine*, 9 (1): 123-128.

Bibliography:

- [89] Wan, S., Parrish, J.A., Anderson, R.R., Madden, M., (1981) Transmittance of Nonionizing Radiation in Human-Tissues. *Photochemistry and Photobiology*, 34 (6): 679-681.
- [90] Weissleder, R., (2001) A clearer vision for in vivo imaging. *Nature Biotechnology*, 19 (4): 316-317.
- [91] Shuhendler, A.J., Prasad, P., Chan, H.K.C., Gordijo, C.R., Soroushian, B., Kolios, M., Yu, K., O'Brien, P.J., Rauth, A.M., Wu, X.Y., (2011) Hybrid Quantum Dot-Fatty Ester Stealth Nanoparticles: Toward Clinically Relevant in Vivo Optical Imaging of Deep Tissue. *Acs Nano*, 5 (3): 1958-1966.
- [92] Muller, M.G., Georgakoudi, I., Zhang, Q.G., Wu, J., Feld, M.S., (2001) Intrinsic fluorescence spectroscopy in turbid media: disentangling effects of scattering and absorption. *Applied Optics*, 40 (25): 4633-4646.
- [93] Yanagida, T. Ishii, Y., (2009) *Principles of fluorescence spectroscopy*. Book, WILEY-VCH Verlag GmbH & Co. KGaA, Weinheim.
- [94] Walla, P., (2009) *Modern biophysical chemistry: detection and analysis of biomolecules*. Book, WILEY-VCH Verlag GmbH & Co. KGaA, Weinheim.
- [95] Lakowicz, J. R., (2006) *Principles of fluorescence spectroscopy*. Book, 3rd Edition, Springer-Verlag Berlin, Heidelberg.
- [96] Macey, M. G., (2007) *Flow cytometry: principles and applications*. Book, Human press, New Jersey, 69.
- [97] Helm, M. Wöfl, S., (2007) *Instrumentelle Bioanalytik: Eine Einführung für Biologen, Biochemiker, Biotechnologen und Pharmazeuten*. Book, WILEY-VCH Verlag GmbH & Co. KGaA, Weinheim.
- [98] Ballou, B., Fisher, G.W., Waggoner, A.S., Farkas, D.L., Reiland, J.M., Jaffe, R., Mujumdar, R.B., Mujumdar, S.R., Hakala, T.R., (1995) Tumor Labeling In-Vivo Using Cyanine-Conjugated Monoclonal-Antibodies. *Cancer Immunology Immunotherapy*, 41 (4): 257-263.
- [99] Tung, C.H., (2004) Fluorescent peptide probes for in vivo diagnostic imaging. *Biopolymers*, 76 (5): 391-403.
- [100] McDonald, D.M., Choyke, P.L., (2003) Imaging of angiogenesis: from microscope to clinic. *Nature Medicine*, 9 (6): 713-725.
- [101] Kirchherr, A.K., Briel, A., Mäder, K., (2009) Stabilization of Indocyanine Green by Encapsulation within Micellar Systems. *Molecular Pharmaceutics*, 6 (2): 480-491.
- [102] Weissleder, R., Tung, C.H., Mahmood, U., Bogdanov, A., (1999) In vivo imaging of tumors with protease-activated near-infrared fluorescent probes. *Nature Biotechnology*, 17 (4): 375-378.

Bibliography:

- [103] Funovics, M., Weissleder, R., Tung, C.H., (2003) Protease sensors for bioimaging. *Analytical and Bioanalytical Chemistry*, 377 (6): 956-963.
- [104] Gross, L.A., Baird, G.S., Hoffman, R.C., Baldrige, K.K., Tsien, R.Y., (2000) The structure of the chromophore within DsRed, a red fluorescent protein from coral. *Proceedings of the National Academy of Sciences of the United States of America*, 97 (22): 11990-11995.
- [105] Chudakov, D.M., Lukyanov, S., Lukyanov, K.A., (2005) Fluorescent proteins as a toolkit for in vivo imaging. *Trends in Biotechnology*, 23 (12): 605-613.
- [106] Shcherbo, D., Merzlyak, E.M., Chepurnykh, T.V., Fradkov, A.F., Ermakova, G.V., Solovieva, E.A., Lukyanov, K.A., Bogdanova, E.A., Zarausky, A.G., Lukyanov, S., Chudakov, D.M., (2007) Bright far-red fluorescent protein for whole-body imaging. *Nature Methods*, 4 (9): 741-746.
- [107] Caysa, H., Jacob, R., Muther, N., Branchini, B., Messerle, M., Soling, A., (2009) A redshifted codon-optimized firefly luciferase is a sensitive reporter for bioluminescence imaging. *Photochemical & Photobiological Sciences*, 8 (1): 52-56.
- [108] Rao, J.H., Dragulescu-Andrasi, A., Yao, H.Q., Yao, H.Q., (2007) Fluorescence imaging in vivo: recent advances. *Current Opinion in Biotechnology*, 18 (1): 17-25.
- [109] Greenspan, P., Mayer, E.P., Fowler, S.D., (1985) Nile Red - A Selective Fluorescent Stain for Intracellular Lipid Droplets. *Journal of Cell Biology*, 100 (3): 965-973.
- [110] Licha, K., (2002) Contrast agents for optical imaging. *Contrast Agents II*, 222: 1-29.
- [111] Lavis, L.D., Raines, R.T., (2008) Bright ideas for chemical biology. *ACS Chemical Biology*, 3 (3): 142-155.
- [112] Packard, B.S., Wolf, D.E., (1985) Fluorescence Lifetimes of Carbocyanine Lipid Analogs in Phospholipid-Bilayers. *Biochemistry*, 24 (19): 5176-5181.
- [113] Hardin, J., (2006) Confocal and Multi-Photon Imaging of Living Embryos. Book, in: J. B. Pawley B. R. Masters (Eds.), *Handbook of Biological Confocal Microscopy*, SpringerScience + Business Media, New York, 43, 746-768.
- [114] Rashid, F., Horobin, R. W., and Williams, M. A., (1991) Predicting the behaviour and selectivity of fluorescent probes for lysosomes and related structures by means of structure-activity models. *The Histochemical Journal*, 23 (10): 450-459.
- [115] Rashid, F., Horobin, R.W., (1990) Interaction of Molecular Probes with Living Cells and Tissues. *Histochemistry and Cell Biology*, 94 (3): 303-308.

Bibliography:

- [116] Park, J.S., Han, T.H., Lee, K.Y., Han, S.S., Hwang, J.J., Moon, D.H., Kim, S.Y., Cho, Y.W., (2006) N-acetyl histidine-conjugated glycol chitosan self-assembled nanoparticles for intracytoplasmic delivery of drugs: Endocytosis, exocytosis and drug release. *Journal of Controlled Release*, 115 (1): 37-45.
- [117] Texier, I., Goutayer, M., Da Silva, A., Guyon, L., Djaker, N., Josserand, V., Neumann, E., Bibette, J., Vinet, F., (2009) Cyanine-loaded lipid nanoparticles for improved in vivo fluorescence imaging. *Journal of Biomedical Optics*, 14 (5): 054005-11.
- [118] Juarranz, A., Horobin, R.W., Proctor, G.B., (1986) Prediction of in situ fluorescence of histochemical reagents using a structure-staining correlation procedure. *Histochemistry*, 84 (4-6): 426-431.
- [119] Lynch, I., de Gregorio, P., Dawson, K.A., (2005) Simultaneous release of hydrophobic and cationic solutes from thin-film "plum-pudding" gels: A multifunctional platform for surface drug delivery? *Journal of Physical Chemistry B*, 109 (13): 6257-6261.
- [120] Wang, X.D., Wang, Y.J., Wei, K., Zhao, N.R., Zhang, S.H., Chen, J.D., (2009) Drug distribution within poly(epsilon-caprolactone) microspheres and in vitro release. *Journal of Materials Processing Technology*, 209 (1): 348-354.
- [121] Product information - SNARF pH indicators, (2003). Book, Molecular Probes.
- [122] Whitaker, J.E., Haugland, R.P., Prendergast, F.G., (1991) Spectral and Photophysical Studies of Benzo[C]Xanthene Dyes - Dual Emission Ph Sensors. *Analytical Biochemistry*, 194 (2): 330-344.
- [123] Opitz, N., Merten, E., Acker, H., (1994) Evidence for Redistribution-Associated Intracellular Pk Shifts of the Ph-Sensitive Fluoroprobe Carboxy-Snarf-1. *Pflugers Archiv-European Journal of Physiology*, 427 (3-4): 332-342.
- [124] Nile Red, (2013) *Public Chemical Database*, URL: http://pubchem.ncbi.nlm.nih.gov/summary/summary.cgi?cid=65182&loc=ec_r_cs (31-5-2013).
- [125] Greenspan, P., Mayer, E.P., Fowler, S.D., (1985) Nile Red - A Selective Fluorescent Stain for Intracellular Lipid Droplets. *J Cell Biol*, 100 (3): 965-973.
- [126] Jores, K., Haberland, A., Wartewig, S., Mäder, K., Mehnert, W., (2005) Solid lipid nanoparticles (SLN) and oil-loaded SLN studied by spectrofluorometry and raman spectroscopy. *Pharmaceutical Research*, 22 (11): 1887-1897.
- [127] Greenspan, P., Fowler, S.D., (1985) Spectrofluorometric Studies of the Lipid Probe, Nile Red. *Journal of Lipid Research*, 26 (7): 781-789.
- [128] Welch, A.J., Gardner, C., RichardsKortum, R., Chan, E., Criswell, G., Pfefer, J., Warren, S., (1997) Propagation of fluorescent light. *Lasers in Surgery and Medicine*, 21 (2): 166-178.

Bibliography:

- [129] Dunsby, C., French, P.M.W., (2003) Techniques for depth-resolved imaging through turbid media including coherence-gated imaging. *Journal of Physics D-Applied Physics*, 36 (14): R207-R227.
- [130] Ntziachristos, V., Ripoll, J., Wang, L.H.V., Weissleder, R., (2005) Looking and listening to light: the evolution of whole-body photonic imaging. *Nature Biotechnology*, 23 (3): 313-320.
- [131] Jacques, S.L., Pogue, B.W., (2008) Tutorial on diffuse light transport. *Journal of Biomedical Optics*, 13 (4).
- [132] Swartling, J., Svensson, J., Bengtsson, D., Terike, K., Andersson-Engels, S., (2005) Fluorescence spectra provide information on the depth of fluorescent lesions in tissue. *Applied Optics*, 44 (10): 1934-1941.
- [133] Keijzer, M., Richards-Kortum, R.R., Jacques, S.L., Feld, M.S., (1989) Fluorescence Spectroscopy of Turbid Media - Autofluorescence of the Human Aorta. *Applied Optics*, 28 (20): 4286-4292.
- [134] Utzinger, U., Richards-Kortum, R.R., (2003) Fiber optic probes for biomedical optical spectroscopy. *Journal of Biomedical Optics*, 8 (1): 121-147.
- [135] Billinton, N., Knight, A.W., (2001) Seeing the wood through the trees: A review of techniques for distinguishing green fluorescent protein from endogenous autofluorescence. *Analytical Biochemistry*, 291 (2): 175-197.
- [136] Wagnieres, G.A., Star, W.M., Wilson, B.C., (1998) In vivo fluorescence spectroscopy and imaging for oncological applications. *Photochemistry and Photobiology*, 68 (5): 603-632.
- [137] Mansfield, J.R., Gossage, K.W., Hoyt, C.C., Levenson, R.M., (2005) Autofluorescence removal, multiplexing, and automated analysis methods for in-vivo fluorescence imaging. *Journal of Biomedical Optics*, 10: 041207-041207-9.
- [138] Graves, E.E., Ripoll, J., Weissleder, R., Ntziachristos, V., (2003) A submillimeter resolution fluorescence molecular imaging system for small animal imaging. *Medical Physics*, 30 (5): 901-911.
- [139] Rice, B.W., Cable, M.D., Nelson, M.B., (2001) In vivo imaging of light-emitting probes. *Journal of Biomedical Optics*, 6 (4): 432-440.
- [140] Zhang, H.F., Maslov, K., Stoica, G., Wang, L.H.V., (2006) Functional photoacoustic microscopy for high-resolution and noninvasive in vivo imaging. *Nature Biotechnology*, 24 (7): 848-851.
- [141] Contag, C.H., Bachmann, M.H., (2002) Advances in vivo bioluminescence imaging of gene expression. *Annual Review of Biomedical Engineering*, 4: 235-260.

Bibliography:

- [142] Dickinson, M.E., Bearman, G., Tille, S., Lansford, R., Fraser, S.E., (2001) Multi-spectral imaging and linear unmixing add a whole new dimension to laser scanning fluorescence microscopy. *Biotechniques*, 31 (6): 1272-1278.
- [143] Zimmermann, T., Rietdorf, J., Pepperkok, R., (2003) Spectral imaging and its applications in live cell microscopy. *Federation of European Biochemical Societies (FEBS) Letters*, 546 (1): 87-92.
- [144] Choy, G., O'Connor, S., Diehn, F.E., Costouros, N., Alexander, H.R., Choyke, P., Libutti, S.K., (2003) Comparison of noninvasive fluorescent and bioluminescent small animal optical imaging. *Biotechniques*, 35 (5): 1022-1030.
- [145] Hobbs, S.K., Monsky, W.L., Yuan, F., Roberts, W.G., Griffith, L., Torchilin, V.P., Jain, R.K., (1998) Regulation of transport pathways in tumor vessels: Role of tumor type and microenvironment. *Proceedings of the National Academy of Sciences of the United States of America*, 95 (8): 4607-4612.
- [146] Brigger, I., Dubernet, C., Couvreur, P., (2002) Nanoparticles in cancer therapy and diagnosis. *Advanced Drug Delivery Reviews*, 54 (5): 631-651.
- [147] Reynolds, L.P., Grazul-Bilska, A.T., Redmer, D.A., (2000) Angiogenesis in the corpus luteum. *Endocrine*, 12 (1): 1-9.
- [148] Faure, A.C., Dufort, S., Josserand, V., Perriat, P., Coll, J.L., Roux, S., Tillement, O., (2009) Control of the in vivo biodistribution of hybrid nanoparticles with different poly (ethylene glycol) coatings. *Small*, 5 (22): 2565-2575.
- [149] Goutayer, M., Dufort, S., Josserand, V., Royère, A., Heinrich, E., Vinet, F., Bibette, J., Coll, J.L., Texier, I., (2010) Tumor targeting of functionalized lipid nanoparticles: assessment by in vivo fluorescence imaging. *European Journal of Pharmaceutics and Biopharmaceutics*, 75 (2): 137-147.
- [150] Tröster, S.D., Müller, U., Kreuter, J., (1990) Modification of the body distribution of poly (methyl methacrylate) nanoparticles in rats by coating with surfactants. *International Journal of Pharmaceutics*, 61 (1-2): 85-100.
- [151] Perez-Soler, R., Lopez-Berestein, G., Jahns, M., Wright, K., Kasi, L.P., (1985) Distribution of radiolabeled multilamellar liposomes injected intralymphatically and subcutaneously. *International Journal of Nuclear Medicine and Biology*, 12 (4): 261-263.
- [152] Harrington, K.J., Rowlinson-Busza, G., Syrigos, K.N., Uster, P.S., Abra, R.M., Stewart, J.S.W., (2000) Biodistribution and pharmacokinetics of ¹¹¹In-DTPA-labelled pegylated liposomes in a human tumour xenograft model: implications for novel targeting strategies. *British journal of cancer*, 83 (2): 232.
- [153] Thurston, G., McLean, J.W., Rizen, M., Baluk, P., Haskell, A., Murphy, T.J., Hanahan, D., McDonald, D.M., (1998) Cationic liposomes target angiogenic

Bibliography:

- endothelial cells in tumors and chronic inflammation in mice. *Journal of Clinical Investigation*, 101 (7): 1401.
- [154] Tröster, S.D., Kreuter, J., (1992) Influence of the surface properties of low contact angle surfactants on the body distribution of ¹⁴C-poly (methyl methacrylate) nanoparticles. *Journal of microencapsulation*, 9 (1): 19-28.
- [155] Zhao, X., Ze, Y., Gao, G., Sang, X., Li, B., Gui, S., Sheng, L., Sun, Q., Cheng, J., Cheng, Z., Hu, R., Wang, L., Hong, F., (2013) Nanosized TiO₂-Induced Reproductive System Dysfunction and Its Mechanism in Female Mice. *Plos One*, 8 (4).
- [156] Elnoury, M.A.H., Azmy, O.M., Elshal, A.O.I., Mohamed, A., Ragab, H., Elsherbini, E.-S.A.M., (2013) Study of the Effects of Silver Nanoparticles Exposure on the Ovary of Rats. *Life Science Journal*, 10 (2): 1887-1894.
- [157] Hirsjärvi, S., Sancey, L., Dufort, S., Belloche, C., Vanpouille-Box, C., Garcion, E., Coll, J.L., Hindré, F., Berges, L., (2013) Effect of particle size on the biodistribution of lipid nanocapsules: Comparison between nuclear and fluorescence imaging and counting. *International Journal of Pharmaceutics*, 453 (2): 594-600.
- [158] Cleland, J.L., Daugherty, A., Mrsny, R., (2001) Emerging protein delivery methods. *Current Opinion in Biotechnology*, 12 (2): 212-219.
- [159] Brunner, A., Mäder, K., Göpferich, A., (1999) pH and osmotic pressure inside biodegradable microspheres during erosion. *Pharmaceutical Research*, 16 (6): 847-853.
- [160] Zhu, G., Mallery, S.R., Schwendeman, S.P., (2000) Stabilization of proteins encapsulated in injectable poly (lactide-co-glycolide). *Nature Biotechnology*, 18 (1): 52-57.
- [161] Kempe, S., Metz, H., Pereira, P.G.C., Mäder, K., (2010) Non-invasive in vivo evaluation of in situ forming PLGA implants by benchtop magnetic resonance imaging (BT-MRI) and EPR spectroscopy. *European Journal of Pharmaceutics and Biopharmaceutics*, 74 (1): 102-108.
- [162] Fu, K., Pack, D.W., Klibanov, A.M., Langer, R., (2000) Visual evidence of acidic environment within degrading poly(lactic-co-glycolic acid) (PLGA) microspheres. *Pharmaceutical Research*, 17 (1): 100-106.
- [163] Mäder, K., Bittner, B., Li, Y.X., Wohlauf, W., Kissel, T., (1998) Monitoring microviscosity and microacidity of the albumin microenvironment inside degrading microparticles from poly(lactide-co-glycolide) (PLG) or ABA-triblock polymers containing hydrophobic poly(lactide-co-glycolide) A blocks and hydrophilic poly(ethyleneoxide) B blocks. *Pharmaceutical Research*, 15 (5): 787-793.
- [164] Shenderova, A., Ding, A.G., Schwendeman, S.P., (2004) Potentiometric method for determination of microclimate pH in poly(lactic-co-glycolic acid) films. *Macromolecules*, 37 (26): 10052-10058.

Bibliography:

- [165] Schmid, W., (2011) Evaluation und Weiterentwicklung der Schonenden Tablettierung unter Anwendung neu entwickelter Messmethoden. PhD Thesis, Martin Luther University Halle-Wittenberg.
- [166] Li, J., (2012) Development, Characterization and In Vivo Evaluation of Biodegradable Nanospheres and Nanocapsules. PhD Thesis, Martin Luther University Halle-Wittenberg.
- [167] Lochmann, A., (2012) Development and Characterization of Controlled Delivery Systems for rhBMP-2. PhD Thesis, Martin Luther University Halle-Wittenberg.
- [168] Comley, J., (2011) In vivo preclinical imaging: an essential tool in translational research. *drug discovery world*, 11.
- [169] Graves, E.E., Yessayan, D., Turner, G., Weissleder, R., Ntziachristos, V., (2005) Validation of in vivo fluorochrome concentrations measured using fluorescence molecular tomography. *Journal of Biomedical Optics*, 10 (4).
- [170] Frangioni, J.V., (2003) In vivo near-infrared fluorescence imaging. *Current Opinion in Chemical Biology*, 7 (5): 626-634.
- [171] Resch-Genger, U., Grabolle, M., Cavaliere-Jaricot, S., Nitschke, R., Nann, T., (2008) Quantum dots versus organic dyes as fluorescent labels. *Nature Methods*, 5 (9): 763-775.
- [172] Sevick-Muraca, E.M., Houston, J.P., Gurfinkel, M., (2002) Fluorescence-enhanced, near infrared diagnostic imaging with contrast agents. *Current Opinion in Chemical Biology*, 6 (5): 642-650.
- [173] Lim, H.J., Parr, M.J., Masin, D., McIntosh, N.L., Madden, T.D., Zhang, G.Y., Johnstone, S., Bally, M.B., (2000) Kupffer cells do not play a role in governing the efficacy of liposomal mitoxantrone used to treat a tumor model designed to assess drug delivery to liver. *Clinical Cancer Research*, 6 (11): 4449-4460.
- [174] Petersen, S., Fahr, A., Bunjes, H., (2010) Flow Cytometry as a New Approach To Investigate Drug Transfer between Lipid Particles. *Molecular Pharmaceutics*, 7 (2): 350-363.
- [175] Ntziachristos, V., (2006) Fluorescence molecular imaging. *Annual Review of Biomedical Engineering*, 8: 1-33.
- [176] Klohs, J., Wunder, A., Licha, K., (2008) Near-infrared fluorescent probes for imaging vascular pathophysiology. *Basic Research in Cardiology*, 103 (2): 144-151.
- [177] Jain, R.K., Munn, L.L., Fukumura, D., (2002) Dissecting tumour pathophysiology using intravital microscopy. *Nature Reviews Cancer*, 2 (4): 266-276.
- [178] Levenson, R.M., Mansfield, J.R., (2006) Multispectral imaging in biology and medicine: Slices of life. *Cytometry Part A*, 69A (8): 748-758.

Bibliography:

- [179] Levenson, R.M., Lynch, D.T., Kobayashi, H., Backer, J.M., Backer, M.V., (2008) Multiplexing with multispectral imaging: From mice to microscopy. *Ilar Journal*, 49 (1): 78-88.
- [180] Li, Z.H., Wu, L.Y., Hu, P.R., Han, S.H., Zhang, T., Fan, H.L., Jin, W., Jin, Q.H., Mu, Y., (2012) Soft nanomaterial-based targeting polymersomes for near-infrared fluorescence multispectral in vivo imaging. *Nanoscale*, 4 (22): 7097-7105.
- [181] User's Manual for Maestro 2.4, (2007). Book, Cambridge Research & Instrumentation, Inc.
- [182] Kempe, S., (2012) Non-invasive Characterization of in situ forming Implants. PhD Thesis, Martin Luther University Halle-Wittenberg.
- [183] Napp, J., Mathejczyk, J.E., Alves, F., (2011) Optical imaging in vivo with a focus on paediatric disease: technical progress, current preclinical and clinical applications and future perspectives. *Pediatric Radiology*, 41 (2): 161-175.
- [184] Montet, X., Ntziachristos, V., Grimm, J., Weissleder, R., (2005) Tomographic fluorescence mapping of tumor targets. *Cancer Research*, 65 (14): 6330-6336.
- [185] Ntziachristos, V., Schellenberger, E.A., Ripoll, J., Yessayan, D., Graves, E., Bogdanov, A., Josephson, L., Weissleder, R., (2004) Visualization of antitumor treatment by means of fluorescence molecular tomography with an annexin V-Cy5.5 conjugate. *Proceedings of the National Academy of Sciences of the United States of America*, 101 (33): 12294-12299.
- [186] Montet, X., Figueiredo, J.L., Alencar, H., Ntziachristos, V., Mahmood, U., Weissleder, R., (2007) Tomographic fluorescence imaging of tumor vascular volume in mice. *Radiology*, 242 (3): 751-758.
- [187] Haller, J., Hyde, D., Deliolanis, N., de Kleine, R., Niedre, M., Ntziachristos, V., (2008) Visualization of pulmonary inflammation using noninvasive fluorescence molecular imaging. *Journal of Applied Physiology*, 104 (3): 795-802.
- [188] Eisenblatter, M., Holtke, C., Persigehl, T., Bremer, C., (2010) Optical techniques for the molecular imaging of angiogenesis. *European Journal of Nuclear Medicine and Molecular Imaging*, 37: 127-137.
- [189] Meier, R., Krug, C., Golovko, D., Boddington, S., Piontek, G., Rudelius, M., Sutton, E.J., Baur-Melnyk, A., Jones, E.F., drup-Link, H.E., (2010) Indocyanine Green-Enhanced Imaging of Antigen-Induced Arthritis With an Integrated Optical Imaging/Radiography System. *Arthritis and Rheumatism*, 62 (8): 2322-2327.
- [190] Slakter, J.S., Yannuzzi, L.A., Guyer, D.R., Sorenson, J.A., Orlock, D.A., (1995) Indocyanine-green angiography. *Current Opinion in Ophthalmology*, 6 (3): 25-32.

Supplemental material

This cumulative dissertation contains the following research articles.

(a) Investigation of the *in vivo* fate of a water soluble polymer

- (I) **Title:** Noninvasive *in vivo* monitoring of the biofate of 195 kDa poly(vinyl alcohol) by multispectral fluorescence imaging.

Authors: Schädlich, A., Naolou, T., Amado, E., Schöps, R., Kressler, J., Mäder, K.

Reprinted with permission from Biomacromolecules 12 (10), Andreas Schädlich, Toufik Naolou, Elkin Amado, Regina Schöps, Jörg Kressler, and Karsten Mäder, Noninvasive in vivo monitoring of the biofate of 195 kDa poly(vinyl alcohol) by multispectral fluorescence imaging. (2011), 3674-3683.

© Copyright (2011) American Chemical Society.

<http://dx.doi.org/10.1021/bm200899h>

- (II) **Title:** In-vivo studies on *intraperitoneally* administrated poly(vinyl alcohol).

Authors: Jiang, Y., Schädlich, A., Amado, E., Weis, C., Odermatt, E., Mäder, K., Kressler, J.

Reprinted with permission from Journal of Biomedical Materials Research Part B-Applied Biomaterials 93B (1), Yanjiao Jiang, Andreas Schädlich, Elkin Amado, Christine Weis, Erich Odermatt, Karsten Mäder, and Jörg Kressler, Kressler (2010), In-vivo studies on intraperitoneally administrated poly(vinyl alcohol), 275-284.

© Copyright 2010 Wiley Periodicals, Inc.

<http://dx.doi.org/10.1002/jbm.b.31585>

- (III) **Title:** Tracking the *in vivo* fate of high molar mass poly(vinyl alcohol) using multispectral fluorescence *in vivo* imaging.

Authors: Schädlich, A., Jiang, Y., Kressler, J., Mäder, K.,

Reprinted with permission from Scientifically Speaking News (Controlled Release Society) 27 (2), Andreas Schädlich, Yanjiao Jiang, Jörg Kressler, Karsten Mäder, Tracking the in vivo fate of high molar mass poly(vinyl alcohol) using multispectral fluorescence in vivo imaging. (2010), 15-16.

© Copyright (2010) Controlled Release Society.

(b) Characterization of nanocarriers and their potential usage in cancer therapy

(IV) Title: How stealthy are PEG-PLA nanoparticles? An NIR *in vivo* study combined with detailed size measurements.

Authors: Schädlich, A., Rose, C., Kuntsche, J., Caysa, H., Mueller, T., Göpferich, A., Mäder, K.

Reprinted with kind permission from Springer Science + Business Media and the original publisher Pharmaceutical Research, 28, 2011, 1995-2007, How stealthy are PEG-PLA nanoparticles? An NIR in vivo study combined with detailed size measurements, Andreas Schädlich, Cornelia Rose, Judith Kuntsche, Henrike Caysa, Thomas Mueller, Achim Göpferich, Karsten Mäder.

© Springer Science + Business Media, LLC 2011.

<http://dx.doi.org/10.1007/s11095-011-0426-5>

(V) Title: Tumor accumulation of NIR fluorescent PEG PLA nanoparticles: impact of particle size and human xenograft tumor model.

Authors: Schädlich, A., Caysa, H., Mueller, T., Tenambergen, F., Rose, C., Göpferich, A., Kuntsche, J., Mäder, K.

Reprinted with permission from ACS Nano, Andreas Schädlich, Henrike Caysa, Thomas Mueller, Frederike Tenambergen, Cornelia Rose, Achim Göpferich, Judith Kuntsche, and Karsten Mäder, Tumor Accumulation of NIR Fluorescent PEG-PLA Nanoparticles: Impact of Particle Size and Human Xenograft Tumor Model. (2011), 8710-8720.

© Copyright (2011) American Chemical Society.

<http://dx.doi.org/10.1021/nn2026353>

(VI) Title: Accumulation of nanocarriers in the ovary: A neglected toxicity risk?

Authors: Schädlich, A., Hoffmann, S., Mueller, T., Caysa, H., Rose, C., Göpferich, A., Li, J., Kuntsche, J., Mäder, K.

Reprinted from Journal of Controlled Release, 160 (1), Andreas Schädlich, Stefan Hoffmann, Thomas Mueller, Henrike Caysa, Cornelia Rose, Achim Göpferich, Jun Li, Judith Kuntsche, Karsten Mäder, Accumulation of nanocarriers in the ovary: A neglected toxicity risk? (2012), 105-112.

© Copyright (2012), with permission from Elsevier.

<http://dx.doi.org/10.1016/j.jconrel.2012.02.012>

(c) Characterization of *in situ* forming implants for potential controlled API release

(VII) Title: Long-term *in vivo* pH measurements of *in situ* forming PLGA implants using multispectral fluorescence imaging.

Authors: Schädlich, A., Kempe, S., Mäder, K.

Submitted to Journal of Controlled Release, Andreas Schädlich, Sabine Kempe, Karsten Mäder, Long-term in vivo pH measurements of in situ forming PLGA implants using multispectral fluorescence imaging. (2013), under peer-review.

(d) Investigating alternative application fields of fluorescence imaging

(VIII) Title: Monitoring of internal pH gradients within multi-layer tablets by optical methods and EPR imaging.

Authors: Eisenächer, F., Schädlich, A., Mäder, K.

Reprinted from International Journal of Pharmaceutics, 417 (1-2), Friederike Eisenächer, Andreas Schädlich, Karsten Mäder, Monitoring of internal pH gradients within multi-layer tablets by optical methods and EPR imaging. (2011), 204-215.

© Copyright (2011), with permission from Elsevier.

<http://dx.doi.org/10.1016/j.ijpharm.2010.10.010>



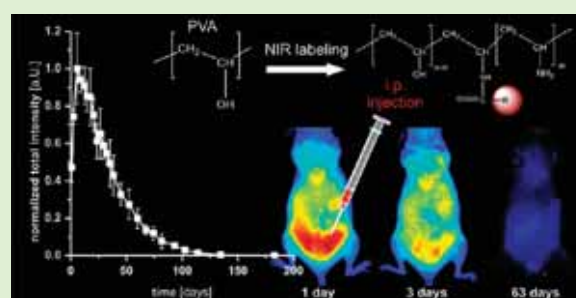
Noninvasive *In Vivo* Monitoring of the Biofate of 195 kDa Poly(vinyl alcohol) by Multispectral Fluorescence Imaging

Andreas Schädlich,[†] Toufik Naolou,[‡] Elkin Amado,[‡] Regina Schöps,[‡] Jörg Kressler,[‡] and Karsten Mäder^{*†}

[†]Martin Luther University Halle-Wittenberg, Department of Pharmaceutical Technology and Biopharmaceutics, Wolfgang-Langenbeck-Strasse 4, D-06120 Halle (Saale), Germany

[‡]Martin Luther University Halle-Wittenberg, Department of Chemistry/Physical Chemistry of Polymers, Von-Danckelmann-Platz 4, D-06120 Halle (Saale), Germany

ABSTRACT: A comprehensive knowledge of the *in vivo* fate of polymers is essential for their potential application in humans. In this study, the body distribution, accumulation, and elimination processes of intraperitoneally (ip) administered poly(vinyl alcohol) (PVA) in mice were investigated in detail. Two derivatives of PVA (195 kDa) having covalently bound fluorescent dye labels were synthesized and used to follow PVA *in vivo* by noninvasive multispectral fluorescence imaging over several months. Detailed *ex vivo* fluorescence imaging was performed additionally and combined with tissue accumulation studies using confocal microscopy. Filtration and confocal imaging at appropriate synthetic membranes, used as models for glomerular filtration, confirmed a considerable PVA permeation. This investigation yields new scientific findings about the fate of PVA *in vivo*. PVA accumulated in fat tissue at high levels, which suggests that PVA is suitable not only for abdominal surgeries but also for controlled release applications after ip or subcutaneous injection.



INTRODUCTION

Biocompatible polymers are being extensively studied for numerous pharmaceutical applications in the form of microspheres, nanoparticles, in situ forming implants, coatings and for protein delivery or as a plasma expander. Poly(vinyl alcohol) (PVA) is already used in various pharmaceutical and biomedical applications as well as in biotechnology and food chemistry.^{1,2} It is a water-soluble, nonionic, nontoxic, nonimmunogenic synthetic polymer. It is relatively inert in body fluids, and it is approved in several market products by the Food and Drug Administration (FDA).^{2–5} The properties of PVA are mainly influenced by its molar mass and the degree of hydrolysis of the precursor polymer poly(vinyl acetate). PVA has a high content of hydroxyl groups, good mechanical strength, high elasticity, and weak protein adsorption.^{5,6} It is reported that PVA hydrogels have high water contents and excellent mechanical properties, because of which they are ideally suitable for soft tissue engineering and for the immobilization of molecules and cells.^{6–9} PVA is also used as articular cartilage, for catheters, and as artificial skin.^{3,10,11} PVA-based hydrogels are being extensively studied for drug delivery applications, too.^{1,7,12} Because of its excellent film forming, emulsifying, and adhesive properties, PVA hydrogels are being considered for accelerating wound healing and preventing postoperative adhesions,^{13–16} which are internal scars affecting patients after abdominal surgeries.^{17,18} Polymeric membranes currently used to prevent adhesions are among others oxidized, regenerated cellulose membranes (Interceed, Ethicon 360),

hyaluronic acid–carboxymethylcellulose membranes (Seprafilm, Genzyme), and expanded polytetrafluoroethylene membranes (Preclude, Gore).^{19,20} Such polymeric membranes have several drawbacks. Some of them are not biodegradable or cannot be reabsorbed after peritoneal healing. A major disadvantage of membranes is that they cannot be applied in every surgical site. In contrast, gels or liquid solutions can easily be injected over the wound and also be applied to less accessible areas. PVA has already been proven as a promising alternative. Also, the additional binding of drug molecules to the PVA backbone is easily achieved and would allow simultaneous drug therapy at the site of application. High-molar mass PVA must be used to prolong the remaining time at the place of application.¹⁶ Some studies showed that PVA polymers with molar masses of 125 or 195 kDa are the most suitable.^{15,16,21} In spite of these potential uses, the detailed *in vivo* fate of high-molar mass PVA after intraperitoneal (ip) application is still unexplored. Until now, only a few studies deal with PVA elimination pathways.^{16,22–24} Because PVA biodegradation is limited to bacteria and fungi^{25,26} and has not been found in humans, the polymer is eliminated without being changed. Recent studies demonstrated that ip administered PVA up to 195 kDa can be excreted through the kidneys without renal glomeruli being damaged.^{16,22} This was

Received: June 30, 2011

Revised: July 30, 2011

Published: August 23, 2011

observed even though the molar mass and the hydrodynamic radius (R_h) of expected PVA spheres (~ 13 nm) are far larger than the reported limits (R_h of <6.5 nm or a molar mass of <30 – 69 kDa) for glomerular protein and polymer filtration.^{24,27} This fact can be explained by the flexibility of the PVA chains.

In this study, extensive long-term *in vivo* investigations were performed to follow the fate of PVA in a noninvasive way. PVA (195 kDa) was labeled either with a rhodamine dye or with Alexa Fluor 750, a near-infrared (NIR) dye. Both dyes possess different imaging characteristics, which allowed complementary extensive *in vivo* studies over several months. The obtained distribution, accumulation, and elimination behaviors were complemented with *ex vivo* experiments, including confocal microscopy studies to follow the fate of PVA at the cellular level. To gain a better understanding of the PVA *in vivo* elimination processes, *in vitro* filtration experiments with commercial available polyethersulfone (PES) membrane filters were performed. The membranes had nominal molecular mass cutoffs (NMMC) of 30 and 50 kDa and nominal pore sizes, which were much smaller than the hydrodynamic diameter of PVA (195 kDa) molecules.

EXPERIMENTAL SECTION

Materials. PVA (Mowiol 56-98, Kuraray) had an average molar mass (M_w) of 195 kDa (4300 repeating units; n in Figure 1), a polydispersity index (PDI) of 2.3, and a degree of hydrolysis of 98.4 mol % (data provided by Kuraray). Dry dimethyl sulfoxide (DMSO, 99.5%), dimethylformamide (DMF), dimethyl ether, dichloromethane (99.9%), methanol (99.5%), and *p*-toluenesulfonyl chloride were purchased from Fluka. Triphenylphosphine (99%), sodium azide (99.99%), and sodium bicarbonate were purchased from Sigma-Aldrich. For PVA labeling synthesis, tetramethylrhodamine-5-carboxyl azide (TMR) and Alexa Fluor 750 were obtained from Invitrogen.

Synthesis of Fluorescent Dye-Labeled PVA. For the *in vivo* fluorescence studies, the PVA backbone was labeled either with TMR ($\lambda_{em} = 577$ nm) (named PVA-TMR) or with the NIR dye Alexa Fluor 750 ($\lambda_{em} = 780$ nm) (named PVA-NIR).

PVA-TMR Labeling. PVA was labeled as described previously.²² Briefly, the reactive fluorescence TMR dye and the PVA were dissolved in anhydrous DMSO (2.2/1 PVA/TMR molar ratio). The reaction was conducted at 80 °C for 12 h. The final labeled PVA (PVA-TMR) with a stable urethane bond²⁸ was freeze-dried and stored in a desiccator, protected from light. The final degree of functionalization with TMR was 0.01 mol %. Thus, it can be assumed that every second polymer chain was labeled. The fluorescence emission maximum was determined to be 577.3 nm and is not shifted compared to that of pure TMR.

PVA-NIR Labeling. For PVA-NIR synthesis, five different steps were necessary (see Figure 1).

Decrystallization of PVA. This procedure was necessary to convert crystalline fractions to an amorphous state that is indispensable for conducting the tosylation reaction. Functional groups in the crystalline polymer would be inaccessible, and the chemical reaction would be limited to the amorphous region.²⁹ PVA crystals were decrystallized using a water/methanol system. PVA (4 g) was dissolved at 70 °C in 50 mL of deionized water. The solution was allowed to cool to room temperature, and the polymer was precipitated into 300 mL of methanol. The resulting polymer was dried under vacuum at 70 °C for 1 day.

Tosylation of PVA. The reaction was performed according to the method of Ikeda et al.²⁹ PVA (1 g) was swollen in 25 mL of pyridine (100 °C, 2 h). One gram (0.25 equiv with respect to the hydroxyl group) of *p*-toluenesulfonyl chloride was added (at 0 °C). The reaction was conducted at room temperature (24 h). Afterward, the polymer was

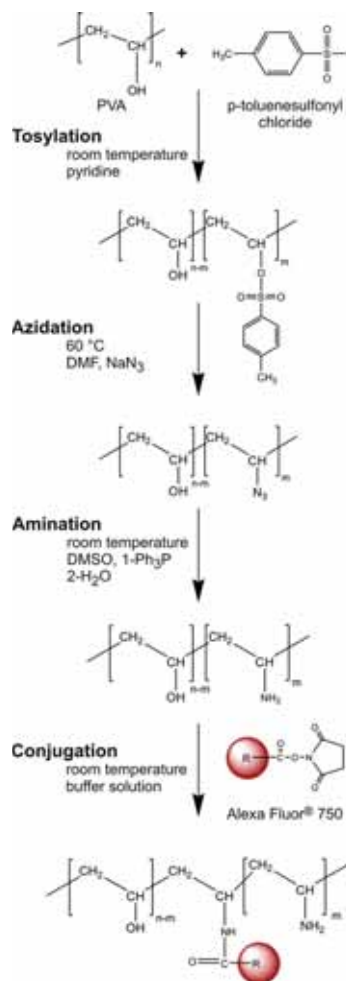


Figure 1. Synthesis of NIR-labeled PVA (from top to bottom): tosylation reaction of PVA, azidation of tosylated PVA, amination of PVA- N_3 , and conjugation reaction of PVA- NH_2 with fluorescence dye Alexa Fluor 750 ($n = 4300$; $m = 30$).

precipitated into methanol (400 mL), washed with methanol, and dried at room temperature under vacuum (24 h). 1H NMR calculation analysis indicated a tosylation ratio of 0.68% of the hydroxyl groups.

Azidation of Tosylated PVA. The azidation, already reported by Gacal et al.,³⁰ of tosylated PVA (0.9 g) by addition of sodium azide (NaN_3 , 0.52 g) was performed in 50 mL of DMF at 60 °C for 60 h. The product (PVA- N_3) was precipitated in 350 mL of dimethyl ether and washed with 700 mL of deionized water. The resulting 1H NMR spectrum showed complete disappearance of all tosyl signals. The azide group was indicated by infrared spectroscopy.

Amination of PVA- N_3 . Amination was achieved via the Staudinger reaction. PVA- N_3 (150 mg) was dissolved at 90 °C in DMSO (25 mL). After the sample cooled down to 24 °C, triphenylphosphine (1- Ph_3P) was added (14 mg), and the solution was stirred for 48 h. Deionized water (5 mL) was added, and the reaction was stopped after 24 h. PVA- NH_2 was precipitated in methanol. The resulting IR spectrum showed the complete disappearance of azide groups.

Conjugation with NIR Dye. This was performed by reacting PVA- NH_2 with the amine-reactive Alexa Fluor 750 carboxylic acid, succinimidyl

ester dye. PVA-NH₂ (40 mg) and a 0.13 M sodium bicarbonate buffer solution (2.5 mL) were dissolved at 70 °C. The NIR Alexa Fluor 750 dye (1 mg) was dissolved in DMSO (100 μ L) and slowly added to the PVA-NH₂ solution. After being stirred for 24 h at room temperature (24 °C), in the dark, the solution was dialyzed (3500 g/mol cutoff dialysis membrane) against DMSO. The DMSO was replaced daily until no free dye was detected by fluorescence spectroscopy. Dialysis was continued to exchange DMSO against deionized water (2 days and 4 times). The final solution was freeze-dried, and a yield of 28 mg of PVA-NIR was obtained.

Filtration Experiments. *Centrifugal Filtration.* Two milliliters of a PVA-NIR solution (0.13 mg/mL) were centrifuged (5000 rpm) at room temperature (21 °C) using a 30K Microsep Centrifugal Device (Pall Corp.) that included an Omega membrane (NMMC of 30 kDa, <4 nm pore size, 0.46 cm² filtration area). At least 1 mL of filtrate was collected to calculate the filtrate concentration by photometric measurements at 750 nm, using an UV–visible spectrophotometer (Ultrospec 3000 from Pharmacia).

Pressure Filtration. Aqueous PVA solutions (100 mL, 0.1–1.0 mg/mL) were filtered at 21 or 37 °C and 1 bar of transmembrane pressure with a stirred Amicon ultrafiltration cell (Millipore Corp.) with a K50 Omega filter disk (NMMC of 50 kDa, \sim 5 nm pore size, 28.7 cm² filtration area) from Pall Corp.; 60 mL of each filtrate were collected and dried by evaporation to a constant weight. The concentration of the filtrate was calculated from the PVA mass and filtration rates from each filtration time.

Gel Permeation Chromatography (GPC). For molar mass distribution control, dried and redissolved filtrate (60 mL, collected over approximately 50 min) and retentate (40 mL) samples from pressure filtration (0.5 mg/mL PVA) were checked against a fresh prepared PVA solution with GPC max (Viscotek GmbH) by refractive index (RI) detection. Hydroxyethyl starch (HES) standards were used for calibration.

Confocal Imaging. Parts of a perfusion-open-closed-reduced (POC-R) chamber (H. Saur Laborbedarf) were used to construct a small filtration unit (bottom/top, base plate with cover glass/silicon seal with the water subphase inside, membrane/silicon seal with PVA-TMR solution inside) for inverse microscopic observation. The permeation of a 2 mg/mL PVA-TMR solution to the water subphase through a K50 Omega filter disk was followed for 20 min by confocal laser scanning microscopy (CLSM), using a Leica TCS SP2 at Leica DM IRE2 microscope with an HC PL Fluotar 10 \times 0.3 dry objective (Leica Microsystems, Wetzlar, Germany). The excitation occurred at 543 nm. Overlay images (47.2 μ m \times 46.9 μ m) were recorded by *x,z*-single scans (frame average, 10) detected at two channels: 534–554 nm (reflection) and 573–587 nm (emission).

In Vivo Imaging and Analysis. All *in vivo* experiments complied with the standards for the usage of animal subjects as stated in the guideline from the animal care and use committee of Saxony Anhalt. *In vivo* studies were performed in nude, female and male mice (CrI:SKH1-Hr^{hr}, 25–30 g) from Charles River Laboratories. They were housed under controlled conditions with a 12 h light–dark schedule at 24 °C (room temperature). Labeled PVA (5 wt % PVA-TMR or 2.5 wt % PVA-NIR) was redispersed in filtered (0.22 μ m) purified water (isotonized with sorbitol). To guarantee complete PVA dissolution, the dispersion was quickly heated to 70 °C and vortexed. After cooling to room temperature, the clear, colored solutions were slowly *ip* injected (100 μ L) into the middle of the abdomen of the narcotized mice (anesthetized with a mixture of isoflurane and oxygen, an initial flow of 4% isoflurane and oxygen at a rate of 3.0 L/min and a steady state flow of 1.8% isoflurane and oxygen at a rate of 1.5 L/min). To prevent the mice from experiencing a lethal decrease in body temperature during the narcosis, they were placed on a 35 °C temperature-controlled heating plate. A first fluorescence image was taken to guarantee correctly placed injections, in the middle of the abdomen.

In vivo measurements were taken using the Maestro *in vivo* fluorescence imaging system (Cambridge Research & Instrumentation) and the Maestro software (version 2.10). A Cermax-type 300 W xenon lamp with 5600 K, a green filter set for PVA-TMR (excitation range, 503–555 nm; emission, 580 nm long-pass), and a deep red excitation filter set for PVA-NIR (excitation range, 671–705 nm; emission, 750 nm long-pass) were used. The imaging proceeded in 2 nm steps for PVA-TMR and 10 nm steps for PVA-NIR. Exposure times were automatically set to optimal values. For time-dependent measurements, primarily determined exposure times were used for all further images. The *in vivo* reference spectra for PVA-TMR and PVA-NIR were generated via extraction of a *sc in vivo* dye signal from the chest area, 24 h after the injection of labeled PVA. This *sc* PVA-TMR or PVA-NIR signal consisted of dye emission and autofluorescence, due to molecules in tissues and fodder that can act as biochemical sources of fluorescence.^{31,32} For exact fluorescence imaging measurements, the autofluorescence was isolated from the mixed *sc* spectra by the manual computing software function. The detected autofluorescence signal was grabbed from an untreated mouse and measured under the same conditions. Using the reference spectra (isolated PVA-TMR or PVA-NIR and the autofluorescence as a background signal) allowed us to unmix and further segment the measured cubes.^{33–35} In the case of PVA-TMR, a further differentiation between subcutaneous [in the following named PVA-TMR (*sc*)] and deeper emitted signals [named PVA-TMR (*ip*)] was possible. To determine the PVA-TMR (*ip*) spectra, a signal from the ventral fat area (as overlay from background, *ip*, and *sc* signals) was manually computed using both pure *sc* (grabbed at the chest area) and background autofluorescence signals.

Computed PVA-TMR (*sc*), PVA-TMR (*ip*), or PVA-NIR and corresponding background spectra allowed generation of monochrome images for each respective emission spectrum. These grayscale images were further calculated to obtain intensity-weighted incremental jet color images. Thereby, pixels with maximal intensities were set to dark red and pixels with no fluorescence to black. Between those two colors, there was a gradation from red to orange, yellow, light blue, and dark blue. All *in vivo* PVA-NIR images of a series of measurements were analyzed together (“compare imaging” function), correlating them to respective exposure times and using the incremental jet color profile simultaneously for all images. For quantitative analysis, an area of interest (ROI) in the size of the whole image was used to extract total and maximal intensities from isolated PVA-TMR (*sc*), PVA-TMR (*ip*), or PVA-NIR channels.

Ex Vivo Imaging and Analysis. Excised tissues (abdominal fat, kidney fat, skin, kidneys, liver, and spleen) of mice, sacrificed after defined periods of time (3 days and 3 months), were imaged with the Maestro *in vivo* imaging system. To ensure reproducible conditions like position and incident angle of the light, the organs were placed into a 24-hole well plate. The imaging setup was in accordance with *in vivo* measurements. Using emitted PVA-NIR signals allowed the calculation of corresponding jet color images, based on above-described compare imaging function.

Ex Vivo Confocal Imaging. Leica TCS SP2, as described for *in vitro* confocal imaging, was also used for confocal tissue imaging. The microscope was equipped with a 40 \times Plan Apo oil immersion objective. PVA-TMR was excited with a 543 nm laser. Emitted fluorescence was detected in the bandwidth from 555 nm to the upper limit. To image *ex vivo* samples, fat tissue was excised and cut into pieces that were as thin as possible into small panels (approximately 0.5 mm), using a racer plate. These were slightly pressed between two cover slides. For extended tests, abdominal fat from an untreated mouse was incorporated for 3 min with 2 droplets of PVA-TMR, washed (20 min in purified water), and imaged.

RESULTS AND DISCUSSION

Synthesis of Dye-Labeled PVA. PVA was successfully labeled with two fluorescent dyes (TMR or Alexa Fluor 750) having

different, well-separated fluorescence emission maxima. The dyes were linked to the PVA backbone by either an urethane bond (PVA-TMR) or an amide bond (PVA-NIR), which has been shown to be very stable *in vivo* and *in vitro*.^{28,36}

The labeling of the PVA backbone with TMR dye was conducted as described previously.²² For NIR labeling, it was necessary to synthesize different intermediates as shown in Figure 1. The main synthesis steps were the tosylation of PVA, followed by the azidation of tosylated PVA, then amination, and finally a conjugation reaction with the fluorescence dye. Both azidation and amination reactions were quantitative. The degree of functionalization of the hydroxyl groups to amine groups was 0.68 mol % ($m = 30$ in Figure 1). Between one and four of the amine groups per chain were then conjugated with the NIR dye. The overall degree of functionalization of the hydroxyl groups with NIR dye was as low as 0.02–0.09 mol % to preserve the properties of PVA.

In Vitro Filtration Experiments. Centrifugal and pressure filtration experiments with modified PES membranes (Omega) were conducted to study the urinary excretion mechanism of high-molar mass PVA (195 kDa). The polymer, with an assumed spherical structure in water because of favorable PVA–water interactions, had a hydrodynamic radius (R_h) of ~ 13 nm.²² Two membrane pore sizes (NMMC of 30 and 50 kDa), much smaller than the molecular size of PVA molecules, were used to simulate the process of renal filtration *in vitro*. To minimize surface binding and gelation effects, which can affect centrifugal filtration, low-concentration PVA solutions (<1 mg/mL) were used. To simulate conditions closer to physiological ones, the filtration experiment with 30 kDa membranes was repeated with sodium chloride- and urea-containing solutions. All aqueous polymer solutions were generally filtered at room temperature. Possible temperature dependencies were furthermore investigated at 37 °C with an aqueous PVA solution (50 kDa membrane). The results of centrifugal (a) and pressure (b and c) filtrations of different PVA or dye-labeled PVA solutions at room temperature are shown in Figure 2.

Filtrate concentrations (Figure 2a,b) demonstrated that there is a considerable permeation of PVA molecules through membranes with a nominal pore size of ~ 5 nm (NMMC of 50 kDa) and also of <4 nm (NMMC of 30 kDa). On average, filtrate concentrations between 20 and 30% of the initial, low concentrations of PVA solutions (0.1–0.2 mg/mL) were found. As expected, an increase in the filtrate concentration and a decrease in the filtration rate were found with increasing initial PVA concentrations (Figure 2b).

We also noticed a decrease in the filtration rate over time (because of the increasing viscosity of the retentate), but no time dependence of the permeation rate (micrograms per minute per square centimeter), calculated as a product of the filtration rate and filtrate concentration, was found (results not shown). Permeation rates calculated for PVA-NIR and PVA filtration experiments (~ 0.1 mg/mL) were $0.3 \mu\text{g mL}^{-1} \text{cm}^{-2}$ on the 30 kDa membrane (centrifugal filtration, Figure 2a) and $4.3 \mu\text{g mL}^{-1} \text{cm}^{-2}$ on the 50 kDa membrane (pressure filtration, Figure 2b), respectively. These results showed clearly the correlation of permeation and pore sizes. Repeating the PVA filtration experiment (50 kDa membrane) at 37 °C resulted in a permeation rate that was twice as high ($8.6 \mu\text{g mL}^{-1} \text{cm}^{-2}$), indicating a strong influence of temperature on the permeation mechanism.

The influence of salt and urea on the permeation of PVA is shown in Figure 2a. Higher ionic concentrations and conditions

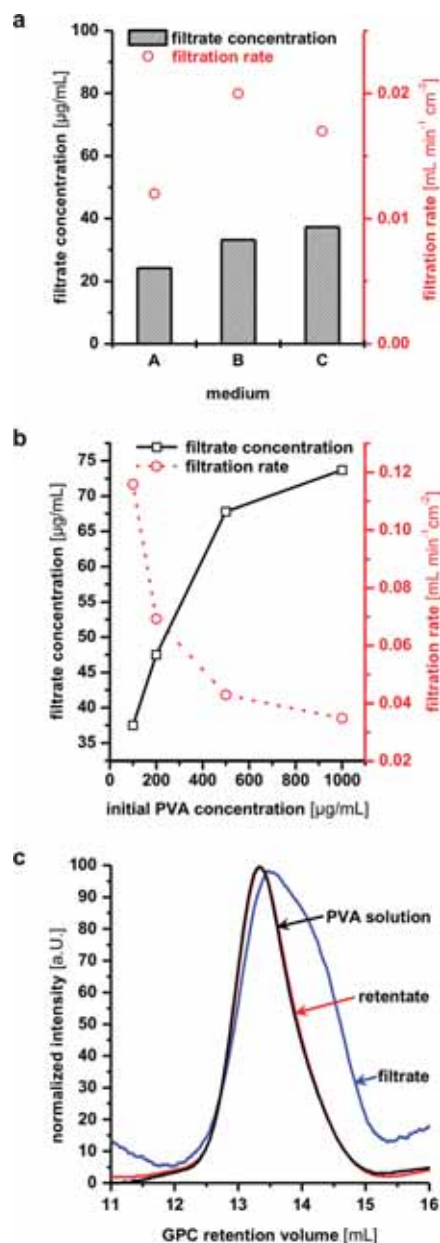


Figure 2. Results of PVA filtration experiments. (a) Centrifugal filtration of PVA-NIR solutions in different media: deionized water (A), aqueous 0.9% NaCl solution (B), and aqueous 0.9% NaCl/2.0% urea solution (C). (b) Pressure filtration of aqueous PVA solutions at varied concentrations. (c) GPC analysis of the fractions obtained from pressure filtration (filtrate and retentate) compared to a freshly prepared PVA solution. Curves of the retentate and fresh PVA solution virtually overlap.

closer to physiological ones facilitated the permeation. The cleavage of hydrogen bonds as a normal effect of salt and urea seemed to allow changes in the molecular shape of PVA and to enhance the flexibility of the chains. This is in accordance with size and conformation studies of Ficoll.³⁷ These also showed that

the conformation of the globular polymer changed in a physiological saline solution to more extended coiled structures, which facilitates their movement through a filtration membrane.

The molar mass distributions of the filtrate ($M_W = 143.2$ kDa) related to the retentate ($M_W = 187.7$ kDa) and to a freshly prepared aqueous PVA solution ($M_W = 174.8$ kDa) are shown in Figure 2c. Compared to that of the filtration experiments, the order of elution is reversed for GPC experiments. Therefore, the shifting of the filtrate curve to longer retention times (volume) inside the GPC column corresponds to an accumulation of lower-molar mass fractions in the filtrate. However, the shape of the filtrate curve at shorter retention times further indicates that PVA with higher molar masses can also cross the pores. The curves of the retentate and fresh PVA solution virtually overlap. This is due to the fact that the samples (filtrate and retentate) were taken after filtration for only ~ 50 min, corresponding to 60 mL of filtrate. At that time, the amount of higher-molar mass PVA in the retentate is still large. If the experiment would be performed in a continuous mode over several days, much larger amounts of high-molar mass PVA would be present in the filtrate.

In summary, these experiments proved that high-molar mass PVA molecules are able to permeate small membrane pores and explained previous *in vivo* findings about renal clearance of high-molar mass PVA molecules.^{16,22} The time independence of permeation rates together with GPC results as well the enhanced permeation from salt and urea solutions (at room and body temperatures) suggests that changes in the molecular shape of the flexible molecules are responsible for the movement of the PVA molecules through small membrane pores. The renal filter process seemed to follow a kind of reptation mechanism, snake-like motion of the polymer chains through the pores that is enhanced under physiological conditions. A pore can be described as a virtual tube. The polymer is limited to a one-dimensional motion inside the tube (local reptation) followed by a slow diffusive creeping motion out of the tube (reptation).³⁸

Confocal Imaging of a Filtration Experiment. The filtration of fluorescence-labeled PVA (PVA-TMR) was visualized in a filtration unit with a 50K Omega filter disk (nominal pore diameter of ~ 5 nm) by confocal x, z -scanning. The fine porous surface of the anisotropically composed membrane (Figure 3a), responsible for size selection, was observed as a white, strong reflecting layer (Figure 3b). The "inner structure" with a lower optical density appeared dark. The air above the membrane surface is colored black because of the absence of optical density and fluorescence (Figure 3b). The same section was further observed by CLSM after addition of a PVA-TMR solution on top of the filter (Figure 3c,d). The detected emissions (after 5 and 10 min) of PVA-TMR were measured and are colored green in the two-channel overlay images (Figure 3c,d). The images clearly show the accumulation of fluorescent material below the surface, inside the membrane. Furthermore, we succeeded in imaging single penetrations of TMR-labeled PVA into the fine porous surface at certain times (marked in Figure 3d by an arrow). Because the recording procedure consists of single scans with average frame accumulations of 10 times, each image represents a period of diffusion of 16 s.

CLSM cannot visualize single PVA-TMR molecules or events inside pores with a 5 nm diameter. In the image, incidental simultaneously occurring diffusion events at neighboring pores of the observed x, z -section were imaged. These confocal images convincingly proved the ability of 195 kDa PVA molecules to pass small membrane pores.

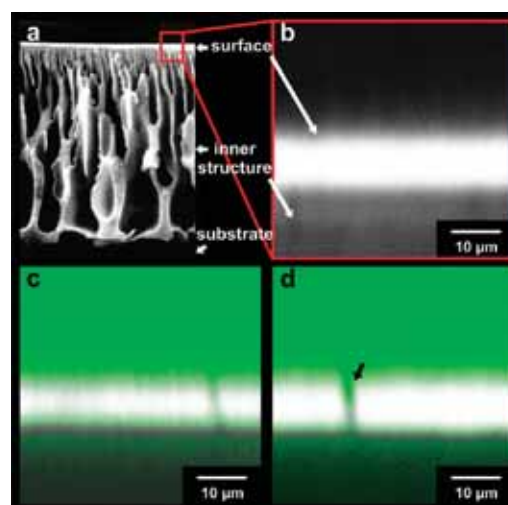


Figure 3. (a) Vertical sliced electron microscopy image of an Omega membrane, illustrating the anisotropic membrane structure (Copyright 2010, Pall Corp.). (b–d) Vertical pseudocolor, two-channel overlay confocal images (reflection signal: gray scale colored, fluorescence TMR signal: colored green) of the surface region of the membrane before (b) and 5 (c) and 10 min (d) after PVA-TMR application. The black arrow marks the penetration of PVA-TMR through the surface.

Noninvasive PVA-TMR *In Vivo* Experiments. *In vivo* measurements were performed using two dyes, the rhodamine dye TMR and the NIR dye Alexa Fluor 750, which had different fluorescence emission maxima (cf. Figure 5f) and varied fluorescence quantum yields. This allowed in the case of PVA-TMR, 20-fold lower exposure times, which strongly reduced the measurement recording time. Therefore, PVA-TMR imaging files (cubes) could be acquired in 2 nm steps (PVA-NIR ones in 10 nm steps) without blurring. This increased the amount of multispectral cube information. The sharp and characteristic emission peak of PVA-TMR (cf. Figure 5f) allowed us to distinguish between tissues that were in different depths and surroundings in the body. Thus, fluorescence from accumulated PVA-TMR molecules in the abdominal fat tissue could be separated from sc PVA-TMR signals (cf. Figure 5f). Because of high photon absorbance (mainly caused by hemoglobin) of dyes with fluorescence emissions in the visible wavelength range (350–700 nm) such as TMR, they are unsuitable for analysis in underlying body tissues. Also, the accumulation of PVA-TMR in organs that are supplied with a high level of blood (kidney, liver, and spleen) would not be detectable.³⁹ Therefore, dyes with fluorescence emissions in the NIR region (700–900 nm) are required.^{34,39,40} The body absorption in the NIR bandwidth was at least 1 order of magnitude lower than in the VIS part. This weakened the influence of light absorption in the NIR region and resulted in dominating elastic scattering effects of emitted photons. Via this phenomenon, NIR light transport in tissues can be modeled as an isotropic diffusing process in which an exact localization of the emitted fluorescence light beyond the surface becomes challenging.⁴¹ Obtained cubes have less spectral information (10 nm acquiring steps) and "smoother" emission spectra (cf. Figure 5f). Diversified determinations of signals from different body areas as described for PVA-TMR were not possible. Because of the lack of background fluorescence within

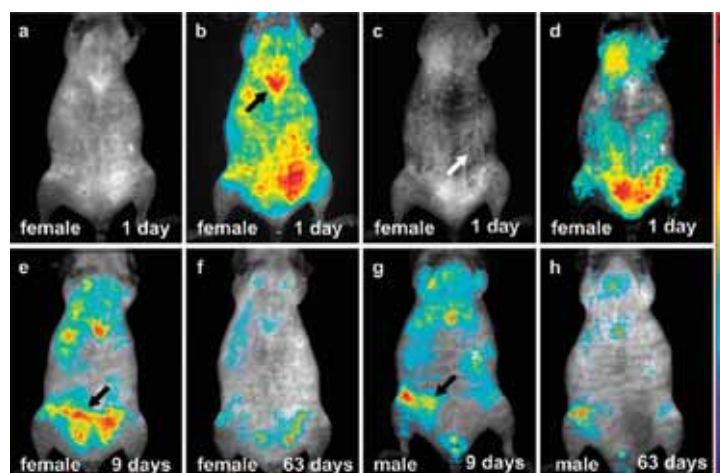


Figure 4. Unmixed, time-dependent fluorescence grayscale and corresponding intensity-weighted incremental jet color images of the sc (a and b) and ip PVA-TMR spectra (c–h) (cp. panel f). The black arrows mark an artifact caused by reflections of the xiphoid cartilage (b) and PVA accumulation in the abdominal fat depot (e and g). The white arrow (c) points to visible blood vessels.

the NIR window, fluorescence emission signals can clearly be separated from nonspecific body backgrounds. Combination experiments with both dyes, TMR and Alexa Fluor 750, were suitable for obtaining detailed overviews of the behavior of PVA in the body.

Grayscale images of detected PVA-TMR emission signals of a female mouse 1 day after injection are shown in panels a and c of Figure 4. Pixels that were allocated to the background were set to black. Pixels that could be 100% assigned to *in vivo* PVA-TMR (sc) (Figure 4a) or PVA-TMR (ip) signals (Figure 4c) were displayed white. Between those colors, there was an incremental gradation according to the respective intensity. The grayscale image of PVA-TMR (sc) (a) shows the homogeneous distributed polymer within and directly under the skin. Specific accumulations were indeterminable in the grayscale image. The corresponding jet color image (Figure 4b) allowed us to visualize the intensity variations within the mouse. Two areas with higher intensities indicating polymer accumulation could be identified. An enrichment between the head and the abdomen (marked by an arrow) was assigned *ex vivo* to the xiphoid cartilage.⁴² The high intensity in this area was the result of fluorescence reflections. Excitation light was strongly reflected by the xiphoid cartilage. Subcutaneously accumulated PVA-TMR polymers were excited by larger amounts of fluorescent light. Thus, the amount of emitted light increased and was furthermore also reflected by the xiphoid cartilage. Both effects influenced the intensity image (Figure 4b) and resulted in an apparent accumulation. Enriched fluorescent PVA-TMR molecules in the abdominal fat area are visible in the second, high-intensity area in the lower part of Figure 4b.

One day after application, the PVA-TMR (ip) signal revealed the blood vessels under the skin (marked by the white arrow in Figure 4c) due to still circulating PVA-TMR polymer chains. This confirms previous PVA results and is in accordance with blood half-life times of high-molar mass PEG molecules.^{22,43} Brighter parts were detected around the bladder and could be clarified in the corresponding jet color image (Figure 4d). This illustrates accumulated PVA-TMR molecules in the lower abdominal area. The same results were obtained within all

female mice. *Ex vivo* studies confirmed the accumulation and identified them as enrichment in the abdominal fat tissue. As described previously,³⁴ PVA was distributed from the ip injection site to the whole body either by bloodstream or by diffusion processes. Physically distributed PVA accumulated at high levels in abdominal-, kidney-, and subcutaneous-fat tissues. Once in fat tissue, incorporated PVA-TMR polymer chains were only slowly released. The PVA accumulation characteristic of the abdominal fat tissue over time is illustrated in panels e and f of Figure 4. A slow decrease in fluorescence intensity in the abdomen area is visible. Similar observations, but in a differing accumulation pattern, were made in biodistribution studies with male mice (Figure 4g,h). *Ex vivo* experiments confirmed the accumulation of PVA-TMR in fat also in male mice. Differences in the fluorescence allocation between male and female mice (marked by black arrows) resulted from varying fat depots (in female mice located mainly in the abdominal and in male mice in the thigh areas of the legs).

Total and maximal fluorescence intensities were calculated with the Maestro software. Therefore, the underlying data of the unmixed grayscale images of the PVA-TMR (sc) and PVA-TMR (ip) signals (Figure 4a,c) were analyzed. Calculated exposure time-weighted total and maximal fluorescence intensities are displayed in Figure 5a–d. The total signal (Figure 5a), as a sum of all PVA-TMR fluorescent pixels, increased up to day 4 and decreased afterward constantly over more than 180 days. This confirmed the expected distribution of PVA in the body. After injection, the PVA-TMR was transported via the bloodstream and by diffusion from the injection site through the body, causing the fluorescent area to be enlarged. The first increase in the magnitude of the total intensity signal was not observed in the normalized maximal intensity graph (Figure 5b). After injection, high PVA-TMR concentrations were located in the abdomen and instantly under the abdominal skin. From there PVA-TMR was slowly eliminated. Therefore, the maximal intensity remained constant for a few days and decreased afterward. An intensity value of 0.35 after 180 days indicated that there was still a small amount of accumulated PVA-TMR molecules.

PVA-TMR (ip) graphs (Figure 4c,d) had different profiles. The total intensity (panel c) was doubled during the first days,

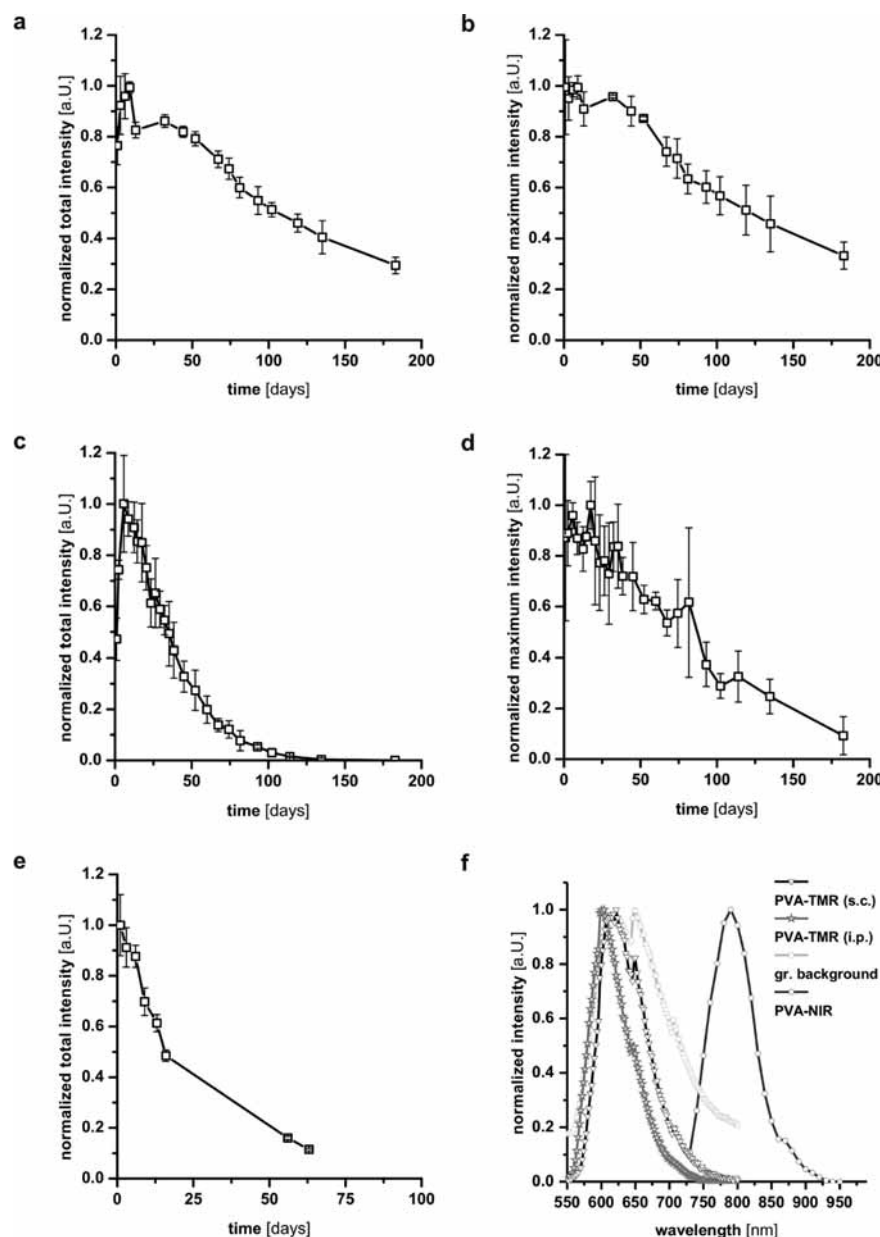


Figure 5. Normalized total (a, c, and e) and maximal (b and d) fluorescence intensities viewed from the abdomen of the entire body of three female mice based on the *in vivo* PVA-TMR (sc) spectra (a and b), the extracted PVA-TMR (ip) signal from the abdominal fat (c and d), and the *in vivo* PVA-NIR signal (e). (f) Normalized emission fluorescence spectra of PVA-TMR (sc), PVA-TMR (ip), PVA-NIR, and the green filter background signal.

because of the depot-forming enrichment in the fat tissue. Afterward, the magnitude of the signal decreased continuously, similar to that of the PVA-TMR (sc) signal, but faster. Comparable characteristics were found for the maximal signal intensities (panel d). After injection, PVA-TMR was physically distributed by diffusion processes throughout the body, which caused it to accumulate in fat tissues. On the basis of the poor blood supply in the fat, accumulated PVA was only slowly eliminated from the borders of the fat tissue (illustrated in Figure 6). Thus, a concentration profile existed from the center to the border of the fat

tissues. Because of these restrictive eliminations, fluorescence from inner fat parts mainly influenced the maximal intensity whereas the whole fat area was represented by total intensity results. Therefore, the total intensity decreased faster than the maximal one.

Noninvasive PVA-NIR *In Vivo* Experiments. Weakened absorption effects of light emitted from NIR dyes result in a domination of the elastic scattering effects during excitation and emission processes. In the case of NIR, multiple scattering is the main mechanism for light propagation. Light transport in tissue

can be modeled as a simple isotropic diffusing process.⁴¹ Resulting images, shown in Figure 7a, are smoother and have less detailed information. The detection of single blood vessels, as shown with PVA-TMR, was not possible. The compare imaging function used for Figure 7a allowed correlations among all images to the comprehensive maximal intensity. One day after injection, PVA-NIR was distributed throughout the whole body. The highest levels of accumulation of dye were visible in the abdomen area (Figure 7a). This underlined the accumulation of PVA in the abdominal fat tissue discussed before. Increased intensities in the upper part (marked by top arrow) were again assigned to reflections by the xiphoid cartilage. The reduced intensity compared to PVA-TMR measurements (Figure 4b) was caused by better penetration depths of NIR light with consequently weakened reflection effects. The left kidney in the figure was marked by the second, black arrow. Both kidneys were detectable *in vivo* from the back side for approximately 3 days (images not shown). Accumulated fluorescence in the liver or spleen was not found within all measured mice *in vivo*. Over time, the whole body intensity decreased continuously (Figure 7a). Sixty-three days after polymer injection, only a homogeneously distributed, weak fluorescence signal was still detectable *in vivo*. Differences from the PVA-TMR image

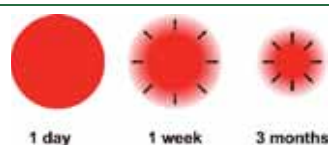


Figure 6. Release of PVA from adipose tissues.

(cf. Figure 4) were attributed to the compare imaging function. Calculated total intensities based on *in vivo* PVA-NIR body images are shown in Figure 5e. The total intensity decrease of the received graph was influenced by the elimination of the polymer from sc and fat tissue accumulations and was intermediate between the PVA-TMT (sc) and PVA-TMT (ip) curves (Figure 5a,c).

PVA-NIR ex Vivo Experiments. Representative *ex vivo* images of different organs that are known for elimination (kidneys, liver, and spleen) and of skin and fat tissues (abdominal and kidney fat and skin) were imaged 3 days and 3 months after injection and are shown in panels b and c of Figure 7, respectively. Three days after injection, highest intensities were found in both kidneys. Only slight accumulations were detected in the liver and none in the spleen (panel b). Three months later, residual accumulation in the kidneys but none in the liver was detectable. The intensity in the kidneys also decreased to zero after 9 months (picture not shown). The images confirmed the preferential renal elimination pathway and were in agreement with earlier results.³⁴ *Ex vivo* images of different fat and skin tissues agreed also with *in vivo* results. The elimination from the main accumulation compartments was followed over several months (Figure 7c). Different intensities between fat tissue from the abdomen or around the kidneys could be attributed to varied distances within the diffusion process after ip injection.

Ex Vivo Confocal Imaging. More detailed cellular *ex vivo* examination was conducted by confocal microscopic analysis. The image of abdominal fat tissue (Figure 7d, 6 months after PVA-TMR injection) confirmed PVA-TMR enrichment in fat tissues. Also, a simultaneous comparison with untreated abdominal fat clarified this (Figure 7e). An *in vitro* experiment included incorporation of untreated fat tissue for 3 min with PVA-TMR,

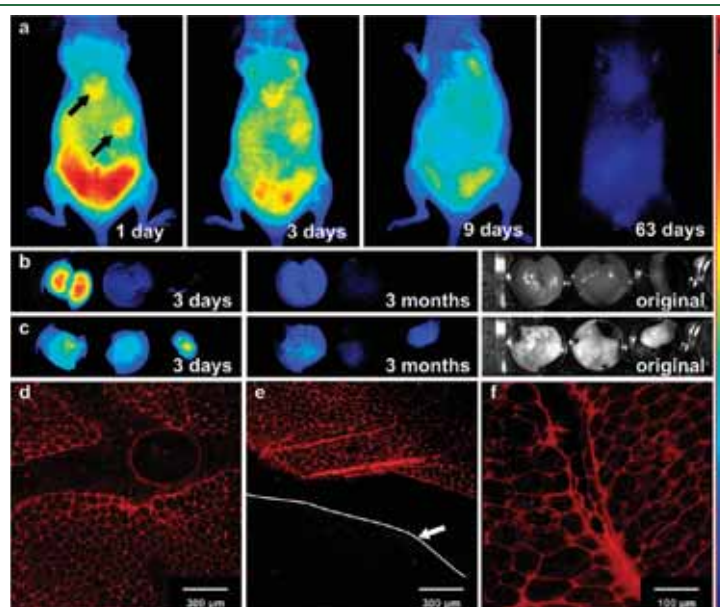


Figure 7. (a) Isolated, time-dependent PVA-NIR fluorescence intensity images (compare imaging function) of a nude, female mouse. The upper arrow marks an artifact, caused by reflections due to the xiphoid cartilage. The lower one points to the highly fluorescent left kidney. (b and c) Time-dependent intensity-weighted and original images of *ex vivo* tissues: kidneys, liver, and spleen (b) and abdominal fat, kidney fat, and abdominal skin (c). (d–f) Confocal microscopy (PVA-TMR) images of abdominal fat tissue, extracted 6 months after ip injection (d), the same abdominal fat tissue simultaneously imaged with fat from an untreated mouse (below the white line, marked with an arrow) (e), and abdominal fat tissue from an untreated mouse, treated *ex vivo* with PVA-TMR (f).

followed by washing and imaging (Figure 7f). This test confirmed the strong tendency of high-molar mass PVA molecules to passively accumulate in fat tissues. Even several washing steps could not elute the PVA-TMR. The image showed further that the highest fluorescence intensities were located between the fat cells. Entering the cells during this *in vitro* experiment is unlikely. *Ex vivo* images of treated mice resulted in a similar accumulation pattern (cf. Figure 7d,f).

CONCLUSION

The *in vivo* fate of high-molar mass PVA (195 kDa) was studied in detail by multispectral fluorescence imaging. For this purpose, two different dyes, TMR (a rhodamine dye) and Alexa Fluor 750 (a NIR dye), were covalently bound to the PVA backbone. Both dyes had different spectral properties, showed satisfactory stability *in vivo*, and allowed extensive *in vivo* studies of body distribution, accumulation, and elimination processes over several months. After *ip* injection into nude mice, the labeled PVA was distributed either in the bloodstream or by diffusion processes. An imaging of the blood vessels after 24 h confirmed the long-term circulation ability of the polymer. Through the second distribution pathway, PVA molecules diffused within the abdomen. Noninvasive fluorescence imaging showed that PVA accumulated at high levels in different body fat tissues such as abdominal fat and kidney fat and also under the skin. *Ex vivo* PVA-TMR and PVA-NIR fluorescence imaging and additionally PVA-TMR confocal microscopy studies confirmed such enrichment. It was found that PVA molecules accumulated between fat cells. Detailed quantitative analysis indicated a continuous, long-term release of PVA. The used dyes allowed us to study different aspects of accumulation of PVA *in*, and release of PVA from, several tissues. The *in vivo* stable PVA-NIR label allowed further characterization of elimination pathways. Strong fluorescence in the kidneys was detectable *in vivo* for up to 3 days. This confirmed previous studies in which PVA was found to be excreted within the urine.^{16,22,23} Slight accumulation of high-molar mass PVA was also detected in liver *ex vivo*. This could be attributed to the high level of blood supply to the liver causing the preferential transport and accumulation of labeled PVA. Finally, PVA was eliminated from the liver by feces, which is in accordance with literature.²³ Nine months after *ip* application, PVA-NIR fluorescence in the liver was below the detection limit, which suggests a complete elimination of PVA.

To confirm the renal excretion of high-molar mass PVA ($M_w = 195000$ g/mol) and to study the involved mechanism in more detail, *in vitro* filtration experiments serving as a model for glomerular filtration were performed. Filtration results and α, ζ -scans by confocal imaging proved that despite their large molar mass and R_h value, PVA molecules were able to permeate through small pores of synthetic membranes with molar mass cutoffs of 30 or 50 kDa. Permeation rates increased with temperature and were time-independent. This suggests, together with GPC results, that changes in the molecular shape of the flexible molecules allowed them to pass through the small membrane pores. Enhanced permeation from salt and urea solutions indicated that this mechanism was favored under conditions that are closer to physiological ones.

The accumulation of PVA molecules in various fat tissues, observed *in vivo* and confirmed *ex vivo*, is not critical for clinical PVA usage. On the basis of this study and previous studies, no evidence indicating that PVA could accumulate permanently in

body tissues or be toxic to cells was found.²² The results regarding the *in vivo* release of PVA from fat tissues attested the excellent properties of PVA for a controlled long-term release of bound drug molecules or proteins. These studies could open a new field of application for PVA as a controlled release drug carrier.

AUTHOR INFORMATION

Corresponding Author

*Phone: +49 345-5525167. Fax: +49 345-5527029. E-mail: karsten.maeder@pharmazie.uni-halle.de.

ACKNOWLEDGMENT

Martina Hennicke and Constanze Gottschalk are acknowledged for animal care.

REFERENCES

- Peppas, N. A.; Hilt, J. Z.; Khademhosseini, A.; Langer, R. *Adv. Mater.* **2006**, *18*, 1345–1360.
- Yao, R. S.; You, Q. D.; Liu, P. J.; Xu, Y. F. *J. Appl. Polym. Sci.* **2009**, *111*, 358–362.
- Noguchi, T.; Yamamuro, T.; Oka, M.; Kumar, P.; Kotoura, Y.; Hyon, S. H.; Ikada, Y. *J. Appl. Biomater.* **1991**, *2*, 101–107.
- Paradossi, G.; Cavalieri, F.; Chiessi, E. *J. Mater. Sci.: Mater. Med.* **2003**, *14*, 687–691.
- Grosova, Z.; Rosenberg, M.; Rebroš, M.; Sipocz, M.; Sedlackova, B. *Biotechnol. Lett.* **2008**, *30*, 763–767.
- Mori, Y.; Tokura, H.; Yoshikawa, M. *J. Mater. Sci.* **1997**, *32*, 491–496.
- Cavalieri, F.; Chiessi, E.; Villa, R.; Vigano, L.; Zaffaroni, N.; Telling, M. F.; Paradossi, G. *Biomacromolecules* **2008**, *9*, 1967–1973.
- Schmedlen, K. H.; Masters, K. S.; West, J. L. *Biomaterials* **2002**, *23*, 4325–4332.
- Zeng, J.; Aigner, A.; Czubyko, F.; Kissel, T.; Wendorff, J. H.; Greiner, A. *Biomacromolecules* **2005**, *6*, 1484–1488.
- Bodugoz-Senturk, H.; Macias, C. E.; Kung, J. H.; Muratoglu, O. K. *Biomaterials* **2009**, *30*, 589–596.
- Wan, W. K.; Campbell, G.; Zhang, Z. F.; Hui, A. J.; Boughner, D. R. *J. Biomed. Mater. Res.* **2002**, *63*, 854–861.
- Hassan, C. M.; Peppas, N. A. *Adv. Polym. Sci.* **2000**, *153*, 37–65.
- Kokabi, M.; Sirousazar, M.; Hassan, Z. M. *Eur. Polym. J.* **2007**, *43*, 773–781.
- Metwally, M.; Cheong, Y.; Li, T. C. *Curr. Opin. Obstet. Gynecol.* **2008**, *20*, 345–352.
- Lang, R. A.; Gruntzig, P. M.; Weisgerber, C.; Weis, C.; Odermatt, E. K.; Kirschner, M. H. *Fertil. Steril.* **2007**, *88*, 1180–1186.
- Besheer, A.; Mäder, K.; Kaiser, S.; Kressler, J.; Weis, C.; Odermatt, E. K. *J. Biomed. Mater. Res., Part B* **2007**, *82B*, 383–389.
- Liakakos, T.; Thomakos, N.; Fine, P. M.; Dervenis, C.; Young, R. L. *Dig. Surg.* **2001**, *18*, 260–273.
- Al-Jaroudi, D.; Tulandi, T. *Obstet. Gynecol. Surv.* **2004**, *59*, 360–367.
- Weis, C.; Odermatt, E. K.; Kressler, J.; Funke, Z.; Wehner, T.; Freytag, D. *J. Biomed. Mater. Res., Part B* **2004**, *70B*, 191–202.
- Yeo, Y.; Kohane, D. S. *Eur. J. Pharm. Biopharm.* **2008**, *68*, 57–66.
- Weis, C.; Odermatt, E. K. *J. Biomed. Mater. Res., Part B* **2007**, *82B*, 174–182.
- Jiang, Y. J.; Schädlich, A.; Amado, E.; Weis, C.; Odermatt, E.; Mäder, K.; Kressler, J. *J. Biomed. Mater. Res., Part B* **2010**, *93B*, 275–284.
- Kaneo, Y.; Hashihama, S.; Kakinoki, A.; Tanaka, T.; Nakano, T.; Ikeda, Y. *Drug Metab. Pharmacokinet.* **2005**, *20*, 435–442.
- Yamaoka, T.; Tabata, Y.; Ikada, Y. *J. Pharm. Pharmacol.* **1995**, *47*, 479–486.

Supplemental material

(a) Investigation of the *in vivo* fate of a water soluble polymer

- (25) Chiellini, E.; Corti, A.; Solaro, R. *Polym. Degrad. Stab.* **1999**, *64*, 305–312.
- (26) Lopez, B. L.; Mejia, A. I.; Sierra, L. *Polym. Eng. Sci.* **1999**, *39*, 1346–1352.
- (27) Comper, W. D.; Hilliard, L. M.; Nikolic-Paterson, D. J.; Russo, L. M. *Am. J. Physiol.* **2008**, *295*, 1589–1600.
- (28) Milton, H. J. *Poly(ethylene glycol) chemistry: Biotechnical and biomedical applications*; Plenum Press: New York, 1992.
- (29) Ikeda, I.; Kurushima, Y.; Suzuki, K. *Polym.-Plast. Technol. Eng.* **1989**, *28*, 877–890.
- (30) Gacal, B. N.; Koz, B.; Gacal, B.; Kiskan, B.; Erdogan, M.; Yagci, Y. *J. Polym. Sci. Polym. Chem.* **2009**, *47*, 1317–1326.
- (31) Billinton, N.; Knight, A. W. *Anal. Biochem.* **2001**, *291*, 175–197.
- (32) Wagnieres, G. A.; Star, W. M.; Wilson, B. C. *Photochem. Photobiol.* **1998**, *68*, 603–632.
- (33) Mansfield, J. R.; Gossage, K. W.; Hoyt, C. C.; Levenson, R. M. *J. Biomed. Opt.* **2005**, *10*, 041207.
- (34) Schädlich, A.; Rose, C.; Kuntsche, J.; Caysa, H.; Mueller, T.; Göpferich, A.; Mäder, K. *Pharm. Res.* **2011**, *28*, 1995–2007.
- (35) Zimmermann, T.; Rietdorf, J.; Pepperkok, R. *FEBS Lett.* **2003**, *546*, 87–92.
- (36) Banks, P. R.; Paquette, D. M. *Bioconjugate Chem.* **1995**, *6*, 447–458.
- (37) Fissell, W. H.; Hofmann, C. L.; Smith, R.; Chen, M. H. *Am. J. Physiol.* **2010**, *298*, F205–F208.
- (38) De Gennes, P. G. *J. Phys. (Paris)* **1981**, *42*, 735–740.
- (39) Weissleder, R. *Nat. Biotechnol.* **2001**, *19*, 316–317.
- (40) Yang, Z.; Zheng, S. Y.; Harrison, W. J.; Harder, J.; Wen, X. X.; Gelovani, J. G.; Qiao, A.; Li, C. *Biomacromolecules* **2007**, *8*, 3422–3428.
- (41) Jacques, S. L.; Pogue, B. W. *J. Biomed. Opt.* **2008**, *13*, 041302.
- (42) Cook, M. J. *The Anatomy of the Laboratory Mouse*; Academic Press: San Diego, 1965.
- (43) Caliceti, P.; Veronese, F. M. *Adv. Drug Delivery Rev.* **2003**, *55*, 1261–1277.

***In-vivo* studies on intraperitoneally administered poly(vinyl alcohol)**

Yanjiao Jiang,¹ Andreas Schädlich,² Elkin Amado,¹ Christine Weis,³ Erich Odermatt,³ Karsten Mäder,² Jörg Kressler¹

¹Physical Chemistry, Institute of Chemistry, Martin Luther University Halle-Wittenberg, Halle (Saale) D-06099, Germany

²Department of Pharmaceutical Technology and Biopharmacy, Institute of Pharmacy, Martin Luther University Halle-Wittenberg, Wolfgang-Langenbeck-Str. 4, Halle (Saale) D-06120, Germany

³Aesculap AG & Co. KG, Tuttlingen, Germany

Received 16 July 2009; revised 3 October 2009; accepted 4 November 2009

Published online 29 January 2010 in Wiley InterScience (www.interscience.wiley.com). DOI: 10.1002/jbm.b.31585

Abstract: The fate of poly(vinyl alcohol) (PVA, 195,000 g/mol) was studied in rabbits and nude mice after intraperitoneal (i.p.) administration. *In-vivo* fluorescence imaging using nude mice allowed for studies of tetramethylrhodamine labeled PVA distribution in the body and tracking the urinary excretion. The excreted PVA was studied in detail after collecting the urine of rabbits over a time period of 28 days. The PVA was separated from the urine by dialysis and analyzed by FTIR spectroscopy, ¹H-NMR spectroscopy, and size exclusion chromatography (SEC). Even after extensive dialysis, it was found that the excreted PVA showed a characteristic brownish color. The spec-

troscopic techniques revealed that this color was caused by the urine pigment (a metabolite of bilirubin) that could not be separated completely from the PVA. SEC showed unambiguously that the PVA with the very high molar mass had a glomerular permeability in the kidneys. Simultaneously, histological studies of the kidneys and the liver demonstrated that the tissues did not show any obvious damage. © 2009 Wiley Periodicals, Inc. *J Biomed Mater Res Part B: Appl Biomater* 93B: 275–284, 2010

Key Words: poly(vinyl alcohol), PVA, *in-vivo* imaging, urinary excretion, fluorescence

INTRODUCTION

Poly(vinyl alcohol) (PVA) is widely used in the area of industrial, medical and pharmaceutical application, cosmetics, textile, and food packaging since the 1930.¹ The high content of hydroxyl groups provides PVA and PVA-based materials with many properties suitable for biomedical applications (e.g. hydrophilic, biocompatible, nontoxic, non-carcinogenic, nonimmunogenic, and inert in body fluids).^{2–5} As a promising biomaterial, diverse research has focused on the application of PVA in biomedical and pharmaceutical fields.^{6–9} High mechanical strength, rubber-like elasticity, low-protein adsorption, high water content, and no adhesion to surrounding tissues make PVA gels a potential material for soft contact lenses,^{10,11} soft tissue replacements,¹² articular cartilage,¹³ intervertebrate disc nuclei,¹⁴ transcatheter arterial embolization agent,¹⁵ artificial skin, and vocal cord.^{16,17} Sponge-like PVA cryogels contain macropores providing properties desired for scaffolds for tissue engineering, for immobilizing of molecules and cells.^{18,19} On the basis of the semicrystalline structure of the PVA gel, it was studied extensively as a drug release system for pharmaceutical applications.^{20–24} Mucoadhesive and nonimmunogenic characteristics of PVA hydrogels were investigated for accelerating wound healing and preventing postoperative adhesion.^{25–27}

Physiological responses of the administered PVA are dependent on molar mass and route of administration. Orally administered PVA is harmless.²⁸ Subcutaneously adminis-

tered PVA was studied using different molar masses of PVA.²⁹ Pharmacokinetics and biodistribution of PVA were studied after intraperitoneal (i.p.), subcutaneous (s.c.), and intramuscular (i.m.) administering, which indicated that the absorption rate from the injection sites into the blood circulation was i.p. > i.m. > s.c.³⁰ The absorption of i.p. administered PVA solutions follows two main pathways through the large area peritoneum to distribute in the whole body. One way is that PVA is absorbed into the peritoneal blood microcirculation and drained into the portal vein by passing through the liver to arrive in the blood circulation.³¹ Another way is that PVA was transported through the peritoneal lymphatic system directly into the blood circulation. The absorption rate of i.p. administered medium molar mass PVA showed no molar mass dependence.³² The blood concentration of PVA reaches a maximum with time after i.p. injection, and decreases more quickly with decreasing molar mass of PVA. The fate of PVA in the body is mainly governed by the hydrodynamic size of the macromolecule (single polymer chain or microgel) and the injection site.³³ The main routes for elimination of PVA from the blood circulation seem to be the excretion via the renal glomeruli and hepatic bile ducts. Low molar mass PVA will be more rapidly excreted through the kidney into the urine.^{34–36} The critical cut-off molar mass of PVAs for the glomerular permeability was reported to be 30,000 g/mol.³⁷ Although the molar mass and the molecule size of PVA is above the size limitation of the glomerular filtration barrier (nonfilterable

Correspondence to: J. Kressler; e-mail: joerg.kressler@chemie.uni-halle.de

Supplemental material

(a) Investigation of the *in vivo* fate of a water soluble polymer

if molar mass $>80,000$ g/mol and radius of molecule >4.4 nm), i.p. administrated high molar mass PVA ($M_w = 195,000$ g/mol, $R_h \approx 13$ nm) can still be excreted through the kidney.^{38,39} High molar mass water soluble polymers take several weeks or months to be finally excreted through urine and feces. A significant accumulation of high molar mass polymers has been observed in the liver and spleen, but minor amounts of them can be deposited in the body.^{40–42} Limited information is available on PVA biodegradation mediated by cells other than microorganisms in soil and bacteria.^{43–45} Until now, PVA is usually regarded as a nonbiodegradable polymer in the body. The delay of renal excretion of high molar mass PVA is still not completely explored. Recent studies mentioned that the chemical structure of renal excreted PVA differs from pre-administered PVA.³⁹ To gain a better understanding on renal excretion of high molar mass PVA, the urinary excreted PVA i.p. administered to rabbits is investigated in this study using GPC, FTIR spectroscopy, and $^1\text{H-NMR}$ spectroscopy. The biocompatibility of PVA is studied by histopathological tests of the kidney. The fluorescence-labeled PVA using a tetramethylrhodamine-5-carbonyl azide dye (PVA-TMR) is used to follow its fate in the body of nude mice after i.p. administration. The main focus is to measure the PVA-TMR distribution from the area of injection into the peritoneum and blood stream. Finally, the labeled PVA-TMR is analyzed in the urine to prove the elimination through the kidneys.

MATERIALS AND METHODS

Materials

The PVA (Mowiol 56–98, Kuraray, Japan) had a weight average molar mass M_w of 195,000 g/mol, a polydispersity index of 2.3, and a degree of hydrolysis of 98.4 mol %. All other chemicals and solvents were used as received.

Preparation of Fluorescence Labeled PVA

The PVA was labeled with the fluorescence dye tetramethylrhodamine-5-carbonyl azide (TMR) (Invitrogen) in anhydrous dimethylsulfoxide (DMSO) at 80°C for 12 h using a molar ratio PVA/TMR (2.2/1) according to the reaction scheme shown in Figure 1.

After completion of the reaction the solution was dialyzed against DMSO through a membrane with molar mass cut off of 3500 g/mol for removing unconjugated tetramethylrhodamine. Both the dialysis bag and the DMSO were changed daily for 1 week. After that, the solution was dialyzed against double distilled water for 3 days for removing the organic solvent. Again, both the dialysis bag and the water were changed daily until no trace of TMR in the external solvent could be detected through fluorescence spectroscopy. Finally, the aqueous solution was freeze-dried for obtaining the conjugated polymer PVA-TMR as a slightly pink powder, readily soluble in water at 80°C . The fluorescence emission spectrum of PVA-TMR for an excitation wavelength $\lambda_{\text{exc}} = 435$ nm shows a maximum at $\lambda = 577.3$ nm that is not shifted compared to the emission maximum of TMR ($\lambda = 577.0$ nm), although the PVA-TMR spectrum is slightly narrower compared to the pure TMR. This indicates

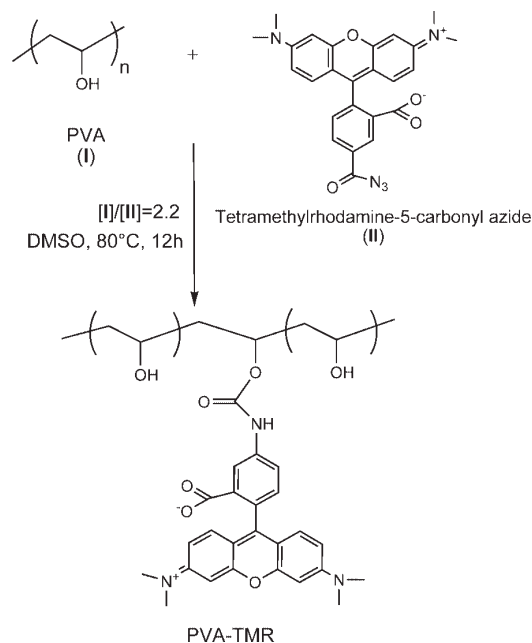


FIGURE 1. Chemical structure of TMR-labeled poly(vinyl alcohol) (PVA-TMR).

that the conjugation did not influence considerably the fluorescence of the original TMR.

In-Vivo Imaging and Analysis

The measurements were carried out using an *in-vivo* fluorescence imaging system (Maestro, Cambridge Research & Instrumentation, Woburn, MA). The distribution and accumulation of the labeled PVA was studied by measuring the fluorescence intensities of the whole body, covering especially the abdominal region, at predetermined time intervals. Therefore, a green excitation filter (503–555 nm) and a 580 nm long-pass emission filter were used. Multispectral imaging cube sets were acquired in 2 nm steps (spectral range between 500 and 800 nm) with an exposure time of 50 ms. An original diluted PVA-TMR solution was used to generate the reference fluorescence spectra for further analyses. By unmixing and further segmentation it was possible to separate the PVA-TMR signal from auto-fluorescence signals of the mice. Corresponding images were saved into a series of monochrome images. RGB (red green blue) images were generated from the original cubes by allocating the respective color to the labeled PVA spectrum.

All procedures of the *in vivo* experiments complied with the standards for use of animal subjects as stated in the guideline from the animal care and use committee of the Martin Luther University Halle-Wittenberg. The *in vivo* studies were performed in nude, female mice (SKH1-*Hr^{hr}*, 25–30 g) from Charles River Lab. They were housed under controlled conditions (12 h light/dark schedule, 24°C). The fluorescent PVA-TMR solution was slowly i.p. injected (5 wt %, 0.1 mL) into the middle of the abdomen. For the

measurements, an inhalation anesthesia system was used with a mixture of isoflurane/oxygen and an initial flow of 4% isoflurane (3.0 L/min oxygen) and a steady state flow of 1.8% isoflurane (1.5 L/min oxygen). To protect the mice against cooling, they were placed on temperature controlled plates which were kept at 35°C.

The urine samples were collected directly before the *in vivo* measurements. Therefore, the mouse was placed into an empty mouse cage for less than 2 h. In this time, the mouse urinated to the bottom of the cage. Immediately after the collection, the urine samples were diluted with acetonitrile (1:100) and measured with the fluorescence imaging system using a blue excitation filter (445–490 nm) and a 515 nm long-pass emission filter as well as the green filter set. A blue filter set was used to detect the native urine components and the green one for analyzing the PVA-TMR signal. Semiquantitative data analysis about the presence of labeled polymer in the urine was possible by combining both spectra.

Extraction and Dialysis of Polymer Obtained by Renal Excretion of Rabbits

Sterilized 20 mL of 10 wt % PVA solution was injected into the abdomen of three female albino rabbits (namely No. 3196, No. 3242, and No. 3965) by laparotomy. PVA-treated rabbits' urine was collected and deep frozen immediately. After 28 days urine collection, all urine samples were thawed and filtered to remove any solid material (e.g. hay particles from the animal cage). The urine of 28 consecutive days (generally 1.1–1.5 L, deep brown color) was filled into a dialysis tube (MWCO 3500 g/mol, Spectra/Por3, Spectrum Laboratories, CA) and dialyzed against distilled water for 4 days with changing distilled water three times per day. Then, the dialyzed urine (light brown color) was distilled under vacuum to remove most of the water. The concentrated urine (generally 30–50 mL, deep brown color) was dialyzed against distilled water for 2 days with changing distilled water three times per day. Precipitates can be collected after pouring the concentrated urine into acetone. The precipitated polymers in acetone were filtered by glass filters. The amounts of collected polymers were about 200, 500, and 140 mg, respectively. The control sample was dialyzed and precipitated by mixing fresh PVA aqueous solution with rabbit urine at room temperature. One milliliter of 10 wt % PVA (100 mg) aqueous solution was added into 200 mL rabbit urine. The control sample then underwent the identical procedure as discussed for the collection of polymer from the rabbit urine samples.

Size Exclusion Chromatography

Molar masses of polymers were measured by SEC at ambient temperature using a Waters size exclusion chromatography (SEC) equipped with a Knauer pump. Poly(ethylene oxide) calibration standards were used to calculate the molar masses. Samples were measured in an aqueous environment. The SEC traces were normalized so that the highest peak represents 100% of detector response.

¹H-NMR Spectroscopy

The molecular structure of the polymers was determined by ¹H-NMR spectroscopy. ¹H-NMR spectra were recorded using a Magnetic Resonance spectrometer (Gemini 2000, Varian, 400 MHz) at 20°C in DMSO-*d*₆.

FTIR Spectroscopy

The polymer powder was pressed into KBr tablets and the spectra were recorded in the transmission mode of a FTIR spectrometer (Tensor 37, Bruker) with a resolution of 2 cm⁻¹. One thousand interferogram scans were averaged to give spectra from 400 to 4000 cm⁻¹.

Histological Test

To observe if the high molar mass PVA can produce toxicities in kidney, the histopathological changes of the kidney tissue of control and PVA-treated rabbits were examined by hematoxylin and eosin (H&E) stained slides. After 28 days of urine collection, three PVA i.p. administrated rabbits and one control rabbit (without PVA administration) were killed and autopsied and the kidneys were removed and deep frozen (at -32°C) immediately. The sections (4 mm × 10 mm × 10 mm) of tissue were sampled from deep frozen organs and fixed in neutral-buffered formaldehyde-solutions, processed through graded alcohols and xylene, and embedded in paraffin blocks. Tissue sections were cut for 2–8 μm at multiple levels and routinely stained with hematoxylin-eosin. Mounted slides were examined and photographed under a light microscope.

RESULTS

Fluorescence Imaging

It has been shown that *in-vivo* fluorescence imaging is a powerful tool for studying the fate of biomedical materials and anatomical changes in the body of animals.^{46–48} The aim of the experiments was to follow the fate of the labeled PVA after i.p. injection. Shortly after administration, the PVA-TMR solution spreads into the abdomen cavity [Figure 2(a)]. At this moment, the PVA-TMR is localized in the middle of the abdomen between the intestinal loops. Parts of the fluorescence signal are absorbed by the intestine which results in apparently nonfluorescent areas [Figure 2(d)]. The fluorescent areas show a quenched, high-intensity signal caused by the highly concentrated PVA-TMR solution [Figure 2(d)]. Over time the labeled PVA distributes inside the abdominal space. From there it is absorbed to the body liquids. It was possible to detect the PVA-TMR signal in the big vasculatures under the skin after 6 h [Figure 2(b)]. The polymer circulates with the bloodstream in the whole body. At the abdominal site the fluorescence area increases whereas the intensity of the signal decreases (i.e. there are less areas with quenched signal). The fluorescence intensity is adapted to a medium value as illustrated in Figure 2(e). It is visible that the total fluorescence area is enlarged and the color changed from dark red to yellow and blue. After 1 day, the PVA-TMR was still visible in the blood vessels [Figure 2(c)]. Furthermore, we detected an accumulation of the polymer in the upper abdomen space. The jet color picture [Figure 2(f)] illustrates the unusual V-profile of the

Supplemental material

(a) Investigation of the *in vivo* fate of a water soluble polymer

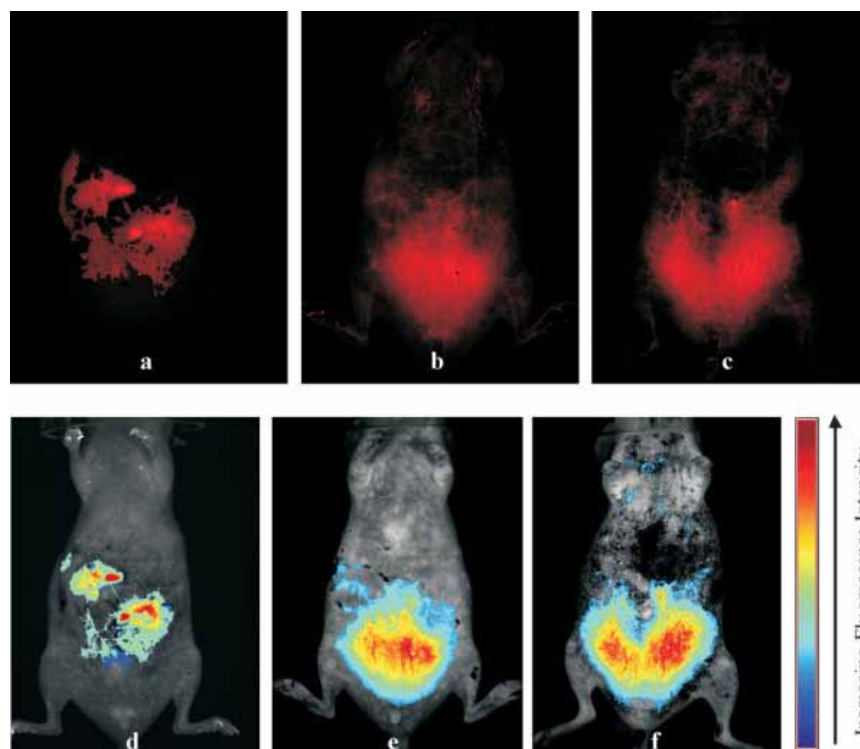


FIGURE 2. Fluorescence images of one nude, female mouse 1 h (a, d), 6 h (b, e), and 24 h (c, f) after i.p. PVA-TMR injection. The red color assigns areas of the detected PVA-TMR signal. The autofluorescence of the mouse was fixed to black. (a–c) The incremental jet color images represent the threshold fluorescence PVA-TMR signal. Red areas marking places with highest fluorescence intensities, yellow and cyan areas stand for decreased intensities and the blue zones are regions with lowest intensities (d–f). [Color figure can be viewed in the online issue, which is available at www.inerscience.wiley.com]

fluorescence TMR signal indicating an accumulation in this area. If this is the result of the blood transport or directly caused by the dispersion, processes of the PVA-TMR in the abdomen fluid has to be further investigated. At any time of the experiment an accumulation in other body regions than the abdomen and the bladder was not detectable but this can finally not be excluded because the emission maximum of PVA-TMR is in a wavelength range where emitted light is absorbed by organs which are highly supplied with blood.

Using the blue filter settings, it was possible to detect the natural fluorescent components in the placebo urine without measuring the PVA-TMR signal. Variations in the urine concentration yielded to darker and brighter green color fluorescence images. Analyzing the *in vitro* PVA-TMR signal of the spectral information of the green filter set images an overlaying picture could be created. The green image of the urine signal was set as background and the incremental jet color images representing the PVA-TMR concentrations in the urine corresponding to their threshold fluorescence signal were overlaid (Figure 3). Red zones represent the highest fluorescence intensities. Decreased intensities are displayed in yellow to cyan to finally blue, which are regions with lowest intensities.

All urine samples were recorded under the same measurement conditions as discussed above. Analyzing the sam-

ples it was obvious that the fluorescence signal that can be assigned to the PVA-TMR spectra decreased with time after i.p. administration. This is shown in the images as a shift

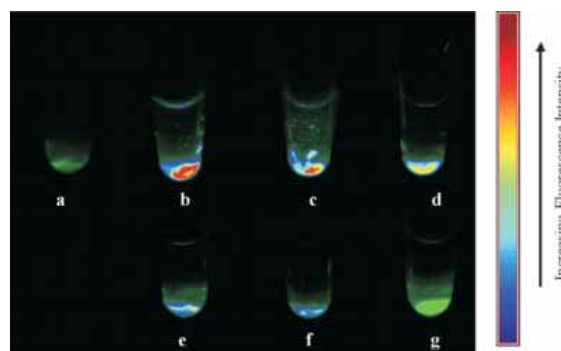


FIGURE 3. Fluorescence images of mouse urine after i.p. PVA-TMR administration and excretion using two filter sets, blue and yellow. The fluorescence urine signal, detected with the blue filter set is displayed in green: (a) placebo urine. The PVA-TMR signal was measured and illustrated in jet colors corresponding to the respective intensities and were overlaid to the green urine pictures after 14 h (b), 24 h (c), 2 days (d), 3 days (e), 4 days (f), and after 5 days (g). [Color figure can be viewed in the online issue, which is available at www.inerscience.wiley.com]

from red to yellow and blue. It is obvious that the PVA-TMR signal can be detected in the mouse urine shortly after i.p. injection. The highest fluorescence intensity was found 14 h after injection indicating that the PVA-TMR was taken up to the body fluid and circulated in the blood stream. Finally, it was eliminated through the kidneys into the urine. After 5 days the amount of renal excreted PVA-TMR decreased under the detection limit of the fluorescence imaging system. It was impossible to detect PVA-TMR in the feces at any time. Thus, we conclude that most of the labeled i.p. administrated high molar mass PVA is excreted through the kidneys. Corresponding to the results of Kaneo and Besheer the way of excretion with the urine could also be confirmed for this labeled PVA.^{30,39} Despite its high molar mass of 195,000 g/mol, PVA was eliminated through the kidneys.³²

Characterization of Dialyzed-Precipitated Polymer

The polymers extracted from the dialyzed urine of rabbits after i.p. administration of PVA show a brown color. To characterize the excreted polymer in more detail, original PVA, control sample (PVA mixed with rabbit urine), three extracted urinary samples, and the urine pigment were investigated by SEC, FTIR spectroscopy, and ¹H-NMR spectroscopy. This brown color is most likely caused by metabolites of bilirubin (urobilin)—the final degradation product of hemoglobin (Figure 4).⁴⁹ The urine pigment sample as a reference is used to identify the influence on the precipitated polymers. The urinary extracted polymer sample was treated by alkaline solution (1 mol/L NaOH). Thus, the aggregates of excreted PVA with urine pigments were partially broken. This treated sample was then poured into acetone. PVA is not soluble in acetone and precipitates. The suspension is centrifuged and the supernatant liquid is collected and evaporated at 70°C. A deep brown solid urine pigment was obtained after evaporation. The dried PVA had still a brownish color.

Figure 5 shows the FTIR spectra of extracted urinary samples, the original PVA, the control sample, and the urine pigment. The IR spectra exhibit several bands characteristic of stretching and bending vibrations of O—H, C—H, C—O, and C=O groups. The significant observed IR band positions and respective functional groups are listed in Table I. The characteristic bands of pure PVA are located at 3332, 2942, 1440, 1325, 1094, 916, and 850 cm⁻¹. The broad and strong band observed at about 3300 cm⁻¹ corresponds to the O—H stretching vibration. A weak band at 1325 cm⁻¹

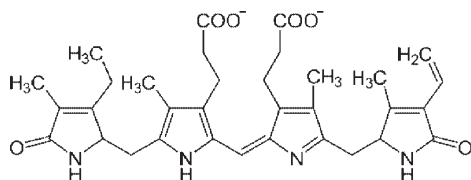


FIGURE 4. Chemical structure of urobilin. (Bilirubin reduction in the gut leads to urobilinogen which is oxidized to urobilin by intestinal bacteria. Urobilin is absorbed into the blood stream and is finally excreted in urine.)

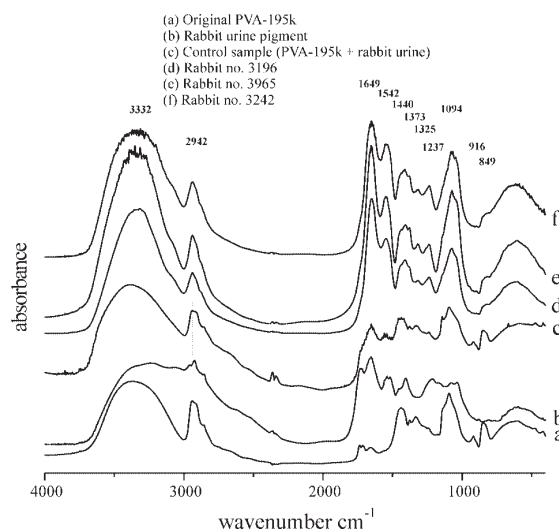


FIGURE 5. FTIR spectra of original PVA, control sample (PVA mixed with rabbit urine and dried), and dialyzed-precipitated polymer of the rabbit urine samples (PVA i.p. administered rabbits No. 3196, No. 3965, and No. 3242) and rabbit urine pigment.

has been assigned to the combination frequency of C—H and O—H groups. The strong band at 1094 cm⁻¹ is attributed to the stretching mode of C—O of PVA. The band at 916 cm⁻¹ is assigned as the stretching mode C—O depending in the tacticity of PVA. The broad band at 2942 cm⁻¹ (3000–2800 cm⁻¹) is assigned to the overlapping of asymmetric and symmetric C—H stretching of CH₃ and CH₂ groups. Other bands appear at 1440 and 850 cm⁻¹ that are related to bending modes of the CH₂ group. Most of the characteristic bands of PVA can also be observed in the IR spectra of urinary extracted polymers. Additional bands at 1649, 1542, 1406, and 1237 cm⁻¹ can be observed in the IR spectra of the extracted urinary samples. These intense bands can be related to the urine compounds by comparing

TABLE 1. Infrared Absorption Frequencies and Vibrational Modes Related to Poly(vinyl alcohol) and Dialyzed-Precipitated Polymer of the Rabbit Urine Samples

IR Band Position (cm ⁻¹)	Functional Group
3332	O—H stretching
2940	C—H stretching
1649	C=O (carboxylate)
1542	C=C stretching in the pyrrole ring (urobilin)
1440	C—H bending in CH ₂ group
1373	Umbrella motion in CH ₃ group
1325	O—H bending and C—H stretching (PVA)
1237	C—C stretching in propionic acid side chain (urobilin)
1094	C—O stretching (PVA)
916	C—O depending on tacticity (PVA)
850	CH ₂ out of plane bending (PVA)

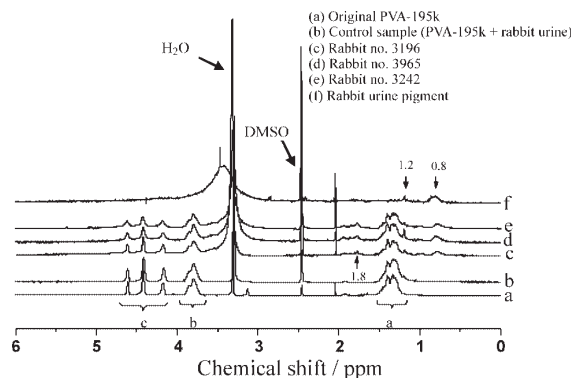


FIGURE 6. $^1\text{H-NMR}$ spectra (DMSO as solvent): original PVA-195k, control sample (PVA-195k mixed with rabbit urine), dialyzed-precipitated polymer of the rabbit urine samples (PVA i.p. administered rabbits No. 3196, No. 3965, and No. 3242).

the IR spectra of the control sample and the urine pigment.^{50,51} The medium band at 1373 cm^{-1} overlapped with the band of the CH_2 bending mode and represents the methyl symmetric bending vibration “umbrella mode,” which can be observed only in IR spectra of extracted urinary samples and indicated the presence of methyl groups in extracted urinary samples (from the urine pigment). The strong band at 1094 cm^{-1} and the weak band at 916 cm^{-1} are attributed to the stretching mode of the C—O group in PVA. The broad band at 1094 cm^{-1} of the urinary extracted sample displays the slight decrease of the absorption peak and a shift to lower frequency compared to pure PVA and the control sample. In conclusion, it can be stated that the majority of the excreted material is clearly PVA that contains a certain amount of urine pigment that could not be separated by dialysis of the urine collected from rabbits.

$^1\text{H-NMR}$ spectroscopy is applied to reveal more structural information of the urinary extracted polymer. The $^1\text{H-NMR}$ spectra were recorded in $\text{DMSO-}d_6$ (Figure 6). Peaks at chemical shift of 2.5 and 3.3 ppm are the proton resonance of the solvent DMSO and the residual water, respectively. Peaks a and b at chemical shifts of 1.29–1.46 and 3.75–3.84 ppm are the proton resonance of CH_2 and CH groups of PVA. The peak c at a chemical shift of 4.11–4.62 ppm is the proton resonance of the OH group of PVA. The small peak at a chemical shift of 1.95 ppm is from the protons of the CH_3 group of residual acetate units of the poly(vinyl acetate) which is the basis polymer for PVA production.^{52,53} All characteristic proton resonances of PVA can be detected in the spectra of the extracted urinary samples. Some additional peaks are also observed at chemical shifts of 1.8, 1.2, and 0.8 ppm in these spectra. The comparison of the PVA spectra with the control sample and the urine pigment indicates that the proton resonances at 1.2 and 0.8 ppm are caused by the urine pigment. The resonance at 1.8 ppm might be related to the presence of some vinyl acetate monomer units PVA.

The SEC traces show strong variations of molar mass and molar mass distribution of the samples under investiga-

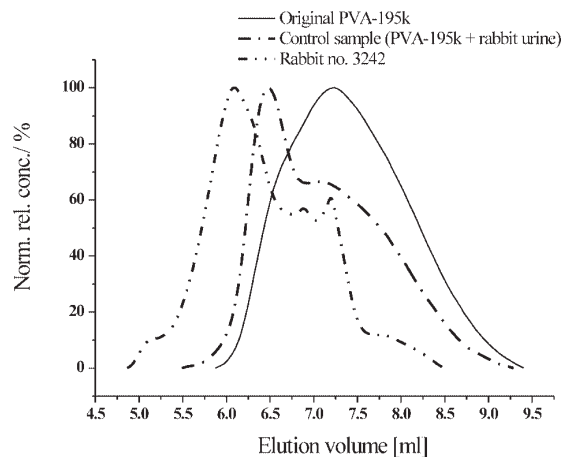


FIGURE 7. SEC traces from original PVA-195k, control of PVA-195k mixed with rabbit urine and dialyzed-precipitated polymer of the rabbit urine sample No. 3242.

tion (Figure 7). The elution volumes (V_E) of all three extracted urinary samples and the control sample shifted to smaller values compared to original PVA. For the sake of clarity, only one SEC trace of a urinary extracted sample is given. The SEC trace of the control sample showed a similar shift to smaller V_E indicating the strong interactions between PVA and urine pigments to form apparently higher molar mass aggregates. For this reason, the present SEC results of extracted urinary samples do not reflect the exact molar mass of excreted PVA. It is important to note that also the control sample is shifted towards smaller retention volumes indicating an apparent molar mass increase. Since the control sample is simply prepared by mixing PVA and urine at room temperature it can be assumed that strong physical interactions between urine pigment and PVA are responsible for this shift. A chemical reaction is very unlikely.

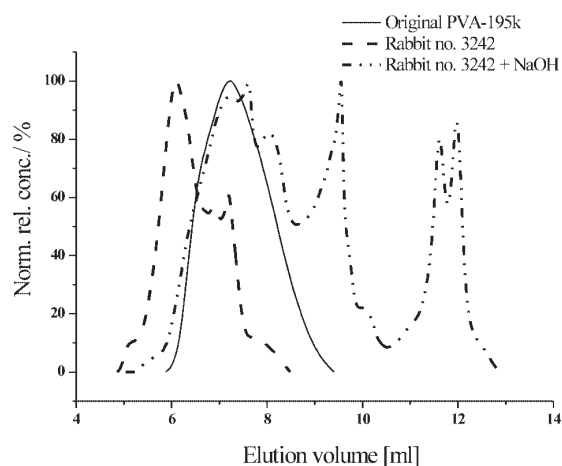


FIGURE 8. SEC traces of dialyzed-precipitated polymer of the rabbit urine sample before and after alkaline treatment.

Supplemental material

(a) Investigation of the *in vivo* fate of a water soluble polymer

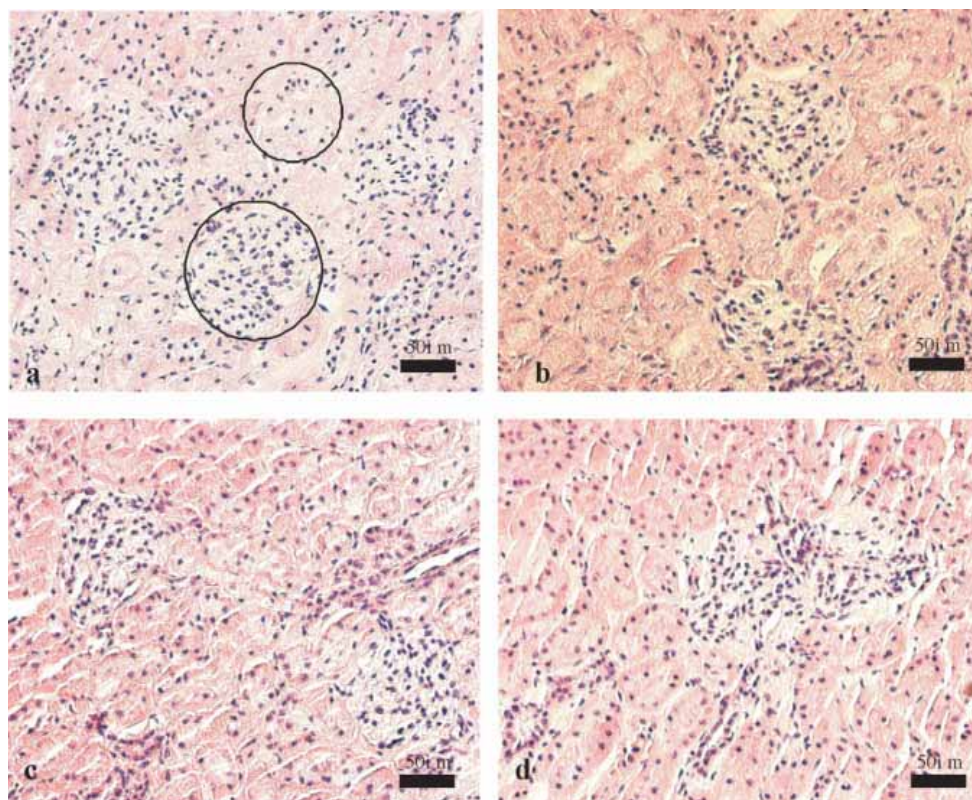


FIGURE 9. Glomerular structures and tubular structures of nephrons in the renal cortex of rabbits (H&E, $\times 20$) (a) control (large circle area: glomerulus, and small circle area: tubule's system of nephron), (b) No. 3196, (c) No. 3242, and (d) No. 3965. [Color figure can be viewed in the online issue, which is available at www.inerscience.wiley.com]

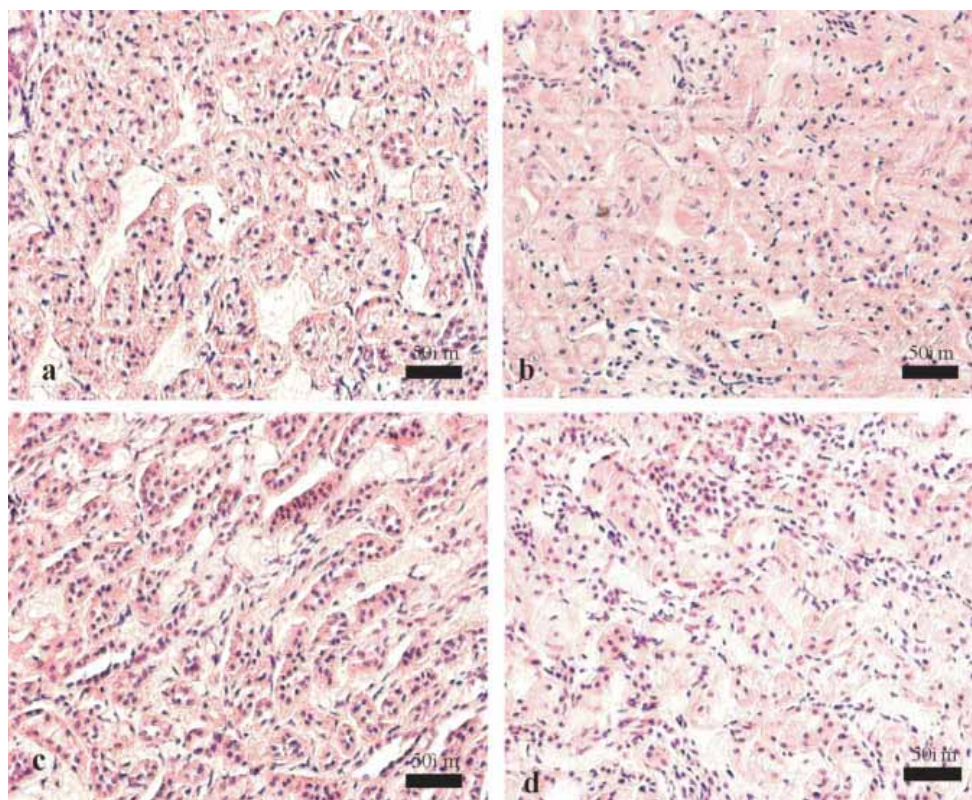


FIGURE 10. Medulla section of the rabbit kidney (a) control (loops of Henle and collecting tubules), (b) No. 3196, (c) No. 3242, and (d) No. 3965 (H&E, $\times 20$). [Color figure can be viewed in the online issue, which is available at www.inerscience.wiley.com]

Supplemental material

(a) Investigation of the *in vivo* fate of a water soluble polymer

To further identify the molar mass of urinary excreted polymer, attempts were made to break the interactions between the polymer and the urine pigments by acid or alkaline treatment. 1 mol/L NaOH or HCl are added to the sample solutions prepared for SEC measurements and heated at 80°C for 1 day. After the hydrolysis in basic or acidic environment, urine pigment interacting with PVA molecules is partly released from the polymer conjugation. Alkaline and acid treatments show a similar influence on the breaking of the aggregates of excreted polymer and urine pigments. NaOH of 1 mol/L is then chosen to hydrolyze all three extracted urinary samples. SEC traces exhibit three obvious peaks in base-treated extracted urinary samples indicate that three main compounds are contained in the urinary extracted sample (Figure 8). The peaks at V_E of 12 mL represent the released urine pigment after basic treatment. The other two peaks distribute broadly at V_E of 6 and 10 mL, respectively. The nonuniform distribution of these two peaks indicates the existence of different polymer-urine pigment aggregates in the urinary excreted samples. The shape and the different shifts of V_E of these peaks make it difficult to characterize the excreted PVA exactly with respect to the molar mass. The peaks that appeared in the range of 9–11 mL can also be observed in SEC traces of the control sample and it must be related to urine pigment-polymer aggregates. The peak at intermediate retention volumes around 9.5 mL might be caused by aggregates that are only partially cleaved under the experimental conditions selected.

Histological Tests

The biocompatibility of PVA was investigated by histopathological tests of the kidneys which were excised from the PVA i.p. administrated rabbits. H&E (hematoxylin and eosin) stain is a popular staining method in histology. The staining method involves application of the basic dye hematoxylin, which colors basophilic structures with blue-purple hue, and alcohol-based acidic eosin, which colors eosinophilic structures bright pink. The basophilic structures are usually the ones containing nucleic acids, such as the ribosomes and the chromatin-rich cell nucleus, and the cytoplasmic regions rich in RNA. The eosinophilic structures are generally composed of intracellular or extracellular protein. Most of the cytoplasm is eosinophilic.

The kidney is the most important organ for the urinary excretion. Histological testing is an important method to evaluate the biocompatibility of biomaterials. In this study, the appearance of nephrotoxicity, PVA accumulation or depositions were not observed in the histological sections of PVA-treated rabbits (No. 3196, No. 3242, and No. 3965) by comparing with the control rabbits (non-PVA-treated). Morphological changes of nephrons, vascular lesions, and inflammation infiltration cannot be seen in renal cortex of PVA-treated rabbits. The elimination of high molar mass PVA through kidney did not cause any visible damage in the renal glomeruli (Figure 9). Renal tubule epithelial cells did not show any degeneration, necrosis, inflammatory infiltration, or fibrous proliferation which could be induced by PVA

accumulation and deposition in the kidney. Similar conclusions can be drawn from the medulla section of the rabbit kidney (Figure 10). There is not any evident damage or degeneration of the tissue.

DISCUSSION

The urinary extracted polymer from PVA i.p. administered rabbits shows the main spectral features of pure PVA in the investigations of FTIR and $^1\text{H-NMR}$ spectroscopy. The characteristic signals represent PVA that can be detected in extracted urinary samples. The SEC traces indicate that strong aggregation occurred between the extracted PVA and urine pigments. The aggregation can partially be broken under alkaline or acid condition. The SEC traces of alkaline-treated extracted urinary samples exhibit multiplex distributions. A characteristic peak occurs at shorter retention times. Control experiments using PVA and rabbit urine mixtures show a similar peak, which is probably caused by aggregates formed due to strong physical interactions between PVA and urobilin. All the results mentioned earlier show that extracted urinary samples exhibit some obvious differences from the original PVA. They are caused by the urine compounds that could not be separated from the collected PVA (e.g. urobilin). This can be clearly seen in FTIR and $^1\text{H-NMR}$ measurements.

The kidney as a main excretion gateway has selection criterions on the molecule size and molar mass of filtered substances. Molecules with $R_h < 1.8$ nm (molar mass $< \text{ca. } 10,000$ g/mol) can be filtered through glomerular membrane without any hindrance. Molecules with $1.8 \text{ nm} < R_h < 4$ nm are only partially filterable. Molecules with $R_h > 4.4$ nm (molar mass $> 80,000$ g/mol, e.g. globulin) usually cannot be filtered. However, additional parameters (charge, shape, and flexibility) are also contributing to the renal filtration efficiency. For example, negative charged substances have lower filtration coefficients when compared with neutral molecules with the same radius.³⁴ It is also known that linear, flexible molecules of the same molar mass are more easily filtered compared to molecules with a spherical shape.³⁴ The reported critical cut-off of PVA in renal filtration is 30,000 g/mol. The molar mass of PVA applied in this study is 195,000 g/mol. Both molar mass and molecule size ($R_h \sim 13$ nm) of PVA-195k are far above the limits of glomerular filtration. I.p. administered PVA-195k can be excreted gradually through kidney for a long time without damaging renal glomeruli as demonstrated in this study. It seems possible that PVA shows some kind of reptation allowing for passing the renal filter.

CONCLUSIONS

The urinary excretion of i.p. administered PVA having a tetramethylrhodamine label can be studied by fluorescence imaging. The amount of excreted PVA decreases over 5 days until the detection limit for this method is reached. With extensive investigations on urinary extracted polymers after intraperitoneal administering of high molar mass PVA (195,000 g/mol) using FTIR spectroscopy, $^1\text{H-NMR}$ spectroscopy, and SEC, it is confirmed that the brownish urinary

extracted sample contains mainly PVA. The results of FTIR spectroscopy and ¹H-NMR spectroscopy are in good agreement with each other. FTIR spectroscopy, ¹H-NMR spectroscopy, and SEC traces of extracted urinary samples show some differences from the original PVA. The changes caused by the urine pigments are identified by the spectroscopic results of the control sample and the urine pigment itself. In histological tests, the appearance of nephrotoxicity cannot be observed in the histological sections of PVA-195k-treated rabbits by comparing with the control rabbits (not treated with PVA).

ACKNOWLEDGMENTS

We thank Prof. Steffen Hauptmann and Dr. Wolfgang Schmitt of the Medical Department of the Martin Luther University Halle-Wittenberg for carrying out the histopathological tests.

REFERENCES

- Cosmetic Ingredient Review (CIR). Final report on the safety assessment of polyvinyl alcohol. *Int J Tox* 1998;17:67–92.
- Paradossi G, Cavaliere F, Chiessi E, Spagnoli C, Cowman MK. Poly(vinyl alcohol) as versatile biomaterial for potential biomedical applications. *J Mater Sci Mater Med* 2003;14:687–691.
- Oka M, Naguchi T, Kumar P, Ikeuchi K, Yamamoto T, Hyon SH, Ikada Y. Development of an artificial articular cartilage. *Clin Mater* 1990;6:361–381.
- Yamaoka T, Tabata Y, Ikada Y. Accumulation of poly(vinyl alcohol) at inflammatory site. In: Ottenbrite RM, editor. ACS Symposium Series No. 545: Polymeric Drugs and Drug Administration. Washington, DC: American Chemical Society; 1994. pp 163–171.
- Noguchi T, Yamamoto T, Oka M, Kumar P, Kotoura Y, Hyon SH, Ikada Y. Poly(vinyl alcohol) hydrogel as an artificial articular cartilage: Evaluation of biocompatibility. *J Appl Biomater* 1991;2:101–107.
- Kaetsu I. Radiation synthesis of polymeric materials for biomedical and biochemical applications. *Adv Polym Sci* 1993;105:81–97.
- Nambu M. U.S. Pat. No. 4,472,542; 1984.
- Hyon SH, Ikada Y. U.S. Pat. No. 4,663,358; 1987.
- Hassan CM, Peppas NA. Cellular PVA hydrogels produced by freeze/thawing. *J Appl Polym Sci* 2000;76:2075–2079.
- Hyon SH, Cha WI, Ikada Y, Kita M, Ogura Y, Honda Y. Poly(vinyl alcohol) hydrogels as soft contact lens material. *J Biomat Sci Polym Ed* 1994;5:397–406.
- Devlin BG, Tena M, Medina NA. U.S. Pat Appl Publ, US 2005056954 A1 2005031; 2005.
- Kobayashi M, Chang YS, Oka M. A two year *in vivo* study of polyvinyl alcohol-hydrogel (PVA-H) artificial meniscus. *Biomaterials* 2005;26:3243–3248.
- Bray JC, Merrill EW. Poly(vinyl alcohol) hydrogels for synthetic articular cartilage material. *J Biomed Mater Res* 1973;7:431–443.
- Bao QB, Higham PA. U.S. Pat. No. 5,047,055; 1991.
- Maluccio MA, Covey AM, Porat LB, Schubert J, Brody LA, Sofocleous CT, Getrajdman G I, Jarnagin W, Dematteo R, Blumgart LH. Transcatheter arterial embolization with only particles for the treatment of unresectable hepatocellular carcinoma. *J Vasc Interv Radio* 2008;19:862–829.
- Sharma CP. Surface modification: tissue compatibility towards the development of artificial skin. ICMR Project Report 1989.
- Peppas NA, Benner RE Jr. Proposed method of intracapsular injection and gelation of poly (vinyl alcohol) solution in vocal cords: Polymer considerations. *Biomaterials* 1980;1:158–162.
- Lozinsky VI, Plieva FM, Galaev IY, Mattiasson B. The potential of polymeric cryogels in bioseparation. *Bioseparation* 2001;10:163–188.
- Chase HA. Purification of proteins by adsorption chromatography in expanded beds. *Trends Biotechnol* 1994;12:296–303.
- Mallapragada SK, Peppas NA. Dissolution mechanism of semi-crystalline poly(vinyl alcohol) in water. *J Polym Sci Part B: Polym Phys* 1998;34:1339–1346.
- Takamura A, Ishii F, Hidaka H. Drug release from poly(vinyl alcohol) gel prepared by freeze-thaw procedure. *J Control Rel* 1992; 20:21–28.
- Peppas NA, Scott JE. Controlled release from poly(vinyl alcohol) gels prepared by freezing-thawing processes. *J Control Rel* 1992; 18:95–100.
- Qiu Y, Park K. Environment-sensitive hydrogels for drug delivery. *Adv Drug Del Rev* 2001;53:321–339.
- Langer R, Folkman J. Polymers for the sustained release of proteins and other macromolecules. *Nature* 1976;263:797–800.
- Peppas NA, Mongia NK. Ultrapure poly(vinyl alcohol) hydrogels with mucoadhesive drug delivery characteristics. *Eur J Pharm Biopharm* 1997;43:51–58.
- Weis C, Odermatt E, Kressler J, Funke Z, Wehner T, Freytag D. Poly(vinyl alcohol) membranes for adhesion prevention. *J Biomed Mater Res B* 2004;70:191–202.
- Weis C, Odermatt Erich K. A-Part gel—An efficient adhesion prevention barrier. *J Biomed Mat Res Part B: Appl Biomater* 2007; 82B:174–182.
- DeMerlis CC, Schoneker DR. Review of the oral toxicity of polyvinyl alcohol (PVA). *Food Chem Toxicol* 2003;41:319–326.
- Hall CE, Hall O. Polyvinyl alcohol nephrosis: Relationship of degree of polymerization to pathophysiological effects. *Proc Soc Exp Bio Med* 1963;112:86–91.
- Kaneo Y, Hashihama S, Kakinoki A, Tanaka T, Nakano T, Ikeda Y. Pharmacokinetics and biodisposition of poly (vinyl alcohol) in rats and mice. *Drug Metabol Pharmacokin* 2005;20:435–442.
- Lukas G, Brindle S, Greengard P. The route of absorption of intraperitoneally administered compounds. *J Pharmacol Exp Ther* 1971;178:562–566.
- Yamaoka T, Tabata Y, Ikada Y. Fate of water—Soluble polymers administered via different routes. *J Pharma Sci* 1995;84:349–354.
- Tabata Y, Murakami Y, Ikada Y. Tumor accumulation of poly(vinyl alcohol) of different sizes after intravenous injection. *J Control Rel* 1998;50:123–133.
- Venturoli D, Rippe B. Ficoll and dextran vs. globular proteins as probes for testing glomerular permselectivity: Effects of molecular size, shape, charge and deformability. *Am J Physiol Renal Physiol* 2005;288:605–613.
- Bohrer MP, Deen WM, Robertson CR, Troy JL, Brenner BM. Influence of molecular configuration on the passage of macromolecules across the glomerular capillary wall. *J Gen Physiol* 1979;74:583–593.
- Ohlson M, Sorensson J, Lindstrom K, Blom AM, Fries E, Haraldsson B. Effects of filtration rate on the glomerular barrier and clearance of four differently shaped molecules. *Am J Physiol Renal Physiol* 2001;281:103–113.
- Yamaoka T, Tabata Y, Ikada Y. Comparison of body distribution of poly(vinyl alcohol) with other water-soluble polymers after intravenous administration. *J Pharm Pharmacol* 1995;47:479–486.
- Silbernagl S, Despopoulos A. *Kidney. Taschenatlas der Physiologie*. Stuttgart: Thieme; 2007. p 148.
- Besheer A, Maeder K, Kaiser S, Kressler J, Weis C, Odermatt EK. Tracking the urinary excretion of high molar mass poly(vinyl alcohol). *J Biomed Mat Res Part B: Appl Biomater* 2007;82:383–389.
- Yamaoka T, Tabata Y, Ikada Y. Body distribution of intravenously administered gelatin with different molar masses. *J Control Rel* 1994;31:1–8.
- Kaneo Y, Nakano T, Tanaka T, Tamaki R, Iwase H, Yamaguchi Y. Characteristic distribution of polysaccharides in liver tissue. *Yakuzaigaku* 2000;60:183–195.
- Matsumura S, Steinbüchel A. *Miscellaneous Biopolymers and Biodegradation of Synthetic Polymers*, Vol. 9. Weinheim, Germany: Wiley-VCH; 2003. pp 329–361.
- Kawai F. *Xenobiotic polymers*. In: Imanaka T, editor. *Great Development of Microorganisms*. Tokyo: NTS; 2002. pp 865–870.
- Matsumura S, Tomizawa N, Toki A, Nishikawa K, Toshima K. Novel poly(vinyl alcohol)—Degradation enzyme and the degradation mechanism. *Macromolecules* 1999;32:7753–7761.
- Chiellini E, Corti A, D'Antone S, Solaro R. Biodegradation of poly(vinyl alcohol) based materials. *Prog Polym Sci* 2003;28: 963–1014.
- Levenson ML, Mansfield JR. Multispectral imaging in biology and medicine: Slices of life. *Cytometry A* 2006;69:748–758.

Supplemental material

(a) Investigation of the *in vivo* fate of a water soluble polymer

47. He X, Nie H, Wang K, Tan W, Wu X, Zhang P. In vivo study of bio-distribution and urinary excretion of surface-modified silica nanoparticles. *Anal Chem* 2008;80:9597–9603.
48. Raymond SB, Skoch J, Hills ID, Nesterov EE, Swager TM, Bacskai BJ. Smart optical probes for near-infrared fluorescence imaging of Alzheimer's disease pathology. *Eur J Nucl Med Mol Imaging* 2008;35:93–98.
49. Watson CJ. Recent studies of the urobilin problem. *J Clin Pathol* 1963;16:1–11.
50. Yang Z, Si S, Fung Y. Bilirubin adsorption on nanocrystalline titania films. *Thin Solid Films* 2007;515:3344–3351.
51. Yang B, Taylor RC, Morris MD, Wang X, Wu J, Yu B, Xu G, Soloway RD. Normal coordinate analysis of bilirubin vibrational spectra: effects of intramolecular hydrogen bonding. *Spectrochim Acta Part A: Mol Biomed Spec* 1993;49:1735–1749.
52. Wang Y, Ono H, Ikeda A, Hori N, Takemura A, Yamada T, Tsukataní T. ¹H NMR and ¹³C NMR investigations of sequence distribution and tacticity in poly(vinyl alcohol-co-vinyl levulinate). *Polymer* 2006;47:7827–7834.
53. Marstokk O, Roots J. Synthesis and characterization of hydrophobically modified poly(vinyl alcohol). *Polym Bull* 1999;42:527–533.



Newsletter

A publication of the Controlled Release Society

Volume 27 • Number 2 • 2010

What's Inside

Interview with Dr. Jindrich Kopecek

Educational Workshops at the CRS Annual Meeting

A Synthetic Mycobacterial Monomycoloyl Glycerol Analogue

Tracking the *In Vivo* Fate of High Molar Mass Poly(vinyl alcohol)

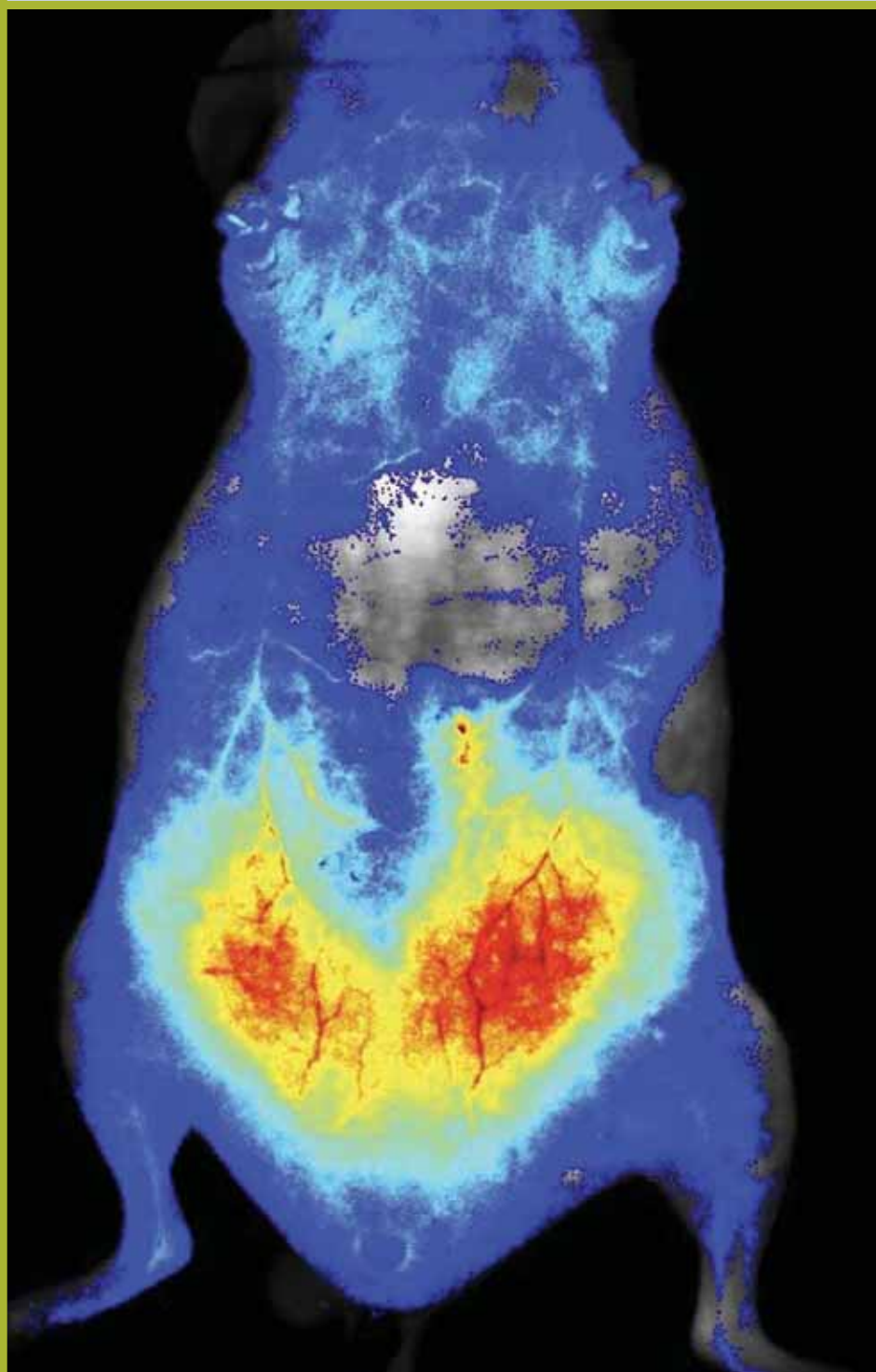
Innovations in Production of Sub-micron Crystals of Therapeutic Agents

Novel Drug Delivery Systems and Animal Health Applications

History of the CRS C&DP Track

2010/2011 CRS Mentorship Program

CRS Satellite Workshop



Tracking the *In Vivo* Fate of High Molar Mass Poly(vinyl alcohol) Using Multispectral Fluorescence *In Vivo* Imaging

Andreas Schädlich,¹ Yanjiao Jiang,² Jörg Kressler,² and Karsten Mäder¹
Martin Luther University Halle-Wittenberg, Halle (Saale), Germany

Introduction

Poly(vinyl alcohol) (PVA) is a nonionic, water-soluble, and biocompatible polymer (1). In the pharmaceutical industry, it is widely used for biomedical applications, such as contact lenses and scaffolds for wound healing and tissue regeneration. PVA hydrogels are also extensively studied for the controlled release of therapeutic molecules. It has also been reported that PVA membranes can be used for adhesion prevention of postsurgical abdominal adhesions (2). Adhesions are internal scars that develop after trauma and involve the injured tissue and peritoneum. An ideal barrier would be a gel or liquid solution that can be injected to the place of interest. Following peritoneal healing, it should be reabsorbed and eliminated. PVA (125,000 g/mol) elimination studies in rabbits showed that PVA passes the kidneys despite its high molar mass (3).

The question is whether the elimination results can be assigned also to a high molecular weight (195,000 g/mol) PVA. The noninvasive method of optical imaging was used to measure how long the PVA is localized at the area of injection to follow possible accumulation in the body and examine whether PVA is still eliminated through the kidneys. PVA was labeled with the fluorescence dye tetramethyl-rhodamine-5-carbonyl azide (TMR) (from Invitrogen) in anhydrous dimethylsulfoxide at

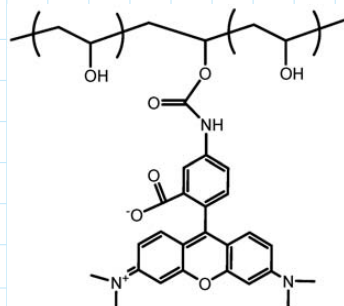


Figure 1. Chemical structure of TMR-labeled poly(vinyl alcohol).

80°C. The dialyzed PVA-TMR was dissolved in water (5%, wt/wt) (Figure 1). Distribution and accumulation were studied by measuring the whole body from the abdominal side at predetermined time intervals using a green filter set (580-nm long-pass emission filter). Multispectral imaging cube sets were acquired. By unmixing and further segmentation, it was possible to separate the PVA-TMR signal from the auto fluorescence signals of the mice. The total signal, as the sum of all pixel values from the extracted PVA-TMR

signal, and the maximum pixel values were then calculated. Confocal microscope pictures were captured using the True Confocal Scanner SP2 fluorescence microscope (Leica Microsystems, Heidelberg, Germany). For excitation an argon laser (488 nm) was used.

Results

Using the Maestro™ software from CRi it was possible to separate the *in vivo* fluorescence PVA-TMR signal from the background signals of the mice (Figure 2). After injection of the PVA-TMR dispersions, high concentrations of labeled polymer could be detected in the area of the abdomen. From there it was distributed via the body liquids throughout the whole body (Figure 3). The circulated polymer was accumulated in the area under the skin but also in the region of the fat pad. Using the Maestro™ software it was possible to separate the accumulated PVA-TMR signals between the skin and other parts like the fat pad that were analyzed the skin signal.

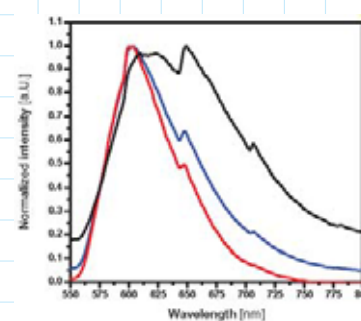


Figure 2. Normalized emission fluorescence spectra; blue: *in vivo* extracted PVA-TMR spectra; black: background signal of an untreated mouse; red: manually computed PVA-TMR spectra.

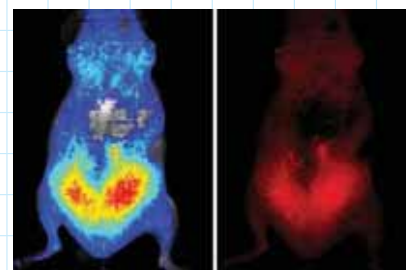


Figure 3. Unmixed images of one nude, female mouse 24 hr after *i.p.* injection. The incremental jet color images represent the threshold fluorescence PVA-TMR signal. The red color indicates areas of detected PVA-TMR signal.

The total fluorescence intensities from the abdomen site of the body increased to a maximum within the first week, which was the result of the distribution throughout the whole body. After this time, the PVA-TMR was continuously released and mainly eliminated through the kidneys (Figure 4). Surprisingly, we detected obvious differences between male and female mice in

¹ Department of Pharmaceutical Technology and Biopharmaceutics;
E-mail: andreas.schaedlich@pharmazie.uni-halle.de.

² Department of Chemistry.

Scientifically Speaking

Scientifically Speaking *Schädlich* continued from page 15

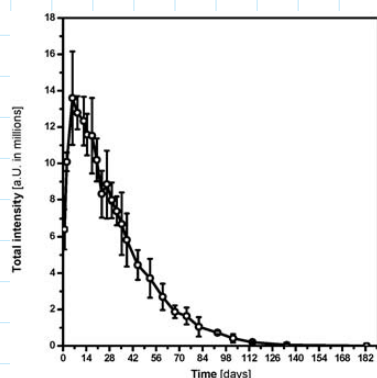


Figure 4. Total fluorescence intensities throughout the whole body from the abdomen side of three female mice over a time period of 26 weeks after *i.p.* administration of the PVA-TMR dispersion.

the region of the celiac fat ($n = 3$ of each group) (Figure 5). In female mice, PVA-TMR accumulated mainly in the abdomen area and was localized there over a time period of about 100 days. In contrast to this, the main intensities measured over nearly the same time period in male mice were found in the thigh (Figure 5).

Analyzing the maximum signal, it could

be shown that this parameter remained constant during the first three weeks. Later on, the signal decreases continuously (Figure 6). The PVA-TMR was released slower compared to other tissues. This can be attributed to the poor perfusion of the fat tissue. Thus, the total fluorescence intensity was reduced faster than the maximum intensity.

The signal accumulation in the fat depot was also studied in more detail *ex vivo* using a confocal microscope. The pictures from fat cells show that PVA-TMR was accumulated in the intra-cellular region of the cells (Figure 7A and B). These results could also be confirmed with an *in vitro* experiment in which fat tissue was treated with PVA-TMR and then washed with water to check whether it was bound (Figure 7C). The experiment confirmed the expectations after *in vivo* measurements.

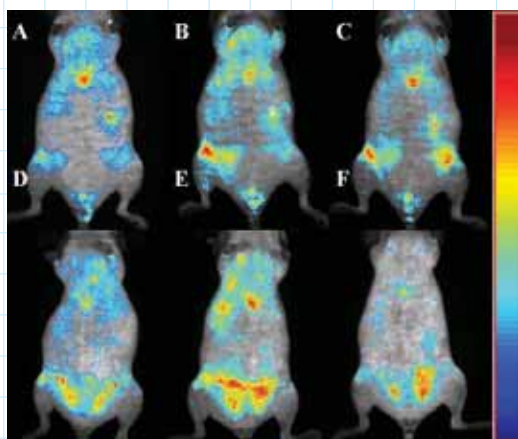


Figure 5. Fluorescence intensity images of one male (A–C) and one female (D–F) mouse after 2 (A and D), 8 (B and E), and 30 (C and F) days. The incremental Jet color represents the threshold fluorescence TMR signal. Differences in PVA-TMR distribution are obvious. The high intensity of the spot in the chest area was identified by autopsy of three mice as an artifact caused by the xiphoid cartilage.

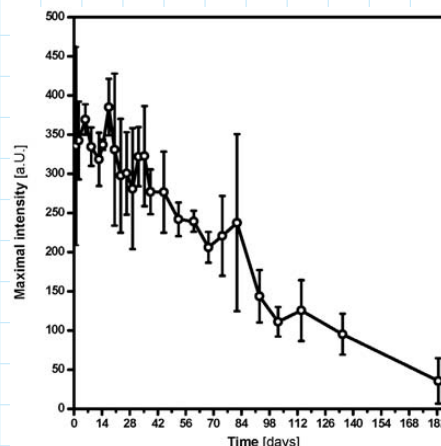


Figure 6. Maximum intensity values of the PVA-TMR signal for 26 weeks after *i.p.* administration ($n = 3$).

Conclusions

The intraperitoneally administered fluorescent-labeled PVA dispersions were successfully characterized using the Maestro™ *in vivo* imaging system. PVA was accumulated in the skin as well as in the fat tissue of mice. We detected differences between the male and female mice.

PVA-TMR was slowly and continuously released over months. Despite its high molar mass, PVA-TMR was mainly eliminated with the urine. Accumulation in the liver and

kidneys, as well as in feces, was not observed. However, the quantum efficiency of the TMR was not high enough to exclude it completely. Therefore, PVA was labeled with a NIR dye, and the *in vivo* experiments will start soon.

References

1. Paradossi, G, Cavalieri, F, Chiessi, E, Spagnoli, C, Cowman, MK. Poly(vinyl alcohol) as versatile biomaterial for potential biomedical applications, *J. Mater. Sci. Mater. Med.* 14: 687-691 (2003).
2. Weis, C, Odermatt, EK, Kressler, J, Funke, Z, Wehner, T, Freytag, D. Poly(vinyl alcohol) membranes for adhesion prevention, *J. Biomed. Mater. Res. Part B* 70B: 191-202 (2004).
3. Besheer, A, Mäder, K, Kaiser, S, Kressler, J, Weis, C, Odermatt, EK. Tracking the urinary excretion of high molar mass poly(vinyl alcohol), *J. Biomed. Mater. Res. Part B* 82B: 383-389 (2007). ■

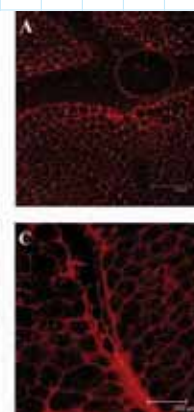


Figure 7. Confocal microscopy images of fat tissue extracted from the abdomen; A, fat 180 days after *i.p.* injection; B (top), fat tissue; B (bottom), untreated fat; C, ex vivo PVA-TMR incorporated fat tissue.

How Stealthy are PEG-PLA Nanoparticles? An NIR *In Vivo* Study Combined with Detailed Size Measurements

Andreas Schädlich · Cornelia Rose · Judith Kuntsche · Henrike Caysa · Thomas Mueller · Achim Göpferich · Karsten Mäder

Received: 18 January 2011 / Accepted: 8 March 2011 / Published online: 27 April 2011
© Springer Science+Business Media, LLC 2011

ABSTRACT

Purpose Detailed *in vivo* and *ex vivo* analysis of nanoparticle distribution, accumulation and elimination processes were combined with comprehensive particle size characterizations.

Methods The *in vivo* fate of near infrared (NIR) nanoparticles in nude mice was carried out using the Maestro™ *in vivo* fluorescence imaging system. Asymmetrical field flow fractionation (AF4) coupled with multi-angle laser light scattering (MALLS), photon correlation spectroscopy (PCS) and transmission electron microscopy (TEM) were employed for detailed *in vitro* characterization.

Results PEG-PLA block polymers were synthesized and used for the production of defined, stable, nontoxic nanoparticles. Nanoparticle analysis revealed narrow size distribution; AF4/MALLS permitted further accurate size evaluation. Multispectral fluorescence imaging made it possible to follow the *in vivo* fate non-invasively even in deep tissues over several days. Detailed fluorescence *ex vivo* imaging studies were performed and allowed to establish a calculation method to compare nanoparticle batches with varying fluorescence intensities.

Conclusion We combined narrow-size distributed nanoparticle batches with detailed *in vitro* characterization and the understanding of their *in vivo* fate using fluorescence imaging, confirming the wide possibilities of the non-invasive technique

and presenting the basis to evaluate future size-dependent passive tumor accumulation studies.

KEY WORDS AF4 · fluorescence imaging · *in vivo* imaging · nanoparticle · PEG-PLA

ABBREVIATIONS

AF4	asymmetrical field flow field fractionation
CHO	Chinese hamster ovary
DiR	1,1'-dioctadecyl-3,3',3'-tetramethylindotricarbocyanine iodide
EMEM	Eagle's minimum essential medium
EPR	enhanced permeability and retention
FBS	fetal bovine serum
MALLS	multi-angle laser light scattering
MTT	3-(4,5-Dimethylthiazol-2-yl)-2,5-diphenyltetrazolium bromide
NIR	near infrared
NR	nile red
PBS	phosphate-buffered saline
PCS	photon correlation spectroscopy
PDI	polydispersity indices
QD	quantum dots
RES	reticuloendothelial system

A. Schädlich · J. Kuntsche · K. Mäder (✉)
Department of Pharmaceutical Technology
and Biopharmaceutics
Martin Luther University Halle-Wittenberg
Wolfgang-Langenbeck-Str. 4
06120 Halle (Saale), Germany
e-mail: Maeder@pharmazie.uni-halle.de
URL: <http://www.pharmtech.uni-halle.de/>

C. Rose · A. Göpferich
Department of Pharmaceutical Technology University of Regensburg
Universitätsstraße 31 93053 Regensburg, Germany

H. Caysa · T. Mueller
Department of Internal Medicine IV, Oncology/Hematology
Martin Luther University Halle-Wittenberg
06120 Halle (Saale), Germany

ROI region of interest
TEM transmission electron microscopy

INTRODUCTION

The development of biodegradable nanoparticles as drug delivery vehicles for therapeutic agents is one of the main promises for future cancer therapies. The major aim is to produce nanoparticles which preferentially accumulate at the tumor site. Loaded with anticancer drugs, they can improve cancer therapy and simultaneously reduce the harmful nonspecific side effects of chemotherapeutics (1). In addition, nanoparticles loaded with contrast agents may provide very efficient cancer diagnostics by *in vivo* imaging. Two main tumor targeting strategies have generally been explored: First, active targeting by conjugating nanocarriers with molecules that can bind to tumor-specific antigens or receptors on the cancer cells (2), and second, the more commonly used passive targeting strategy. The first marketed products were introduced more than 10 years ago as liposomes or polymer-protein conjugates (2). The passive accumulation of nanoparticles is based on the enhanced permeability and retention (EPR) effect of tumor tissues (3). Several studies have shown that particle size plays a key role in accumulation effectiveness. Experiments using liposomes have demonstrated that the upper size limit for extravasations into tumors is about 400 nm (4). Others showed that smaller particles with sizes below 200 nm are even more effective (5–7). However, particles smaller than 20–30 nm are eliminated faster by renal excretion (8). It was also noticed that liposomes, which are smaller than 70 nm, were more rapidly cleared from the circulation than larger (between 70 and 300 nm) ones (9, 10). Therefore, the optimal size of nanoparticles for cancer treatment should be between about 70 and 200 nm (11). Accurate knowledge of the particle size, size distributions, and particle morphology is a key requirement for *in vivo* applications of newly developed nanoparticles, although this is often neglected. Gaumet *et al.*, for example, criticized that conclusions of size-dependent studies of nanoparticle biodistribution are often done without providing accurate particle size data (12). High polydispersity indices (PDI) varying between 0.2 and 0.5 may result in particle overlapping and hamper accurate size-dependent interpretation of the *in vivo* results (12). Besides the size, surface properties of nanoparticles also play an important role for their *in vivo* fate. It is well established that hydrophilic surfaces, which can be achieved, for example, by polymer modification with polyethylene glycol (PEG), reduce opsonisation and thus uptake by the mononuclear phagocytic system (MPS) (11,13). Furthermore, such PEG shells provide sterical stabilization of the particles in aqueous systems (14).

In this study, detailed non-invasive *in vivo* fluorescence imaging experiments were combined with fundamental *in vitro* tests to allow meaningful data interpretation and to gain information about the *in vivo* fate of PEG-PLA nanoparticles. Multispectral *in vivo* fluorescence imaging has already been used for fluorescence tissue imaging with nanocarriers like quantum dots (QD) (15–17). Using NIR QD, it could be shown that fluorescence imaging is possible even in deep tissues (18). Nevertheless, QD are criticized due to the high production costs and the potential *in vivo* toxicity depending on their surface properties (19). The incorporation of the very lipophilic NIR carbocyanine dye DiR into PEG-PLA nanoparticles combined the advantages of NIR light with low toxicity risks for the animals. Fluorescence imaging thus allowed the study of distribution, accumulation and elimination processes of the nanoparticles over several days non-invasively. The distribution of the nanoparticles within the body was comprehensively researched further by additional *ex vivo* experiments. However, fluorescence imaging with different nanoparticle batches (differing in sizes and in polymer composition) may pose constraints, such as varying fluorescence intensities. Due to diversity in dye loading and dye allocation in the particles, direct comparison of the results and particularly quantification in tissues obtained with different nanoparticle batches proved challenging. In this work a new calculation approach is discussed as a basis for future evaluations of size-dependent tumor accumulation studies with different nanoparticle batches. Beyond that, exact size characterization is an important issue, as mentioned above. Particle sizing at the nanoscale is, however, by no means a trivial task. The several methods are based on different measurement principles and the potential existence of various particle species as well as heterogeneous size distribution. These are only some of the challenges in size determination of colloidal formulations. In the present study, the combination of PCS, AF4 coupled with MALLS and TEM provided comprehensive information about the size and morphology of the nanoparticles as a basis for drawing meaningful conclusions about the *in vivo* fate of nanoparticles.

MATERIALS AND METHODS

Materials

3,6-Dimethyl-1,4-dioxan (D,L-lactide), poly(ethylene glycol) monomethyl ether (mPEG2000; MW=2000 Da), stannous 2-ethylhexanoate (>95%), phosphotungstic acid (reagent grade), Nile red (NR), Eagle's minimum essential medium (EMEM), nutrient mixture HAM's F-12, sodium dodecyl sulphate and sorbitol were obtained from Sigma Aldrich, Germany. PLGA

75:25 (Resomer® 756) was kindly provided by Boehringer Ingelheim AG, Biberach, Germany. Trypsin-EDTA 0.25%, Dulbecco's phosphate-buffered saline (PBS) and 1,1'-dioctadecyl-3,3',3'-tetramethylindotricarbocyanine iodide (DiR) were purchased from Invitrogen, Germany. Sucrose and Triton-X (p.a.) were obtained from Merck KGaA, Germany, and Pluronic® F68 as well as sodium azide from Riedel-de Haën, Seelze, Germany. Polystyrene standard nanoparticles were obtained from Duke Scientific, Paolo Alto, United States (50, 100, 200 nm) and from Beckman Coulter, Germany (300 nm). Fetal bovine serum (FBS) was purchased from Biochrom KG, Berlin, Germany and 3-(4,5-Dimethylthiazol-2-yl)-2,5-diphenyltetrazolium bromide (MTT) from Appli-Chem GmbH, Darmstadt, Germany. All other substances and solvents were used as received.

Synthesis and Characterization of PEG-PLA Polymers

Biodegradable diblock copolymers PEG₂PLA₂₀ and PEG₂PLA₄₀ were synthesized following a previously established method (20). The numbers refer to the molecular weight (kDa) of the respective polymer block. The PLA part was attached to the mPEG part by a ring-opening polymerization of 3,6-dimethyl-1,4-dioxan (D,L-dilactide) using stannous 2-ethyl hexanoate as catalyst. First of all, any trace amounts of water were removed from the educts. Therefore, about 2 g of the mPEG₂₀₀₀ were dissolved in 100 mL toluene in a three-neck round-bottom flask and heated; the reflux of 50 mL toluene was distilled off using a water separator. D,L-dilactide and 100 mL toluene (20 g and 40 g, respectively) were added, and again 50 mL of the solvent was distilled off. The final volume of toluene thus did not exceed 100 mL. After addition of 500 µL glacial acid and about 400 mg of the catalyst, the mixture was refluxed for at least 8 h under nitrogen atmosphere. Afterwards, the toluene was removed by distillation with

200 mL methylene chloride and acetone using a rotary evaporator. The obtained viscous polymer was dissolved in acetone and precipitated by dropping into water at 4°C to remove residual catalyst and water-soluble by-products. The precipitate was separated, frozen at -80°C and freeze-dried. Afterwards, the dried polymer was stored under vacuum. The molecular weight of the synthesized polymers was determined by ¹H-NMR and GPC (data not shown).

Preparation of Polymer Nanoparticles

Unloaded (batch A, B and C) and loaded (DiR, batch D and NR, batch E) polymeric nanoparticles were prepared by nanoprecipitation (21). Preparation conditions, like polymer concentration, temperature, impact of volumes (polymer phase and external phase) and the influence of stabilizer, were studied preliminarily (22). For nanoparticle preparation, the respective polymer (2.5, 5 or 10 mg) and—if applicable—the fluorescence dye were dissolved in 5 mL acetone (cp. Table I). This organic solution was drop by drop (2 mL per minute) added to 40 mL of an aqueous poloxamer solution (0.25% w/v Pluronic® F68) to facilitate immediate nanoparticle formation. After evaporation of the organic solvent overnight at room temperature, the particles were collected by centrifugation (12,500 g; 30 min; 10°C) using an Avanti JE high-speed centrifuge (Beckman Coulter, Germany) and washed with filtrated (<1 µm) water. The particles were resuspended in a solution of either 5 or 10% (w/v) sucrose. Subsequently, particles were frozen at -80°C for 24 h and freeze-dried at 15°C and 0.120 mbar over at least 2 days using a lab-scale freeze-dryer (Martin Christ Gefriertrocknungsanlagen, Osterode am Harz, Germany). Dried samples were sealed and stored in a desiccator at room temperature under light protection. For stability evaluation, samples of batch A, B and C were redispersed in bi-distilled water preserved with

Table I Nanoparticle Compositions and Particle Sizes of Different Nanoparticle Batches Measured Directly After Redispersion

Batch Polymer ^{a)}	A PLGA	B PEG ₂ PLA ₂₀	C PEG ₂ PLA ₄₀	D PEG ₂ PLA ₄₀ -DiR	E PEG ₂ PLA ₄₀ -NR
Dye loading ^{b)}	–	–	–	0.5%	0.6%
Polymer concentration ^{c)}	1.0%	1.0%	1.0%	2.0%	1.0%
PCS - z-average in nm (PDI)	339 (0.52) 209 (0.15) ^{d)}	113 (0.09)	104 (0.08)	166 (0.13)	103 (0.08)
TEM (nm)	128 ± 13	82 ± 15	–	–	–
MALLS D10 (nm)	127 ± 10.4	66 ± 0.9	62 ± 0.1	48 ± 9.8	59 ± 0.4
MALLS D50 (nm)	222 ± 9.0	95 ± 0.2	86 ± 1.0	99 ± 4.0	81 ± 0.3
MALLS D90 (nm)	403 ± 29.8	141 ± 0.6	132 ± 0.4	230 ± 3.3	121 ± 0.2

^{a)} The numbers 2 and 20 refer to the molar mass of the polymer block (kDa)

^{b)} Dye loading in percent related to the polymer amount

^{c)} Polymer concentration in percent related to the organic solvent

^{d)} Sample was filtered (pore size 0.8 µm) prior measurements

0.02% (w/v) sodium azide and stored in the fridge (5°C) for 3 months.

Particle Size Characterization of Nanoparticles

Photon Correlation Spectroscopy (PCS)

Dynamic light scattering was measured at 25°C in the backscattering mode (173°) with a High Performance Particle Sizer (HPPS) from Malvern Instruments (Malvern, Herrenberg, Germany). Samples were diluted with purified, filtered (0.2 µm) water (nanoparticle concentration was about 0.1 mg/mL) and measured 4 times with 12–16 runs over 10 s each at fixed measurement position in the middle of the cuvette. Due to macroscopic inhomogeneities, PLGA suspensions were filtrated (pore size 0.8 µm, PALL medical, Dreieich, Germany) and measured once again. Z-average diameters and PDI were determined by the instruments cumulant analysis software (version 4.20). Results are given as average with standard deviation of the 4 measurements ($n=4$).

Asymmetrical Flow Field-Flow Fractionation (AF4)

Samples were analyzed as described earlier (23). In brief, the fractionation system (Eclipse AF4, Wyatt, Dernbach, Germany) was coupled with a multi-angle laser light scattering (MALLS) detector (DAWN EOS, Wyatt). The trapezoidal channel (length 265 mm, largest width 21 mm, height 350 µm) was equipped with a membrane of regenerated cellulose or polyethersulfone (MWCO 5 kDa, Microdyn-Nadir, Wiesbaden, Germany). Bi-distilled water preserved with 0.02% sodium azide and filtered through 0.1 µm was used as carrier liquid. One hundred µL dispersion (nanoparticle concentration about 1 mg/mL) was injected during focusing (focus flow 2 mL/min), and samples were eluted with a constant detector flow of 1 mL/min and decreasing cross flow. Initially, a high cross flow gradient (cross flow decreasing from 2 to 0.5 mL/min within 5 min) was applied to assure baseline separation of the nanoparticles from the void peak followed by a decreasing cross flow (0.5–0 mL/min within 35 min) to separate the nanoparticles. Size evaluations were done by the Astra software 4.90 (Wyatt) using the particle mode and assuming compact spheres (23). Mass weighted size distributions and the characteristic diameters (D10, D50, and D90) were calculated using the binning method (23). Similarly as in PCS measurements, the dispersion of PLGA nanoparticles was filtered (pore size 0.8 µm) prior to the measurements. The separation accuracy of the A4F/MALLS system was checked by using a mixture of 50, 100, 200 and 300 nm polystyrene standard nanoparticles as described earlier (23). All samples were measured in triplicate, and results are given as average with standard deviation ($n=3$).

Transmission Electron Microscopy (TEM)

About 10 µL of diluted aqueous nanoparticle dispersions were placed on 3.05 mm formvar/carbon-coated copper grids (300 mesh) and negatively stained with phosphotungstic acid (2% in water) for 30 s. Samples were subsequently dried under vacuum and viewed in a Zeiss EM C/CR (Carl Zeiss AG, Germany) at 60 kV operating voltage. Particle size was estimated by manually measuring the diameter of 100 randomly chosen particles for each sample. The mean size was determined for each sample in triplicate ($n=3$).

In Vitro Cytotoxicity Assay

Biocompatibility was tested with hamster endothelia (chinese hamster ovary (CHO)) cells and mouse fibroblasts (L929). They were cultured in HAMs F12 and EMEM, respectively, each supplemented with 10% FBS at standard cell culture conditions (37°C; 95% relative humidity and 5% CO₂). Evaluation was done using the well-established MTT assay (24). Twenty four h after seeding the cells in 96 well-plates, media were removed and 0.01, 0.1 and 1 mg/mL of PLGA or PEG₂PLA₂₀ nanoparticles, redispersed in cell culture medium, were added. After 4 h of incubation at standard conditions, the cell culture medium was removed, and cells were washed once with PBS (pH=7.2). Afterwards, 200 µL of a MTT in PBS solution was added to each well (final concentration of 0.4 mg/mL), and cultures were again incubated for 4 h under the same conditions. Thereafter, the supernatant was carefully aspirated, and a solution of sodium dodecyl sulphate (10% in PBS) was added for cell lysis. For the dissolution of the precipitated formazan crystals, the well-plates were stored over 24 h at room temperature under exclusion of light. Subsequently, quantitative formazan concentration was determined by measuring the optical density at 550 nm with a background correction at 630 nm using an automatic microplate reader (TiterTek Plus, Germany). The water-soluble MTT is only converted into an insoluble formazan dye by the mitochondrial dehydrogenase by living cells (25). Cytotoxicity is expressed as cell viability of the treated cells relative to the untreated ones (negative control). A solution of Triton X 0.5% in PBS was used as a positive control; untreated cells with medium served as a negative control, and blank values were obtained from cell-free medium.

In Vivo Imaging and Analysis

Distribution, accumulation and elimination processes were studied by measuring the fluorescence signal of the respective dye which was incorporated into the nanoparticles. All procedures of the *in vivo* experiments complied with the standards for use of animal subjects as stated in the

guideline from the animal care and use committee of Saxony Anhalt. All *in vivo* studies were performed in nude, female and male mice (Crl:SKH1-*H^h*, 25–30 g) from Charles River Lab, which have humoral and cellular immunity comparable to C57B1/6 mice (26). All mice were housed under controlled conditions (12 h light/dark schedule, 24°C).

An aliquot (2.0, 4.0, 6.0 and 6.5 mg polymer, 5% sucrose) of the freeze-dried fluorescent nanoparticles was redispersed in 1 ml of purified water and isotonised with sorbitol. Sixty μL of each sample were then slowly injected into the tail vein of non-narcotized mice. During the imaging procedure, a mixture of isoflurane/oxygen was used as anaesthesia gas with an initial flow of 4% isoflurane (3.0 L/min oxygen) and a steady-state flow of 1.8% isoflurane (1.5 L/min oxygen). All mice were placed under same conditions (stage height, mouse position, objective adjustment) on a 35°C temperature-controlled heating plate to protect them for cooling out.

All *in vivo* fluorescence imaging measurements were carried out using the MaestroTM *in vivo* fluorescence imaging system (Cambridge Research & Instrumentation, Woburn, United States) and the MaestroTM software (version 2.10) (27). A Cermax®-type 300 Watt Xenon lamp with 5600 K, a NIR excitation filter (710–760 nm) and an 800 nm long-pass emission filter were used to detect DiR. The software acquired multispectral image cubes in 10 nm steps in the spectral range between 780 and 950 nm. The exposure time was automatically set to optimum values by the software (autoexpose function). An *in vitro* reference spectrum was obtained from the aqueous dispersion of DiR-loaded nanoparticles prior to injection, and the *in vivo* reference DiR spectrum was generated 45 min after the injection by the signal from the nanoparticles accumulated in the liver. This signal was corrected by the manual compute function using the auto-fluorescence signal of an untreated mouse, which was measured under the same conditions. This auto-fluorescence signal was also set as background for all further data evaluations. This way, the received emission information could be divided (unmixed) into parts allocated to auto-fluorescence of the body and those caused by the nanoparticles (28,29). Using both spectra, grayscale images were generated from each of the respective emission spectra. These pictures were then used for the calculation of intensity weighted images using an incremental jet color profile. The software's 'compare images' function allows comparison of images taken under different conditions (*e.g.* exposure times). Therefore, all grayscale DiR images were correlated to the respective exposure times. Pixels with maximum intensities are set to dark red, and pixels with zero fluorescence to black with a gradation from red to orange, yellow, light and dark blue in between. Detection of NR was carried out with the green filter set (excitation filter: 503–555 nm, emission filter:

580 nm long-pass, acquisition setting: 550–800 nm) in 2 nm steps. Fluorescent imaging files were acquired during the first hour after injection. All other parameters accorded to the DiR measurements.

Ex Vivo Imaging and Analysis

For *ex vivo* analysis, the mice were sacrificed using carbon dioxide 24 h after injecting the nanoparticles. Excised organs were imaged with the MaestroTM *in vivo* imaging system. To ensure reproducible conditions like the arrangement of the organs, positioning in the MaestroTM, incident angle of the light, *etc.*, the organs or respective organ parts (intestine and liver in the size of the hole) were placed into a 24-holes well-plate. The imaging procedure accorded with the *in vivo* measurements. To detect potential minor accumulation in different organs, exposure times above the autoexposed values were used. Therefore, the liver was masked with a black plastic plate to inhibit an overexposure. For further calculation and evaluation, a region of interest (ROI) in the size of the holes of the well-plate was generated, and the corresponding exposure-time weighted total and maximum fluorescence signals were calculated. To exclude the influence of different dye amounts due to varying nanoparticle concentration, the *ex vivo* total intensity value was divided through the maximum intensity of the *in vitro* emission spectra of the nanoparticles. These *in vitro* spectra were measured prior to injection, all in equal volumes and under the same measurement conditions. Afterwards, all values were normalized to 100% related to the highest fluorescence intensity.

RESULT AND DISCUSSION

Physicochemical Properties

Photon Correlation Spectroscopy (PCS)

PCS allows fast, robust and reproducible measurements of intensity weighed, hydrodynamic mean diameters of particles in the size range between about 5 nm and 2 μm . For the PEG-PLA nanoparticles, hydrodynamic diameters between 104 and 166 nm were measured (Table I and Fig. 1a). PDI values below 0.13 indicate that the nanoparticles are, compared to literature data, rather homogeneous in size (12). A higher polymer amount and the incorporation of DiR increased the particle size to about 60 nm and also slightly the PDI. PLGA nanoparticles were distinctly larger, and the high PDI (0.52) indicates inhomogeneity, which was already macroscopically visible. For the filtered (0.8 μm) dispersion, a z-average of 209 nm and a PDI of 0.15 were measured.

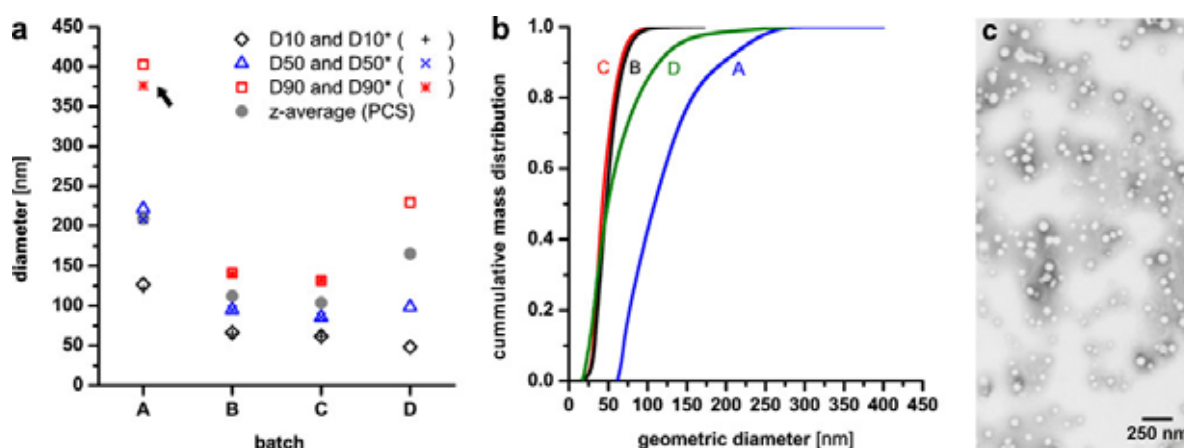


Fig. 1 (a) D10, D50 and D90 diameters determined by AF4/MALLS and PCS z-averages measured immediately after redispersion and after 3 months storage (batch **a**, **b** and **c**) at 5°C (marked with *); (b) AF4/MALLS cumulative size distributions of freshly redispersed PLGA (**a**), PEG₂PLA₂₀ (**b**), PEG₂PLA₄₀ (**c**) and PEG₂PLA₂₀ – DiR (**d**) nanoparticle suspensions. (c) TEM image of batch B nanoparticles.

Transmission Electron Microscopy (TEM)

Visualization of two nanoparticle batches was carried out by TEM of negatively stained samples (Fig. 1c). The dimensions of the nanoparticles are shown in Table I. The sizes were generally smaller than those determined by PCS (30,31) and AF4/MALLS. However, PCS determines the hydrodynamic diameter of particles, which is sensitive to the hydrated PEG chains on the surface of the nanoparticles. In contrast, dried nanoparticles were viewed in TEM, and size calculations are weighted by the number of the particles. Bigger particles are less frequent in the prepared batch than smaller ones. Furthermore, in the light scattering methods larger sample volumes are measured compared to TEM. If there are bigger particles present in the batch, they have a distinct effect to the calculation in PCS, but they will probably not be detected with TEM.

Asymmetrical Flow Field-Flow Fractionation (AF4)

AF4 combined with MALLS allows accurate size evaluation due to sample separation prior size determination (23,32). The characteristic D10, D50 and D90 diameters of the mass-weighted size distributions are shown in Table I and Fig. 1a. PCS z-averages were larger than the median (D50) determined by AF4/MALLS. This is the result of the water binding between the PEG chains on the nanoparticle surfaces as discussed above. This influences the movement of the nanoparticles during the PCS measurements and thereby the detected nanoparticle size. Due to principle of MALLS measurements, which was applied to retrieve geometrical mass weighted particle sizes (RMS radius or radius of gyration) (33), the influence of the water shell is reduced. However, overall the D50 diameters confirm the

size trend between the different nanoparticle batches measured in PCS and TEM. The larger difference between the PCS and MALLS results of batch D compared to batch B and C can probably be attributed to the higher sensitivity at both ends of the particle size distribution in the AF4/MALLS, which allows better quantification of smaller and larger particles in the sample. Size distribution was clearly broader in batch D compared to those of batch B and C (Fig. 1b). This is in good agreement with the higher PDI measured with PCS for batch D nanoparticles. The possibility of analyzing the amount of smaller and bigger particles in the dispersion is of great importance for meaningful interpretation of the *in vivo* results. The broad distribution of batch A (PLGA nanoparticles) with D90 values up to 400 nm is also visible in the cumulative size distribution (Fig. 1b), although the sample was filtered before the measurements. Due to this inhomogeneity in size as well as the absence of PEG, which would yield in higher accumulations in the RES (11,13), the PLGA nanoparticles were not studied *in vivo*.

Stability Evaluation

Potential physical instability and polymer degradation during storage in aqueous dispersion were investigated by PCS and AF4/MALLS. The results are shown in Table II. D10, D50 and D90 diameters (AF4/MALLS) are also given in Fig. 1a (marked with *). The size of both PEG-PLA nanoparticle batches stayed constant during storage. This is in accordance with literature data which has shown that such nanoparticles are comparatively stable for several months when stored at 5°C (34,35). They also reported *in vitro* studies at 37°C where they showed polymer and particle degradation within several months. This can be

Table II PCS and AF4/MALLS Particle Sizes of Freshly Dispersed Nanoparticle Batches and After Storage the Diluted Samples for 3 Month at 5°C

Batch	A ^{b)}		B		C	
	PLGA		PEG ₂ PLA ₂₀		PEG ₂ PLA ₄₀	
	fresh	3 Months	fresh	3 Months	fresh	3 Months
PCS - Z-average in nm (PDI)	209 (0.15)	207 (0.13)	113 (0.09)	113 (0.09)	104 (0.08)	103 (0.05)
MALLS D10 (nm)	127 ± 10.4	121 ± 1.7	66 ± 0.9	65 ± 1.2	62 ± 0.1	62 ± 1.1
MALLS D50 (nm)	222 ± 9.0	208 ± 1.6	95 ± 0.2	95 ± 0.4	86 ± 1.0	86 ± 0.5
MALLS D90 (nm)	403 ± 29.8	377 ± 1.7	143 ± 0.6	140 ± 0.7	132 ± 0.4	132 ± 0.3

^{a)} The numbers 2 and 20 refer to the molar mass of the polymer block (kDa)

^{b)} Sample was filtered (pore size 0.8 μm) prior measurements

assigned to possible *in vivo* behaviour and attest comparatively slow particle degradation. The high reproducibility of both PCS and AF4/MALLS results underlines the narrow distribution of the produced nanoparticle batches. The AF4/MALLS size results of (filtered) PLGA nanoparticles showed a slight decrease of the particle size, mainly in the upper size range, which may be an indication of starting polymer degradation (marked with black arrow in Fig. 1a). It has been reported that the rate of PLGA degradation is slightly increased in bigger particles, although this was more pronounced at higher temperatures (35). Overall, results indicate accurate stability of the nanoparticles in the dry state and even in aqueous dispersion, which makes them ideal for further applications.

In Vitro Cytotoxicity Assay

More than 90% of the cells were still viable after treatment with the nanoparticles in a concentration range between 0.01 and 0.1 mg/mL. This is in good accordance with literature data (36). Batch A and B (PLGA and PLA₂-PEG₂₀) nanoparticles might thus be recognized as biocompatible, which was the requirement for further *in vivo* experiments. Good biocompatibility can also be assumed for the PLA₂PEG₄₀ nanoparticles due to the similar chemical composition.

In Vivo Imaging

Dialkylcarbocyanine dyes like DiI and DiR are widely used as tracers in living and fixed tissues, cells and *in vivo* imaging experiments (37–39). The emission spectrum of the dyes is very broad, which facilitates exact detection also *in vivo*. Furthermore, they are very stable, have low bleaching properties (38) and remain fluorescent also *in vivo* for up to one year (40). Dyes with fluorescence emission in the NIR region (700–900 nm) are required for detailed *in vivo* characterizations, particularly in deeper tissues (18). Biological

tissues have a high photon absorbance of fluorescence emission light in the visible wavelength range (350–700 nm), mainly caused by hemoglobin but also in the upper infrared range (above 900 nm) due to the presence of water (41). In contrast, many tissues are optically transparent in the narrow spectral NIR area. DiR is a favorable dye with a fluorescent emission in the near infrared. Furthermore, as DiR is very lipophilic (42), it is tightly incorporated between the lipophilic PLA chains into the nanoparticles. Representative, measured *in vitro* and extracted *in vivo* emission spectra of DiR and of NR are shown in Fig. 2a. Compared with literature data, the *in vitro* emission maxima of DiR is slightly shifted bathochrom to higher wavelengths. This is caused by the cut-on of the emission filter set of the Maestro™ imaging system. Thus, for DiR the emission maximum was measured *in vitro* at about 818 nm instead of the manufacturer's and published information of about 775 nm (38). However, this effect has no influence on the results and data interpretation, since all spectral analyses were only done with the Maestro™ system and the respective *in vitro* and *in vivo* reference spectra. It is furthermore visible that the DiR emission spectra were similar *in vitro* and *in vivo*, indicating that the penetration of emitted fluorescence light through living tissue has no influence on the spectra profile, thus allowing exact detection of nanoparticles *in vivo*. In contrast, a spectral shift is visible between the *in vitro* and *in vivo* spectra when NR was incorporated into the nanoparticles (batch E, Fig. 2a). This finding can be attributed to the influence of the local polarity on the NR emission maxima. Increasing polarities result in a shift of the emission maxima to higher wavelengths and a decrease of the quantum yield. NR is nearly non-fluorescent in pure aqueous media (43).

Figures 2b and c show the images of a mouse 15 and 40 min after injection of nanoparticles loaded with NR (batch E), indicating that *in vivo* imaging of the nanoparticle distribution is in principal possible also with non-NIR dyes. However, nanoparticle accumulation in liver and spleen could not be detected due to the above-mentioned high

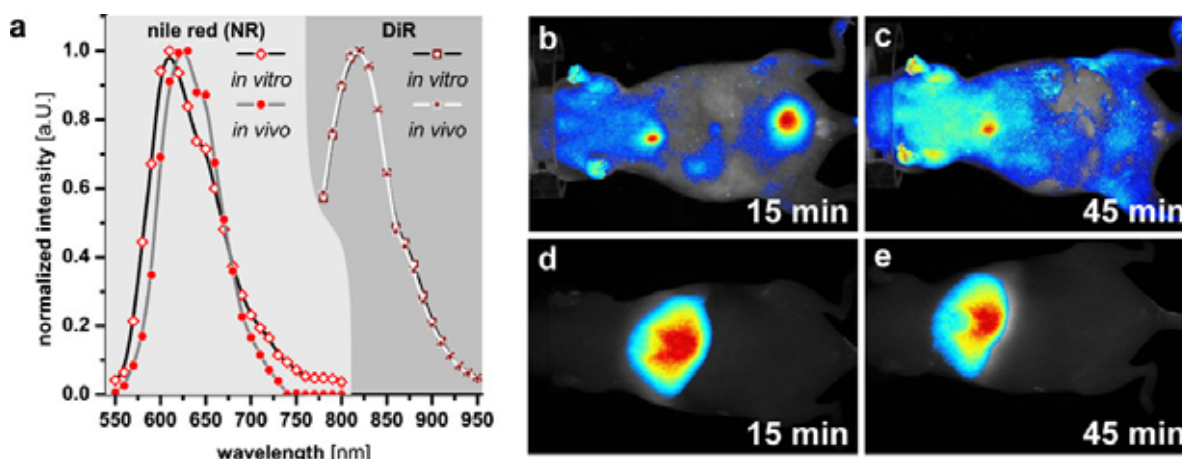


Fig. 2 (a) Normalized fluorescence *in vitro* and extracted *in vivo* emission spectra of NR and DiR. The DiR spectra are virtually overlapped. (b-e) Fluorescence intensity images of two mice 15 (b, d) and 40 min (c, e) after injecting NR (b, c) or rather DiR nanoparticles (d, e).

photon absorbance of biological tissues. Furthermore, the images agree with *in vitro* NR release studies (44) that showed a fast release of NR from the particles and elimination of the dye through the urine pathway. Due to the low log P value of NR (reported to be 3.8 (45)-5.1 (46)) compared to lipophilic carbocyanine dyes like DiR (log P values between 17.4 (42,47) and 20 (48)), NR is fast released from the particles. Although NR does not fluoresce in water (43), the dye may bind to proteins which are circulating through the blood stream, thus remaining fluorescent (49). The high fluorescence signal in the urine could be caused by binding of NR to smaller proteins, which are normally eliminated by the kidneys via the urine (50).

The very lipophilic properties of the DiR dye prevents a release from the nanoparticles. This is confirmed by other groups who showed that dialkylcarbocyanine is not or is only very slowly released from lipophilic nanocarriers (44, 51). Overall, these results confirm the expectation that for accumulation studies highly lipophilic dyes have to be incorporated to image the fate of nanoparticles in detail. The results after injecting DiR nanoparticles are shown in Fig. 2d and e. An accumulation in the bladder was not detected, as expected.

Distribution Studies

Tests about the *in vivo* fate of nanoparticles as well as the constraints of detection the distribution and accumulation were started by intravenous (i.v.) injection of batch D nanoparticle dispersions. The animals were imaged at various time points (*i.e.*, 5 min after injection, 2 days). The visualized information from the abdomen of a mouse is shown as an inverted grayscale image in Fig. 3. Black is allocated to high DiR emission intensities and white to the

background signal. Five min after injection, the blood vessels are clearly visible (Fig. 3b). During the first 6 h these vessels were still detectable, but sharpness and fluorescence

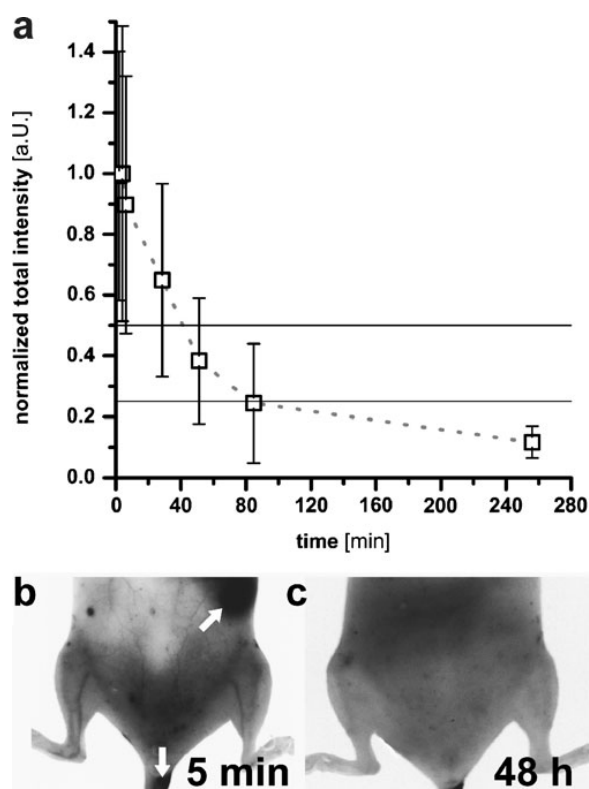


Fig. 3 (a) Normalized intensity profile of total signals from the whole body of 5 mice in dependence on time. (b and c) *In vivo* images of the DiR emission signal from the abdomen of a nude mouse. Arrows mark areas with high fluorescence intensities (spleen and tail due to injection procedure).

intensity decreased slowly. This is in agreement with literature data where the plasma half-life time of about 6 h is given (52). Furthermore, there are two black parts in the image (marked by white arrows). They point to a part of the tail as well as the spleen at the right side of the mouse. A nanoparticle accumulation in the tail can be assigned to the injection procedure, where the tail is slightly fixed by hand to immobilize it. This may result in micro lesions where nanoparticles can pass the vascular wall resulting in a nanoparticle accumulation near the injection site. After 48 h (Fig. 3c), no defined fluorescent areas are identifiable anymore. All nanoparticles are eliminated or at least accumulated in RES body structures.

Due to the resolution of the CCD camera chip, analysis of the blood vessels on their own to calculate blood half-life times was not possible. Instead, the total signal of the whole body from five mice was measured at different time points (Fig. 3a). The calculated values are the sum of all subcutaneous dye signals (from blood vessels, upper parts of liver and spleen). They indicate that 50% of the initially detectable nanoparticles were eliminated after about 45 min and 75% after 95 min. However, as the blood vessels were detectable during the first 6 h, sufficient nanoparticles were still circulating. It is widely known that PLA nanoparticles without surface modification or ones which are only stabilized with poloxamer 188 have a half-life of just a few minutes (52,53). Due to the fact that PEG chains can adopt brush-like structures, they have the ability to reduce phagocytosis *in vivo* (54). The prolonged circulation due to reduced phagocytosis and opsonisation yields a subsequently reduced clearance by the reticuloendothelial system (RES). Consequently, nanoparticles are not eliminated as fast and may accumulate in, e.g., tumor tissues (1,7).

Accumulation Studies

Nanoparticle distribution and accumulation was followed in more detail by imaging the abdominal site of female mice at different time points (Fig. 4a–h). Five min after injection the whole body of the abdomen is homogeneous colored blue with some brighter blue parts in the chest (Fig. 4a), confirming that nanoparticles circulate homogeneously through the body and accumulate in the RES as a part of the immune system where the phagocytic cells are located in reticular connective tissues. After 4 h, the maximal fluorescence is visible in the area of the liver (Fig. 4b). Accumulation of the DiR nanoparticles in the spleen is also visible in the right part of the image (marked by arrow). Accumulation in the spleen could clearly be shown in the jet color images where the color is scaled to the respective image (Fig. 4e and f). Figure 4e shows the homogeneous fluorescent liver and the minor fluorescent spleen (marked

by an arrow). During the next few days, nanoparticle accumulation in the RES decreased continuously, but fluorescence was still detectable after five days (Fig. 4d). *In vitro* tests have shown that the polymer degradation strongly depends on temperature and accelerates when temperature is increased, e.g. from 5 to >25°C rapidly (34, 35). However, even at 37°C, complete polymer degradation takes still more than one month depending on the dissolution media. Therefore, it can be assumed that the nanoparticles will be also slowly disintegrated *in vivo* and can be detected in the jet color images even five days after injection (Fig. 4h).

Ex Vivo Imaging

Ex vivo studies could provide more detailed information about the nanoparticle accumulation in the different tissues. Mice were sacrificed 24 h after nanoparticle injection, and the respective organs were placed in a 24-holes well-plate (Fig. 4i). Measuring the viscera of an untreated mouse resulted in a black image without any detectable fluorescence signal as shown in Fig. 4j. This control confirms the selectivity in detecting the DiR dye using fluorescence imaging. Figure 4k shows the isolated organs. As expected, high fluorescence intensity was visible in the liver but could also be detected in small parts of the ovaries. No signals were visible in the other organs. However, after masking the liver tissue with a black plastic plate, which allowed higher exposure times, nanoparticle accumulation could also be visualized in the intestine, uterus and spleen (Fig. 4l). The absence of fluorescence in the kidneys indicates that the nanoparticles as well as the dye are not eliminated by urine. This was expected due to the highly lipophilic character of the dye and the size of the nanoparticles. Very lipophilic molecules are often eliminated by bio-conjugation in the liver and excretion via the gall into the intestine (53). Afterwards, they are excreted with the feces. This elimination route was confirmed by the detected fluorescence in the intestine in Fig. 4l.

By implementing a round region of interest (ROI) in the size of the well-plate hole (cp. Fig. 4k) measuring different parameters of each organ became possible, determining total, maximum and average signal intensities, which are related or not related to the respective exposure times. By detailed analysis of this data, quantitative information can be obtained. Maximum and total signal intensities correlated well to the exposure times and were most suitable for further calculations. The maximum intensity values allow the comparison of nanoparticle accumulation in organs differing in size. For example, a high enrichment in a part of a tissue leads to high maximum intensity values within the ROI. The total signal of the same sample, as the sum of all pixels in the ROI, would be, however, only slightly

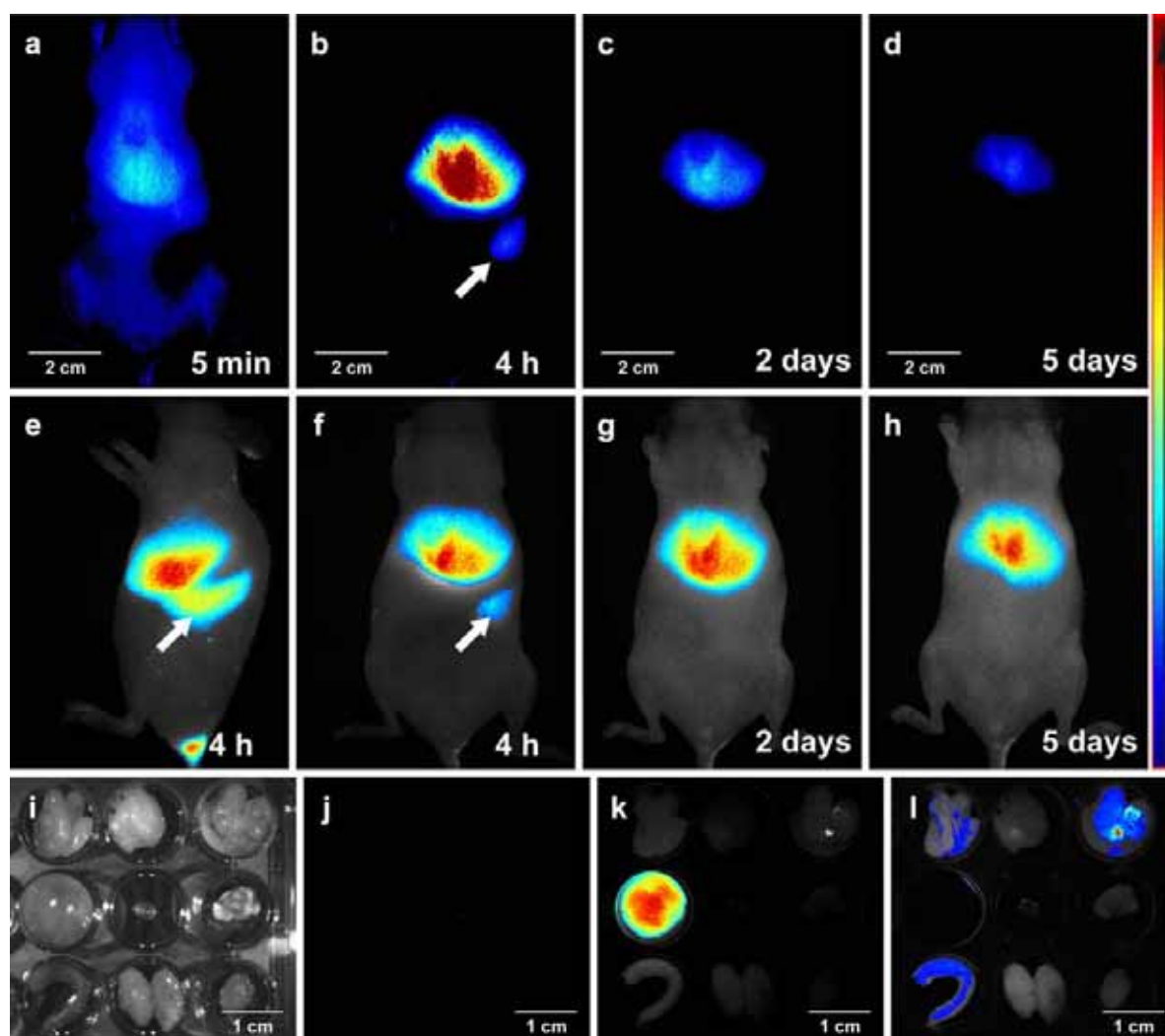


Fig. 4 (a–d) Comparative fluorescence intensity images of a nude, female mouse as chronological sequence; (e–h) jet color fluorescence intensity images of the left (e) and ventral side (f–h) of the same nude, female mouse (exposure time = 200 ms); (i–l) *ex vivo* intensity images of several organs in the following order from left to right, initiating from the top: intestine, fat, uterus with ovary, liver, gall bladder, lung, spleen, kidneys and heart; (i) original image; (j) untreated mouse and jet color intensity images 24 h after application; (k) (exposure time = 400 ms) and (l) (2000 ms exposure time and with masked liver).

increased. Nevertheless, the total signal is a value with lower variability between different measurements. The normalized maximum and total intensities from selected organs are shown in Fig. 5. Neither exposure time nor usage of the black plastic plate had an influence on the results (except the liver). Thus, potential errors caused by different exposure times which are not in the optimum range of the respective organ can be excluded, and results obtained by automatically set exposure times can be compared. It is also worth noting that the standard deviation is much larger for the maximum signal (Fig. 5b) compared to total intensity (Fig. 5a).

As shown in Fig. 5a, *ex-vivo* results confirm the nanoparticle accumulation in the RES organs liver and spleen as already detected *in vivo*. No total intensity was noticed in fat tissues and the lungs, and only slight signals were present in the intestines and in the kidneys. Overall, the same trend was found when analysing the normalized maximum intensities (Fig. 5b). Interestingly, a maximum signal of about 25% was also found in the lung. However, a distinct accumulation of the nanoparticles in the lungs appears not to be due to the standard deviation. This was very high and there was neither a signal found in the evaluation of the total signal nor in the images as shown in Fig. 4l. Other

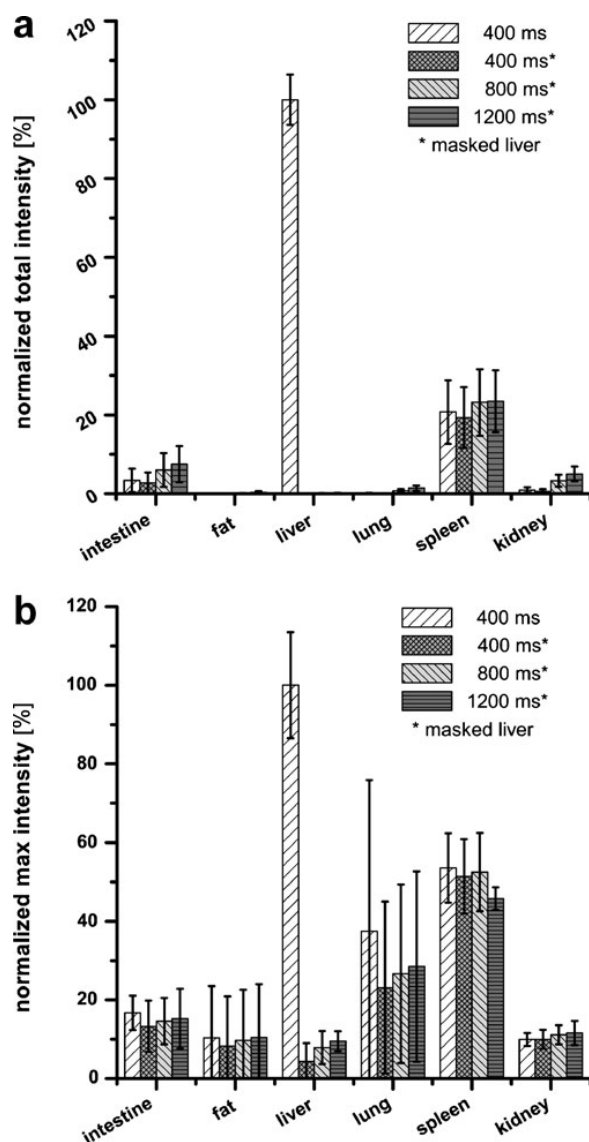


Fig. 5 Exposure time related total (a) and maximum (b) intensities from different organs measured with different exposure times ($n=4$).

viscera like fat tissue and kidneys showed maximum intensity levels of 10% or less, which is in the same range of the masked liver values. This can be attributed to the detection limits using the maximum intensity values. Intensities of about 15% were found in the intestine, confirming the image results (Fig. 4l) as well as the calculated total intensity (Fig. 5a). The different fluorescence ratios (liver to spleen) of about 5:1 for the total signal and 2:1 for the maximum are due to differences in the size of the organs. The spleen is much smaller than the liver.

The influence of the nanoparticle concentration on their biodistribution is shown in Fig. 6. These experiments were carried out to evaluate the influence of varying nanoparticle amounts on the accumulation behaviour and to determine the detection limits for imaging. The injection of 60 μ L with a nanoparticle concentration of 2.0 mg/mL (injected mass 0.12 mg) did not allow meaningful data analysis due to the too low fluorescence intensity. The range between 4.0 and 6.5 mg/mL (injected mass between 0.24 and 0.39 mg) yielded reproducible results with an average variation of about 15% or less. The total signals were independent of the sex of the mice. However, the age of the mice may be an important factor: Total signals in the spleen were higher in the mice that were three times older (Fig. 6), probably due to the increase in organ size with age. Age dependence was not observed in the liver signal, but this organ is bigger than the hole of the well plate, and only a part of the liver (similar in size for all mice) was studied.

CONCLUSION

This work demonstrates the preparation, characterization and application of PEG-PLA block polymer nanoparticles with defined sizes and narrow size distribution. To prolong the *in vivo* circulation time, PEG with an average molecular weight of 2000 was covalently bound to PLA,

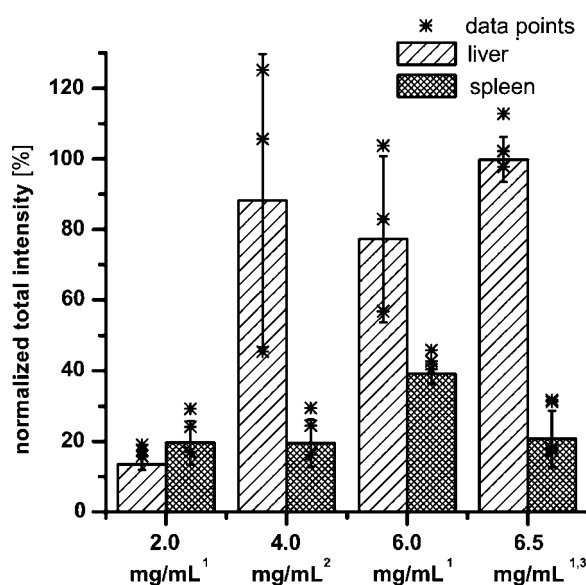


Fig. 6 Normalized total ex vivo intensities of different batch D nanoparticle injection concentrations: 2.0, 4.0, 6.0 and 6.5 mg per 1 mL with an age of 3, 3, 9 and 3 months from the left (¹=female, ²=male; $n=3$, ³ $n=4$).

and nanoparticles composed of PEG-PLA block copolymers could be prepared. Nanoparticles were lyophilized to assure long-term stability, but even the aqueous dispersions were stable over at least three months when stored at 5°C. PEG-PLA nanoparticles were biocompatible and non-toxic to CHO and L929 cells, and detailed particle size characterization by PCS, AF4/MALLS and TEM provided accurate size information. AF4/MALLS results showed that even in batches with rather low polydispersity indices (PCS z-average=166 nm, PDI=0.13, batch D), 10% of the nanoparticles were smaller than 48 nm (D10) and the same amount larger than 230 nm (D90). This confirms the need to combine different size measurement techniques for detailed particle size characterization as consumption for size-dependent biodistribution studies and underlines the necessity of preparing and characterizing homogeneous nanoparticles for further *in vivo* experiments.

First, *in vivo* experiments with NR-loaded nanoparticles indicated a fast release of the dye from the particles after injection, resulting in rapid dye elimination from the bloodstream. In contrast, incorporation of the highly hydrophobic DiR allowed direct detection of the nanoparticles in the blood stream for up to 6 h. Consequently, these nanoparticles will have sufficient time to accumulate in tumor tissue due to the EPR effect. Detailed information about nanoparticle accumulation in various organs was obtained by fluorescence imaging and measuring the total and maximum fluorescence signals in the organs *ex vivo*. Based on our results, the combination of these values and the comparison with the *in vivo* imaging data appears to be a promising approach to study nanoparticle accumulation in different organs. Furthermore a new calculation approach was described, which allows the comparison of nanoparticle batches with varying fluorescence intensities. This provides the basis for the determination of the influence of varying particle sizes on the *in vivo* fate. In the future, tumor accumulation should be studied using PEG-PLA nanoparticle batches with different sizes but narrow and well-established size distribution in two tumor models with different shapes and growth rates: the colon carcinoma (Ht29) and the ovarian carcinoma (A2780).

ACKNOWLEDGMENTS

Jörg Teßmar is acknowledged for the discussions during the polymer synthesis and nanoparticle preparation steps. We also thank also Anna Hezinger for the help with the TEM measurements and Martina Hennicke and Constanze Gottschalk for taking care of the animals. Parts of the studies were supported by grants from the Federal State of Saxony Anhalt (FKZ 3646A/0907).

REFERENCES

1. Brigger I, Dubernet C, Couvreur P. Nanoparticles in cancer therapy and diagnosis. *Adv Drug Deliv Rev.* 2002;54:631–51.
2. Peer D, Karp JM, Hong S, Farokhzad OC, Margalit R, Langer R. Nanocarriers as an emerging platform for cancer therapy. *Nature Nanotech.* 2007;2:751–60.
3. Maeda H. Tumor-selective delivery of macromolecular drugs via the EPR effect: background and future prospects. *Bioconjugate Chem.* 2010;21:797–802.
4. Yuan F, Dellian M, Fukumura D, Leunig M, Berk DA, Torchilin VP, et al. Vascular-permeability in a human tumor xenograft - molecular-size dependence and cutoff size. *Cancer Res.* 1995;55:3752–6.
5. Hobbs SK, Monsky WL, Yuan F, Roberts WG, Griffith L, Torchilin VP, et al. Regulation of transport pathways in tumor vessels: role of tumor type and microenvironment. *Proc Natl Acad Sci USA.* 1998;95:4607–12.
6. Moghimi SM, Porter CJH, Muir IS, Illum L, Davis SS. Non-phagocytic uptake of intravenously injected microspheres in rat spleen - influence of particle-size and hydrophilic coating. *Biochem Biophys Res Commun.* 1991;177:861–6.
7. Moghimi SM, Hunter AC, Murray JC. Long-circulating and target-specific nanoparticles: theory to practice. *Pharmacol Rev.* 2001;53:283–318.
8. Nakaoka R, Tabata Y, Yamaoka T, Ikada Y. Prolongation of the serum half-life period of superoxide dismutase by poly(ethylene glycol) modification. *J Controlled Release.* 1997;46:253–61.
9. Litzinger DC, Buiting AMJ, Vanrooijen N, Huang L. Effect of liposome size on the circulation time and intraorgan distribution of amphiphatic Poly(Ethylene Glycol)-Containing Liposomes. *Biochim Biophys Acta, Biomembr.* 1994;1190:99–107.
10. Liu DX, Mori A, Huang L. Role of liposome size and red blockade in controlling biodistribution and tumor uptake of Gm1-containing liposomes. *Biochim Biophys Acta.* 1992;1104:95–101.
11. Storm G, Belliot SO, Daemen T, Lasic DD. Surface modification of nanoparticles to oppose uptake by the mononuclear phagocyte system. *Adv Drug Deliv Rev.* 1995;17:31–48.
12. Gaumet M, Vargas A, Gurny R, Delie F. Nanoparticles for drug delivery: the need for precision in reporting particle size parameters. *Eur J Pharm Biopharm.* 2008;69:1–9.
13. Dunn SE, Coombes AGA, Garnett MC, Davis SS, Davies MC, Illum L. *In vitro* cell interaction and *in vivo* biodistribution of poly(lactide-co-glycolide) nanospheres surface modified by poloxamer and poloxamine copolymers. *J Controlled Release.* 1997;44:65–76.
14. Kwon GS, Kataoka K. Block-copolymer micelles as long-circulating drug vehicles. *Adv Drug Deliv Rev.* 1995;16:295–309.
15. Hezinger AFE, Tessmar J, Gopferich A. Polymer coating of quantum dots—A powerful tool toward diagnostics and sensorics. *Eur J Pharm Biopharm.* 2008;68:138–52.
16. Medintz IL, Uyeda HT, Goldman ER, Mattoussi H. Quantum dot bioconjugates for imaging, labelling and sensing. *Nature Mater.* 2005;4:435–46.
17. Smith AM, Duan HW, Mohs AM, Nie SM. Bioconjugated quantum dots for *in vivo* molecular and cellular imaging. *Adv Drug Deliv Rev.* 2008;60:1226–40.
18. Frangioni JV. *In vivo* near-infrared fluorescence imaging. *Curr Opin Chem Biol.* 2003;7:626–34.
19. Derfus AM, Chan WCW, Bhatia SN. Probing the cytotoxicity of semiconductor quantum dots. *Nano Lett.* 2004;4:11–8.
20. Lucke A, Tessmar J, Schnell E, Schmeer G, Gopferich A. Biodegradable poly(D, L-lactic acid)-poly(ethylene glycol)-monomethyl ether diblock copolymers: structures and surface properties relevant to their use as biomaterials. *Biomaterials.* 2000;21:2361–70.

21. Fessi H, Puisieux F, Devissaguet JP, Ammoury N, Benita S. Nanocapsule formation by interfacial polymer deposition following solvent displacement. *Int J Pharm.* 1989;55:R1–4.
22. Rose C. Particulate systems for Fluorescence Imaging and Drug Delivery. Thesis: University of Regensburg; 2010.
23. Kuntsche J, Klaus K, Steiniger F. Size determinations of colloidal fat emulsions: a comparative study. *J Biomed Nanotechnol.* 2009;5:384–95.
24. Westedt U, Kalinowski M, Wittmar M, Merdan T, Unger F, Fuchs J, *et al.* Poly(vinyl alcohol)-graft-poly(lactide-co-glycolide) nanoparticles for local delivery of paclitaxel for restenosis treatment. *J Controlled Release.* 2007;119:41–51.
25. Mosmann T. Rapid colorimetric assay for cellular growth and survival—Application to proliferation and cyto-toxicity assays. *J Immunol Methods.* 1983;65:55–63.
26. Schaffer BS, Grayson MH, Wortham JM, Kubicek CB, McCleish AT, Prajapati SI, *et al.* Immune competency of a hairless mouse strain for improved preclinical studies in genetically engineered mice. *Mol Cancer Ther.* 2010;9:2354–64.
27. Leblond F, Davis SC, Valdes PA, Pogue BW. Pre-clinical whole-body fluorescence imaging: review of instruments, methods and applications. *J Photoch Photobio B.* 2010;98:77–94.
28. Mansfield JR, Gossage KW, Hoyt CC, Levenson RM. Autofluorescence removal, multiplexing, and automated analysis methods for *in-vivo* fluorescence imaging. *J Biomed Opt.* 2005;10.
29. Zimmermann T, Rietdorf J, Pepperkok R. Spectral imaging and its applications in live cell microscopy. *FEBS Lett.* 2003;546:87–92.
30. Cheng FY, Wang SPH, Su CH, Tsai TL, Wu PC, Shieh DB, *et al.* Stabilizer-free poly(lactide-co-glycolide) nanoparticles for multimodal biomedical probes. *Biomaterials.* 2008;29:2104–12.
31. Putaux JL, Buleon A, Borsali R, Chanzy H. Ultrastructural aspects of phytylglucosylated cryo-transmission electron microscopy and quasi-elastic light scattering data. *Int J Biol Macromol.* 1999;26:145–50.
32. Lohrke J, Briel A, Mader K. Characterization of superparamagnetic iron oxide nanoparticles by asymmetrical flow-field-flow-fractionation. *Nanomedicine.* 2008;3:437–52.
33. Stauch O, Schubert R, Savin G, Burchard W. Structure of artificial cytoskeleton containing liposomes in aqueous solution studied by static and dynamic light scattering. *Biomacromolecules.* 2002;3:565–78.
34. Coffin MD, McGinity JW. Biodegradable pseudolatexes—the chemical-stability of Poly(D, L-Lactide) and poly (Epsilon-Caprolactone) nanoparticles in aqueous-media. *Pharm Res.* 1992;9:200–5.
35. Dunne M, Corrigan OI, Ramtoola Z. Influence of particle size and dissolution conditions on the degradation properties of polylactide-co-glycolide particles. *Biomaterials.* 2000;21:1659–68.
36. Lin WJ, Chen YC, Lin CC, Chen CF, Chen JW. Characterization of pegylated copolymeric micelles and *in vivo* pharmacokinetics and biodistribution studies. *J Biomed Mater Res Part B.* 2006;77B:188–94.
37. Honig MG, Hume RI. Fluorescent carbocyanine dyes allow living neurons of identified origin to be studied in long-term cultures. *J Cell Biol.* 1986;103:171–87.
38. Texier I, Goutayer M, Da Silva A, Guyon L, Djaker N, Jossierand V, *et al.* Cyanine-loaded lipid nanoparticles for improved *in vivo* fluorescence imaging. *J Biomed Opt.* 2009;14.
39. Chen J, Corbin IR, Li H, Cao WG, Glickson JD, Zheng G. Ligand conjugated low-density lipoprotein nanoparticles for enhanced optical cancer imaging *in vivo*. *J Am Chem Soc.* 2007;129:5798.
40. Kuffler DP. Long-term survival and sprouting in culture by motoneurons isolated from the spinal-cord of adult frogs. *J Comp Neurol.* 1990;302:729–38.
41. Weissleder R. A clearer vision for *in vivo* imaging. *Nat Biotechnol.* 2001;19:316–7.
42. Hardin J. Confocal and multi-photon imaging of living embryos. In Pawley JB, Masters BR, editors. *Handbook of biological confocal microscopy.* J Biomed Opt. 2008;760.
43. Jores K, Haberland A, Wartewig S, Mader K, Mehnert W. Solid lipid nanoparticles (SLN) and oil-loaded SLN studied by spectrofluorometry and raman spectroscopy. *Pharm Res.* 2005;22:1887–97.
44. Petersen S, Fahr A, Bunjes H. Flow cytometry as a new approach to investigate drug transfer between lipid particles. *Mol Pharmaceutics.* 2010;7:350–63.
45. N.n. Public Chemical Database. Public Chemical Database. 2010.
46. Greenspan P, Mayer EP, Fowler SD. Nile red—A selective fluorescent stain for intracellular lipid droplets. *J Cell Biol.* 1985;100:965–73.
47. Rashid F, Horobin RW, Williams MA. Predicting the behaviour and selectivity of fluorescent probes for lysosomes and related structures by means of structure-activity models. *Histochem J.* 1991;23:450–9.
48. Rashid F, Horobin RW. Interaction of molecular probes with living cells and tissues.2. A structure-activity analysis of mitochondrial staining by cationic probes, and a discussion of the synergistic nature of image-based and biochemical approaches. *Histochem Cell Biol.* 1990;94:303–8.
49. Ivanov AI, Gavrilov VB, Furmanchuk DA, Aleinikova O, Konev SV, Kaler GV. Fluorescent probing of the ligand-binding ability of blood plasma in the acute-phase response. *Clin Exp Med.* 2002;2:147–55.
50. Gordon S, Tee RD, Taylor AJN. Analysis of rat urine proteins and allergens by sodium Dodecyl-Sulfate Polyacrylamide-Gel electrophoresis and immunoblotting. *J Allergy Clin Immun.* 1993;92:298–305.
51. Lim HJ, Parr MJ, Masin D, McIntosh NL, Madden TD, Zhang GY, *et al.* Kupffer cells do not play a role in governing the efficacy of liposomal mitoxantrone used to treat a tumor model designed to assess drug delivery to liver. *Clin Cancer Res.* 2000;6:4449–60.
52. Bazile D, Prudhomme C, Bassoullet MT, Marlard M, Spenlehauer G, Veillard M. Stealth Me.Peg-Pla nanoparticles avoid uptake by the mononuclear phagocytes system. *J Pharm Sci.* 1995;84:493–8.
53. Verrecchia T, Spenlehauer G, Bazile DV, Murrybrelie A, Archimbaud Y, Veillard M. Non-stealth (Poly(Lactic Acid Albumin)) and stealth (Poly(Lactic Acid-Polyethylene Glycol)) nanoparticles as injectable drug carriers. *J Controlled Release.* 1995;36:49–61.
54. Gref R, Miralles G, Dellacherie E. Polyoxyethylene-coated nanoparticles: effect of coating on zeta potential and phagocytosis. *Polym Int.* 1999;48:251–6.

Tumor Accumulation of NIR Fluorescent PEG–PLA Nanoparticles: Impact of Particle Size and Human Xenograft Tumor Model

Andreas Schädlich,[†] Henrike Caysa,^{†,*} Thomas Mueller,[‡] Frederike Tenambergen,[†] Cornelia Rose,[§] Achim Göpferich,[§] Judith Kuntsche,[†] and Karsten Mäder^{†,*}

[†]Department of Pharmaceutical Technology and Biopharmaceutics, and [‡]Department of Internal Medicine IV, Oncology/Hematology, Martin Luther University Halle-Wittenberg, Wolfgang-Langenbeck-Strasse 4, 06120 Halle (Saale), Germany, and [§]University of Regensburg, Department of Pharmaceutical Technology, Universitätsstrasse 31, 93053 Regensburg, Germany

Unfortunately, a high percentage of potent drug candidates for anticancer therapy are poorly soluble in water.^{1,2} Many of them possess a polycyclic structure which enhances the ability of the molecules to reach cellular targets.³ Owing to their hydrophobic characteristics many of these therapeutic agents never enter the formulation development stage.¹ This remains one of the main challenges in future anticancer chemotherapy. Nanoparticles with a hydrophobic matrix provide an excellent possibility for the formulation of such poorly water-soluble drugs. The biodegradable and biocompatible polyesters poly(lactide) (PLA) and poly(lactide-co-glycolide) (PLGA) are frequently used for this purpose and are approved in several market products for parenteral application by the FDA.⁴ PLA is more hydrophobic as compared to PLGA. Therefore, PLA nanoparticles can homogeneously incorporate very lipophilic drugs in their core. After intravenous (i.v.) application and possible accumulation into tumor tissue the slow degradation of PLA^{5,6} provides a continuous release of the drug at the place of its action. Such nanoparticles thus present an interesting approach for a convenient therapy with extended drug administrations. However, the nanoparticles have to reach and accumulate in tumor tissues where the drug is needed. Both steps, transport *via* the bloodstream as well as tumor enrichment are triggered by two main parameters, the particle size and the surface properties of the nanoparticles.

It is well established that flexible hydrophilic surfaces like polyethylene glycol (PEG) have the ability to extend circulation time

ABSTRACT Cancer therapies are often terminated due to serious side effects of the drugs. The cause is the nonspecific distribution of chemotherapeutic agents to both cancerous and normal cells. Therefore, drug carriers which deliver their toxic cargo specific to cancer cells are needed. Size is one key parameter for the nanoparticle accumulation in tumor tissues. In the present study the influence of the size of biodegradable nanoparticles was investigated in detail, combining *in vivo* and *ex vivo* analysis with comprehensive particle size characterizations. Polyethylene glycol–polyesters poly(lactide) block polymers were synthesized and used for the production of three defined, stable, and nontoxic near-infrared (NIR) dye-loaded nanoparticle batches. Size analysis based on asymmetrical field flow fractionation coupled with multiangle laser light scattering and photon correlation spectroscopy (PCS) revealed narrow size distribution and permitted accurate size evaluations. Furthermore, this study demonstrates the constraints of particle size data only obtained by PCS. By the multispectral analysis of the Maestro *in vivo* imaging system the *in vivo* fate of the nanoparticles next to their accumulation in special red fluorescent DsRed2 expressing HT29 xenografts could be followed. This simultaneous imaging in addition to confocal microscopy studies revealed information about the accumulation characteristics of nanoparticles inside the tumor tissues. This knowledge was further combined with extended size-dependent fluorescence imaging studies at two different xenograft tumor types, the HT29 (colorectal carcinoma) and the A2780 (ovarian carcinoma) cell lines. The combination of two different size measurement methods allowed the characterization of the dependence of nanoparticle accumulation in the tumor on even rather small differences in the nanoparticle size. While two nanoparticle batches (111 and 141 nm in diameter) accumulated efficiently in the human xenograft tumor tissue, the slightly bigger nanoparticles (diameter 166 nm) were rapidly eliminated by the liver.

KEYWORDS: *in vivo* imaging · fluorescence imaging · AF4 · PEG–PLA · nanoparticle · HT29 · A2780

and retention half-life of nanoparticles as they reduce opsonisation and the subsequent clearance by the mononuclear phagocytic system (MPS) also known as reticuloendothelial system (RES). The RES has been shown to be the major barrier for an effective tumor targeting using nanoparticles.⁷ Thereby, mainly the Kupffer cells of the liver

* Address correspondence to karsten.maeder@pharmazie.uni-halle.de.

Received for review July 14, 2011 and accepted October 3, 2011.

Published online October 03, 2011 10.1021/nn2026353

© 2011 American Chemical Society

as well as the macrophages of the spleen have been identified to be responsible for the rapid clearance of nanocarriers from the bloodstream.^{7,8} Tumor tissue is often characterized by a leaky vasculature with an enhanced permeability.^{7,9} Intravenously injected nanoparticles can accumulate by passive diffusion due to this hyper-permeable tumor vasculature. This retention of nanoparticles in the tumor tissue is called EPR (enhanced permeability and retention) effect.¹⁰ Individual molecules like drugs and dyes are transported through the bloodstream for only a few minutes up to 1 h until they are eliminated rapidly. In contrast, properly designed, nanoparticles can reach much longer circulation times and have the ability to be retained in tumor tissues due to the EPR effect. It has been shown that the upper size limit for extravasation into solid tumors is about 400 nm.¹¹ Other groups showed that particles with diameters <200 nm accumulate even more effectively than bigger ones.^{9,12,13} This can be explained by an increased nanoparticle uptake by the RES in the size range between 150 and 300 nm.¹⁴ A lower size limit based on size is difficult to define due to further influencing parameters like structure, surface charge, and molecular-flexibility.¹⁵ Studies have shown that the size limit for renal excretion of proteins and water-soluble polymers is approximately 45 kDa (hydrodynamic diameters <8 nm), depending on the particle size, shape, density, and the surface charge.^{15–18} It is furthermore known, that also liposomes which are smaller than 70 nm are faster cleared from the bloodstream than larger ones.^{19,20} This is the effect of extravasation and accumulation in the parenchymal cells of the liver.²⁰ On the basis of this knowledge and of other reports, the optimum nanoparticle size for tumor accumulation is between about 70 and 200 nm.²¹ This rather narrow size range clarifies the necessity of the preparation of nanoparticle formulations with well-defined and characterized sizes and sufficiently narrow size distributions. Only some few publications discuss nanoparticle-dependent tumor accumulation and *in vivo* biodistribution, however, based on particle batches with polydispersity indexes (PDI) between 0.2 and 0.5.^{22,23} Because of the broad particle size distribution in these studies, information about the *in vivo* fate can only be drawn with care. This again underlines the necessity to control the size of the nanoparticles during preparation. In addition, reliable and appropriate size determinations using different size measurement techniques are necessary as the basis for meaningful interpretation of *in vivo* data.²⁴

The aim of the present work was to investigate the *in vivo* fate and tumor accumulation of three PEG₂-PLA₂₀ or PEG₂-PLA₄₀ (numbers in kDa) nanoparticle formulations with different and defined sizes. Storage stability, homogeneity after redispersing, and sufficient stability in aqueous media as well as high

biocompatibility were already established, and the results evidenced the high potential of these nanoparticles as drug delivery systems.²⁵ In addition, nanoparticle sizes were studied in detail using asymmetrical field flow fractionation (AF4) coupled with multi-angle laser light scattering (MALLS) and photon correlation spectroscopy (PCS). These size evaluations were the main requirement to correlate the influence of particle size on the *in vivo* distribution, studied by near-infrared (NIR) fluorescence imaging.²⁵ This imaging technique provided a noninvasive monitoring modality with high temporal resolution also in deep tissues.²⁶ Fluorescence imaging, especially the Maestro *in vivo* imaging system allowed the detection of multispectral emission curves and also the exclusion of the autofluorescence from the mice.^{25,27} Hence, contemporaneous imaging analysis of fluorescent tumors, dyed nanoparticles and autofluorescence of the mice was possible.

In the present study, tumor accumulation of PEG–PLA nanoparticles differing in size was evaluated on two different xenograft tumor types simultaneously to improve the understanding of the *in vivo* nanoparticle tumor targeting capacity. Xenograft tumors derived from the HT29 colon carcinoma cell line and the A2780 ovarian carcinoma cell line were selected due to their differences in structural shape and growth.

To the best of our knowledge, it is the first time that the influence of size of narrow distributed nanoparticle batches were studied in detail using AF4/MALLS as well as PCS and combined with extensive biodistribution studies. The results of this study provide information about the influence of the particle size on the *in vivo* fate and tumor accumulation behavior of PEG–PLA nanoparticles up to the cellular level. This study serves as the basis for further nanoparticle applications to enhance the therapeutic activity and safety of chemotherapeutic agents.

RESULTS AND DISCUSSION

Nanoparticle Preparation. By variation of the polymer concentration in a fixed volume of the organic solvent, the particle size of the nanoparticles can be controlled. Higher polymer concentrations lead to increased particle sizes. On the other hand, the ratio of the external aqueous phase or the amount of the polymer solution (at fixed polymer concentration) had nearly no effect on the size of the produced nanoparticles.²⁸ On the basis of this knowledge, different amounts of PEG–PLA were used to produce three batches of DiR-loaded nanoparticles with different sizes (Table 1). One unloaded batch was produced for extended size characterizations (batch D). Previous studies on the physical stability and polymer degradation attested the nanoparticles to be stable in the dried state for more than 6 months. The nanoparticles were even

TABLE 1. Nanoparticle Compositions and Particle Sizes of Freshly Dissolved Nanoparticle Batches

batch polymer ^a	A, PEG ₂ PLA ₂₀	B, PEG ₂ PLA ₄₀	C, PEG ₂ PLA ₄₀ ^d
DiR loading ^b	0.5%	1%	1%
polymer concentration ^c	0.75%	1%	2%
PCS, z-average in nm (PDI)	111 ± 2 (0.16)	141 ± 1 (0.13)	166 ± 2 (0.13)
MALLS D10 (nm)	36 ± 2	40 ± 1	48 ± 10
MALLS D50 (nm)	43 ± 2	64 ± 1	99 ± 4
MALLS D90 (nm)	80 ± 3	153 ± 1	230 ± 2
fluorescence intensity	~ 32	~ 100	~ 76

^a The number 2, 20, and 40 refers to the molar mass of the polymer block (kDa).

^b Dye loading in percent related to the polymer amount. ^c Polymer concentration in percent related to the organic solvent. ^d Data is based on previously shown results.²⁵

stable in aqueous dispersion for up to 3 months when stored in the refrigerator at about 5 °C, and no agglomeration or degradation was observed.²⁵ These findings are in good accordance with literature data.^{29,30}

Physicochemical Properties. Fluorescence Spectroscopy. Fluorescence intensities of the different nanoparticle batches are shown in Table 1. Lowest intensities were measured for batch A nanoparticles due to the lower DiR-load of these nanoparticles. Batch B showed highest fluorescence intensities indicating high incorporated dye amounts. The intensity of batch C was in between where the dye loading was decreased due to the higher amount of polymer.

Photon Correlation Spectroscopy (PCS). The hydrodynamic mean particle diameters (z-averages) are presented in Table 1. The results confirmed the production of nanoparticles with different sizes. The size range was between 111 nm (batch A) and 166 nm (batch C), hence within the size range which is reported to be ideal for cancer treatment (70–200 nm).²¹ All PDI values were between 0.13 and 0.16 indicating an overall narrow particle size distribution.

Asymmetrical Flow Field Flow Fractionation (AF4). AF4/MALLS measurements allowed an accurate determination of size distributions due to the fractionation step prior to size determination.^{31,32} The calculated D10, D50, and D90 diameters of all three batches are shown in Table 1. The D50-diameters (median) were considerably smaller compared to the PCS z-averages. This was caused by geometrical mass weighed particle sizing in AF4 measurement which reduced the influence of the water shell and the presence of minor amounts of larger particles in all batches. All three nanoparticle batches had small fractions of larger particles (>200 nm) but no particles with diameters larger than 600 nm could be detected.

Nevertheless, the LS detector signals over the whole elution time as well as the corresponding cumulative mass distributions (Figure 1) confirmed the overall narrow size distribution of the nanoparticle batches. The analysis of batch A indicated that the predominant fraction of nanoparticles was in the size

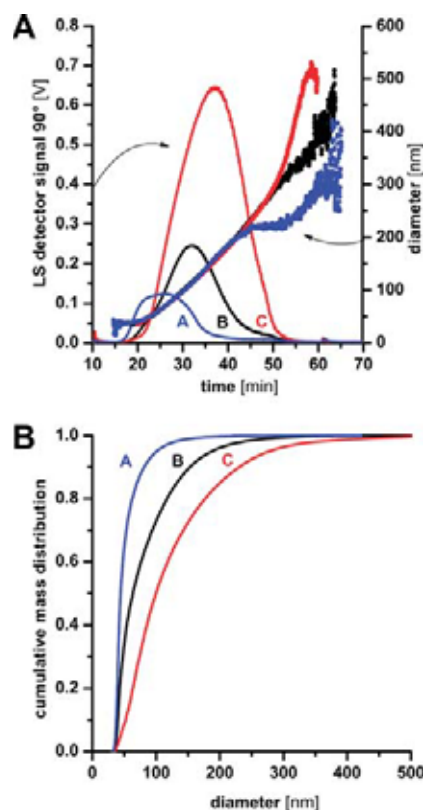


Figure 1. (A) AF4/MALLS elution profiles (light scattering signal at 90°) and corresponding diameters of the nanoparticle dispersions (arrows indicate the assignment). (B) Cumulative mass weighted size distributions of PEG–PLA nanoparticles, determined by AF4/MALLS.

range between 36 and 80 nm. Only less than 10% were larger than 100 nm (Table 1). Size distribution was broadest for batch C. The amount of nanoparticles which was smaller than 48 nm was similar to that with sizes larger than 230 nm. The results indicated that PCS z-averages are mainly influenced by larger particles. This underlined the advantages of AF4 to get more detailed information of the nanoparticle size distribution which has a major influence to possible *in vivo* behavior.

Nanoparticle Stability in FBS and PBS Containing Media. The PCS and AF4 measurements were extended to investigate the influence of physiological conditions to the particle size distribution (Table 2). The z-average in water was determined to be 112 nm with a PDI of 0.08 indicating an even narrower distribution than that of the loaded nanoparticles. Consequently, the D50 value of 100 nm based on the AF4 results was comparable to the PCS result. The difference of 12 nm can be attributed to the water binding between the PEG chains, which influence the movement of the particles in the PCS measurement. The addition of PBS had no influence on the z-average although the

TABLE 2. Particle Size of PEG₂PLA₄₀ Nanoparticles in Different Dispersing Media

	PCS, z-average in nm (PDI)	MALLS D10 in nm	MALLS D50 in nm	MALLS D90 in nm
water	112.0 (0.08)	69	100	150
water (10% PBS) ^a	112.3 (0.10)			
water (10% FBS) ^a	91.1 (0.29)	71	101	151
water (10% FBS, 10% PBS) ^a	90.8 (0.30)			
water (50% FBS) ^a		68	101	151

^a Particle sizes were determined 24 h after incubation.

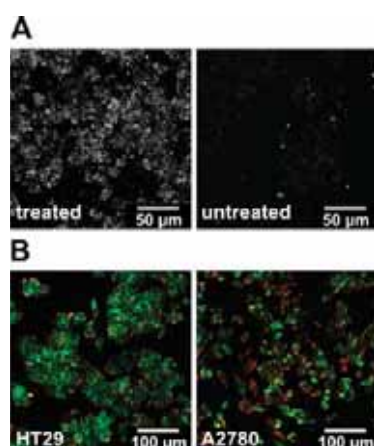


Figure 2. (A) Grayscale intensity confocal microscopic images of HT29 tumor cells (incubated with batch A and untreated). (B) Carcinoma cells, incubated with batch A nanoparticles (red) and stained by membrane dye DiO (green).

PDI was slightly increased (0.10). Measurements in FBS containing media yielded in z-averages of 91.1 and 90.8 nm with PDI values of 0.29 and 0.30 (Table 2). The increase of the PDI values and the reduced particle size is caused by the proteins in the serum (mainly albumin, high- and low-density lipoproteins) which influenced the PCS measurements. This is not the case in the AF4 measurements where the sample is fractionized prior to size determination. The measured D10, D50, and D90 values in FBS containing media are in the same range as in measurements of the samples dispersed in pure water. The results indicate that the nanoparticles are stable also in physiological media.

Cellular Confocal Microscopy Studies. On the basis of reported size-dependent nanoparticle adsorption and uptake by cells,³³ smaller particles should be more suitable to study the nanoparticle behavior on the cellular level. Therefore, cell experiments were performed using the smallest nanoparticles (batch A). First tests were carried out with unstained HT29 cells, the same cell line as used for further *in vivo* experiments. The images of treated and untreated cells are given exemplarily as grayscale intensity images in Figure 2A

with clear differences in the fluorescence intensities. The results indicate that the nanoparticles have the ability to bind to or to accumulate in the cells. On the basis of these experiments, the tests were repeated using both A2780 cells, the second cell line used *in vivo*, and HT29 cells. Cell membranes were stained with DiO for better localization of fluorescent nanoparticles. Overall, the results indicate that the nanoparticles were mainly bounded to the cell membranes in both cell lines but with a higher association tendency to A2780 tumor cells (Figure 2B). This might be caused by the PEG shell which inhibits the nanoparticle uptake into the cells.³⁴ But it has to be kept in mind that PEG is necessary to circumvent nanoparticle recognition by the RES. If they are fast eliminated by the liver they will not reach tumor tissues and *in vitro* observed nanoparticle uptake will fail *in vivo*. But even nanoparticles, which stick on the surface, will slowly be eroded and degraded. Thereby, the dyes or drugs will be released and diffuse into the cells effectively.

In Vivo Accumulation Studies in DsRed2 Fluorescent HT29 Tumors. Nanoparticle accumulation was studied in male nude mice bearing two subcutaneous (s.c.) HT29 xenograft tumors, one on each flank. For clear visualization of nanoparticle accumulation in the tumor tissue and normal nanoparticle distribution within the body, DsRed2 expressing HT29 cells were used. This allowed multispectral *in vivo* imaging of dyed NIR nanoparticles (red) and the fluorescent tumor cells (green) simultaneously (Figure 3A). At 10 min after i.v. application of NIR fluorescent nanoparticles high fluorescence intensities were detected in the s.c. blood vessels in the abdominal area. Also the blood vessels above both tumor grafts (green fluorescence) were well visible. The intensity of the circulating particles decreased continuously with time after injection and were detectable in the blood vessels for about 6 h. Afterward the intensity fell below the detection limit of the fluorescence imager.²⁵

The scaled intensity images (Figure 3B) were obtained by using the “compare imaging” function of the extracted DiR signal. This allowed time dependent visualization of nanoparticle accumulation in tumor tissues. Different measurement conditions like varying exposure times were recomputed by the software and all four images were displayed in relation to each other.

The big blood vessels under the skin were well visible within the first minutes after injection (Figure 3B). Already 3 h later there was a clear accumulation in the area of the tumor accompanied by a simultaneously decreased intensity in other parts of the body. The enrichment within the HT29 tumors increased distinctly up to 24 h (Figure 3B). This was probably caused by the EPR effect by what the passive accumulation of nanocarriers occurs after a single application during the first 24 h.^{35,36} After 48 h the DiR intensity in the tumor decreased continuously but remained visible

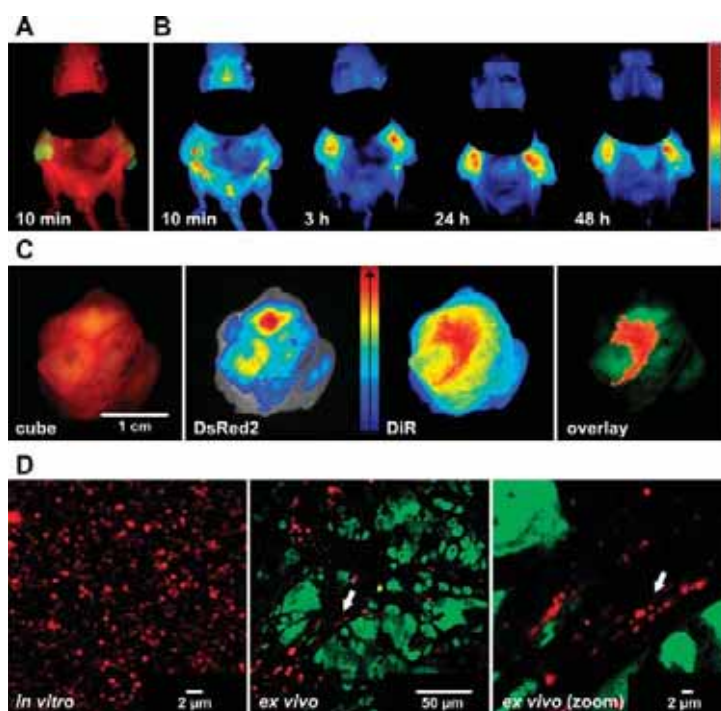


Figure 3. (A) Unmixed fluorescence image (DiR signal = red, DsRed2 = green) of a mouse bearing 2 DsRed2 expressing HT29 xenograft tumors (left and right). (B) Time-dependent intensity images (isolated DiR signal) of the same mouse. The area of the liver was masked. (C) *Ex vivo* fluorescence images of a DsRed2 fluorescent HT29 colon carcinoma (from left to right: raw image, intensity weighted jet color image of the extracted DsRed2 and DiR signal, overlay of high intensity DiR parts and in green displayed DsRed2 areas). (D) Confocal microscopic images: *in vitro* DiR nanoparticle dispersion and *ex vivo* images, DsRed2 tumor cells in green with accumulated DiR nanoparticles in red (same areas are marked by an arrow).

over several days as shown exemplarily in Figure 3B. This result is in agreement with the understanding of the EPR effect.¹⁰ Owing to polymer degradation at 37 °C which is reported to take *in vitro* more than 1 month^{29,30} we expect a continued long-term release of the dye from the nanoparticles.

Ex Vivo Accumulation Studies in DsRed2 Fluorescent HT29 Tumors. A DsRed2 fluorescent tumor bearing mouse was sacrificed 48 h after nanoparticle injection (Figure 3B). The tumor was imaged *ex vivo* using the Maestro (Figure 3C). Analyzing the cube to assign DiR and DsRed2 signals allowed the generation of respective corresponding jet color intensity images. The DsRed2 image (Figure 3C) revealed clusters with high fluorescence intensity of DsRed2 expressed cell clusters. DiR jet color image in Figure 3C illustrated the fluorescent areas where DiR nanoparticles accumulated. Highest concentrations were located between DsRed2 expressing cells. This was confirmed by the overlay image (Figure 3C). The highest threshold values of the DiR signal were displayed red, and this information was afterward overlaid on the green displayed DsRed2 areas.

After *ex vivo* imaging a sliced tumor part was analyzed by confocal microscopy. By this, the detection of NIR fluorescent nanoparticles in addition to the

DsRed2 expressing tumor cells was possible. Figure 3D shows the plain-imaged nanoparticle suspension for comparison. The red-appearing DiR-loaded nanoparticles were homogeneously distributed and scaled in the nanometer size range. Compared to the size results obtained by PCS and AF4/MALLS, the particles appeared bigger due to also laterally emitted fluorescence light. Examination of the sliced tumor tissue (Figure 3D) allowed visualization of the PEG–PLA nanoparticles (red spots) between the xenograft tumor cells (green). Most nanoparticles were located in non-DsRed2 fluorescent, channel-like areas. These consist either of necrotic tumor tissue or of nonfluorescent mouse cells. On the basis of additional performed hematoxylin and eosin (H&E) analyses, an accumulation of nanoparticles mainly in necrotic/fibrotic tumor tissue was proven.

In Vivo Fluorescence Imaging Studies. Nonfluorescent HT29 and A2780 cell lines were used as xenograft models to evaluate tumor accumulation dependent on the nanoparticle size. The HT29 tumors are characterized by their bright and firm shape; they grow slower than A2780 tumors and generally contain large central necrotic/fibrotic areas which are surrounded by peripherally arranged vital tumor cells.³⁷ The A2780 tumors grow faster and are highly vascularized. Their

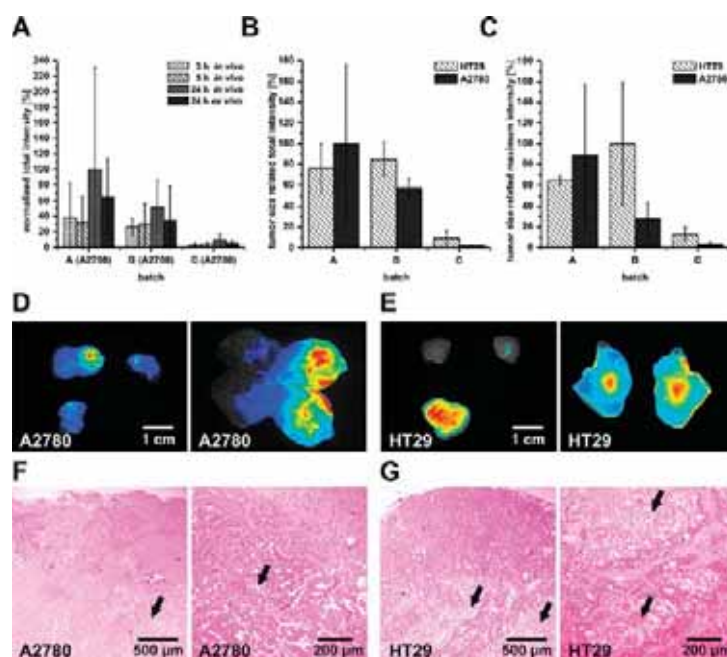


Figure 4. Normalized total fluorescence intensity amounts (A, B) and maximum intensities (C). (A) Time-dependent nanoparticle accumulation in A2780 tumors, *in vivo* measured compared to 24 *ex vivo* results. (B and C) Tumor size related fluorescence intensities of HT29 and A2780 tumor accumulation values, 24 h after *i.v.* injection, measured *ex vivo* (SD, $n = 3$). (D and E) *Ex vivo* fluorescence images of excised (left) and sliced (right) xenograft tumors (group A, 24 h after *i.v.* injection). (F and G) Light microscopic images of excised and sliced xenograft tumor tissues (H&E stained). Arrows point to blood vessels (F) and central necrotic areas (G).

blue color attests a high perfusion and vascular permeability which is more than 4 times higher than that in neighboring tissues.³⁸ Owing to the smaller amount of connective tissue, A2780 tumors are more soft compared to HT29 tumors.

For direct comparison, both of these xenograft tumors were established in the same mouse, one to the right and to the other to the left side. The A2780, known as a fast growing tumor, reached in all groups average tumor sizes between 1.25 and 2.25 cm³. They were 3–6 fold bigger than the HT29 ones (0.3–0.5 cm³) and showed larger size variations within the respective group. All mice were imaged for 24 h after nanoparticle injection of batches A, B, and C (Table 1). The resulting *in vivo* images yielded overall similar nanoparticle distributions as shown in Figure 3A,B. NIR nanoparticles accumulated slowly but continuously in the tumor during the first 24 h after injection. Nanoparticle tumor accumulation was clearly detectable *in vivo* in more than 80% of the mice. However, pharmacokinetic data and tumor enrichment differences between all three nanoparticle batches could not be visualized due to the limited resolution of the fluorescence images.

Ex Vivo Fluorescence Imaging Studies. The distribution pattern inside both tumor models was further investigated by the comparison of fluorescence images of complete and sliced tumor tissues. The results of group

A are exemplarily shown in Figure 4D,E. Nanoparticles were highly enriched in all three A2780 tumors (Figure 4 D). In contrast the smaller HT29 tumors showed no or only slight fluorescence, whereas the bigger one was highly fluorescent (Figure 4 E). After cutting the HT29 tumor into two pieces, inhomogeneous fluorescence of accumulated nanoparticles was visible. Two areas with highest fluorescence intensity could be identified: the boundary and the central area. On the basis of Figure 4D an irregular distributed nanoparticle accumulation in the A2780 tumor tissue can be assumed. Different inner and surface parts are dark-red. In contrast there are large areas appearing dark-blue with only low fluorescence intensity, indicating areas with less accumulated nanoparticles. Dark-red and dark-blue areas as found in the A2780 tissue (Figure 4D) indicating only very high or minor nanoparticle concentrations could not be seen in the HT29 tumors (Figure 4E). This confirmed a more homogeneous nanoparticle distribution throughout the tumor. The low interstitial pressure in parts of the HT29 tumor tissue causes that after extravasation, the nanoparticles diffuse and accumulate in the tumor center (Figure 4E). As it is visible in the H&E stained light microscopic images shown in Figure 4G, this is an area with low central microvessel densities but with central fibrotic and or necrotic areas which is in accordance with literature.^{37,39,40} Jain *et al.* characterized the

TABLE 3. Normalized Total and Maximum Intensities of Different Mouse Organs and Tissues, Measured *ex Vivo*

batch:	total intensity signal						maximum intensity signal					
	A		B		C		A		B		C	
gender:	m ^a	f ^b	m ^a	f ^b	m ^a	f ^{b, c}	m ^a	f ^b	m ^a	f ^b	m ^a	f ^{b, c}
liver	39.8	45.0	34.8	37.4	100.0	88.8	53.4	47.4	56.2	29.6	100.0	89.0
spleen	8.8	9.3	9.0	0.5	12.4	15.2	34.9	25.4	27.4	4.8	41.8	37.9
gall bladder		0.1				0.4	1.1	11.2	5.5	4.2	2.4	33.2
intestine		1.5	1.2	0.5	1.2	4.5	5.3	7.9	11.6	6.2	9.0	14.2
kidney		0.4	0.2	0.1		0.1	2.1	4.7	4.6	1.0	4.8	7.3
lung		0.1	0.2		0.1	0.1	22.5	17.8	4.9	0.5	4.3	5.6
fat			0.1				2.5	4.9	2.3	0.4	2.1	9.6
heart		1.5	1.2	0.5	1.2	4.5	5.3	7.9	11.6	6.2	9.0	14.2

^a Data in percent based on three male mice per nanoparticle batch, 24 h after injection. ^b Data in percent based on four female mice per nanoparticle batch, 24 h after injection.

^c Data are based on previously shown results.²⁵

necrotic tissues as regions with less blood vessels and low blood flows.⁴¹ Immediately after i.v. injection, the nanoparticles are transported to perfused regions. Owing to the low interstitial pressure in parts of the tumor, tissue extravasation of nanoparticles is possible. Afterward they can diffuse to necrotic areas where they accumulate. Thus loaded nanoparticles would allow high intratumoral drug concentrations, and the anticancer therapy could start from the tumor center. The low interstitial pressure would also explain that no size dependent differences between the accumulation of batch A and B nanoparticles were found within HT29 tumor tissues. A2780 tumor tissues are better supplied with blood (Figure 4 F). Numerous blind ends, occlusions, and wall defects of the tumor blood vessels promote nanoparticle accumulation.⁴²

Ex Vivo Biodistribution Analysis. The degree of nanoparticle accumulation in different organs and tissues based on *ex vivo* fluorescence measurements is shown as normalized total and maximum intensities in Table 3. Owing to the linear relationship between exposure time and fluorescence intensity, the Maestro software allows the calculation of exposure-time independent total and maximum intensities. By a previously described calculation method, different nanoparticle batches with consequently varying DiR concentration could be compared.²⁵

Measured total intensities as the sum of all pixels of the respective organ and tissue are shown in the left rows of Table 3. It is visible that highest intensities were found in both organs of the RES, the liver, and the spleen. Batch A and B nanoparticles accumulated in similar amounts in the liver. The smaller size and the higher PLA/PEG ratio of batch A nanoparticles (PLA with a molecular weight of 20 kDa and consequently a higher amount of PEG) compared to batch B had no positive effect to reduce liver accumulation. This might be explained by an optimum size range for both batches and a completely PEG covered surface already

in the case of batch B nanoparticles with an PLA:PEG ratio of 20:1 which cannot be improved by higher PEG amounts. However, for batch C nanoparticles with the largest mean size, liver accumulation was clearly highest. The larger fraction of nanoparticles with bigger size (Figure 1) yielded in a nearly double amount of nanoparticles in the liver. This observation is in agreement with other published data where an increased nanoparticle uptake by the RES was found in size ranges between 150 and 300 nm.¹⁴

The intensity levels of all other organs and tissues were in the single-digit range. Nearly the same values were obtained for the male and the female mouse group. This underlines the reproducibility of our *in vivo* studies. The corresponding maximum intensity signals are also given in Table 3 (right rows). The maximum intensities allow a restricted comparison of organs and tissues varying in size although the errors of the measurement especially at the lower limit highly increase. Liver and spleen have comparable optical properties. Therefore, the maximum intensity allows a comparison of the accumulation rate between the bigger liver and the much smaller spleen. The results indicate a slightly decreased liver and an increased spleen uptake for the smaller nanoparticles. The maximum intensity results further confirm that no specific accumulation occurred in the kidneys, the lung, the fat, and the heart. An accumulation of nanoparticles based on higher maximum fluorescence intensities, measured for batch A in the lung and for batch B and C in the heart, could not be confirmed in the fluorescence images as fundamental accumulation. The slightly higher intensity level in the gall bladder and the intestine indicate the renal excretion of the particles, which was visually confirmed earlier.²⁵

In Vivo and ex Vivo Tumor Accumulation Analysis. Normalized total and maximum tumor intensities based on *in vivo* and *ex vivo* imaging data for all three batches are shown in Figure 4A,B. The calculated total intensities of

the A2780 tumors based on *in vivo* and *ex vivo* measurements are shown in Figure 4A. It is visible that the total intensity remained constant between 3 and 5 h and was doubled after 24 h. This might be explained by the long circulation time of the nanoparticles. Blood vessels were detectable up to 6 h, still indicating circulating nanoparticles. During the next hours an increasing number of nanoparticles accumulated in the tumor and those still circulating were continuously removed by the RES. The *ex vivo* signals, measured 24 h after injection are in good agreement with the *in vivo* obtained total intensities (Figure 4A). The decreased level of the total intensity measured *ex vivo* is the result of the slightly imprecise tumor definition within the ROI analysis of the *in vivo* cube file. The degrees of nanoparticle accumulation in A2780 and HT29 tumor tissues based on *ex vivo* data are shown in Figure 4B,C. To allow comparison between the larger A2780 and the smaller HT29 tumors both the normalized total and the normalized maximum intensities were divided by the respective *ex vivo* determined tumor volume. It is clearly visible that nearly the same tendencies were obtained for both normalized total and normalized maximum intensities. Lowest tumor accumulation generally was found for batch C nanoparticles. This can be explained by the above-discussed efficient elimination of the particles from the bloodstream by the RES (Table 3). For the A2780 ovarian carcinoma xenograft a strong size dependence of tumor accumulation was found (Figure 4B): Batch A nanoparticles with the smallest size (*z*-average = 111 nm, D90 = 80 nm) showed ~50-fold higher total intensities compared to the total intensities measured for batch C and ~2-fold compared to that of batch B. Examining the normalized maximum intensity of the A2780 tumor (Figure 4C), even a ~27-fold increase of the intensity between batch C and A was observed. The size difference between both batches A and B of 30 nm based on the *z*-average values (PCS measurements) and of 70 nm based on the D90 diameter results (AF4/MALLS analysis) resulted in a more than doubled enrichment for the smaller nanoparticles (Figure 4B,C). Within comparable liver accumulations between batch A and B nanoparticles we expected that the smaller size of batch A had a positive tumor-enhancing effect. Owing to high perfusion and vascular permeability of the A2780 ovarian carcinoma, this might be based on the EPR effect which is known to be highly size dependent.

In contrast to the A2780 tumors, the highest accumulation in the HT29 tumor was detected for the medium-sized nanoparticles (batch B, *z*-average = 141 nm, D90 = 153 nm). Batch A nanoparticles showed comparable but slightly decreased accumulation rates. Batch C (*z*-average = 166 nm, D90 = 230 nm) appeared to be not suitable for tumor accumulation. The tumor-size-related total and maximum intensity of batch C

were 5- to 9-fold reduced compared to the values of the other two batches. Based on the tumor size related calculations nearly the same normalized maximum and total intensity values (Figure 4B,C) indicate for HT29 and A2780 a homogeneous tumor accumulation.

CONCLUSION

In the present study, we investigated the size-dependent *in vivo* fate of PEG–PLA nanoparticle batches with different but well-defined sizes. Therefore, detailed particle size characterizations prior to the *in vivo* studies were carried out. We could show that nanoparticle batches with different sizes (*z*-averages between 111 and 166 nm in our study) within the optimum size range for tumor accumulation²¹ can be produced. Noninvasive multispectral NIR fluorescence imaging studies allowed nanoparticle detection just after injection up to 48 h. Combining DsRed2 expressing HT29 tumor cells with *in vivo* fate studies permitted nanoparticle tracking simultaneously next to tumor visualization from *in vivo* to *ex vivo*, up to cellular ranges. The confocal microscopic pictures confirmed the *ex vivo* imaging results where particles were located between fluorescent, DsRed2 expressing cells.

In vivo studies with HT29 and A2780 tumor bearing mice showed that nanoparticles accumulated in both tumors. Interestingly, the *ex vivo* studies furthermore demonstrated that the accumulation pattern mainly differs between both used tumor models. In the HT29 tumor tissue nanoparticles enriched in the tumor center primarily, whereas A2780 showed no centralized nanoparticle accumulation. Furthermore, highest tumor enrichments were found with batch A nanoparticles for the A2780 and comparable accumulations for batch A and B nanoparticles in the case of HT29 tumors. This points to the fact that the accumulation in centralized necrotic fields (HT29) is not as size dependent as it is for vascular permeation (A2780). *Ex vivo* viscera distribution studies showed distinct differences between the larger particles of batch C compared to those of batches A and B. The increased particle size yielded in high uptake rates by the RES and therewith to very low tumor accumulations. The presented results showed impressively the size-dependent *in vivo* behavior of produced nanocarriers. Slight differences between the *z*-averages of ~30 nm (between batch A and B) and of ~20 nm (between batch B and C) with—compared to literature—rather low PDI values (between 0.13 and 0.16) resulted in strongly different *in vivo* results. The addition of AF4/MALLS as a further particle size measurement method attested that all three nanoparticle batches varied more in size than PCS data would let expect. Whereas D50 values yielded same size intervals as measured within the PCS results (~20 and ~30 nm), D90 results attested size differences of ~70 nm (between batches A and B) and

~80 nm (between batches B and C). On the basis of these results, the combination of extended accurate size determinations with *in vivo* fluorescence imaging

technique appears to be a very promising approach to study the size-dependent fate and tumor accumulation of nanoparticles.

MATERIALS AND METHODS

Materials. 3,6-Dimethyl-1,4-dioxan (D,L -lactide), poly(ethylene glycol) monomethyl ether (mPEG2000; MW = 2000 Da), stannous 2-ethylhexanoate (>95%), phosphate buffered saline (PBS) buffer solution, and sorbitol were obtained from Sigma Aldrich, Germany. Sucrose was obtained from Merck KGaA, Germany, poloxamer 188 (Pluronic F68) from Riedel-de Haën, Germany, and paraffin as well as formalin ($\geq 35\%$) from Carl Roth, Germany. The fluorescence dye 1,1'-diiodo-3,3',3'-tetramethylindotricarbocyanine iodide (DiI), Dulbecco's phosphate buffered saline (PBS) and the Vybrant DiO cell-labeling solution (DiO) were purchased from Invitrogen, Germany. RPMI-1640 medium, 1% streptomycin/penicillin solution, and fetal bovine serum (FBS) were provided from PAA, Austria, and 10% fetal bovine serum came from Biochrom AG, Germany. Polystyrene standard nanoparticles were obtained from Duke Scientific, United States (50, 100, 200 nm), and from Beckman Coulter, Germany (300 nm). All other substances and solvents were used as received.

Synthesis and Preparation of PEG-PLA Nanoparticles. The synthesis of the diblock copolymers PEG₂PLA₂₀ and PEG₂PLA₄₀ followed a previously established procedure.²⁵ The numbers refer to the molecular weight of the respective polymer block (in kDa). A nanoprecipitation method was used for the nanoparticle preparation as described earlier.²⁵ In brief, a solution containing different amounts of polymer in 5 mL of chloroform and the NIR dye DiI (for batches A–C) was dropwise added to 40 mL of an aqueous solution containing 0.25% (w/v) poloxamer 188. Thereafter, the organic solvent was removed by evaporation under stirring the dispersion at room temperature. The nanoparticles were then collected by centrifugation, washed with purified water, resuspended in 5% sucrose solutions and subsequently freeze-dried.

Physicochemical Nanoparticle Characterization. *Fluorescence Spectroscopy.* Fluorescence spectra (775–900 nm) of the nanoparticles redispersed in water (nanoparticle concentration 0.23 mg/mL) were recorded using a LS 55 spectrophotometer (PerkinElmer, United States) equipped with a red-sensitive R928 photomultiplier (750 V), following excitation with 750 nm. The measured intensities were subsequently normalized to the particle concentration.

Photon Correlation Spectroscopy (PCS). For PCS measurements, all three DiI-loaded nanoparticle batches (batch A–C, Table 1) as well as a dye free PEG₂PLA₄₀ batch (batch D) were diluted with purified, filtered (0.2 μ m) water to reach a nanoparticle concentration of 0.1 mg/mL. The unloaded nanoparticles were furthermore dispersed in purified water containing 10% PBS buffer, 10% FBS, and 10% of both, PBS and FBS, respectively. The measurements were carried out with a high performance particle sizer (HPPS, Malvern Instruments, Germany). The samples were measured four times in the backscattering mode (173°) at room temperature (25 °C) with 12–16 runs over 10 s each at a fixed measurement position in the middle of the cuvette. Samples in PBS and FBS were measured after 24 h of storage to detect possible interactions between the nanoparticles themselves or between the nanoparticles and serum components. The mean particle size (z-average) and the PDI were determined by the instruments cumulant analysis software (version 4.20), $n = 4$ for batches A–C and $n = 3$ for batch D.

Asymmetrical Field Flow Fractionation (AF4). Particle size distributions of the nanoparticles were measured by AF4 (Eclipse, Wyatt Technology Europe, Germany) coupled with a MALLS detector (DAWN EOS, Wyatt) under the same conditions as used in our previous study.²⁵ Size distributions were calculated by the Astra software 4.90 (Wyatt) using the particle model and assuming compact spheres. Characteristic diameters (D10, D50, and D90) were obtained from cumulative size distributions. All three nanoparticle batches (Table 1) were diluted with purified, filtered (0.2 μ m) water (concentration, 1 mg/mL).

The unloaded nanoparticles (1 mg/mL) were also dispersed in purified water and water supplemented with 10% and 50% FBS, respectively. All samples were measured with purified water (preserved and 0.2 μ m filtered) as carrier liquid in triplicate, and results are given as an average with standard deviation. The accuracy of the AF4/MALLS separation system was routinely checked using a mixture of 50, 100, 200, and 300 nm polystyrene standard nanoparticles.³¹

Cell Culture for Confocal Microscopy. Human colon carcinoma cells (HT29) and human ovarian carcinoma cells (A2780) were cultivated as monolayers on round cover glasses with 80,000 HT29 or 85,000 A2780 cells per cm². Both cell lines were seeded and incubated in RPMI 1640 medium supplemented with 10% fetal bovine serum and 1% streptomycin/penicillin at 37 °C, 95% humidity, and 5% carbon dioxide. After 24 h the medium was removed and each of three round cover glasses with cells were incubated for 24 h with either unloaded, DiI-loaded nanoparticles (batch A, Table 1), or pure dispersion medium. A second series of each of three round cover glasses with cells were equally handled but stained additionally with DiO (Vybrant standard procedure) to visualize the cell membranes next to nanoparticles. After 24 h of incubation, the medium was removed and the cells were fixed with formalin in PBS (2% v/v) for 20 min at 37 °C. After washing the cells with PBS for three times, they were immediately imaged in a confocal microscope.

Confocal Microscopic Analysis. The LSM 710, a flexible confocal microscope (Zeiss, Germany), allows studying the cellular uptake of nanoparticles as well as of *ex vivo* excised tissues. The microscope was equipped with 40 \times or 63 \times Plan Apo oil immersion objectives. The DiI was excited with a 633 nm laser. Emitted fluorescence light was detected from 650 nm to the upper detection limit. The excitation of DsRed2, a red fluorescent protein, was carried out using the 514 nm laser. The 458 nm laser was used to excite DiO. Images were acquired in a sequential scan mode and processed using the ZEN software (Zeiss, Germany). To image the *ex vivo* samples the tumor tissue was excised and cut into small panels (thickness approximately 0.5 mm) by a racer plate. Afterward the tissue was slightly pressed between two cover glasses and immediately viewed with the LSM 710.

Animal Models and Nanoparticle Injection. Nanoparticle accumulation studies were performed in male NMRI-nu (nu/nu) mice from JANVIER SAS in Le Genest Saint Isle, France. All experiments complied with the standards for use of animal subjects as stated in the guideline from the animal care and use committee of Saxony Anhalt. Aqueous nanoparticle dispersions (6 milligram nanoparticles per milliliter) were prepared by redispersing adequate amounts of the freeze-dried nanoparticles (stabilized with 5% sucrose) in purified water containing 2.25% sorbitol to adjust tonicity. A 100 μ L portion of the dispersion was slowly *i.v.* injected into the tail vein of non-narcotized mice using a 30 Gauge needle. During imaging the mice were narcotized and protected for cooling out.²⁵

Xenograft Tumor Model and Application. HT29 and A2780 cells were maintained as monolayer cultures as given above. DsRed2 expressing HT29 cells were generated by lentiviral transduction according to the protocol described previously.⁴³

After growing, 3×10^6 DsRed2 HT29 cells were subcutaneously injected into both flanks of nude mice. At a size of approximately 1.5 cm³, 100 μ L of batch A nanoparticles was injected and time dependent images were grabbed by fluorescence imaging.

For detailed size dependent tumor accumulation studies nonfluorescent *s.c.* xenograft tumors were established in 13 nude mice. A total of 3×10^6 HT29 cells were *s.c.* injected to the right flank of the mice and 3×10^6 cells of A2780 were injected into the left side. Body weights and tumor sizes were measured

twice a week. After the A2780 achieved a maximum tumor size of about 2 cm³, the mice were separated into three groups (three mice each) and care was taken for a preferably homogeneous tumor size distribution. One untreated mouse was used as *in vivo* control and for further *ex vivo* microscopy studies. A 100 μ L portion of each nanoparticle batch was injected in all three mice of the respective group: A, B, and C (named like the nanoparticle batch as in Table 1). The mice were imaged 24 h after injection and sacrificed, and the respective tumors were excised. The tumor was exactly determined with a caliper, and the tumor volume was calculated using the tumor dimensions of all 3 room directions assuming an elliptic tumor shape. All excised tumors were imaged as complete tissue and after slicing into 2 pieces.

In Vivo and ex Vivo Tumor Imaging. *In vivo* and *ex vivo* fluorescence imaging experiments were performed using the Maestro *in vivo* fluorescence imaging system (Cambridge Research and Instrumentation, United States).^{25,44} The green filter set (503–555 nm excitation and 580 nm long-pass emission filters) was used to detect DsRed2 tumor cells. For nanoparticle imaging the NIR filter set with a 710–760 nm excitation and an 800 nm long-pass emission filter was used as described in our previous study.²⁵ To prevent fluorescence interferences between nanoparticle accumulations in the tumor and in the RES, the area of the liver was masked with a black plastic plate in selected imaging experiments. Recordings (cubes) were analyzed using *in vitro* DiR and cellular DsRed2 spectra as references, and the signal from an untreated mouse was set as background. The cubes were unmixed and segmented using these respective 2 or 3 spectra and saved as monochrome images. On the basis of these images, RGB (red green blue) pictures were generated allocating a respective color (DsRed2 in green and DiR in red) to the spectra. The generated grayscale images were also intensity-weighted illustrated.²⁵

For *ex vivo* analysis the mice were sacrificed using carbon dioxide 24 h after injection of the nanoparticles (48 h in the case of DsRed2 expressing HT29 experiments). The excised tumors and organs (liver and spleen) were imaged with the Maestro *in vivo* imaging system using the same parameters as in the *in vivo* study. To ensure reproducible conditions the organs (liver and spleen) were placed in a 24 holes well-plate. An area of interest (ROI) in the size of the well-plate hole was generated. Total and maximum intensities of all pixels in the ROI were measured and correlated to the respective exposure times by the software. To exclude intensity variations due to different initial dye concentrations and intensities between the nanoparticle batches, a previously described correction method was applied.²⁵ The total signal (correlated to the exposure time) was divided through the *in vitro* emission peak maximum which was determined prior to the *in vivo* measurements. The *ex vivo* total and maximum intensity signals of the nanoparticle accumulation in the tumor tissues were furthermore divided through the *ex vivo* determined tumor size (volume of an ellipsoid, based on three room directions). All graphs are normalized to 100% related to the highest result. Excised tumors were fixed with 4% formalin for 1 week and afterward embedded in paraffin. Resulted blocks were sliced (4 nm), dewaxed, and stained with hematoxylin and eosin (H&E). Light microscopic images of the stained tissues were obtained using a Zeiss Axiolab microscope (Zeiss, Germany).

Acknowledgment. We thank Jürgen Vogel and Marcus Nipel for supporting the confocal microscopic measurements. Mr Jörg Tessmar is acknowledged for the discussions during polymer synthesis and nanoparticle preparation. We thank also Martina Hennicke and Constanze Gottschalk for the animal care. The *in vivo* studies were partly supported by the Federal State of Saxonia Anhalt (FKZ 3646A/0907) and the confocal microscopy studies by the Deutsche Forschungs-gemeinschaft (LSM: INST 271/250-1).

REFERENCES AND NOTES

- Lipinski, C. A.; Lombardo, F.; Dominy, B. W.; Feeney, P. J. *Experimental and Computational Approaches to estimate Solubility and Permeability in Drug Discovery and Development Settings.* *Adv. Drug Delivery Rev.* **1997**, *23*, 3–25.
- Milne, G. *Pharmaceutical Productivity—The Imperative for New Paradigms.* *Annu. Rep. Med. Chem.* **2003**, *38*, 383–396.
- Yokogawa, K.; Nakashima, E.; Ishizaki, J.; Maeda, H.; Nagano, T.; Ichimura, F. *Relationships in the Structure Tissue Distribution of Basic Drugs in the Rabbit.* *Pharm. Res.* **1990**, *7*, 691–696.
- Feng, S. S. *New-Concept Chemotherapy by Nanoparticles of Biodegradable Polymers: Where are we now?.* *Nanomedicine* **2006**, *1*, 297–309.
- Musumeci, T.; Ventura, C. A.; Giannone, I.; Ruozi, B.; Montenegro, L.; Pignatello, R.; Puglisi, G. *PLA/PLGA Nanoparticles for Sustained Release of Docetaxel.* *Int. J. Pharm.* **2006**, *325*, 172–179.
- Xing, J.; Zhang, D. R.; Tan, T. W. *Studies on the Oridonin-loaded Poly(D,L-lactic acid) Nanoparticles in Vitro and in Vivo.* *Int. J. Biol. Macromol.* **2007**, *40*, 153–158.
- Brigger, I.; Dubernet, C.; Couvreur, P. *Nanoparticles in Cancer Therapy and Diagnosis.* *Adv. Drug Delivery Rev.* **2002**, *54*, 631–651.
- Dunn, S. E.; Coombes, A. G. A.; Garnett, M. C.; Davis, S. S.; Davies, M. C.; Illum, L. *In Vitro Cell Interaction and in Vivo Biodistribution of Poly(lactide-co-glycolide) Nanospheres Surface Modified by Poloxamer and Poloxamine Copolymers.* *J. Controlled Release* **1997**, *44*, 65–76.
- Moghimi, S. M.; Hunter, A. C.; Murray, J. C. *Long-Circulating and Target-Specific Nanoparticles: Theory to Practice.* *Pharmacol. Rev.* **2001**, *53*, 283–318.
- Maeda, H. *Tumor-Selective Delivery of Macromolecular Drugs via the EPR Effect: Background and Future Prospects.* *Bioconjugate Chem.* **2010**, *21*, 797–802.
- Yuan, F.; Dellian, M.; Fukumura, D.; Leunig, M.; Berk, D. A.; Torchilin, V. P.; Jain, R. K. *Vascular-Permeability in a Human Tumor Xenograft—Molecular-Size Dependence and Cut-off Size.* *Cancer Res.* **1995**, *55*, 3752–3756.
- Hobbs, S. K.; Monsky, W. L.; Yuan, F.; Roberts, W. G.; Griffith, L.; Torchilin, V. P.; Jain, R. K. *Regulation of Transport Pathways in Tumor Vessels: Role of Tumor Type and Micro-environment.* *Proc. Natl. Acad. Sci. U.S.A.* **1998**, *95*, 4607–4612.
- Moghimi, S. M.; Porter, C. J. H.; Muir, I. S.; Illum, L.; Davis, S. S. *Non-phagocytic Uptake of Intravenously Injected Microspheres in Rat Spleen—Influence of Particle-Size and Hydrophilic Coating.* *Biochem. Biophys. Res. Commun.* **1991**, *177*, 861–866.
- Moghimi, S. M. *Mechanisms of Splenic Clearance of Blood-Cells and Particles—Towards Development of New Splenotropic Agents.* *Adv. Drug Delivery Rev.* **1995**, *17*, 103–115.
- Nakaoka, R.; Tabata, Y.; Yamaoka, T.; Ikada, Y. *Prolongation of the Serum Half-Life Period of Superoxide Dismutase by Poly(ethylene glycol) Modification.* *J. Controlled Release* **1997**, *46*, 253–261.
- Lammers, T.; Kuhnlein, R.; Kissel, M.; Subr, V.; Etrych, T.; Pola, R.; Pechar, M.; Ulbrich, K.; Storm, G.; Huber, P.; Peschke, P. *Effect of Physicochemical Modification on the Biodistribution and Tumor Accumulation of HPMA Copolymers.* *J. Controlled Release* **2005**, *110*, 103–118.
- Lammers, T.; Subr, V.; Ulbrich, K.; Hennink, W. E.; Storm, G.; Kiessling, F. *Polymeric Nanomedicines for Image-Guided Drug Delivery and Tumor-Targeted Combination Therapy.* *Nano Today* **2010**, *5*, 197–212.
- Seymour, L. W.; Miyamoto, Y.; Maeda, H.; Brereton, M.; Strohal, J.; Ulbrich, K.; Duncan, R. *Influence of Molecular-Weight on Passive Tumor Accumulation of a Soluble Macromolecular Drug.* *Carrier. Eur. J. Cancer* **1995**, *31A*, 766–770.
- Litzinger, D. C.; Buiting, A. M. J.; Vanrooijen, N.; Huang, L. *Effect of Liposome Size on the Circulation Time and Intraorgan Distribution of Amphiphatic Poly(Ethylene Glycol)-Containing Liposomes.* *Biochim. Biophys. Acta, Biomembr.* **1994**, *1190*, 99–107.
- Liu, D. X.; Mori, A.; Huang, L. *Role of Liposome Size and RES Blockade in Controlling Biodistribution and Tumor Uptake*

- of Gm1-Containing Liposomes. *Biochim. Biophys. Acta* **1992**, *1104*, 95–101.
21. Storm, G.; Belliot, S. O.; Daemen, T.; Lasic, D. D. Surface Modification of Nanoparticles to Oppose Uptake by the Mononuclear Phagocyte System. *Adv. Drug Delivery Rev.* **1995**, *17*, 31–48.
 22. Beletsi, A.; Panagi, Z.; Avgoustakis, K. Biodistribution Properties of Nanoparticles Based on Mixtures of PLGA with PLGA-PEG Diblock Copolymers. *Int. J. Pharm.* **2005**, *298*, 233–241.
 23. Pegaz, B.; Debeve, E.; Ballini, J. P.; Konan-Kouakou, Y. N.; van den Bergh, H. Effect of Nanoparticle Size on the Extravasation and the Photothrombic Activity of Meso (*p*-Tetracarboxyphenyl) Porphyrin. *J. Photochem. Photobiol. B* **2006**, *85*, 216–222.
 24. Gaumet, M.; Vargas, A.; Gurny, R.; Delie, F. Nanoparticles for Drug Delivery: The Need for Precision in Reporting Particle Size Parameters. *Eur. J. Pharm. Biopharm.* **2008**, *69*, 1–9.
 25. Schädlich, A.; Rose, C.; Kuntsche, J.; Caysa, H.; Mueller, T.; Göpferich, A.; Mäder, K. How Stealthy Are PEG–PLA Nanoparticles? An NIR *in Vivo* Study Combined with Detailed Size Measurements. *Pharm. Res.* **2011**, *28*, 1995–2007.
 26. Shuhendler, A. J.; Prasad, P.; Chan, H. K. C.; Gordijo, C. R.; Soroushian, B.; Kolios, M.; Yu, K.; O'Brien, P. J.; Rauth, A. M.; Wu, X. Y. Hybrid Quantum Dot-Fatty Ester Stealth Nanoparticles: Toward Clinically Relevant *in Vivo* Optical Imaging of Deep Tissue. *ACS Nano* **2011**, *5*, 1958–1966.
 27. Jiang, Y. J.; Schädlich, A.; Amado, E.; Weis, C.; Odermatt, E.; Mäder, K.; Kressler, J. *In-Vivo* Studies on Intraperitoneally Administrated Poly(vinyl alcohol). *J. Biomed. Mater. Res. Part B* **2010**, *93B*, 275–284.
 28. Rose, C. Particulate Systems for Fluorescence Imaging and Drug Delivery. Thesis, University of Regensburg, Germany, December, 2010.
 29. Coffin, M. D.; McGinity, J. W. Biodegradable Pseudolatexes—The Chemical-Stability of Poly(D,L-Lactide) and Poly(ϵ -caprolactone) Nanoparticles in Aqueous-Media. *Pharm. Res.* **1992**, *9*, 200–205.
 30. Dunne, M.; Corrigan, O. I.; Ramtoola, Z. Influence of Particle Size and Dissolution Conditions on the Degradation Properties of Polylactide-co-glycolide Particles. *Biomaterials* **2000**, *21*, 1659–1668.
 31. Kuntsche, J.; Klaus, K.; Steiniger, F. Size Determinations of Colloidal Fat Emulsions: A Comparative Study. *J. Biomed. Nanotechnol* **2009**, *5*, 384–395.
 32. Lohrke, J.; Briel, A.; Mader, K. Characterization of Superparamagnetic Iron Oxide Nanoparticles by Asymmetrical Flow-Field–Flow-Fractionation. *Nanomedicine* **2008**, *3*, 437–452.
 33. Desai, M. P.; Labhasetwar, V.; Walter, E.; Levy, R. J.; Amidon, G. L. The Mechanism of Uptake of Biodegradable Microparticles in CaCo₂ Cells Is Size Dependent. *Pharm. Res.* **1997**, *14*, 1568–1573.
 34. Gref, R.; Luck, M.; Quellec, P.; Marchand, M.; Dellacherie, E.; Harnisch, S.; Blunk, T.; Muller, R. H. 'Stealth' Corona–Core Nanoparticles Surface Modified by Polyethylene Glycol (PEG): Influences of the Corona (PEG Chain Length and Surface Density) and of the Core Composition on Phagocytic Uptake and Plasma Protein Adsorption. *Colloid Surface B* **2000**, *18*, 301–313.
 35. Fang, J.; Nakamura, H.; Maeda, H. The EPR Effect: Unique Features of Tumor Blood Vessels for Drug Delivery, Factors Involved, and Limitations and Augmentation of the Effect. *Adv. Drug Delivery Rev.* **2011**, *63*, 136–151.
 36. Seki, T.; Fang, J.; Maeda, H. Enhanced Delivery of Macromolecular Antitumor Drugs to Tumors by Nitroglycerin Application. *Cancer Sci.* **2009**, *100*, 2426–2430.
 37. Caysa, H.; Metz, H.; Mäder, K.; Mueller, T. Application of Benchtop-Magnetic Resonance Imaging in a Nude Mouse Tumor Model. *J. Exp. Clin. Cancer Res.* **2011**, *30*, 69.
 38. Minko, T.; Kopeckova, P.; Kopecek, J. Efficacy of the Chemotherapeutic Action of HPMA Copolymer-Bound Doxorubicin in a Solid Tumor Model of Ovarian Carcinoma. *Int. J. Cancer* **2000**, *86*, 108–117.
 39. Buadu, L. D.; Murakami, J.; Murayama, S.; Hashiguchi, N.; Sakai, S.; Toyoshima, S.; Masuda, T.; Kuroki, S.; Ohno, S. Patterns of Peripheral Enhancement in Breast Masses: Correlation of Findings on Contrast Medium Enhanced MRI with Histologic Features and Tumor Angiogenesis. *J. Comput. Assist. Tomogr.* **1997**, *21*, 421–430.
 40. Schmid, S. A.; Dietrich, A.; Schulte, S.; Gaumann, A.; Kunz-Schughart, L. A. Fibroblastic Reaction and Vascular Maturation in Human Colon Cancers. *Int. J. Radiat. Biol.* **2009**, *85*, 1013–1025.
 41. Jain, R. K. Transport of Molecules, Particles, and Cells in Solid Tumors. *Annu. Rev. Biomed. Eng.* **1999**, *1*, 241–263.
 42. Minko, T.; Kopeckova, P.; Pozharov, V.; Jensen, K. D.; Kopecek, J. The Influence of Cytotoxicity of Macromolecules and of VEGF Gene Modulated Vascular Permeability on the Enhanced Permeability and Retention Effect in Resistant Solid Tumors. *Pharm. Res.* **2000**, *17*, 505–514.
 43. Luetzkendorf, J.; Mueller, L. P.; Mueller, T.; Caysa, H.; Nerger, K.; Schmoll, H. J. Growth Inhibition of Colorectal Carcinoma by Lentiviral TRAIL-Transgenic Human Mesenchymal Stem Cells Requires Their Substantial Intratumoral Presence. *J. Cell. Mol. Med.* **2010**, *14*, 2292–2304.
 44. Kobayashi, H.; Koyama, Y.; Barrett, T.; Hama, Y.; Regino, C. A. S.; Shin, I. S.; Jang, B. S.; Le, N.; Paik, C. H.; Choyke, P. L.; Urano, Y. Multimodal Nanoprobes for Radionuclide and Five-Color Near-Infrared Optical Lymphatic Imaging. *ACS Nano* **2007**, *1*, 258–264.



Contents lists available at SciVerse ScienceDirect

Journal of Controlled Release

journal homepage: www.elsevier.com/locate/jconrel

Accumulation of nanocarriers in the ovary: A neglected toxicity risk?

Andreas Schädlich^a, Stefan Hoffmann^a, Thomas Mueller^b, Henrike Caysa^{a,b}, Cornelia Rose^c, Achim Göpferich^c, Jun Li^a, Judith Kuntsche^a, Karsten Mäder^{a,*}

^a Martin Luther University Halle-Wittenberg, Department of Pharmaceutical Technology and Biopharmaceutics, D-06120 Halle (Saale), Germany

^b Martin Luther University Halle-Wittenberg, Department of Internal Medicine IV, Oncology/Hematology, D-06120, Halle (Saale), Germany

^c University of Regensburg, Department of Pharmaceutical Technology, D-93053, Regensburg, Germany

ARTICLE INFO

Article history:

Received 3 October 2011

Accepted 10 February 2012

Available online 21 February 2012

Keywords:

Nanocarrier

Nanoparticle

Toxicity

In vivo imaging

Fluorescence imaging

Ovary

ABSTRACT

Several nanocarrier systems are frequently used in modern pharmaceutical therapies. Within this study a potential toxicity risk of all nanoscaled drug delivery systems was found. An accumulation of several structurally different nanocarriers but not of soluble polymers was detected in rodent ovaries after intravenous (*i.v.*) administration. Studies in different mouse species and Wistar rats were conducted and a high local accumulation of nanoparticles, nanocapsules and nanoemulsions in specific locations of the ovaries was found in all animals. We characterised the enrichment by *in vivo* and *ex vivo* multispectral fluorescence imaging and confocal laser scanning microscopy. The findings of this study emphasise the role of early and comprehensive *in vivo* studies in pharmaceutical research. Nanocarrier accumulation in the ovaries may also comprise an important toxicity issue in humans but the results might as well open a new field of targeted ovarian therapies.

© 2012 Elsevier B.V. All rights reserved.

1. Introduction

Today various types of nanocarrier formulations like liposomes, nanoparticles, nanocapsules, nanotubes and others are intensively investigated or already commercially available [1–3]. Those nanoscaled drug delivery systems are commonly used in clinical therapy and in research to enhance circulation time or to achieve passive drug targeting [4–6]. Although toxicity and potential risks of such carriers have already been studied in detail, many effects are still poorly understood [7]. Unexpected accumulation of drug delivery systems in specific regions after intravenous (*i.v.*) injection could result in harmful side effects. Therefore, potential accumulation of nanocarriers in various tissues should be investigated during the development of new drug carrier systems. The fate of the carriers in the body depends mainly on their size, charge, shape and flexibility. Carriers larger than 150 nm often accumulate in liver and spleen, whereas very small carriers like polymers with hydrodynamic diameters <8 nm, can be rapidly eliminated by the kidneys [2,3,8–11]. Studies have also shown that liposomes <70 nm are eliminated faster than larger ones due to extravasation and accumulation in the parenchymal cells of the liver [12,13]. Therefore, *in vivo* distribution, accumulation and elimination studies must be combined with particle size analysis to obtain a comprehensive understanding of the properties of modern drug formulations.

Until now, a possible accumulation in ovarian tissue has not been investigated in biodistribution studies of nanocarriers. Therefore, extensive *in vivo* and *ex vivo* studies were performed within this study to examine this in detail. In our present study we measured the accumulation of differently composed nanoscaled drug delivery systems in the ovaries of rodents. To investigate the correlation of carrier size and ovary accumulation, detailed size distributions of all systems were measured by asymmetrical flow-field-flow fractionation (AF4). The accumulation in ovaries was characterized *in vivo* and *ex vivo* in different mouse strains and Wistar rats using non-invasive fluorescence imaging and confocal laser scanning microscopy (CLSM). Fluorescence imaging is a powerful technique to investigate the body fate of drug delivery systems noninvasively over several hours up to days or months in the same organism. The fluorescence imaging studies were carried out using consequently near infrared (NIR) fluorescent dyes that provided information also from deep tissues as well as from tissues which are highly supplied with blood. Those dyes were either covalently stable bound via amide bonds (polymers) or physically entrapped into the carriers (nanoparticles, nanocapsules and nanoscaled lipid emulsion). In total, we were able to prove the ovary accumulation of 5 different nanocarrier batches with diameters between 45 and 350 nm.

2. Materials and methods

2.1. Materials

3,6-dimethyl-1,4-dioxan (D,L-lactide), poly(ethylene glycol) monomethyl ether (mPEG2000; MW = 2000 Da), stannous 2-ethylhexanoate

* Corresponding author. Tel.: +49 345 5525167; fax: +49 345 5527029.

E-mail address: karsten.maeder@pharmazie.uni-halle.de (K. Mäder).

Supplemental material

(b) Characterization of nanocarriers and their potential usage in cancer therapy

106

A. Schädlich et al. / Journal of Controlled Release 160 (2012) 105–112

(>95%), 1,1'-Dioctadecyl-3,3,3',3'-tetramethylindocarbocyanine perchlorate (DiI), 3,3'-Dioctadecyloxycarbocyanine perchlorate (DiO), ethylene diamine, toluene sulfonyl chloride and sorbitol were obtained from Sigma Aldrich, Germany. Sucrose was obtained from Merck KGaA, Germany and poloxamer 188 (Pluronic F68) from Riedel-de Haën, Germany. The fluorescence dye 1,1'-dioctadecyl-3,3,3',3'-tetramethylindocarbocyanine iodide (DiR) was purchased from Invitrogen, Germany. The fluorescence dye IRDye 800CW was obtained from LI-COR, US. The diblock copolymer PLGA-PEG 45–5 (PLGA 50:50 45 kDa and PEG 5 kDa) and the Lipofundin 20 N were purchased from Boehringer Ingelheim, Germany and Lipiodol (Lipiodol Ultra fluid) from Guerbet GmbH, Germany. Hydroxyethyl starch 200/0,5 (batch HES) and dextran 500 (batch DEX) were kindly provided by Serumwerke Bernburg AG, Germany. Formaldehyde was purchased from Carl Roth GmbH, Germany. All other substances and solvents were used as received.

2.2. Preparation of nanoparticles

As described earlier [14] a nanoprecipitation method was used for the preparation of 3 NIR fluorescent nanoparticle batches, differing in size (batch NP1–NP3, Table 1). 37.5 mg (batch NP1) PEG₂PLA₂₀ or PEG₂PLA₄₀ (50 mg for batch NP2 or 100 mg for batch NP3), the numbers refer to the molecular weight in kDa, were dissolved in 5 mL chloroform. Referring to the polymer, 0.5% (batch NP1) or 1.0% (batch NP2 and NP3), of the NIR emitting fluorescence dye 1,1'-dioctadecyl-3,3,3',3'-tetramethylindocarbocyanine iodide (DiR) were added. To form solid nanoparticles, the solution was dropped into 40 mL of an aqueous solution containing 0.25% Pluronic F68. After removal of organic solvent by evaporation, the nanoparticles were collected by centrifugation and washed with purified water. Subsequently 5% sucrose was added and the dispersion was freeze-dried.

2.3. Preparation of nanocapsules

Nanocapsules were prepared by interfacial polymer deposition after solvent displacement (batch NC, Table 1). 20 mg PLGA-PEG

45–5 (PLGA (45 kDa) and PEG (5 kDa), 50:50) and 50 µL Lipiodol, loaded with 100 µg DiR (batch NC) or with 100 µg DiI (batch NC–DiI, Table 1) were dissolved in 2 mL acetone. The solution was dropwise injected into 4 mL water under stirring. The acetone was evaporated (under reduced pressure at 30 °C) and all samples were centrifuged (for 15 min at 4000 rpm) using a MiniSpin from Eppendorf, Germany. The supernatant containing dye loaded nanocapsules was 2 mL.

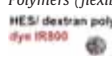



2.4. Dye loading of a nanosized lipid emulsion

For comparison also a commercially available lipid emulsion (Lipofundin 20 N) was loaded with DiR. An ethanolic DiR solution (100 µg/mL) was dropwise added under continuous stirring (batch LE, Table 1) to get a final dye loading with the same fluorescence intensity as it was achieved for the nanocapsule batch.

2.5. Preparation of soluble polymers

Hydroxyethyl starch (batch HES, Table 1) and dextran (batch DEX, Table 1) were amino-modified using ethylene diamine and covalently coupled with the NIR-fluorescent dye IR800CW. The amino groups were introduced to the molecules based on a previously described method [16]. Toluene sulfonyl chloride (0.5 g) was slowly added to a DMF solution (30 mL) of 1 g polymer and 1 mL triethyl amine. The mixture was cooled on ice and reacted for 2 h in the dark. After precipitating in acetone, the polymers were dialysed against water (3.5 kDa membrane from Spectrum Labs, United States) and subsequently freeze dried. The tosyl-modified polymers (0.25 g) were reacted with ethylene diamine (1.5 g) in DMF (50 mL) and borax buffer (pH 10) for 20 h. Resulting polymers were precipitated in methanol and isopropanol (1:1), afterwards several times dialysed against water and subsequently lyophilised. The amino-modified polymers (100 mg) were dissolved in water (50 mL), reacted with 0.5 mg IRDye 800CW in the dark for 3 h and once again dialysed against water and afterwards lyophilised.

Table 1
Composition and particle sizes of used nanocarriers.

	Batch	Polymer/ carrier	Size	Animals per batch
Polymers (flexible)				
 HES/ dextran polymer dye IR800	Batch HES	HES 200	30 nm (D _w) ^{a)}	3 SKH1 mice (♀)
	Batch DEX	Dextran 500	35 nm (D _w) ^{a)}	
Nanoparticles (solid)				
 PEG-PLA particle	Batch NP1	PLA ₂₀ PEG ₂	45 nm (D ₅₀) ^{b)} c)	4 SKH1 mice (♀)
	Batch NP2	PLA ₄₀ PEG ₂	65 nm (D ₅₀) ^{b)} c)	3 SKH1 mice (♂)
	batch NP3	PLA ₄₀ PEG ₂	100 nm (D ₅₀) ^{b)} c)	
Nanocapsules (solid shell)				
 PEG-PLGA shell	Batch NC	PLGA ₄₅ PEG ₅ , Lipiodol	55 nm (D ₅₀) ^{b)}	4 SKH1 mice (♀) ^{d)}
	Batch NC–DiI ^{d)}	PLGA ₄₅ PEG ₅ , Lipiodol	Not determined	3 BALB/c mice (♀) ^{d)} 3 Wistar rats (♀) ^{d)}
Nanosized lipid emulsion droplets				
 Lipofundin 20 N	Batch LE	Lipofundin 20 N	350 nm (D ₅₀) ^{b)}	4 SKH1 mice (♀)

^{a)} D_w means the weight-average mean square diameter, measured by AF4/MALLS.

^{b)} D₅₀ means the mass weighted distribution median diameter, measured by AF4/MALLS.

^{c)} D₅₀ values were published previously [15].

^{d)} Batch NC–DiI was only used for additional confocal microscopy studies. It was injected into 2 SKH1-*H^{tr}* mice (♀).

2.6. Particle size measurement

All nanocarrier batches were analysed by AF4 based on a method previously described [14]. The fractionation system (AF4/ MALLS) was composed of an Eclipse AF4 (Wyatt, Germany) which was coupled with a multi-angle laser light scattering (MALLS) detector (DAWN EOS, Wyatt). Particles were separated in a trapezoidal-shaped channel (length 265 mm, largest width 21 mm, height 350 μm) in dependence on their size and shape by applying appropriate cross flow rates. A 5 kDa membrane (regenerated cellulose or polyethersulfone (MWCO 5 kDa, Microdyn-Nadir, Germany) was used as accumulation wall. Bi-distilled water served as carrier liquid (preserved with 0.02% sodium azide and filtered through 0.1 μm pore sized filter). A volume of 100 μL of the nanocarrier dispersions (1 mg/mL for batch NP1–NP3, for batch NC and for batch HES and batch DEX, 0.1 mg/mL for batch LE) was injected during focusing (focus flow 2 mL/min). Samples were eluted with a constant (1 mL/min) and decreasing cross-flow (from 2 to 0.5 mL/min within 5 min and from 0.5 to 0 mL/min within 35 min). The particle sizes were calculated based on the light scattering signal. For the batches NP1–NP3, NC and LE the particle mode was used for size evaluations (assuming compact spheres), whereas for the polymers the molecular weight mode was used. The Astra software 4.90 (Wyatt, Germany) allowed determining the corresponding mean diameters (D50) from the mass weighted distributions [14]. Polymer sizes were calculated based on weight-average mean square diameters (D_w) using RI detector signal. All dispersions were measured in triplicate, and results are given as average in Table 1.

2.7. Animal handling

All experiments complied with the standards for use of animal subjects as stated in the guideline from the animal care- and use-committee of Saxony Anhalt. As listed in Table 1 *in vivo* studies were performed in pubescent female (batches NP1–NP3, NC and LE, all in quadruplicate, batches HEX and DEX in triplicate and batch NC–DiI in duplicate) and male (batches NP1–NP3, all in triplicate), nude SKH1-Hr^{hr} mice (age: 2–12 months). Further *in vivo* studies were performed in female BALB/c mice (batch NC, n = 3, age: 6 months) and in female Wistar rats (batch NC, n = 3, age: 12 months). The animals were housed under controlled conditions (12 h light/dark schedule, 24 °C). Respective samples were isotonised with sorbitol and slowly *i.v.* injected into the tail vein (100 μL for mice and 1 mL for rats, in a concentration of 8 mg/mL for the nanoparticle and nanocapsule batches and 10 mg/mL for the polymers). For *in vivo* fluorescence imaging, the mice were anaesthetised using a mixture of isoflurane and oxygen with an initial flow of 4% isoflurane (3.0 L/min oxygen) and a steady state flow of 1.8% isoflurane (1.5 L/min oxygen). The mice were placed on a 35 °C temperature-controlled heating plate to prevent a decrease of body temperature. For *ex vivo* analysis mice and rats were sacrificed using carbon dioxide 24 h after injection.

2.8. Fluorescence imaging

In vivo and *ex vivo* fluorescence imaging experiments were performed using the Maestro *in vivo* fluorescence imaging system (CRi, now Caliper Life Sciences, United States) and the Maestro software (version 2.10) [14,15]. The NIR filter set (710–760 nm excitation and 800 nm long-pass emission filter) was used for the detection of both NIR dyes, the DiR and the IRDye 800CW. The measurement files (cubes) were grabbed in the spectral range between 780 and 950 nm using auto exposure times. The tuneable filter was automatically stepped in 10 nm increments and intensity weighted greyscale images were acquired at each step.

The single spectral species were unmixed from the recorded cubes using reference spectra of DiR or IRDye 800CW and the background signal of an untreated mouse that was measured under same conditions.

During the unmixing process, each pixel was intensity weighted allocated to the respective reference spectra. The resulted greyscale images of the respective fluorescence signals were used for further analysis or to generate jet color images [14]. Those have an intensity weighted incremental color profile. Pixels with maximum intensities are set to dark red and pixels with no fluorescence to dark blue/black. In between there is a graduation from red to orange, yellow, light and dark blue.

For *ex vivo* analysis, the mice and rats were sacrificed 24 h after injection. The uteri with ovaries (female mice and rats) or seminal vesicles, testes (male mice) were excised and imaged with highest possible magnification on a plastic plate. The spectral species were unmixed from the image cubes as described above. Ovaries and uteri from untreated mice served as negative controls.

For batches NP1–NP3, the accumulation in the ovaries was also compared with the distribution of the nanoparticles in other organs and tissues. Therefore, the intestine, fat, liver, gall bladder, lung, spleen, kidney and heart were placed next to uterus with ovaries into 9 separate holes of a 24 holes well-plate. This allowed reproducible measurement conditions for the organs and tissues of all mice. The plate was imaged with the Maestro *in vivo* imaging system. To detect also minor nanocarrier accumulations, the measurements were repeated after masking the liver with a black plastic plate. Organs from untreated mice served as negative controls. A region of interest (ROI) in the size of the well-plate hole (1.9 cm^2) was generated to extract total and maximum intensities of the organs and tissues. The software correlated them to the respective exposure times. To exclude intensity variations due to different initial dye concentrations and intensities between the 3 different nanoparticle batches (NP1–NP3), a previously described correction method was applied [14]: For this, the total signal (correlated to the exposure time) was divided by the *in vitro* emission peak maximum which was determined prior to the *in vivo* measurements. All values were normalised to 100% referring to the highest result.

2.9. Confocal laser scanning microscopy (CLSM)

CLSM experiments were carried out using a LSM 710 (Zeiss, Germany). Dyes were excited using an Ar-Laser for DiI (514 nm) and DiO (488 nm) and a HeNe-Laser for DiR (633 nm). Samples were prepared from just extracted ovaries that were cut into small slices of app. 0.5 mm using a razor blade. Afterwards the slices were transferred to an object slide. Further, frozen sections of extracted ovaries were stained with DiO to visualise the cellular membranes. The 40x or the 63x Plan Apo oil immersion objectives were used for microscopy. For comparison, also a pure solution of DiI stained nanocapsules was imaged under the same conditions like the sliced ovaries. To obtain a 3-dimensional impression of the nanoparticles distribution in the microscopic ovary structures Z-stacks were applied using 80 μm steps. All images were grubbled and processed with scale bars using the software ZEN 2008 (version 1.0.3).

2.10. Light microscopy

An Axiolab Microscope from Carl Zeiss Microimaging (Germany) was used for light microscopy of ovarian tissue. Excised ovaries were fixed with 4% paraformaldehyde and embedded in paraffin. Thin slices (4 μm) were cut using a microtome and transferred to object slides. The slices were dewaxed and stained with Haematoxylin and Eosin. Images were grabbed and processed using the Zeiss Axiolab software.

3. Results

3.1. Particle size measurements

For particle size measurements AF4 was combined with MALLS. This allowed accurate size evaluation of all batches due to sample

Supplemental material

(b) Characterization of nanocarriers and their potential usage in cancer therapy

108

A. Schädlich et al. / Journal of Controlled Release 160 (2012) 105–112

separation prior size determination. The characteristic D_{50} (for nanocarriers) and D_w (for polymers) are shown in Table 1. All used nanocarriers were within the size range between 45 and 350 nm, whereas diameters of 30 and 35 nm were measured for the flexible polymers with the covalently bound NIR dye. The lipid nanoemulsion was rather broad distributed. All nanoparticle batches were narrow distributed [15]. Based on the determined D_{50} values of 45 nm (batch NP1), 65 nm (batch NP2) and 100 nm (batch NP3) it is possible to draw conclusions about the size dependent accumulation of nanocarriers in rodent ovaries.

3.2. *In vivo* and *ex vivo* fluorescence imaging studies

Within this study, the ovary accumulation of 7 differently composed nanoscaled drug delivery systems (Table 1) was investigated using the Maestro *in vivo* imaging system. For our study we selected NIR fluorescent dyes, as they can be detected also in deep tissues [17]. Generally, fluorescent dyes can be loaded to the carrier systems by incorporation or by covalent attachment. As incorporation of the fluorescent dye does normally not affect the surface characteristics of the nanocarriers, this method was used for the nanoparticle, nanocapsule and lipid nanoemulsion batches. In case of soluble polymers (batches HES and DEX) the fluorescent dye was covalently

coupled to the polymer. For a physical entrapment, a very hydrophobic dye is required which will not diffuse out of the drug delivery system until the carrier is degraded. Therefore, dialkylcarbocyanine dyes (DiR and DiI) were chosen. DiR is a very lipophilic NIR fluorescence dye that has already been used in several *in vivo* studies to track nanocarriers by fluorescence imaging noninvasively [18,19]. A distinct diffusion of the dye out of the nanocarriers into the blood can be excluded due to the very high partition coefficient of the utilised dye. Reported log P values of dialkylcarbocyanine dyes are between 17 [20] and 20 [21]. The release of those dyes from lipophilic nanocarriers is reported to be less than 4% within the first week [22,23].

In this study (Table 1) DiR was incorporated into 3 batches of different sized PEG-PLA nanoparticles (batch NP1: PEG₂PLA₂₀, batch NP2 and NP3: PEG₂PLA₄₀), 1 batch of oil loaded PEG₅PLGA₄₅ nanocapsules (batch NC) and 1 batch of a common lipid emulsion (Lipofundin 20 N, batch LE). Due to the fact that a physical incorporation is not possible for soluble hydrophilic polymers, the 2 polymer batches HES and DEX were successfully amino-modified and covalently stable labelled with the amine reactive NIR fluorescent dye IR 800CW (NHS-ester).

The long-term *in vivo* fate was investigated over about 3 weeks in nude female mice (SKH1-Hr^{hr}). Detailed *in vivo* distribution studies as

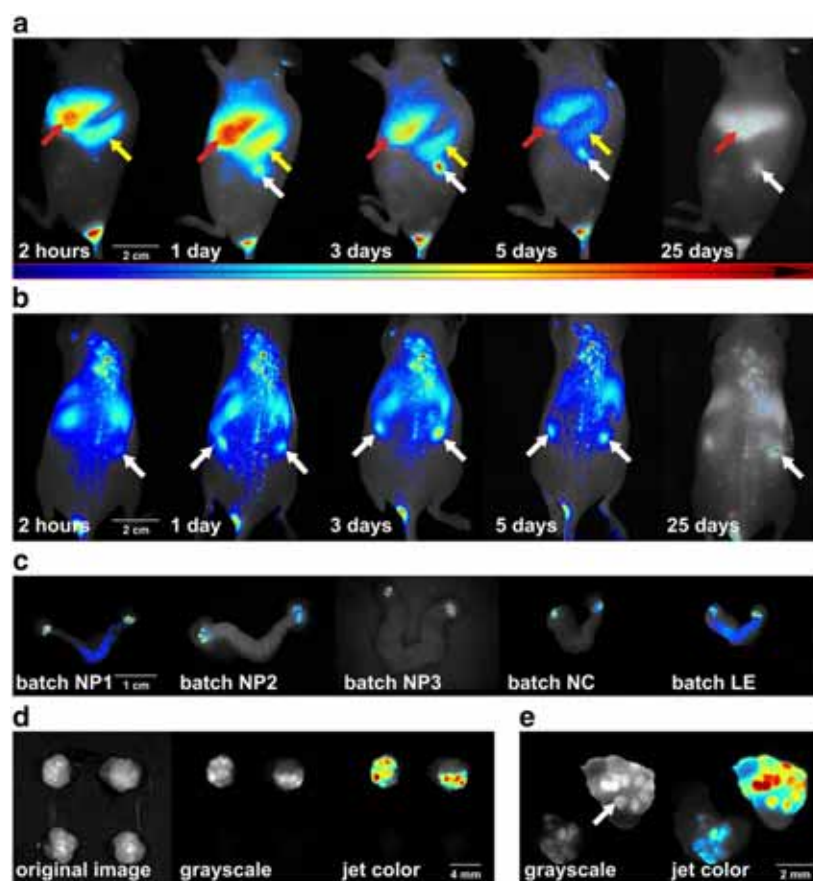


Fig. 1. *In vivo* and *ex vivo* fluorescence images of accumulated nanocarriers. a, Time dependent lateral optical images of a nude mouse after *i.v.* nanoparticle injection (batch NP2) presented as an intensity weighted visualization of the extracted fluorescence dye signal (jet color). Areas with highest dye intensities are red and those with lowest dye concentrations are blue. The red arrow marks the liver, the yellow one the spleen and the white one the ovaries. b, Intensity weighted jet color images of the dorsal side from the same mouse as shown in a (arrows point to ovaries). The long term enrichment of the carrier system in the ovaries is visible. c, *Ex vivo* jet color images of the excised uterus with ovaries 24 h after nanocarrier injection. While the uterus is not or only slightly fluorescent, high fluorescence intensities were detected in the ovaries. d, *Ex vivo* images of excised ovaries (original photograph (from left to right), grayscale image of the extracted dye signal and corresponding jet color image for a better visualization of the intensity allocation), 24 h after batch NP3 administration (upper row), negative control (lower row). e, Grayscale and corresponding jet color image of the sliced ovary in the highest possible magnification. The fluorescence in the ovaries is concentrated in highly fluorescent spots (marked by arrow).

well as size dependent tumor accumulation studies of used nanoparticle batches NP1–NP3 have been discussed previously [14,15]. The resulting *in vivo* images are exemplarily shown for medium sized batch NP2 (PEG₂PLA₄₀) nanoparticles in Fig. 1a and b.

An accumulation of the nanoparticles in the organs of the RES was already observed after 2 h. One day after injection, the fluorescence intensity in the RES reached maximum values and decreased continuously thereafter. Additionally, an accumulation of the nanoparticles in the ovaries (Fig. 1a and b marked by white arrows) was detectable already 2 h after administration. The fluorescence intensity from the ovaries further increased within 24 h and remained constant at a high level over several days. Even 25 days after injection a bright fluorescence signal could be detected noninvasively in the area of the ovaries *in vivo*.

To confirm the ovarian accumulation of nanoparticles, *ex vivo* experiments with all 3 nanoparticle batches were conducted. For that purpose the uteri with ovaries were excised 24 h after *i.v.* injection. Representative *ex vivo* images are presented in Fig. 1c. As it is visible exemplarily in the first 3 images, strong fluorescence intensities were detected in the ovaries of all 12 mice that were treated with nanoparticles (batch NP1–batch NP3). To evaluate if this observation is not related to the type of nanocarrier e.g. due to a characteristic property of the polymer surface, the experiment was repeated with 2 further nanoscaled formulations (batch NC and batch LE) with a completely different composition. Representative images are shown in Fig. 1c. As it is clearly visible in all images, the uterus itself was low or even not fluorescent. However, the ovaries of all 20 mice were highly fluorescent independently of the size and the surface properties of the administered nanocarrier batches.

To exclude the possibility of measurement artefacts, the ovaries of treated (batch NP2) and untreated mice were measured simultaneously (Fig. 1d). The resulting images of the isolated DiR signal indicate a high nanocarrier accumulation in fluorescent spots whereas no fluorescence at all was found in the control tissues. Magnified images of sliced ovaries, shown in Fig. 1e, confirmed the local and punctual enrichment. To eliminate the possibility of a species specific accumulation in SKH1-Hr^{hr} mice, *in vivo* and *ex vivo* studies with oil loaded PEG₅PLGA₄₅

nanocapsules were repeated in 3 female BALB/c mice and 3 Wistar rats. Comparable accumulation results were found in all of the experiments.

An original photograph of the excised rat ovary in comparison to the corresponding intensity weighted jet color image of the same part is shown in Fig. 2a. Due to the increased size of the rat ovary compared to the mouse ones more details are distinguishable. Also in the ovaries of the Wistar rats, local accumulations of the nanocapsules in varying intensities and tissue depths were detectable (marked by arrows in Fig. 2a). The direct comparison of both images also shows that some ball like structures visible in the original photograph are not fluorescent, whereas others are highly fluorescent. This fact indicates that the nanocarrier accumulations might depend on the progress stage within the ovarian cycles.

3.3. Confocal microscopy studies

To characterise the local areas of highest fluorescence intensities in more detail, confocal microscopy studies were conducted. Z-stack CLSM images (80 µm steps) confirmed the accumulation in round, ball like tissue structures with an average diameter of approximately 200–300 µm (Fig. 2f). No fluorescence signals were detected in the area of nuclei-like structures (Fig. 2b). However, by CLSM highly fluorescent spots in the ovarian tissue (Fig. 2c, top image) were assignable to the injected nanocarrier dispersion (lower image). In combination with the *in vivo* results presented in Fig. 1a and b, where fluorescence in the ovaries was detectable for more than 25 days a local long term release of incorporated dyes or drugs from the nanocarriers can be expected. *Ex vivo* studies were extended by frozen section sliding of excised tissues. In Fig. 2d, accumulated nanoparticles (red) are visible next to cells where the cellular membrane was stained with DiO (green). Fig. 2e shows a stained light microscopic picture of a growing follicle from mouse ovarian tissue.

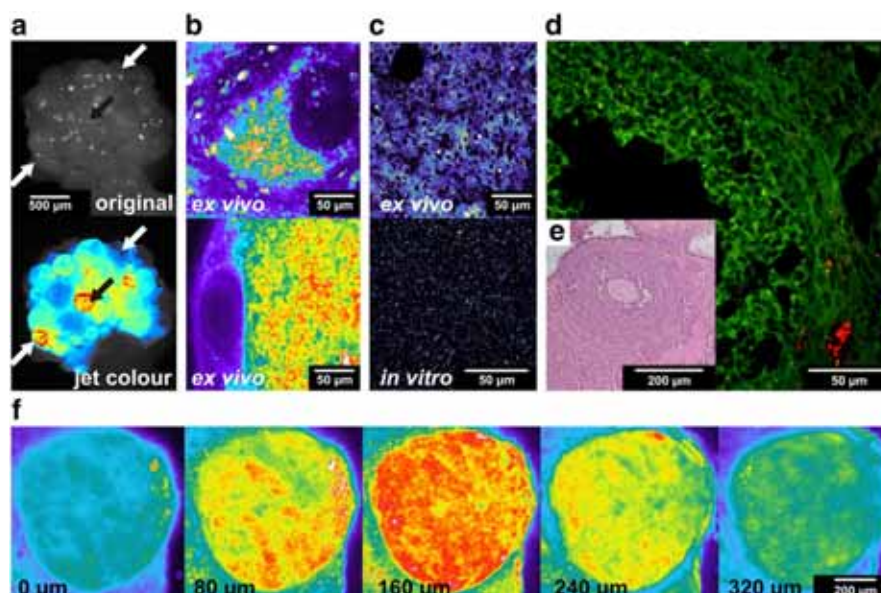


Fig. 2. *Ex vivo* fluorescence images, confocal and light microscopic pictures of ovarian tissue. a, *Ex vivo* photograph (top) and corresponding jet color image (bottom) of a rat ovary (batch NC). Arrows point to same positions and mark characteristic ball like regions. b, Intensity weighted CLSM images of ovarian tissue (batch NP3). c, CLSM images (batch NC-DiI) of ovarian tissue from a treated mouse (top, *ex vivo*) in comparison to the *in vitro* NC-DiI dispersion (bottom). d, Frozen section CLSM image of excised ovary tissue, batch NP3 (red), cells stained with DiO (green). e, Light microscopic picture of ovarian tissue, stained with haematoxylin and eosin. f, Z-stack series of intensity weighed CLSM images (80 µm steps) of ovarian tissue (batch NC-DiI).

Supplemental material

(b) Characterization of nanocarriers and their potential usage in cancer therapy

110

A. Schädlich et al. / Journal of Controlled Release 160 (2012) 105–112

3.4. Size dependent *ex vivo* fluorescence imaging analysis

To investigate a potential size dependent accumulation of nanocarriers in the ovaries *ex vivo* studies of 3 nanoparticle batches (batch NP1–NP3), varying in particle sizes (Table 1) were performed. Nine organs of each mouse (known for nanocarrier accumulation or excretion) were placed, each into a separate hole of a 24 holes well-plate (Fig. 3a). All organs in the well-plate were imaged simultaneously. The well plate allowed the arranging of the tissues and organs of each mouse in the same position for all fluorescence imaging measurements and thus ensured reproducible measurement conditions. The intensity weighted DiR signal as a jet color images are shown in Fig. 3b–d. Organs from untreated mice were imaged as an control. Accumulations in the liver (dark red) as well as in small parts of the ovary (marked by arrow) are visible (Fig. 3c). After covering the liver with a black plastic plate, also weak fluorescence signals from intestine and spleen were detectable (Fig. 3d).

Based on the measured DiR intensity signals, normalised maximum and total intensities of all excised organs were calculated. Corresponding graphs are displayed exemplarily for batch NP3 in Fig. 3e and f. The maximum fluorescence intensity, measured from local spots of the ovaries, was as high as it was detected in the liver, which is the major organ for nanocarrier elimination within the RES. Related to that, the spleen and the gall bladder showed half maximum intensities. All other organs and tissues had intensities near the detection limit. The maximum intensity values allow a comparison of accumulations in organs differing in size. A high enrichment situated

only in a local part of a tissue for example leads to high maximum intensity values, but the total signal of the same sample, as the sum of all pixels, would only be slightly increased. Thus, the normalised total intensities yielded in divergent results compared to the normalised maximum intensities. The calculated total signal of the ovary with the uterus was below 10%, comparable to the much larger intestine. The difference between the total and the maximum signal (10 fold compared to liver results) underline the inhomogeneous and local nanoparticle accumulation in specific regions of the ovary as already above discussed for the *ex vivo* images.

As shown by the maximum intensities in Fig. 3g, nanoparticles from all 3 batches (NP1–NP3) accumulated in the ovaries. This corresponds to the analysis of the total intensities (Fig. 3h). Compared to male tissues (seminal vesicles and testes), the nanoparticle accumulation in the ovaries was reflected by a 20 fold higher maximum intensity and a 200 fold higher total intensity.

Normalized maximum intensities of batch NP1 and NP2 between 10 and 30% in comparison to 100% for batch NP3 indicate that bigger particles accumulated more than smaller ones, although the standard deviation is rather high here. A higher accumulation was also found by analyzing the total fluorescence intensities. Further investigations using small (≤ 35 nm diameter) water soluble polymers (batch HES and batch DEX) were conducted to investigate whether there is a minimum size required for the accumulation of nanocarriers or not. For this purpose, a dose of 1 mg of each fluorescent labelled polymer in 100 μ L isotonic sorbitol solution was injected to the tail vein of 3 female mice (SKH1-Hr^{hr}). No specific accumulation in mouse ovaries

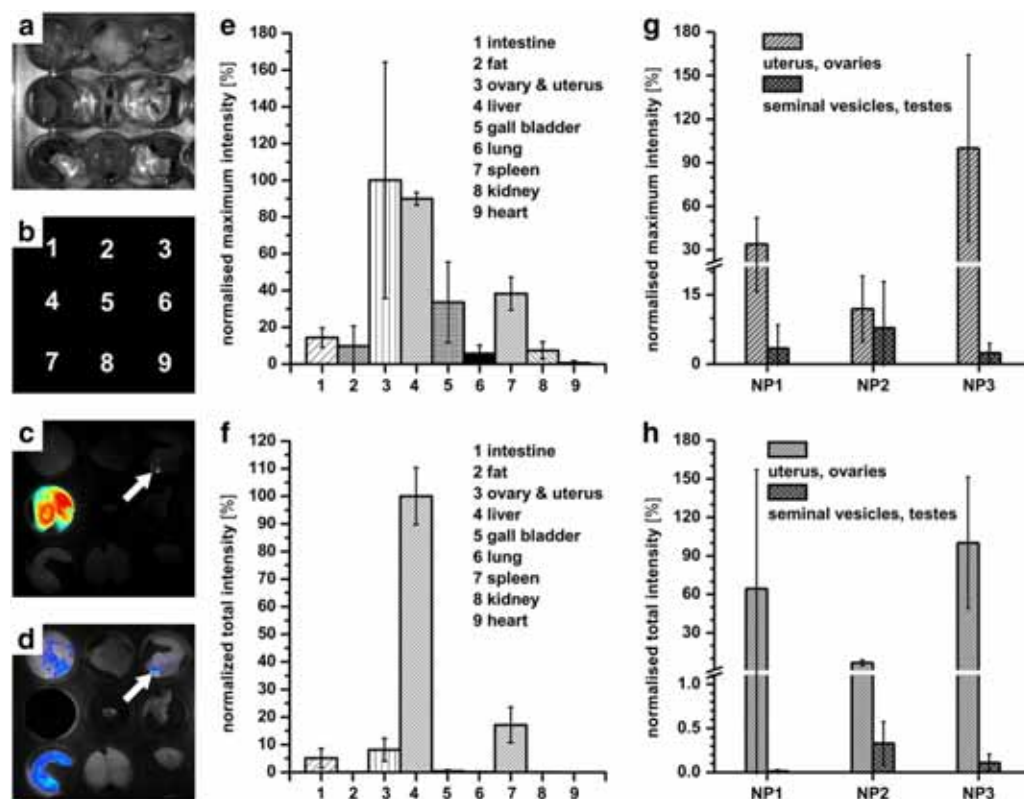


Fig. 3. *Ex vivo* fluorescence images and analysis of different PEG-PLA nanoparticle batches (NP1–NP3). a–d, Original photograph (a) and jet color images of excised mouse organs from an untreated (b, negative control) and a treated (c and d) mouse (24 h after *i.v.* injection of batch NP3). For reproducible measurements, these were placed in the following order into 9 holes of a 24-well plate (related to b): intestine, fat, uterus with ovary, liver, gall bladder, lung, spleen, kidney and heart. Jet color images grabbed with 800 ms (c) and 1200 ms (d, liver was masked with a black plastic plate) exposure time. Both show the accumulation of nanoparticles in the RES and in the ovary (marked by white arrow). e and f, Normalised maximum (e) and total (f) fluorescence intensity graphs of organs, shown in c (n = 4). g and h, normalised maximum (g) and total (h) fluorescence intensity graphs of female and male genital tissues of the nanocarrier batches NP1–NP3 (female: n = 4, male: n = 3).

was found in any of the 6 treated mice. A minimum size limit above 35 nm diameter can be concluded from this experiment.

4. Discussion

An accumulation of nanocarriers in the ovaries is mentioned in a small number of other publications based on *in vivo* and *ex vivo* studies with different kinds of nanoparticles and liposomes [24–30]. However, in all of them, the accumulation was neither investigated in detail nor thoroughly discussed. In these publications an ovary accumulation is (I) either visible in the presented pictures or (II) it can be derived from the presented data or (III) is briefly described. The reason, why the accumulation in rodent ovaries may not have attracted attention yet might be the fact that many research groups tend to use male mice. Another reason could be that the accumulation occurs only in mature, pubescent female mice. Furthermore, no accumulation in mouse ovaries was reported in a recent study of Daou *et al.* with very small nanoparticles (diameters below 50 nm) [31]. This might be related to the small size of the particles, which would correlate with our results, or to the mice age between 5 and 6 weeks, an age at which they were probably not yet pubescent. Another potential reason for the scarcity of published data on ovarian accumulation could be the observation that the nanocarrier accumulation appears to be restricted only to local parts of the ovaries. The overall amount of fluorescence signal from the ovaries was rather small (Fig. 3f) and not higher compared to other organs and tissues where no nanoparticles accumulated. Commonly, only the average amounts of the tissues or the percentages per administered dosages are compared in *in vivo* studies. Accumulations in the ovaries might thus often remain unnoticed. Few studies showed that an accumulation of nanoparticles in ovaries is detectable when the accumulation is calculated in μg per tissue weight (g) but not, when it is calculated as the percentage of the dose [26,30]. Anyhow, two fluorescence imaging studies of hybrid- and of lipid-nanoparticles also reported an accumulation [24,25]. Perez-Soler *et al.* even found liposome accumulations in the ovaries after subcutaneous injection [27]. Harrington *et al.* also detected a low but significant accumulation of pegylated, radiolabeled liposomes in the uterus and ovaries while non-pegylated liposomes were eliminated nearly completely within the first hour [28]. This short circulation time was probably not sufficient to achieve accumulations. Based on the size and structures of the accumulation areas from the *ex vivo* Maestro and CLSM images of our study, an enrichment in tertiary vesicular follicles might be possible but an accumulation in cells of the corpus luteum seem even more likely.

The corpus luteum is formed from the wall of the ruptured follicles after the ovulation. It is responsible for the production of progesterone which is a key factor during the pregnancy. Progesterone is in high concentrations needed shortly after the ovulation. Thus the ovarian corpus luteum grows and vascularizes extremely fast. Finally, the corpus luteum is typically very large in relation to the size of the ovary. It has been described that the rates of tissue growth and angiogenesis in the corpus luteum rival those of fast growing tumors [32]. This permits the assumption that an accumulation of nanocarriers in the corpus luteum is related to the EPR (enhanced permeability and retention) effect known for tumor tissues. Due to the EPR effect, *i.v.* injected nanocarriers can accumulate by passive diffusion due to a hyper-permeable tumor vasculature. By this, nanocarriers have the ability to be retained in tumor tissues which is a highly size dependent effect. An accumulation in the corpus luteum would be in agreement with the study of Thurston *et al.* They found accumulated liposomes in blood vessels around large ovarian follicles and in just formed corpora lutea but not inside follicles and only to a low degree in smaller, regressing corpora lutea [29].

Although the detailed mechanism still has to be enlightened, we could clearly prove specific nanocarrier accumulation in rodent ovaries. This effect might bear a potential toxicity risk if incorporated drugs are

locally released in the ovaries. Although, the overall amount was rather small in our study, this effect should be considered and further investigated in future drug delivery studies.

5. Conclusion

By use of *in vivo* fluorescence imaging, we detected the accumulation of nanoparticles, nanocapsules and nanosized lipid emulsions in specific locations in the rodent ovaries. This effect was further characterized by *ex vivo* fluorescence imaging and CLSM. The investigated nanocarrier systems were completely differently composed, including multiple excipients, carrier sizes and surfaces. Based on the extensive *in vivo* and *ex vivo* studies it was found that the enrichment seems to be size dependent: whereas, polymers ≤ 35 nm diameter were not accumulated, all tested nanocarrier batches with diameters between 45 and 350 nm highly accumulated in the ovaries. A comparison of 3 nanoparticle batches varying in size led to the conclusion that bigger particles seemed to be more accumulated than smaller ones although this is based on a limited number of experiments. Finally it has to be noted that the accumulation of the nanocarriers in the ovaries does not necessarily need to result in a risk for the widespread use of nanoscaled carrier systems in medicine. Especially due to the fact that the accumulation is limited to special regions in the ovaries, the toxic risk for humans might be rather low. However, this effect needs to be further investigated, particularly also in other species to elucidate the mechanism of accumulation. But also the chances of these results for a new ovarian targeted therapy should be taken into consideration. Our results strongly emphasise the relevance of early explorative *in vivo* studies in the development of drug delivery systems using sensitive analytical imaging techniques, like fluorescence imaging using NIR fluorescence dyes.

Acknowledgements

Jürgen Vogel and Marcus Niepel are acknowledged for supporting the confocal microscopic measurements and Gerd Hause for performing the frozen section slides. We thank also Martina Henniecke and Constanze Gottschalk for the animal care. The *in vivo* studies were partly supported by the Federal State of Saxonia Anhalt (FKZ 3646A/0907) and the Deutsche Forschungsgemeinschaft (MA 1648/7-1). The Deutsche Forschungsgemeinschaft further supported the confocal microscopy studies (LSM: INST 271/250-1).

References

- [1] S.S. Feng, New-concept chemotherapy by nanoparticles of biodegradable polymers: where are we now? *Nanomedicine* 1 (2006) 297–309.
- [2] S.M. Moghimi, Mechanisms of splenic clearance of blood-cells and particles - towards development of new splenotropic agents, *Adv. Drug Deliv. Rev.* 17 (1995) 103–115.
- [3] I. Brigger, C. Dubernet, P. Couvreur, Nanoparticles in cancer therapy and diagnosis, *Adv. Drug Deliv. Rev.* 54 (2002) 631–651.
- [4] S.S. Suri, H. Fenniri, B. Singh, Nanotechnology based drug delivery systems, *J. Occup. Med. Toxicol.* 2 (2007) 16.
- [5] O.C. Farokhzad, R. Langer, Impact of nanotechnology on drug delivery, *ACS Nano* 3 (2009) 16–20.
- [6] V. Wagner, A. Dullaart, A.K. Bock, A. Zweck, The emerging nanomedicine landscape, *Nat. Biotechnol.* 24 (2006) 1211–1218.
- [7] H.C. Fischer, W.C.W. Chan, Nanotoxicity: the growing need for *in vivo* study, *Curr. Opin. Biotechnol.* 18 (2007) 565–571.
- [8] S.E. Dunn, A.G.A. Coombes, M.C. Garnett, S.S. Davis, M.C. Davies, L. Illum, *In vitro* cell interaction and *in vivo* biodistribution of poly(lactide-co-glycolide) nanospheres surface modified by poloxamer and poloxamine copolymers, *J. Control. Release* 44 (1997) 65–76.
- [9] R. Nakaoka, Y. Tabata, T. Yamaoka, Y. Ikada, Prolongation of the serum half-life period of superoxide dismutase by poly(ethylene glycol) modification, *J. Control. Release* 46 (1997) 253–261.
- [10] T. Yamaoka, Y. Tabata, Y. Ikada, Comparison of body distribution of poly(vinyl alcohol) with other water-soluble polymers after intravenous administration, *J. Pharm. Pharmacol.* 47 (1995) 479–486.
- [11] H.S. Choi, W. Liu, P. Misra, E. Tanaka, J.P. Zimmer, B.I. Ipe, M.G. Bawendi, J.V. Frangioni, Renal clearance of quantum dots, *Nat. Biotechnol.* 25 (2007) 1165–1170.

- [12] D.C. Litzinger, A.M.J. Buiting, N. Vanrooijen, L. Huang, Effect of liposome size on the circulation time and intraorgan distribution of amphiphatic poly(ethylene glycol)-containing liposomes, *Biochim. Biophys. Acta, Biomembr.* 1190 (1994) 99–107.
- [13] D.X. Liu, A. Mori, L. Huang, Role of liposome size and res blockade in controlling biodistribution and tumor uptake of GM1-containing liposomes, *Biochim. Biophys. Acta* 1104 (1992) 95–101.
- [14] A. Schädlich, C. Rose, J. Kuntsche, H. Caysa, T. Mueller, A. Göpferich, K. Mäder, How stealthy are PEG-PLA nanoparticles? An NIR in vivo study combined with detailed size measurements, *Pharm. Res.* 28 (2011) 1995–2007.
- [15] A. Schädlich, H. Caysa, T. Mueller, C. Rose, A. Göpferich, J. Kuntsche, K. Mäder, Tumor accumulation of NIR fluorescent PEG-PLA nanoparticles: Impact of particle size and human xenograft tumor model, *ACS Nano* 5 (2011) 8710–8720.
- [16] A. Besheer, T.C. Hertel, J. Kressler, K. Mäder, M. Pietzsch, Enzymatically catalyzed HES conjugation using microbial transglutaminase: proof of feasibility, *J. Pharm. Sci.* 98 (2009) 4420–4428.
- [17] F. Leblond, S.C. Davis, P.A. Valdes, B.W. Pogue, Pre-clinical whole-body fluorescence imaging: Review of instruments, methods and applications, *J. Photochem. Photobiol. B* 98 (2010) 77–94.
- [18] I. Texier, M. Goutayer, A. Da Silva, L. Guyon, N. Djaker, V. Josserand, E. Neumann, J. Bibette, F. Vinet, Cyanine-loaded lipid nanoparticles for improved in vivo fluorescence imaging, *J. Biomed. Opt.* 14 (2009).
- [19] J. Chen, I.R. Corbin, H. Li, W.G. Cao, J.D. Glickson, G. Zheng, Ligand conjugated low-density lipoprotein nanoparticles for enhanced optical cancer imaging in vivo, *J. Am. Chem. Soc.* 129 (2007) 5798–5799.
- [20] J. Hardin, Confocal and Multi-Photon Imaging of Living Embryos, in: J.B. Pawley, B.R. Masters (Eds.), *Handbook of Biological Confocal Microscopy*, J. Biomed. Opt., 43, 2008, p. 760.
- [21] F. Rashid, R.W. Horobin, Interaction of molecular probes with living cells and tissues, *Histochem. Cell Biol.* 94 (1990) 303–308.
- [22] H.J. Lim, M.J. Parr, D. Masin, N.L. McIntosh, T.D. Madden, G.Y. Zhang, S. Johnstone, M.B. Bally, Kupffer cells do not play a role in governing the efficacy of liposomal mitoxantrone used to treat a tumor model designed to assess drug delivery to liver, *Clin. Cancer Res.* 6 (2000) 4449–4460.
- [23] S. Petersen, A. Fahr, H. Bunjes, Flow cytometry as a new approach to investigate drug transfer between lipid particles, *Mol. Pharm.* 7 (2010) 350–363.
- [24] A.C. Faure, S. Dufort, V. Josserand, P. Perriat, J.L. Coll, S. Roux, O. Tillement, Control of the in vivo biodistribution of hybrid nanoparticles with different poly(ethylene glycol) coatings, *Small* 5 (2009) 2565–2575.
- [25] M. Goutayer, S. Dufort, V. Josserand, A. Royère, E. Heinrich, F. Vinet, J. Bibette, J.L. Coll, I. Texier, Tumor targeting of functionalized lipid nanoparticles: assessment by in vivo fluorescence imaging, *Eur. J. Pharm. Biopharm.* 75 (2010) 137–147.
- [26] S.D. Tröster, U. Müller, J. Kreuter, Modification of the body distribution of poly(methyl methacrylate) nanoparticles in rats by coating with surfactants, *Int. J. Pharm.* 61 (1990) 85–100.
- [27] R. Perez-Soler, G. Lopez-Berestein, M. Jahns, K. Wright, L.P. Kasi, Distribution of radiolabeled multilamellar liposomes injected intralymphatically and subcutaneously, *Int. J. Nucl. Med. Biol.* 12 (1985) 261–263.
- [28] K.J. Harrington, G. Rowlinson-Busza, K.N. Syrigos, P.S. Uster, R.M. Abra, J.S.W. Stewart, Biodistribution and pharmacokinetics of ¹¹¹In-DTPA-labelled pegylated liposomes in a human tumour xenograft model: implications for novel targeting strategies, *Br. J. Cancer* 83 (2000) 232–238.
- [29] G. Thurston, J.W. McLean, M. Rizen, P. Baluk, A. Haskell, T.J. Murphy, D. Hanahan, D.M. McDonald, Cationic liposomes target angiogenic endothelial cells in tumors and chronic inflammation in mice, *J. Clin. Invest.* 101 (1998) 1401–1413.
- [30] S.D. Tröster, J. Kreuter, Influence of the surface properties of low contact angle surfactants on the body distribution of ¹⁴C-poly(methyl methacrylate) nanoparticles, *J. Microencapsul.* 9 (1992) 19–28.
- [31] T.J. Daou, L. Li, P. Reiss, V. Josserand, I. Texier, Effect of poly(ethylene glycol) length on the in vivo behavior of coated quantum dots, *Langmuir* 25 (2009) 3040–3044.
- [32] L.P. Reynolds, A.T. Grazul-Bilska, D.A. Redmer, Angiogenesis in the corpus luteum, *Endocrine* 12 (2000) 1–9.

Non-invasive in vivo characterization of microclimate pH inside in situ forming PLGA implants using multispectral fluorescence imaging

Andreas Schädlich, Sabine Kempe, Karsten Mäder

Faculty of Biosciences, Institute of Pharmacy, Martin Luther University Halle-Wittenberg, Wolfgang-Langenbeck-Str. 4, 06120 Halle (Saale), Germany

Corresponding author: Tel.: +49 3455525167; Fax: +49 3455527029.

E-mail address: karsten.maeder@pharmazie.uni-halle.de

Abstract

The pH inside drug delivery systems directly influences the physical and chemical behavior of its ingredients especially their stability and solubility. Therewith the release performance of the systems and the pharmacological effect is affected. Thus the determination of the microclimate pH (μpH) inside the drug delivery systems is of great interest.

Implants are considered to be attractive parenteral drug delivery systems for the long-term application of drugs and of peptides. Poly(lactide-co-glycolide) (PLGA) is the most frequently used and extensively researched polymer for the implant preparation. It is known that the microclimate pH (μpH) in PLGA implants can drop dramatically causing peptide or protein instabilities as well as drug insolubilities and further decomposition. Although the internal pH behavior of PLGA implants and microparticles has been studied *in vitro*, no direct and continuous investigations about the μpH in *in situ* forming implants have been published yet. This is caused by the absence of non-invasive methods to measure the pH value *in vivo*. Thus it is unclear whether *in vitro* pH measurement results are assignable or not. In this study the μpH of *in situ* forming PLGA implants were mapped *in vitro*, *in vivo*, and *ex vivo*. A non-invasive *in vivo* pH measurement method using the multispectral Maestro fluorescence imaging system was explored. Performed *in vivo* experiments did not only enable to make conclusions regarding the μpH . Also expectations regarding the solvent replacement in the core area of the implant and of the release profile of the hydrophilic substances could be made.

The experiments emphasized the broad application range of the fluorescence imaging technique to non-invasively monitor the μpH values in drug delivery systems *in vivo*.

Introduction

In the last 20 years parenteral drug delivery systems especially for the long-term protein and peptide release have received increasing research interests. They enable controlled release of the incorporated therapeutic agents for time periods lasting over several days, weeks up to months. This enhances the compliance of patient by reducing the application frequency of the therapeutic agents. Furthermore, these depot formulations can minimize undesirable side effects caused by fluctuating drug plasma levels. Already marketed controlled release systems used for the application of peptides are microspheres, solid implants, and *in situ* forming implants (ISFI) [1; 2]. These systems provide flexible delivery characteristics. However, these possess certain advantages and disadvantages. Microspheres for example have to be thoroughly suspended prior the injection in an oily or aqueous liquid, in order to achieve the complete injection of the entire dose desirable. Solid implants, normally in cylindrical geometry, can directly be deposited *subcutaneously* (*s.c.*) via large needles. This however, might be painful for the patient and limits the application doses [1; 2]. Nevertheless, the versatility of possible sizes, different materials and shapes permits the adjustment of drug release rates from solid implants. *In situ* forming systems can be injected with a syringe through a small needle into the target site, where the implant is formed immediately.

The implants can be formed either by *in situ* cross-linking of monomers or by *in situ* solidifying of polymeric materials due to the changes in the environmental pH or temperature. Another method is based on the solvent removal which induces polymer precipitation. Within this approach, the polymeric matrix material is dissolved in a water-miscible, biocompatible solvent. Upon administration, the polymer precipitates due to the replacement of the solvent with the tissue fluids. Potential disadvantages to be considered are the inconsistent shapes of the formed implant, undesired burst effects and possible solvent toxicity [3; 4]. Compared to the pre-shaped parenteral depot systems, biodegradable implants formed by injectable fluids have the advantages being both, less invasive and less painful.

Among plenty of the investigated synthetic and natural polymers the biodegradable PLGA is most widespread utilized for implants. PLGA is well characterized for its safety and biocompatibility record data [1; 5].

PLGA is used in several commercially available parenteral controlled release products like Sandostatin LAR, Lupron Depot, Decapetyl SR, Suprecur MP and Risperdal Consta [6-9]. Two other marked products deploying phase separation by solvent exchange technique based on a PLGA are Atridox [6] and Eligard [7]. PLGA is dissolved in the water miscible, physiological compatible organic solvent N-methyl-2-pyrrolidone (NMP). However, there is controversial data on application of NMP published in the literature. It is described that NMP can cause the degradation of proteins as well as of PLGA and may damage the muscle tissue [10-12]. Emerging scientific data shows that PEG 400 can be an alternative non-toxic solvent for PLGA [4; 13].

Besides the use of the right solvent, another property of the PLGA implants, proved to be critical especially for the delivery of proteins and peptides as well as of poorly water soluble drugs. This is caused by the accumulation of the PLGA degradation products in the implant which are acidic in its nature [14]. *In vitro* experiments with PLGA microspheres emphasized that the pH value in the microspheres during the incubation period under physiologic conditions can drop from pH 7.4 to approximately pH 3 [15; 16]. This dramatic change in the pH can cause protein instabilities or pH-dependent changes in the drug solubility- as well as decomposition- and deactivation processes [14; 17; 18]. It has been shown, that the pH drop can result in the deformylation of the incorporated vincristin and in the acid-induced aggregation of bovine serum albumin (BSA) [19; 20]. In addition, also accelerated polymer degradation at low pH-values can cause additional protein instabilities and strongly influence the release profiles. Therefore, the μ pH quantification and determination of other affecting factors is critical for the better understanding of PLGA delivery systems and for the formulation design. Thus the methods to determine the microclimate pH (μ pH) inside *in situ* forming implants are of great interest. However, techniques that enable to continuously and non-invasively measure the μ pH are missing. Compared to the overall amount of published data based on PLGA drug delivery systems only few articles dealing with the measurement of the μ pH. Those are predominantly limited to the *in vitro* experiments.[16; 19; 21-23]. Many research groups have used indirect methods by measuring pH values in the incubation media with pH-meter and an attached microelectrode [24]. By this, assumptions of the change of the internal μ pH and the accumulation of degradation products were

made. These were based on the acidic liberation of degradation products which consequently changed the pH of the incubation media. However, this pH drop of the media may further accelerate ester hydrolysis and thus does not represent the *in vivo* conditions.

Only a few numbers of techniques are available to measure *in vitro* the μpH directly in PLGA systems. Potentiometric measurements of μpH values were performed by using the PLGA coated glass electrodes [20]. Within this approach it has been shown that the μpH varied with the thickness of the coating. Highly acidic μpH values (pH 2 - 3.5) were measured after one day of incubation in neutral buffer solution. After one week neutral values (μpH 6.5) were detected in the case of 7 μm thick coatings. Whereas, the μpH remained acidic up to 4 weeks in the case of 30 μm - 250 μm thick films. Others characterized injection-molded implants by puncturing the tissues surrounding the implants with a microelectrode [25]. However, the experimental setup of using an electrode is not suited for small scale systems like microspheres or even for non-invasive *in vivo* application.

Other groups are dealing with the visualization of acidic μpH values in PLGA microspheres using confocal microscopy with pH sensitive dyes [22; 23; 26]. The confocal laser scanning microscope (CLSM) technique combines non-invasive pH measurements with the visualization of the pH allocation. Therefore, pH sensitive fluorescence dyes like SNARF-1 were incorporated into PLGA spheres. The emission spectrum of this dye undergoes specific pH-dependent wavelength shift. This enables calculating the ratio of the fluorescence intensities based on two emission wavelengths and consequently to determine and to visualize the local μpH value [22]. *In vitro* experiments with PLGA microspheres using CLSM confirmed a pH drop to pH 3 [15; 16]. Thus CLSM findings proofed potentiometric measured *in vitro* results and enabled to measure the μpH also in micrometer structures. Nevertheless, light transmission through the measurement object is a prerequisite for CLSM measurements. Therefore, it is challenging to transfer the measurement principles to *in vivo* studies where they would be by default limited to the skin surface [27].

Other approaches using ^{31}P -Nuclear Magnetic Resonance (NMR) probes [16] or to pH sensitive spin probes which are analyzed by electron paramagnetic resonance (EPR) spectroscopy [21; 28-30]. Until now EPR was the only technique which allowed to demonstrated that pH drops down to pH 2 can occur inside PLGA implants after they were administered s.c. to mice *in vivo* [28]. However, EPR spectroscopy is limited to the measurement of the average pH values. The visualization of pH distributions in implants by this method is currently not possible.

Although, it can be expected that under *in vivo* conditions complex factors like perfusion, body liquids, enzymes, elimination processes strongly influence the μpH in PLGA implants the lack of techniques available to measure the μpH in *in situ* forming implants non-invasively *in vivo* hampered further research [13; 31; 32]. Former multispectral *in vivo* fluorescence imaging studies of water soluble polymers and nanocarriers demonstrated, that the technique is able to detect reproducible smallest spectral emission changes of the peak profile *in vivo* [33-35]. However, information if this technique can also be applied to track *in vivo* for the first time and in detail μpH changes of *in situ* forming implants was missing. As *in vivo* fluorescence measurements of the pH values using non-invasive imaging are hampered by a multitude of influencing factors like auto-fluorescence of skin, lack of capable dyes with sufficient quantum yields, wavelength dependent light absorption, intensity variations, possible bleaching and many others, detailed *in vitro* and *ex vivo* experiments had to be performed prior *in vivo* statements about the pH behavior could be made. Based on the knowledge gained from numerous performed pretests *in vivo* fluorescence imaging studies were designed in order to non-invasively determine the μpH of the PLGA implants *in vivo*. In addition comparative pH *in vitro* EPR studies and *in vivo* MRI imaging were performed to investigate the implant shape and to compare the obtained findings with previous published results.

Materials and Methods

A 1. Materials

PLGA (Resomer RG503H, poly(lactide-co-glycolide), molar ratio 50:50, Mw = 34 kDa), was received from Boehringer Ingelheim, Germany. All buffer substances (citric acid/ di-sodium hydrogen phosphate (buffer 1), potassium dihydrogen phosphate/ di-sodium hydrogen phosphate (buffer 2) and mono-sodium phosphate/ di-sodium hydrogen phosphate (buffer 3) as well as 3 Hanna pH standard buffer solutions (pH 4.01, 7.01 and 10.01) were purchased from Sigma Aldrich, Germany. The fluorescence dye SNARF-4F (5-(and-6)-carboxylic acid, pKa 6.4 [36]) was purchased from Invitrogen, Germany. The EPR probes AT (4-Amino-2,2,5,5-tetramethyl-3-imidazoline-1-oxyl, pKa 6.1 [37]) and HM (2,2,3,4,5,5-Hexamethyl-imidazoline-1-oxyl, pKa 4.7 [37]) were obtained from the Institute of Chemical Kinetics and Combustion, Russia. Lutrol 400 (PEG 400) was a kind gift from BASF, Germany.

A 2. Implant preparation

30 % (w/v) of PLGA were dissolved in PEG 400 under stirring at room temperature. Either one of the spin probes AT or HM (400 µg/mL) used for EPR experiments or the fluorescence dye SNARF-4F (40.0 µg/mL) were homogeneously incorporated.

A 3. EPR experiments

The EPR *in vitro* experiments followed the recently published protocol [38]. Calibration curves of both used pH-sensitive nitroxide spin probes (AT and HM) were made over a pH range from pH 1.0 to pH 12.0 [39]. Therefore, the recorded EPR spectra (1st derivative, measured at 1.3 GHz) were integrated and the distances between the 1st and the 3rd peaks were determined as the magnitude of $2a_N$ (hyperfine splitting parameter). Corresponding pH-calibration curves were obtained by a sigmoid Boltzman fit. To achieve a sufficient signal-to-noise ratio of the EPR spectra during the *in vitro* pH measurements 0.2 mmol/L spin probe were added to 50 mL phosphate buffer (buffer 3, 0.1 M, pH 7.4; 37 °C). 200 µL of the prepared implant dispersions (containing the spin probe AT or HM) were injected through a needle (25 gauge) into perforated plastic *Eppendorf* cups. Immediately afterwards, the cups were placed into 100 mL flasks which contained 50 mL buffer. Thereafter, the flasks were placed on an incubation shaker (30 rpm, 37 °C). For the measurements, the cups were removed from the buffer, dried with a cellulose tissue and wrapped by a plastic foil to prevent drying. Subsequently they were transferred to the EPR spectrometer, measured and afterwards replaced to the buffer after removing the foil. The incubation buffer was exchanged every second day to prevent the accumulation of the degradation products. The EPR spectra were obtained using an L-Band (1.3 GHz) spectrometer from Magnostech, Germany equipped with a re-entrant resonator. The detailed measurement parameters were set as follows: field centre 49 mT, scan range 10 mT, scan time 30 sec, modulation amplitude 0.1 mT. All measurements were performed triplicate, data were reported as mean ± SD (standard deviation).

A 4. Fluorescence imaging

All *in vivo* experiments complied with the standards for the usage of animal subjects as stated in the guideline from the animal care and use committee of Saxony-Anhalt. The housing, handling and measuring of the nude mice was performed as published recently [33; 35; 40]. 200 µL of the PLGA/PEG 400 dispersion, loaded with

SNARF-4F were slowly s.c. injected into the neck or to both abdominal sides of the thighs, depending on the respective experiment. For the injection as well as prior each measurement mice were anesthetized.

All *in vitro* and *in vivo* fluorescence imaging experiments were carried out using the Maestro *in vivo* fluorescence imaging system from Cambridge Research & Instrumentation (Cri), United States (now PerkinElmer (Caliper Life Sciences), United States and the Maestro software (version 2.10). The equipment was used applying previously investigated measurement settings [33; 34; 40]. Briefly, a Cemax-type 300 Watt Xenon lamp and two, the green and yellow filter-sets were used. Multispectral imaging cube sets were acquired in 2 nm steps using automatic exposure times. Both filter sets were used simultaneously for the generation of each measurement file. Respective emission spectra as well as an auto-fluorescence signal as background were defined based on reference *in vitro* and *in situ* pH measurements. Therefore, *Eppendorf* cups with buffer solutions of defined pH values were placed s.c. under the skin of three sacrificed mice. The generated reference library allowed the visualization of the pH distribution as well as allocation of the dye. In addition averaged emission spectra of different regions of interest (ROI) were extracted from the measurement cubes. The ratios of the emission maxima were determined and corresponding μpH values were calculated.

A 5. Benchtop Magnetic Resonance Imaging (Bt-MRI)

Bt-MRI measurements were performed using a 20 MHz NMR benchtop system (prototype based on Maran DRX2, Oxford Instruments Molecular Biotools, UK). The system was equipped with a 23 mm sample access. The mice were placed on glass slides with a fixed inhalation mask for anesthetization. Same measurement parameters were used as published earlier [13]. Briefly, a standard spin-echo sequence was used with a spin echo time (TE) of 9.8 ms and a repetition time (TR) of 178 ms. 16 averages were applied resulting in an acquisition time of about 352 s for each image. The field of view was 40 mm x 40 mm had a resolution of 128 x 128 points.

Results and Discussion

A 6. *In vitro* EPR pH measurements

Non-destructive EPR spectroscopy was chosen as an established method to measure μpH values *in vitro* [29; 41]. The EPR experiments were performed to provide *in vitro* information as basis for future *in vivo* fluorescence imaging experiments. To achieve sufficient signal-to-noise ratio even over the long time release process, the pH sensitive spin probe was incorporated in both, the polymeric solutions and the incubation buffer. To assure that the spin probe containing buffer does not interfere with the μpH determination in the implants, the absorbed buffer was carefully removed prior the EPR measurements.

The used nitroxide probe is sensitive to changes of the μpH [41] as well as to the micro-polarity and micro-viscosity. Therefore, the spin probes migrated with the solvent outside the implant as the incorporated hydrophilic spin probes were readily soluble in PEG 400 and did not precipitate within the hydrophobic polymer matrix. After 6 h no solid signals were no more detectable indicating that the solvent exchange has been completed. This is in accordance with the previous results [13]. Due to the fact that the solvent replacement dominated in the first day of incubation at all investigated implants, no reliable data about the μpH within the first 24 hours could be obtained. Calculated pH values based on performed *in vitro* measurements are shown in Figure 1. It can be concluded that the pH decreased of pH within the first 6 days below pH 3 is caused by the accumulation of acidic degradation products in the implants.

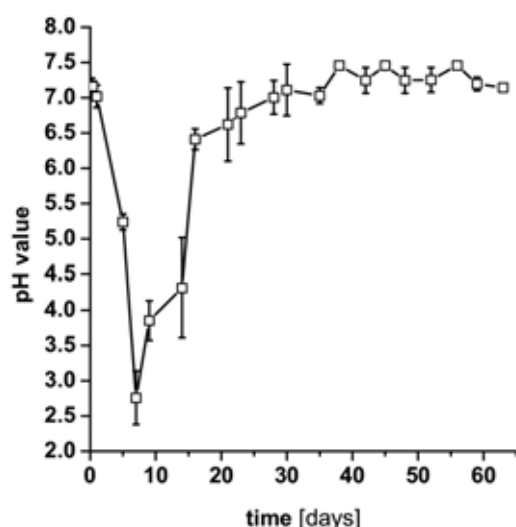


Figure 1: Time dependent pH change of PLGA implants, determined *in vitro* by EPR spectroscopy.

Afterwards, due to the increased pore formation, accompanied by medium exchange, the pH inside the implants rose again to the neutral range after 21 days.

Under the current conditions the EPR method was restricted to *in vitro* measurements. Therefore, further *in vitro* and *in vivo* experiments were focused on fluorescence imaging experiments investigating if the observed pH drop within the first week occurs also *in vivo*.

A 7. Evaluation a pH measurement method using fluorescence imaging

Many different fluorescence imaging systems are currently on the market [42]. Compared to those the Maestro imaging system allows multispectral analysis [43-45] and the export of spectral data as an ASCII-file, the American Standard Code for Information Interchange. Based on the Maestro system, emission spectra can be extracted from each pixel of the measurement cube but also from a group of pixels in a desired region of interest (ROI) within the cube [30]. This allowed both the external analysis of spectral intensities in spreadsheets as well as the image processing using the Maestro auto-fluorescence removal tools. To use these functionalities for *in vivo* pH measurements of PLGA implants, extensive preliminary *in vitro* experiments had to be performed. Therefore, different possibilities of pH calculations based on the spectral intensity values were evaluated. Due to the fact, that fluorescence intensities may vary in *in vivo* surroundings, dyes with pH-dependent wave length shifts of the emission spectra should be used [16; 22; 46]. Another important prerequisite for *in vivo* measurements is the necessity of using dyes with emissions above 550 nm, otherwise the emission of the dye would be overlaid by the auto-fluorescence of the skin. The SNARF dyes were the only commercially available ones which fulfilled these both requirements. Within this group of dye, SNARF-4F has the lowest pKa value (pKa of about 6.4). Dyes with low pKa values are needed to measure acidification processes in implants. Thus SNARF-4F was chosen to calculate pH values within this study. The chemical structure and the pH dependent equilibrium of SNARF-4F are shown in Figure 2. The chemical structures of the SNARF dyes exist like fluorescein in a 'closed' lactone and an 'open' quinoid form. The lactone form is dominant especially in non-aqueous environments and is non or only very weak fluorescent known also from fluorescein [47-49]. The ring opening of the lactone and its subsequent ionization at the different acidities (anion) of the microenvironment results in characteristic fluorescence emission maximums at two different wavelengths (using the Maestro system at 606 nm and 648 nm, see also Figure 3).

The pH dependent equilibrium can be used to measure fluorescence ratios reliably and to quantitatively determine pH values [48].

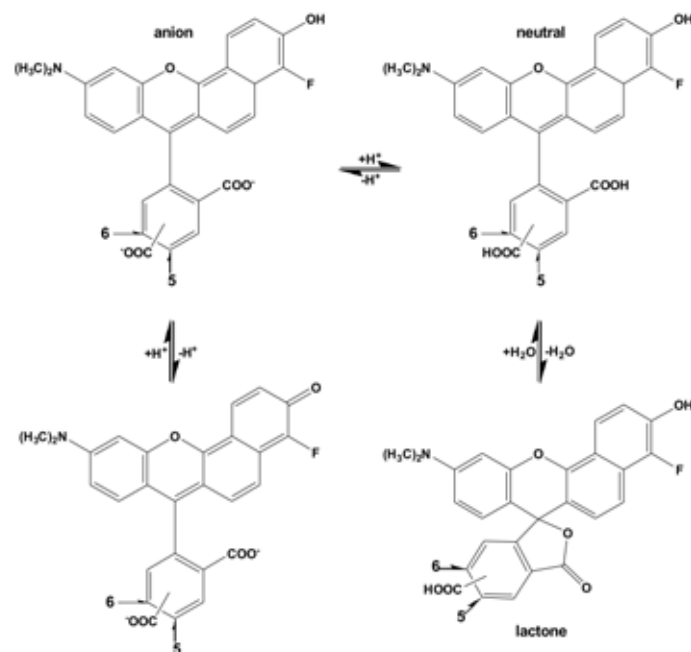


Figure 2: Chemical structure and the pH dependent equilibrium of SNARF-4F

The disturbing auto-fluorescence for s.c. measurements is mainly caused by the skin. To reduce the influence of spectral changes of the emission light due to the skin passage several measurement and calculation approaches were tested. The auto-fluorescence occurs mainly below 650 nm. Thus using two filter sets within one measurement, the green and the yellow one emphasized to be best suitable. Two filter sets reduced the influence of the auto-fluorescence signals. The obtained pH dependent emission spectra of SNARF-4F are shown in Figure 3.

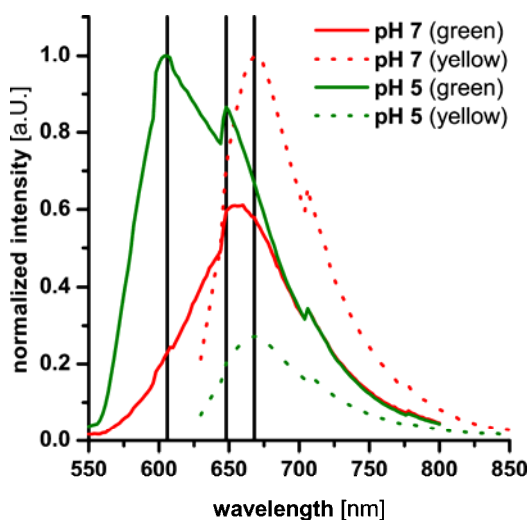


Figure 3: Normalized emission intensities of SNARF-4F in two different buffer solutions: pH 5 (green) and pH 7 (red), measured with the green filter set (line) and the yellow one (dashed). Three vertical, black lines refer to the emissions at 606, 648 and 668 nm, used for pH calculations.

Subtracting the intensity value at 668 nm (yellow filter set) from that measured at 606 nm (green filter set) and dividing the result by the intensity value at 648 nm (green filter set) was evaluated to be the best method for further pH calculation. The subtraction step reduced the influence of spectra broadening due to the emission spectra disturbing auto-fluorescence signals. The dividing step in the calculation eliminated the influence intensity variations due to both, varying dye concentrations as well as of different exposure times. The calculated pH dependent ratios are displayed in Figure 4 a. Reproducible pH values were also detected when measurements were performed with exposure times below or above the optimum.

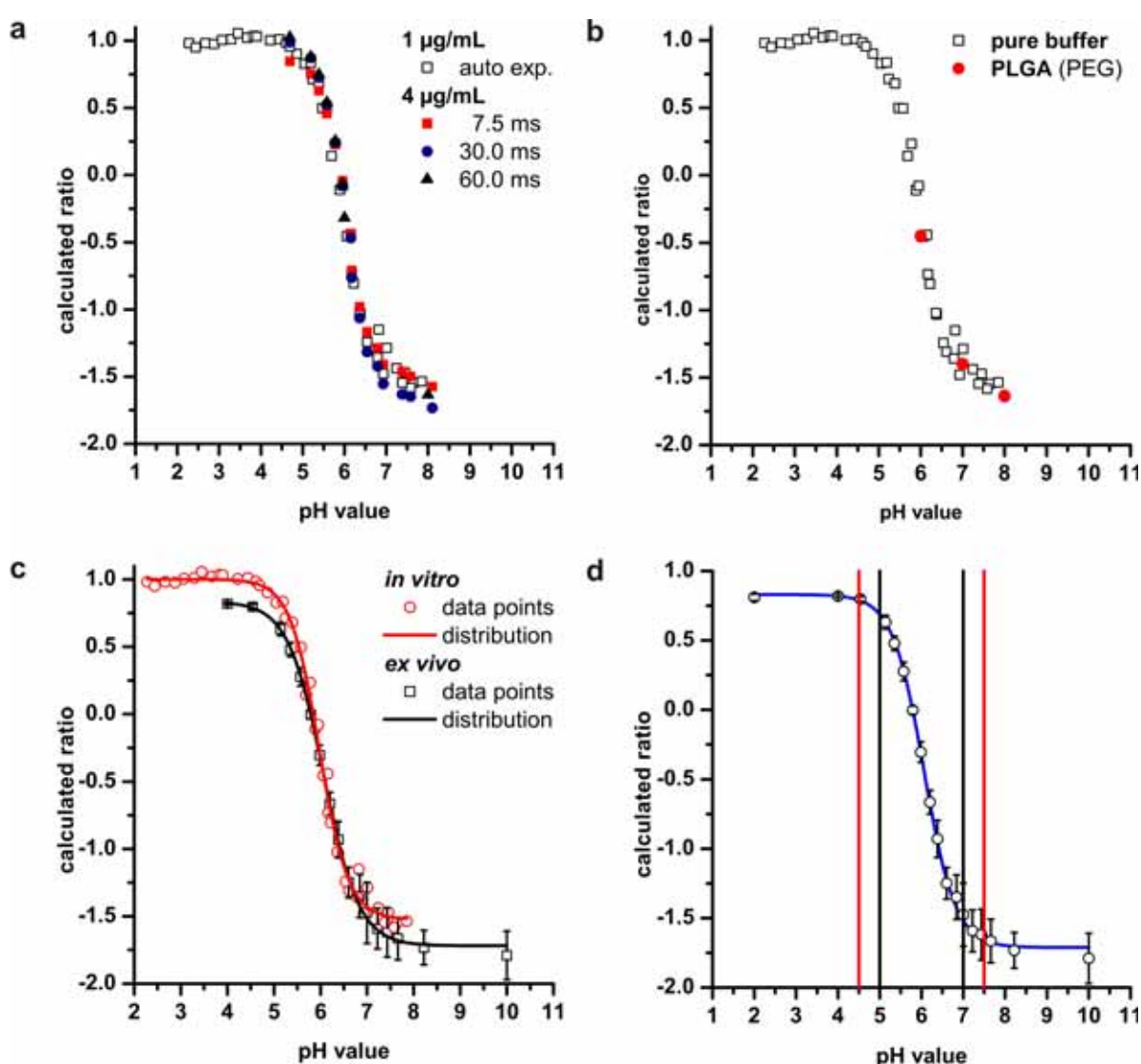


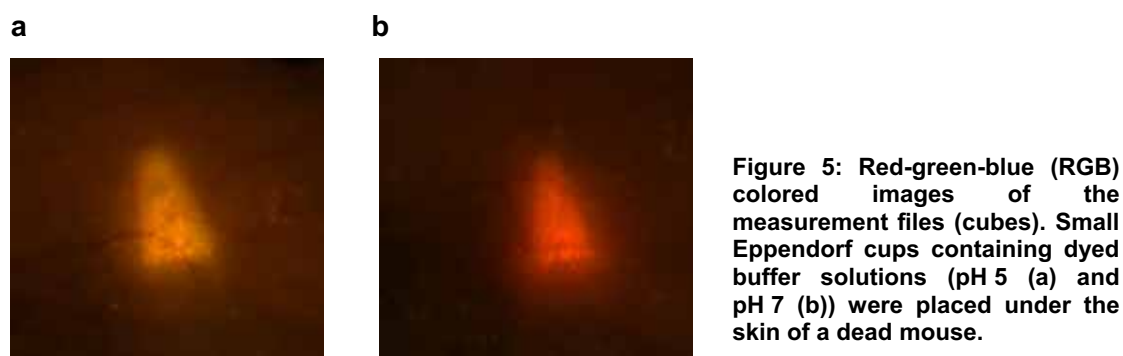
Figure 4: (a) Calculated ratios of pure pH buffer solutions as well as after varying dye concentration and exposure time. (b) Influence of PLGA/PEG400 to the pH calculation. (c) Boltzmann plots and respective raw data of *in vitro* and *s.c. ex vivo* measured pH solutions. (d) Boltzmann plot (blue) and limits of reproducible (black lines, at pH 5 and 7) and sufficient (red lines) pH calculation.

Supplemental material

(c) Characterization of *in situ* forming implants for potential controlled API release

The same method has been used to measure the pH values of buffer solutions after PLGA / PEG 400 mixtures were added. The results are displayed in Figure 4 b. The experiment results emphasized that the addition of the implant polymer has no influence to the reliable detection of the pH values.

The spectral shape of the detected emission spectra can be changed if the emitted light is passing tissues like the skin. This could falsify calculated pH values. In order to investigate this influence buffer containing *Eppendorf* cups were measured *subcutaneously* served for the calculation of a reference Boltzmann plot. Three dead mice varying in age (3, 6 and 12 months) and consequently in skin thickness and partly in skin compositions were used to increase the robustness of the resultant ratios. Obtained original measurement images of the two *Eppendorf* cups (pH 5 and pH 7) are shown in Figure 5. The resulted Boltzmann plot in comparison to the *in vitro* measured one is displayed in Figure 4 c. A shift of the *ex vivo* measured ratios to lower values has been observed.



The *ex vivo* measured Boltzmann plot was used for all further calculations. As depicted in Figure 4 d pH values can be calculated based on the obtained emission intensity ratios within the pH range of pH 4.5 to pH 7.5 (marked by red lines). However, determinations below pH 5 and above pH 7 are highly error-prone as small variations in calculated ratios highly influence the calculated pH value. Thus, fluorescence pH measurements can only be reproducibly performed at the range between pH 5 and pH 7 (marked in Figure 4 d by black lines).

It is also evident in Figure 4 d that error bars of calculated ratios increase to higher pH values. This can be explained by the emission spectra drop down at 606 nm (cp. Figure 3). Thus, the intensity value used for the pH calculation is highly influenced by the auto-fluorescence of the skin.

Further *ex vivo* experiments followed in order to investigate the optimum dye concentration. Therefore, *Eppendorf* cups with the buffer solutions varying in pH (pH 5, pH 6 and pH 7) and in dye concentrations (0.25, 0.50, 0.75 and 1.00 $\mu\text{g/mL}$)

were analyzed. The results are shown in Figure 6 a. It has been observed that low pH values can be reproducibly measured even at low dye concentrations. Same results were found at pH 6 although the results were less accurate. For buffer solutions of pH 7 a trend to lower pH values was identified if the dye concentration is reduced. Due to the decreased emission intensities the influence of the auto-fluorescence of the skin increased. As discussed above, the background signal influences especially the intensity value at 606 nm (cp. Figure 3). Consequently this has an impact to the calculation of higher pH values (pH 7) if samples are low concentrated. Based on the experimental results it can be concluded that SNARF-4F concentrations of 1.00 $\mu\text{g/mL}$ or above are optimal for reproducible pH calculations.

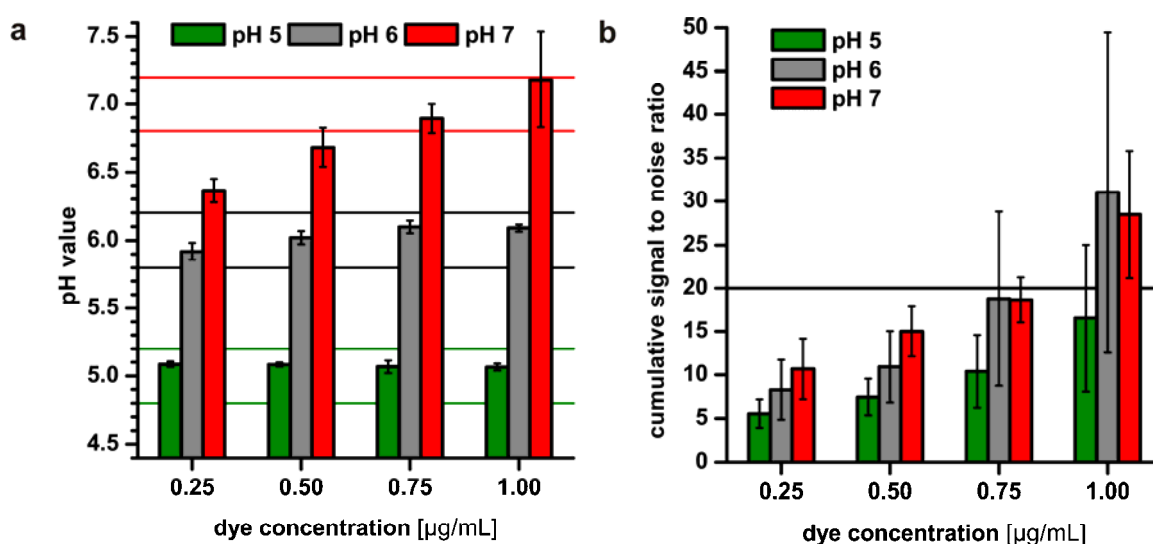


Figure 6: (a) Concentration-dependent pH detection of *s.c. ex vivo* measured *Eppendorf* cups (pH 5, pH 6 and pH 7). (b) Results of the corresponding cumulative signal to noise ratios. The black line marks the lower signal to noise ratio limit for pH determinations.

As dye concentrations can not be determined *in vivo*, cumulative signal to noise ratios were calculated and evaluate in order to ensure correct pH determinations. Therefore, *in vitro* data shown in Figure 6 a was used to calculate cumulative signal to noise ratios for all tested concentrations. As it is visible in Figure 6 b, reproducible pH values can be calculated if the calculated cumulative signal to noise ratio is 20 or above.

Additionally to the pH calculation method also the visualization of the pH allocation using the Maestro imaging system was evaluated *in vitro*. Therefore, emission reference spectra of pH 5 and pH 7 (cp. Figure 3) were defined for the spectral library. Thus, each pixel of the multispectral measurement cube could be assigned in the automatic unmixing process by the software to the defined emission reference spectra of pH 5 or pH 7 considering also ratios between both of them. The pixel is

displayed in the color which was manually pre-assigned to the respective reference spectrum. This allowed visualizing the pH allocation in the desired measurement range of the SNARF-4F dye. If no conformity was found the pixel has been displayed in black.

The reproducibility of the image processing was evaluated with the PLGA / PEG 400 dispersion planned to be used in the upcoming *in vivo* experiments. The mixture was placed on a flat bowl and imaged time dependently before and after adding buffer solutions varying in pH. Figure 7 a shows the obtained and unmixed RGB images. Pixels which were allocated to pH 5 are displayed green; others, which were assigned to pH 7 are red. The background signal was set to black.

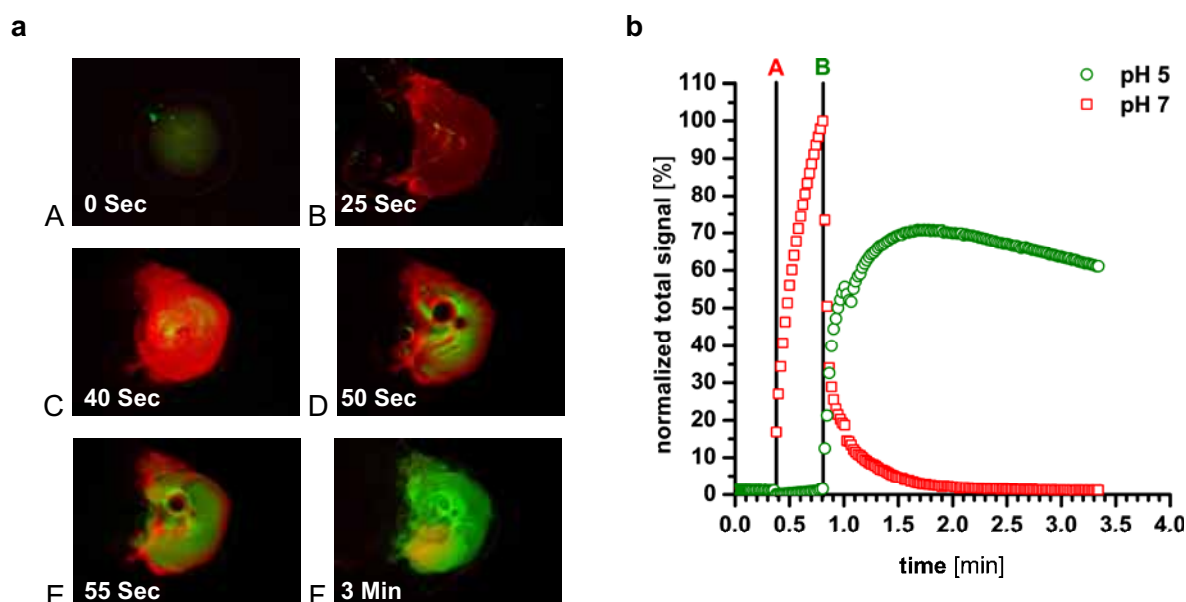


Figure 7: (a) Time-dependent, unmixed RGB images of a PLGA implant before buffer was added (A), directly after buffer addition (B), shortly before (C) during (D) and after (E) pH readjustment to pH 5 and at the end (F) of the experiment. Pixels were colored, depending to their allocation to pH 5 (green) or pH 7 (red). (b) Analyzed total signals of pH 5 and pH 7 of the same *in vitro* experiment. A marks the time point when buffer solution (pH 7) was added and B the point where the pH was adjusted to pH 5.

As it is seen in Figure 7 a (A) the dye is quenched nearly completely in pure PLGA/ PEG 400 solutions. Only slight fluorescence signal was detectable. It can be expected that the absence of water promotes the formation of the lactone form which is non-fluorescent. After adding buffer solution with pH 7 PEG 400 mixed with water, the entrapped dye immediately got fluorescent as seen in Figure 7 a (B). Even smallest amounts of water result in a ring opening of the lactone. The fluorescence intensity increased within the continuous permeation of water (Figure 7 a (C)). As PLGA is not water-soluble it precipitated immediately and the implant formed.

As shown in Figure 7 a (B and C) after a few seconds all pixels of the fluorescent PLGA implant in the obtained image were allocated by the Maestro software to the reference spectra of pH 7 and thus displayed in red.

Afterwards, the pH of the surrounded buffer solution was adjusted to pH 5. Consequently also the buffer in the surface of the PLGA implant decreased. As it is visible in the images of Figure 7 a (C to E), the green amounts in the images increased over time. This evidenced by the observed pH change from pH 7 to pH 5. After 3.3 min nearly all pixels of the PLGA implant were allocated to the emission spectra of pH 5 (Figure 7 a (F)). The experiment verified that the visualization of pH values within the pH range between pH 5 and pH 7 is possible.

The underlying data of the RGB images shown respectively in Figure 7 a were used to calculate additionally the total signals for pH 5 as well as for pH 7. Therefore, the intensity ratio between pH 5 and pH 7 of each pixel of all single measurement files was calculated. All intensity values of the pixels assigned pH 5 or to pH 7 were summated to the respective total signal. The resulted values are displayed in Figure 7 b and confirmed the visual findings. Nearly no fluorescence has been detected at the beginning of the experiment. After adding the buffer solution (pH 7, marked by the first black line, A), the total intensity increased rapidly. After 45 s the buffer pH was lowered to pH 5 (marked by the second black line, B). Consequently, the total intensity of the detected pH 7 signal decreased continuously and reached zero after about 2 min. During this time the total intensity of pH 5 increased. The maximum total signal was measured after approximately 90 s. Thereafter, the total signal of the hydrophilic SNARF-4F dye decreased continuously. This can be explained by the release of the dye out of the implant, by what the total pixel intensity decreased.

A 8. *In vivo* dye distribution studies

First, *in vivo* studies were initiated by injecting the PLGA / PEG 400 dispersion containing the SNARF-4F dye into the abdominal side of the both thighs. The mixture itself was visually colorless. Time-dependent images after 15 min, 60 min and 48 h are shown in Figure 8. The fluorescence signal assigned to the dye emission spectra was colored in magenta. 15 min after injection a distinct fluorescence signal was detectable. This is caused by the exchange of PEG 400 with the aqueous body fluids. The measurable fluorescence intensity increased as it was also observed in the *in vitro* experiment. The maximum intensity was measured after about 60 min indicating that most of the PEG 400 was already exchanged. This is in accordance with the previously published *in vitro* EPR results [13]. Furthermore, as seen in

Supplemental material

(c) Characterization of *in situ* forming implants for potential controlled API release

Figure 8, the physically entrapped dye is spread from the injection site into the surrounded body tissue. The solidified PLGA implants at both sides of the thighs are still detectable after 2 days indicating that sufficient dye amounts were still entrapped in the PLGA implants. Released dye molecules diffused to the surrounding tissues and were eliminated quickly as the dye is hydrophilic.

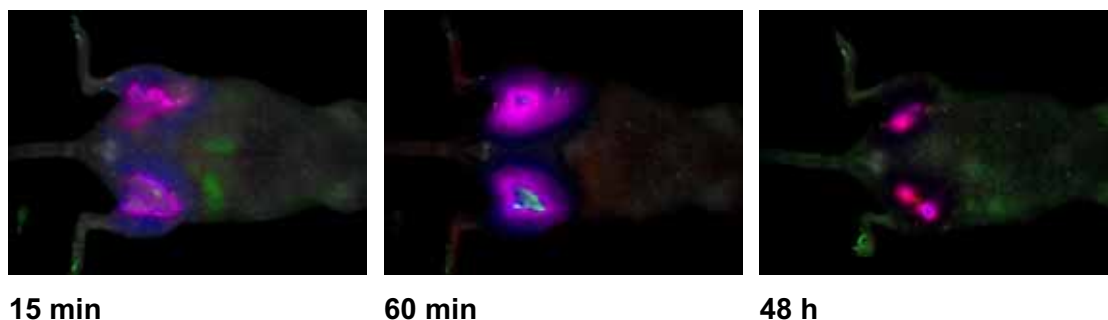


Figure 8: Time dependent, unmixed RGB images of the abdominal site of a mouse. The isolated SNARF-4F signal was colored in magenta. The PLGA / PEG mixture was ventrally s.c. injected to both sites of the hind legs.

The implant was deformed over time due to the movement of the mouse between the experimental measurements. This hampered surface analyzes. Therefore, the injection site was changed for followed long-term experiments. The PLGA / PEG 400 mixture was henceforth injected into the neck of the mice subcutaneously. The resultant non-invasively measured images of a mouse using the 'compared' jet color visualization method are displayed in Figure 9. This function enabled to display SNARF-4F emission intensity distributions independently from the pH. In addition, it facilitated to compare images of different measurements even if they were captured with different measurement settings like exposure times and binning. Thus, time dependent image analysis of intensity changes can be performed.

Already 3 hours after injection, wide parts of the already formed implant were displayed in dark red indicating high fluorescence intensities. This confirmed previous *in vivo* experiment (see Figure 8) and is in concordance with previous ESR and MRI studies [13]. These former studies showed that initially a thin polymer shell was formed that entrapped the PLGA / PEG 400 solution. Within the further exchange of PEG 400 by water through the thin shell the polymer precipitation process proceeded. The solvent / non-solvent exchange observed was very fast, after 1 h about 70 % of the PEG 400 was replaced by water [13]. This has been also confirmed by the present study. The outer edge of the implant is indistinct and light blue confirming the diffusion of the dye out of the implant. Still 1 day after injection wide parts of the implant were highly fluorescent. Therefore, it can be concluded that small amounts of the aqueous body liquids were still present in the matrix. The

Supplemental material

(c) Characterization of *in situ* forming implants for potential controlled API release

fluorescence intensity decreased however within the next 3 days. This can be explained by the discharge of remaining hydrophilic body liquids out of the implant and the final solidification of the implant matrix. Thus, the remaining dye in the implant is quenched. 4 days after injection the intensity at was lowest level indicating that the implant was completely solidified. As PLGA is insoluble in aqueous solvents liquids are removed during the solidification and equilibrium of the dye is shifted to the non-fluorescent form.

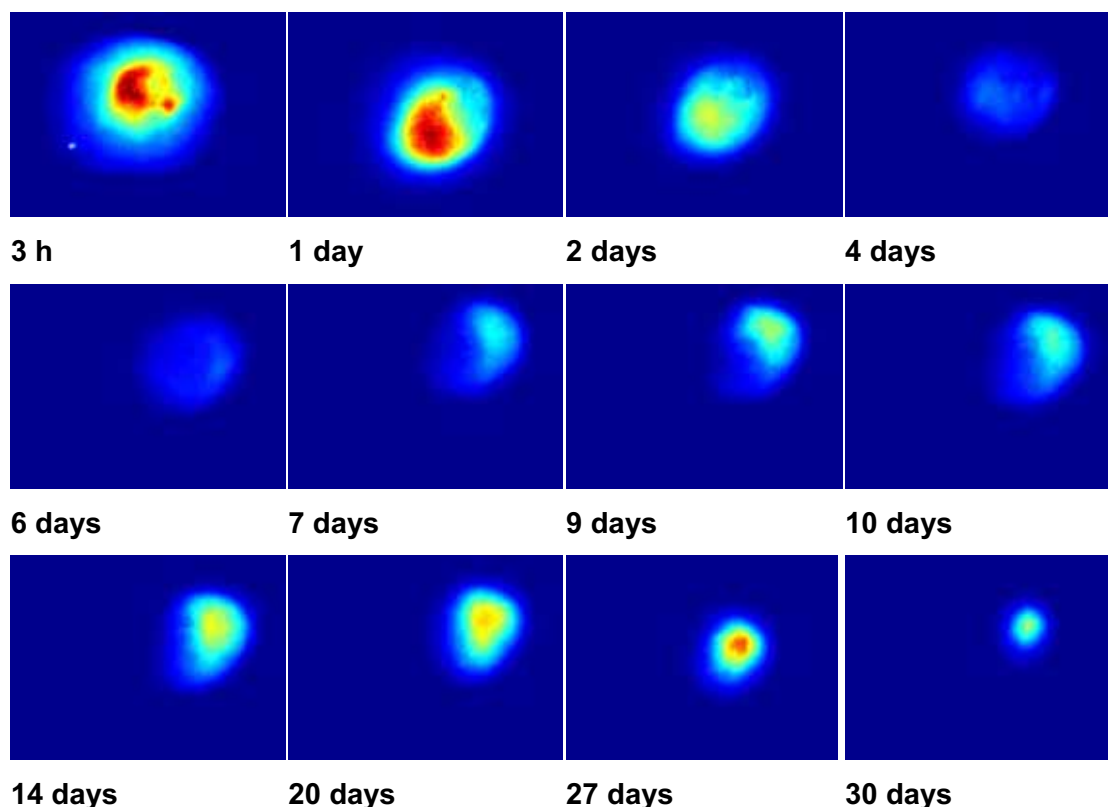


Figure 9: Time dependent, intensity weighted jet color images of the SNARF-4F signal of a PLGA / PEG 400 implant, injected to the neck of a mouse.

The fluorescence intensity increased continuously between day 6 and day 20. This can be explained by the accumulation of acidic PLGA degradation products [14] which accumulated in the implant [31]. During this process, more and more pores are formed and small amounts of water can further pass into the implant. Comparable results were also obtained from the pre-shaped PLGA implants [50]. It is furthermore detectable, that the size of the implant remains nearly constant until day 20 and decreased during the next 10 days gradually. This size reduction can be explained by the progressive softening of the implant. Through the formed pores the degradation products as well as part of the entrapped dye can diffuse out of the implant. The dye was eliminated nearly completely 30 days after injection.

A 9. *In vivo* and *ex vivo* investigation of implant size and implant pH allocation

Fluorescence imaging as well as MRI were also used to investigate the size and the position of the implant in the body. Benchtop MRI (BT-MRI) was applied as a complimentary *in vivo* method to non-invasively visualize the shape of the implant. The used BT-MRI is an alternative low cost system based on permanent magnets [51; 52]. It is successfully utilized for the characterization of tumors and of PLGA implants [13; 53]. It has been shown, that the contrast and the signal intensities between the PLGA / PEG 400 implant and the surrounding tissue were sufficient to distinguish both substances, even without adding additional contrast agents [13]. Due to high PEG 400 amounts at the beginning, the injected polymer solution had nearly the same relaxation times as s.c. fat and appears bright [13]. As it has been observed in the fluorescence images the PEG 400 was quickly exchanged with water, causing PLGA solidification. The solidified PLGA implant was imaged by MRI 9 days after injection (Figure 10 a). The implant (marked by arrow) appeared black. Thus it can be easily distinguished between the brighter skin, the fat tissues and the implant. The shape of the implant can be described as a thick disk. This is the result of the compressive tissue forces *in vivo* [54].

After the BT-MRI measurement, the implant was excised, sliced in the middle and analyzed by fluorescence imaging technique. RGB images of the implant cutting section are shown in Figure 10 b and c. In Figure 10 b different colors were assigned to the emission reference spectra of pH 4.5, pH 5.0 and pH 5.5. Within the unmixing step the Maestro software tags all pixels with an emission spectrum related to the reference of pH 4.5 in blue. Pixels which were assigned to pH 5.0 were displayed yellow and those which were allocated to pH 5.5 red respectively. In between a slight graduation of the respective mixed colors occurred. This enabled visualisations of pH distributions in the implant. As it can be observed from Figure 10 b, areas with lowest pH values were found in the middle of the implant. Higher acidity in the center was caused by the accumulation of the degradation products and is in accordance with the formerly published *in vitro* results of PLGA microspheres [31]. Regions with the higher pH values were primarily detected in surface areas of the implant especially near the skin. An increased pH under the skin can be explained by the better s.c. perfusion by what acidic degradation components are eliminated faster.

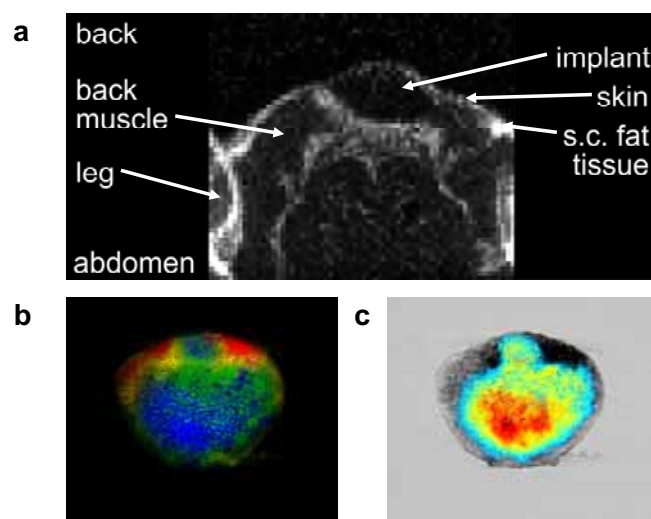


Figure 10: (a) *In vivo* MRI lateral profile picture of a mouse, 9 days after injection. The solid PLGA implant is visible. (b) *Ex vivo* fluorescence RGB image of the same, excised implant. The blue color is related to areas with the lowest detected pH values (pH 4.5), green and yellow indicate an increased pH and red regions are assigned to pH 5.5. (c) Intensity weighted jet color image of the same implant indicating areas with highest dye concentrations.

The intensity allocation in the implant is shown in Figure 10 c. Highest fluorescence intensities were measured in the middle of the implant. This is in concordance with the previously discussed results and is caused by the two factors. First, dye molecules in outer regions diffuse out of the implant during the solidification, directly after the injection. Second, the dye is only weak fluorescent in pure PLGA surroundings.

Due to the light properties, excitation and emission, light in the visible bandwidth has limited penetration depth. Thus emitted light of excited SNARF-4F dye molecules can only pass a few millimeters depending on the dye concentration. By this, an *in vivo* measured pH represents the surface pH values. In the case of the implant shown in Figure 10 b only areas which were assigned to pH values around pH 5.5 and displayed in red and yellow would be non-invasively detectable *in vivo*.

A 10. *In vivo* pH measurements based on fluorescence imaging

Based on the previous *in vitro* and first *in vivo* results, long-term *in vivo* study with nude mice was conducted to measure non-invasively the pH of PLGA implants. The analyzed results of three mice are shown in Figure 11 a.

The presented pH value is the average pH of the total surface area of the whole implant. The red line defines the upper pH detection limit (pH 7.0) and the green one, the lower pH calculation limit at pH 5.0. In between this bandwidth, pH values could be measured *in vivo* for more than 25 days. The pH remained constant for the first 2 -

3 days which conforms the above discussed *in vivo* dye intensity analysis. After 3 days, the pH decreased continuously due to the accumulation of acidic degradation products down to the lower pH detection limit of pH 5.0 [13; 31].

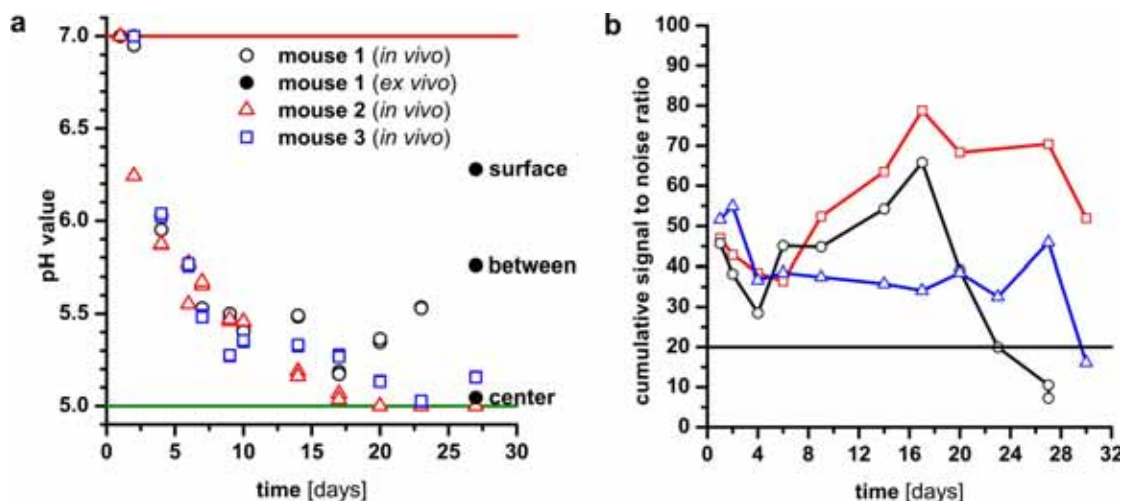


Figure 11: (a) Time dependent *in vivo* pH values of PLGA implants, injected into the neck of 3 mice. The 3 black dots represent pH values of an excised, sliced implant. The 2 horizontal lines mark the upper and the lower pH detection limit. (b) Cumulative signal to noise ratios of *in vivo* fluorescence imaging measurements. Black line marks the lower limit of reproducible pH determination.

The pH values of all three implants correlated well. This acidification catalyzes the further polymer degradation process. Generally, these results are in accordance with the performed *in vitro* EPR experiment. However, the process of the pH decrease was found to be slower *in vivo*. In Figure 11 a it is depicted a reversal kick point after which pH increases for mouse 1 at day 17 and for mouse 3 after day 23. This time point depends on the size and the geometry of the implant. Due to the strength of the skin and the mouse muscles there is an outer force to the implant. This influences the implant surface to bulk fluid volume ratios which have a strong impact on the degradation behavior [11; 32]. Degradation products are accumulated in the center of the implant. Over time period, the small pores are formed. Both effects cause deformation and corruption of the implant as soon as the center is highly destabilized. Consequently, acidic products are exchanged with body liquids which results in an increase of the pH value in the implant. For mouse 1 (Figure 11 a), the pH increase began at day 17. 27 days after the injection the implant was destabilized completely and the dye diffused out of the implant. Thus the fluorescence dye concentration decreased and the cumulative signal to noise ratio fell below the previously defined limit (Figure 11 b). After day 27 the implant of mouse 1 was excised and sliced through the middle. *Ex vivo* pH values from the top, the upper middle and from the center of the cutting area were measured. As it can be seen in

Figure 11 a (black points) the spectrum of the pH values in the cutting area is quite high. While, the pH at the surface was measured to be 6.3, the pH in the middle was still 5.0. The pH of 5.75 determined in the upper half which is in accordance to the *in vivo* measured pH values. Based on the final height of the excised implant of approximately 4 mm the measurement depth of the fluorescence imaging method can be expected to be approximately 1.5 mm.

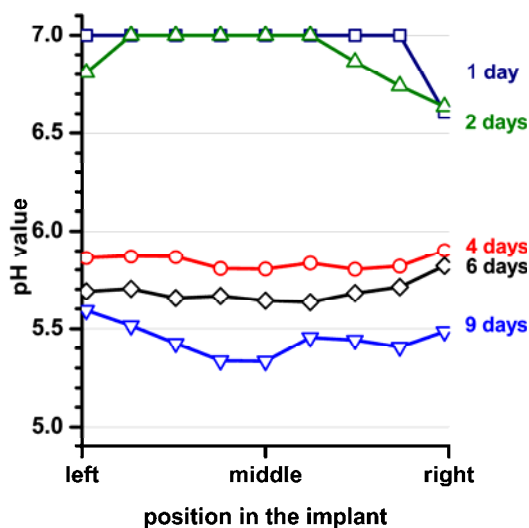


Figure 12: pH profiles of a PLGA implant over time.

In order to investigate the pH distribution in more detail, additional analysis was performed for one implant where the pH was determined *in vivo* on an intended line from one side of the implant via the middle to the other side of the implant. The results are shown in Figure 12. Within the first 2 days lower pH values were calculated for the outer regions of the implant. This can be explained by the decreased dye concentration in those areas. Thus the cumulative signal to noise ratio falls below the defined detection limit. As it has been previously discussed for Figure 11 b this leads to an error in the pH calculation for pH values between pH 6 and pH 7. Thus lower values than the actual ones are calculated. The pH decreased within the first 4 to 6 days at nearly constant speed. After 9 days, lowest pH values were detected in the center of the implant confirming the above discussed results.

Conclusion

PLGA solutions in organic solvents have been extensively investigated as potential novel drug depots over the last decade. However, the uncontrolled pH drop in PLGA systems is one of the most critical factors for the instability of the encapsulated drugs

or proteins in PLGA controlled release drug-delivery-systems. Therefore, it is important to measure the microenvironment in PLGA systems and to understand the relationship between pH shift and the implant degradation. Though, systemic investigations regarding the internal pH of the formed implants were missing. So far there exist no analytical methods to determine and visualize directly the *in vivo* changes in the microclimate pH (μpH) in a continuous and nondestructive manner within the same sample on the same animal model. Due to their non-destructive nature, EPR spectroscopy and fluorescence imaging were chosen for serial μpH measurements of the PLGA based *in situ* forming depots. *In vitro* EPR experiments showed that during incubation under 'physiologic' conditions the pH-value in the system can drop from pH 7 to values around pH 3. Extensive *in vitro* and *ex vivo* fluorescence imaging experiments were performed to evaluate the influence of factors like auto fluorescence of skin, dye selection, light absorption, intensity variations and measurement conditions. Based on the obtained information an *in vivo* fluorescence imaging method was evaluated. It has been demonstrated within this study that the μpH of PLGA implants could be non-invasively measured in complex *in vivo* surroundings. Due to the lack of the alternative dyes the lower detection limit for the *in vivo* fluorescence μpH measurements is considered to be pH 5. The physical entrapping of the hydrophilic dye enabled the measurement of the pH as well as of the dye release profiles from the implant. The results are in concordance with the performed *in vitro* EPR as well as *in vitro* confocal laser scanning microscopy results. However, the pH drop caused by the PLGA degradation products appears to be slower in its nature in *in vivo* conditions. This could be explained by different interactions with body liquids and due to varying implant geometries *in vivo*. The current study demonstrated that the evaluated fluorescence imaging method proves to be an efficient method to non-invasively measure μpH values *in vivo*.

Literature

- [1] S.P. Schwendeman, Recent advances in the stabilization of proteins encapsulated in injectable PLGA delivery systems, *Crit Rev Ther Drug* 19 (2002), 73-98.
- [2] J.L. Cleland, A. Daugherty, R. Mrsny, Emerging protein delivery methods, *Current Opinion in Biotechnology* 12 (2001), 212-219.

Supplemental material

(c) Characterization of *in situ* forming implants for potential controlled API release

- [3] W.Y. Dong, M. Korber, V. Lopez Esguerra, R. Bodmeier, Stability of poly(D,L-lactide-co-glycolide) and leuprolide acetate in in-situ forming drug delivery systems, *J Controlled Release* 115 (2006), 158-167.
- [4] S. Kempe, K. Mäder, In situ forming implants - an attractive formulation principle for parenteral depot formulations, *J Controlled Release* 161 (2012), 668-679.
- [5] W.R. Gombotz, D.K. Pettit, Biodegradable Polymers for Protein and Peptide Drug-Delivery, *Bioconjugate Chem* 6 (1995), 332-351.
- [6] D. Steinberg, M. Friedman, Dental drug-delivery devices: Local and sustained-release applications, *Crit Rev Ther Drug* 16 (1999), 425-459.
- [7] O. Sartor, Eligard: Leuprolide acetate in a novel sustained-release delivery system, *Urology* 61 (2003), 25-31.
- [8] H. Okada, Y. Inoue, T. Heya, H. Ueno, Y. Ogawa, H. Toguchi, Pharmacokinetics of Once-A-Month Injectable Microspheres of Leuprolide Acetate, *Pharm Res* 8 (1991), 787-791.
- [9] C. Wischke, S.P. Schwendeman, Principles of encapsulating hydrophobic drugs in PLA/PLGA microparticles, *Int J Pharm* 364 (2008), 298-327.
- [10] J.P. Payan, D. Beydon, J.P. Fabry, I. Boudry, B. Cossec, E. Ferrari, Toxicokinetics and metabolism of N-[C-14]methylpyrrolidone in male Sprague-Dawley rats. A saturable NMP elimination process, *Drug Metabolism and Disposition* 30 (2002), 1418-1424.
- [11] K. Schoenhammer, H. Petersen, F. Guethlein, A. Goepferich, Injectable in situ forming depot systems: PEG-DAE as novel solvent for improved PLGA storage stability, *Int J Pharm* 371 (2009), 33-39.
- [12] Y.X. Lu, Y.L. Yu, X. Tang, Sucrose acetate isobutyrate as an in situ forming system for sustained risperidone release, *J Pharm Sci* 96 (2007), 3252-3262.
- [13] S. Kempe, H. Metz, P.G.C. Pereira, K. Mäder, Non-invasive in vivo evaluation of in situ forming PLGA implants by benchtop magnetic resonance imaging (BT-MRI) and EPR spectroscopy, *Eur J Pharm Biopharm* 74 (2010), 102-108.
- [14] M.L. Houchin, E.M. Topp, Chemical degradation of peptides and proteins in PLGA: A review of reactions and mechanisms, *J Pharm Sci* 97 (2008), 2395-2404.
- [15] W.Q. Lu, T.G. Park, In-Vitro Release Profiles of Eristostatin from Biodegradable Polymeric Microspheres - Protein Aggregation Problem, *Biotechnol Prog* 11 (1995), 224-227.
- [16] A.G. Ding, S.P. Schwendeman, Acidic Microclimate pH Distribution in PLGA Microspheres Monitored by Confocal Laser Scanning Microscopy, *Pharm Res* 25 (2008), 2041-2052.

Supplemental material

(c) Characterization of *in situ* forming implants for potential controlled API release

- [17] C. Perez, I.J. Castellanos, H.R. Costantino, W. Al-Azzam, K. Griebenow, Recent trends in stabilizing protein structure upon encapsulation and release from bioerodible polymers, *J Pharm Pharmacol* 54 (2002), 301-313.
- [18] V.R. Sinha, A. Trehan, Biodegradable microspheres for protein delivery, *J Controlled Release* 90 (2003), 261-280.
- [19] A. Shenderova, A.G. Ding, S.P. Schwendeman, Potentiometric method for determination of microclimate pH in poly(lactic-co-glycolic acid) films, *Macromolecules* 37 (2004), 10052-10058.
- [20] G. Zhu, S.R. Mallery, S.P. Schwendeman, Stabilization of proteins encapsulated in injectable poly (lactide-co-glycolide), *Nat Biotechnol* 18 (2000), 52-57.
- [21] A. Brunner, K. Mäder, A. Göpferich, pH and osmotic pressure inside biodegradable microspheres during erosion, *Pharm Res* 16 (1999), 847-853.
- [22] L. Li, S.P. Schwendeman, Mapping neutral microclimate pH in PLGA microspheres, *J Controlled Release* 101 (2005), 163-173.
- [23] A. Shenderova, T.G. Burke, S.P. Schwendeman, The acidic microclimate in poly(lactide-co-glycolide) microspheres stabilizes camptothecins, *Pharm Res* 16 (1999), 241-248.
- [24] R. Astaneh, M. Erfan, H. Mobedi, H.R. Moghimi, Formulation of An Injectable Implant for Peptide Delivery and Studying the Effect of Polymer Molecular Weight on Its Release Behavior, *J Pept Sci* 10 (2004), 142.
- [25] W. Heidemann, S. Jeschkeit-Schubbert, K. Ruffieux, J.H. Fischer, H. Jung, G. Krueger, E. Wintermantel, K.L. Gerlach, pH-stabilization of predegraded PDLLA by an admixture of water-soluble sodiumhydrogenphosphate-results of an *in vitro*- and *in vivo*-study, *Biomaterials* 23 (2002), 3567-3574.
- [26] K. Fu, D.W. Pack, A.M. Klibanov, R. Langer, Visual evidence of acidic environment within degrading poly(lactic-co-glycolic acid) (PLGA) microspheres, *Pharm Res* 17 (2000), 100-106.
- [27] R.A. Gatenby, E.T. Gawlinski, A.F. Gmitro, B. Kaylor, R.J. Gillies, Acid-mediated tumor invasion: a multidisciplinary study, *Cancer Res* 66 (2006), 5216-5223.
- [28] K. Mäder, B. Gallez, K.J. Liu, H.M. Swartz, Non-invasive *in vivo* characterization of release processes in biodegradable polymers by low-frequency electron paramagnetic resonance spectroscopy, *Biomaterials* 17 (1996), 457-461.
- [29] K. Mäder, B. Bittner, Y.X. Li, W. Wohlauf, T. Kissel, Monitoring microviscosity and microacidity of the albumin microenvironment inside degrading microparticles from poly(lactide-co-glycolide) (PLG) or ABA-triblock polymers containing hydrophobic poly(lactide-co-glycolide) A blocks and hydrophilic poly(ethyleneoxide) B blocks, *Pharm Res* 15 (1998), 787-793.

Supplemental material

(c) Characterization of *in situ* forming implants for potential controlled API release

- [30] F. Eisenächer, A. Schädlich, K. Mäder, Monitoring of internal pH gradients within multi-layer tablets by optical methods and EPR imaging, *Int J Pharm* 417 (2011), 204-215.
- [31] Y.J. Liu, S.P. Schwendeman, Mapping Microclimate pH Distribution inside Protein-Encapsulated PLGA Microspheres Using Confocal Laser Scanning Microscopy, *Mol Pharmaceutics* 9 (2012), 1342-1350.
- [32] E. Pamula, E. Menaszek, In vitro and in vivo degradation of poly(L-lactide-co-glycolide) films and scaffolds, *J Mater Sci-Mater M* 19 (2008), 2063-2070.
- [33] A. Schädlich, H. Caysa, T. Mueller, F. Tenambergen, C. Rose, A. Göpferich, J. Kuntsche, K. Mäder, Tumor Accumulation of NIR Fluorescent PEG PLA Nanoparticles: Impact of Particle Size and Human Xenograft Tumor Model, *Acs Nano* 5 (2011), 8710-8720.
- [34] A. Schädlich, T. Naolou, E. Amado, R. Schöps, J. Kressler, K. Mäder, Noninvasive in Vivo Monitoring of the Biofate of 195 kDa Poly(vinyl alcohol) by Multispectral Fluorescence Imaging, *Biomacromolecules* 12 (2011), 3674-3683.
- [35] A. Schädlich, S. Hoffmann, T. Mueller, H. Caysa, C. Rose, A. Göpferich, J. Li, J. Kuntsche, K. Mäder, Accumulation of nanocarriers in the ovary: A neglected toxicity risk?, *J Controlled Release* 160 (2012), 105-112.
- [36] *Molecular Probes Handbook, A Guide to Fluorescent Probes and Labeling Technologies*, 11th edition, (2011).
- [37] S. Capancioni, K. Schwach-Abdellaoui, W. Kloeti, W. Herrmann, H. Brosig, H.H. Borchert, J. Heller, R. Gurny, In vitro monitoring of poly(ortho ester) degradation by electron paramagnetic resonance imaging, *Macromolecules* 36 (2003), 6135-6141.
- [38] S. Kempe, H. Metz, M. Bastrop, A. Hvilsorn, R.V. Contri, K. Maeder, Characterization of thermosensitive chitosan-based hydrogels by rheology and electron paramagnetic resonance spectroscopy, *Eur J Pharm Biopharm* 68 (2008), 26-33.
- [39] S. Kempe, "Non-invasive Characterization of *in situ* forming Implants." Martin Luther University Halle-Wittenberg, 2012.
- [40] A. Schädlich, C. Rose, J. Kuntsche, H. Caysa, T. Mueller, A. Göpferich, K. Mäder, How Stealthy are PEG-PLA Nanoparticles? An NIR In Vivo Study Combined with Detailed Size Measurements, *Pharm Res* 28 (2011), 1995-2007.
- [41] S. Kempe, H. Metz, K. Mäder, Application of Electron Paramagnetic Resonance (EPR) spectroscopy and imaging in drug delivery research - Chances and challenges, *Eur J Pharm Biopharm* 74 (2010), 55-66.
- [42] F. Leblond, S.C. Davis, P.A. Valdes, B.W. Pogue, Pre-clinical whole-body fluorescence imaging: Review of instruments, methods and applications, *J Photoch Photobio B* 98 (2010), 77-94.

Supplemental material

(c) Characterization of *in situ* forming implants for potential controlled API release

- [43] M.E. Dickinson, G. Bearman, S. Tille, R. Lansford, S.E. Fraser, Multi-spectral imaging and linear unmixing add a whole new dimension to laser scanning fluorescence microscopy, *Biotechniques* 31 (2001), 1272-1278.
- [44] R.M. Levenson, D.T. Lynch, H. Kobayashi, J.M. Backer, M.V. Backer, Multiplexing with multispectral imaging: From mice to microscopy, *Ilar J* 49 (2008), 78-88.
- [45] R.M. Levenson, J.R. Mansfield, Multispectral imaging in biology and medicine: Slices of life, *Cytom Part A* 69A (2006), 748-758.
- [46] N. Opitz, E. Merten, H. Acker, Evidence for Redistribution-Associated Intracellular pK Shifts of the Ph-Sensitive Fluoroprobe Carboxy-Snarf-1, *Pflug Arch Eur J Phy* 427 (1994), 332-342.
- [47] L.D. Lavis, R.T. Raines, Bright ideas for chemical biology, *ACS Chem Biol* 3 (2008), 142-155.
- [48] E. Nakata, Y. Yukimachi, Y. Nazumi, Y. Uto, H. Maezawa, T. Hashimoto, Y. Okamoto, H. Hori, A newly designed cell-permeable SNARF derivative as an effective intracellular pH indicator, *Chemical Communications* 46 (2010), 3526-3528.
- [49] J.E. Whitaker, R.P. Haugland, F.G. Prendergast, Spectral and Photophysical Studies of Benzo[C]Xanthene Dyes - Dual Emission Ph Sensors, *Anal Biochem* 194 (1991), 330-344.
- [50] K. Mäder, G. Bacic, A. Domb, O. Elmalak, R. Langer, H.M. Swartz, Noninvasive *in vivo* monitoring of drug release and polymer erosion from biodegradable polymers by EPR spectroscopy and NMR imaging, *J Pharm Sci* 86 (1997), 126-134.
- [51] P. Cornillon, L.C. Salim, Characterization of water mobility and distribution in low- and intermediate-moisture food systems, *Magn Reson Imaging* 18 (2000), 335-341.
- [52] G.E. Schaumann, E. Hogley, J. Hurrass, W. Rotard, H-NMR relaxometry to monitor wetting and swelling kinetics in high-organic matter soils, *Plant Soil* 275 (2005), 1-20.
- [53] H. Caysa, H. Metz, K. Mäder, T. Mueller, Application of Benchtop-magnetic resonance imaging in a nude mouse tumor model, *J Exp Clin Cancer Res* 30 (2011), 69.
- [54] R.B. Patel, L. Solorio, H.P. Wu, T. Krupka, A.A. Exner, Effect of injection site on *in situ* implant formation and drug release *in vivo*, *J Controlled Release* 147 (2010), 350-358.



Contents lists available at ScienceDirect

International Journal of Pharmaceutics

journal homepage: www.elsevier.com/locate/ijpharm

Monitoring of internal pH gradients within multi-layer tablets by optical methods and EPR imaging

Friederike Eisenächer, Andreas Schädlich, Karsten Mäder*

Martin Luther University Halle-Wittenberg, Department of Pharmaceutical Technology and Biopharmaceutics, D-06120 Halle, Saale, Germany

ARTICLE INFO

Article history:

Received 7 September 2010
Received in revised form 1 October 2010
Accepted 1 October 2010
Available online 10 October 2010

Keywords:

pH dependent solubility
EPR
MRI
Benchtop NMR
Multi-layer tablet
Weakly acidic drug

ABSTRACT

The high variability of gastrointestinal pH is a general challenge regarding constant release from oral drug delivery systems, especially for ionisable drugs. These drugs often show a pH-dependent solubility and therewith associated intra- and inter-individual variability of emerging drug plasma levels. Several strategies have been investigated with the intention to influence the microenvironmental pH (pH_M) within solid formulations and therefore achieve pH-independent release profiles. Because of the heterogeneity of solid systems, a precise prediction of the occurring pH_M is rather difficult. It is therefore important to monitor the pH_M within the formulations to achieve requested release as well as to minimise pH-dependent degradation processes of the active compound. The purpose of the current study was the analysis of pH_M gradients within 2- and 3-layer tablets during hydration using 3 different techniques for comparison intentions, in particular a pH indicator dye, fluorescence imaging and EPR imaging. The influence of the presence or absence of pH modifying substances and of an additional lipophilic inter layer on the pH_M was investigated as well as the variation of matrix forming excipient and buffer pH. The influence of the pH_M on drug release was analysed as well. In addition, benchtop MRI was accomplished to gain a deeper insight on the hydration and erosion behaviour of 2- and 3-layer tablets.

© 2010 Elsevier B.V. All rights reserved.

1. Introduction

The oral route is still the most commonly used way for the application of drugs because of its convenient administration leading to high patient compliance. However, the variability of physiological conditions within the human gastrointestinal tract (pH, gastric residence time, intestinal motility, food intake) can be a serious challenge for a predictable release and effect of oral drug delivery systems (Grundy and Foster, 1996). Especially the variability of the gastrointestinal pH has shown to be an important parameter for drugs with ionisable functional groups (weak acids/bases). In most cases, the unionized form shows a low aqueous solubility leading to changed solubility under acidic (stomach) and neutral (intestine) conditions. The dissolution rate of a drug with diffusion-controlled release behaviour is dependent on the solubility of the drug in the diffusion layer (Gibaldi, 1984). Thus, pH-dependent solubility may lead to incomplete drug release and remarkable intra- and inter-individual variability of emerging drug plasma levels.

The concept of microenvironmental pH (pH_M) is often used in conjunction with solid formulations characterising the pH, which is generated within the formulation during hydration by surrounding

media or humidity (Siepe et al., 2006; Badawy and Hussain, 2007). The pH_M has shown to affect drug stability inside solid formulations as well as dissolution behaviour, both influencing the bioavailability of an active compound (Badawy and Hussain, 2007). For this reason, several attempts have been published with the intention to modify and measure the pH_M within solid formulations to achieve pH-independent release or enhance storage stability of weakly acidic and basic drugs. One strategy is the incorporation of enteric polymers into hydrogel matrix devices. These polymers show a pH dependent solubility and are supposed to act as pore formers (Akiyama et al., 1994; Streubel et al., 2000) and pH modulators (Tatavarti et al., 2004) for weakly basic drugs. Another attempt is to influence the pH_M by incorporation of pH modifying substances. Organic acids, showing different solubilities and acid strengths, were used to enhance the release of weakly basic drugs (Thoma and Zimmer, 1990; Streubel et al., 2000; Varma et al., 2005; Siepe et al., 2006; Tatavarti and Hoag, 2006; Gutsche et al., 2008). On the other hand, basic salts were reported to improve the release of weak acids (Doherty and York, 1989; Riis et al., 2007; Tran et al., 2008).

The pH_M is influenced by many factors including excipients, active compounds, amount of water penetration, diffusion processes and pH of surrounding media. Therefore, a certain prediction is rather difficult. There is a need to monitor the local pH within solid formulations to optimise the pH_M regarding drug stability

* Corresponding author. Tel.: +49 345 55 25167; fax: +49 345 55 27029.
E-mail address: Maeder@pharmazie.uni-halle.de (K. Mäder).

and requested drug release. Although the pH of solutions is easy to determine potentiometrically, it is much more challenging to analyse the pH_M of solid or nearly solid formulations. Several techniques were used to gain information on the pH_M , however, there are no well-established methods available for all purposes. Diffuse reflectance spectroscopy was used to determine the pH_M of dry tablets (Glombitza et al., 1994; Glombitza and Schmidt, 1995; Scheef et al., 1998; Zinchuck et al., 2005; Pudipeddi et al., 2008). However, only the surface pH could be determined and possible interactions between the pH sensitive dye and excipients should be kept in mind. Incorporation of pH indicator dyes and following examination of occurring colours over time of hydration was also reported (Streubel et al., 2000; Varma et al., 2005; Adhikary and Vavia, 2008; Ching et al., 2008). This dye method was easy to apply but only a rough, imprecise estimation could be obtained. To achieve information concerning pH_M within the tablet core during contact with buffer, tablets had to be cross-sectioned. Another attempt was the usage of a surface pH electrode to analyse the surface pH_M of solid dispersions (Tran et al., 2008) as well as the pH_M of cryosections of hydrated tablets (Gutsche et al., 2008). Again, to gain insight on the pH_M of the inner regions, tablets had to be cut in pieces. Confocal laser scanning microscopy was used to non-invasively image pH sensitive fluorescent dyes, giving a spatial resolution of pH_M (Cope et al., 2002; Li and Schwendeman, 2005). One restriction of this technique is the limited object size, thus, only eroding microspheres were analysed. Electron paramagnetic resonance (EPR electron spin resonance, ESR) spectroscopy allows the non-invasive detection of paramagnetic compounds. The majority of drug delivery devices are not directly detectable by EPR because of the absence of naturally occurring radicals. Thus, it is necessary to incorporate paramagnetic substances e.g. stable nitroxide radicals within the objects of interest. Depending on the used substance (so called spin probe), information about microviscosity, micropolarity and pH_M inside drug delivery systems can be obtained based on the spectral sensitivity of the nitroxides to their environment (Mäder et al., 1997; Brunner et al., 1999; Lurie and Mäder, 2005; Kempe et al., 2010). EPR imaging now combines spectral information with the spatial distribution of a spin probe. Therefore, EPR imaging can be used as continuous, non-invasive technique for the spatial determination of pH_M within hydrated devices.

The purpose of the current study was the analysis of pH_M gradients within multi-layer tablets (2- and 3-layer tablets). Multi-layer tablets can be used for different purposes. It is possible to separate incompatible substances as well as to combine immediate- and prolonged-release profiles of an active compound. Furthermore, floating multi-layer tablets were developed for gastric retention consisting of a floating and a drug-containing tablet layer (Ingani et al., 1987; Wei et al., 2001; Rahman et al., 2006). The aim was to investigate the influence of (1) the presence or absence of pH modifying substances within tablet layers, (2) the variation of matrix forming excipients, (3) the variation of the pH of surrounding buffer and (4) the incorporation of an additional lipophilic inter layer on the pH_M within multi-layer tablets. The influence of the pH_M on the drug release of two model drugs, Metformin-HCl and Ketoprofen, was also analysed. An internal buffer system (IBS) composed of citric acid and disodium hydrogenphosphate was used as pH modifier. The IBS was incorporated either in one or two tablet layers to generate a pH_M gradient within the tablets. Furthermore, different matrix forming excipients were analysed for their ability to maintain a specified pH_M over time of buffer contact. Hydroxypropylmethylcellulose (HPMC) was analysed as most frequently used hydrophilic polymer which is able to form hydrogel matrices upon contact with water. HPMC is a non-ionic cellulose ether forming a stable hydrogel over the pH range of 3–11. Kollidon SR, a commercially available excipient in the form of a physical mixture of 8 parts of polyvinylacetate (PVAc) and 2 parts of polyvinylpyrrolidone (PVP), was used as

well. Kollidon SR shows excellent tableting properties and can be used for direct compression (BASF AG, 1999). Because of its aqueous solubility, PVP acts as pore former during contact with water and therefore facilitates drug diffusion. Sponge-like matrices can be observed after 12 h of buffer contact. Three different techniques were used to determine the pH_M within multi-layer tablets for comparison of results regarding application spectrum and expenses, in particular, a pH indicator dye, fluorescence imaging and EPR imaging. In addition to the analysis of the pH_M , the hydration behaviour of 2- and 3-layer tablets was monitored using nuclear magnetic resonance imaging (NMR-imaging/MRI) in order to gain a deeper insight on proceeding hydration and erosion processes during contact with buffer. MRI has proven to be a non-invasive, well established method to investigate drug delivery systems in vitro and in vivo (Richardson et al., 2005; Metz and Mäder, 2008; Nott, 2010). A commercial, low-cost benchtop MRI (BT-MRI) system was used as alternative to common superconducting MRI machines. Recently, BT-MRI has been successfully used to characterise different solid drug delivery devices (Metz et al., 2007; Strübing et al., 2008a,b; Malaterre et al., 2009). Therefore, BT-MRI was intended to provide detailed information about the differences in the hydration behaviour of 2- and 3-layer tablets.

2. Materials and methods

2.1. Materials

Kollidon® SR was kindly supplied by BASF, Ludwigshafen, Germany. Disodium hydrogenphosphate dihydrate and citric acid were obtained from Carl Roth GmbH & Co KG, Karlsruhe, Germany. They were ground in a mortar and passed through a 250 μm sieve for further use. Aerosil® was purchased from Evonik Degussa GmbH, Essen, Germany. Magnesium stearate was obtained from Magnesia GmbH, Lüneburg, Germany. Lactose-monohydrate was purchased from Euro OTC Pharma GmbH, Bönen, Germany. Methocel K100 CR was kindly supplied by Colorcon GmbH, Idstein, Germany. The fluorescence dye Carboxy SNARF®-1 was purchased from Invitrogen GmbH, Darmstadt, Germany. Bromocresol purple was obtained from Merck KGaA, Darmstadt, Germany. EPR spin probe 4-Amino-2.2.5.5-tetra-methyl-3-imidazoline-1-oxyl (AT) was obtained from N.N. Vorozhtsov Institute of Organic Chemistry, Novosibirsk, Russia. Metformin-HCl was purchased from Biotrend Chemicals AG, Wangen/Zurich, Switzerland. Ketoprofen was obtained from Sigma-Aldrich Chemie GmbH, Steinheim, Germany.

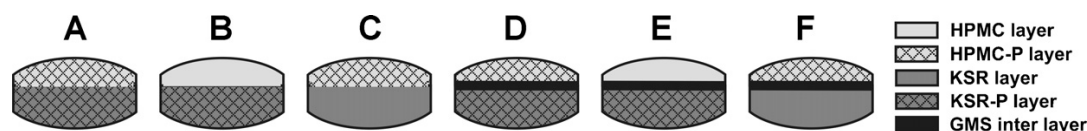
2.2. Preparation of tablets

The powder mixtures for the manufacturing of tablets were prepared according to compositions shown in Table 1 by blending all ingredients except magnesium stearate with pestle and mortar for 10 min. After adding magnesium stearate, the mixtures were blended for another 2 min. For the preparation of 2- and 3-layer tablets, weighed amounts of the different layers were fed successively into the die of the tablet press and precompacted manually. The final compression force was adjusted to receive tablets with a crushing force of 75 N after compression. Biconvex 2-layer tablets consisting of 200 mg of KSR-P or KSR layer and 100 mg of HPMC-P or HPMC layer were prepared by direct compression using a rotary tablet press (RL 12, Kilian GmbH & Co KG, Germany). Resulting 2-layer tablets had a weight of 300 mg and a diameter of 9 mm. Furthermore 3-layer tablets with an additional inter layer of 50 mg of glycerol monostearate were produced. The inter layer should achieve a better adhesiveness of both layers and decrease diffusion processes between the layers. All analysed tablet preparations are illustrated in Fig. 1.

Table 1

Composition of powder mixtures for tablet preparation (Metformin-HCl (MF) and Ketoprofen (Keto) were used as model drugs).

Components (%)	KSR layer	KSR-P layer	HPMC layer	HPMC-P layer	KSR drug layer	KSR-P drug layer
Kollidon SR	70.0	70.0	–	–	70.0	70.0
Lactose	28.5	17.4	43.5	32.4	11.1	–
Methocel K100	–	–	55.0	55.0	–	–
Na ₂ HPO ₄ × 2H ₂ O	–	9.9	–	9.9	–	9.9
Citric acid × H ₂ O	–	1.2	–	1.2	–	1.2
Drug (MF/Keto)	–	–	–	–	17.4	17.4
Aerosil	0.5	0.5	0.5	0.5	0.5	0.5
Mg-stearate	1.0	1.0	1.0	1.0	1.0	1.0

**Fig. 1.** Tablet compositions of tablets A–F, each tablet consisted of 200 mg KSR/-P layer and 100 mg of HPMC/-P layer, an additional inter layer of glycerol monostearate (GMS, 50 mg) was included in 3-layer tablets D–F.

2.3. Microacidity measurements using a pH indicator dye

Tablets, containing bromocresol purple (1 mg/layer) as pH indicator dye, were prepared as described before. These tablets were subjected to 100 ml of a citric acid/phosphate buffer consisting of 0.01 M citric acid solution and 0.02 M disodium hydrogenphosphate solution in a ratio of 4:1 with a resulting pH of 3 (=buffer pH 3). The pH 3 of the surrounding buffer was used as typical pH of the late phase of the fed stomach (Jantratid et al., 2008) which is important especially for gastroretentive systems. Photographs of the tablets as whole and cross-sectioned were taken after predefined time intervals (10 min, 2 h, 4 h and 6 h) of contact with buffer with a digital camera (μ 850 SW, Olympus, Japan). Every tablet could be analysed only once, therefore, a new tablet incubated in the buffer for the dedicated time interval was used for every photograph. The pH of the buffer was analysed regularly and showed a stable pH of 3.

2.4. Microacidity measurements using multispectral fluorescence imaging

2-Layer tablets, containing the fluorescence dye Carboxy SNARF[®]-1 (0.2 μ mol/g powder), were used. The tablets were placed into tubes with the diameter of the tablets and two open ends to allow a constant measuring area and a one-dimensional hydration only from top and bottom of the tablet. The tubes with incorporated tablets were transferred to 100 ml of buffer pH 3 (see Section 2.3). They were removed from the buffer at different time points and analysed by fluorescence imaging. The measurements were done with a Maestro[™] in vivo imaging system (Cambridge Research & Instrumentation, Woburn, USA). A green and a yellow filter set were used. Multispectral imaging cube sets were acquired in 2 nm steps using automatic exposure times. Averaged spectra were extracted from different image regions to allow a pH_M calculation of both tablet layers. The ratios of the maxima were determined. Corresponding pH_M values were calculated using a calibration curve of the fluorescence dye. Furthermore, pseudo-coloured fluorescence images were generated by separating the microacidities of the measured images using an acidic spectrum (assigned colour red) and a neutral spectrum (assigned colour green) of the spectra library. The measured spectrum of each data point was assigned to the closest matching spectrum. Therefore, acidic domains of the measured tablets appear red; areas with a $pH > 6$ appear green within the pseudo-coloured images.

2.5. Microacidity measurements using spatial spectral EPR imaging

2- and 3-layer tablets containing EPR spin probe AT (1 μ mol/g powder) were used. Measurements were performed with a L-band EPR spectrometer (Magnetech GmbH, Berlin, Germany) using following parameters: B_0 -field 48.9 mT, scan range 8 mT, scan time per projection 30 s, modulation amplitude 0.1 mT, attenuation 6 dB, maximum gradient of 2.5 mT/cm, points per projections 1024, 31 projections/6 missing projections, image reconstruction giving an image matrix of 512×512 points and a spatial resolution of about 200 μ m. The KSR/KSR-P layer of the tablet used for analysis was glued to a plastic bar which was placed into 100 ml of buffer pH 3 (see Section 2.3). The plastic bar with the affixed tablet was removed from the buffer at different time points. Adhering water on the surface of the tablet was removed carefully using absorbent paper before measuring. Two dimensional EPR images were collected for all tablet compositions after 10 min, 30 min, 1, 2, 3, 4 and 6 h of buffer contact. The pH of the buffer was analysed regularly and showed a stable pH of 3. The EPR spectra of the different image layers were extracted from the images. Only image domains with signal intensities over 30% were used for further analysis. The values of $2a_N$ (distance 1st to 3rd peak) were determined from the extracted spectra. Resulting pH_M values were obtained using a pH calibration curve of AT and plotted against the spatial position within the tablet. Experiments were performed in triplicate.

2.6. Influence of the microenvironmental pH on the drug release

Dissolution studies were carried out to investigate if different pH_M within a tablet could influence the drug release. Metformin-HCl and Ketoprofen were used as model drugs. Drug containing tablets were prepared by incorporating 17.4% of drug instead of lactose into the Kollidon SR layer giving a drug content of 34.8 mg per tablet (Table 1). The drug release was determined from 2-layer tablets B and C and 3-layer tablets E and F. Dissolution studies were carried out with an automatic dissolution tester (PTWS 310, Pharmatest Apparatebau, Hainburg, Germany) in 900 ml of buffer pH 3 (see Section 2.3) at 37 °C and 50 rpm. The drug release was analysed by measuring UV absorbance at 233 nm for Metformin-HCl, and 275 nm for Ketoprofen and calculated using calibration curves. Dissolution experiments were carried out over 12 h and performed in triplicate.



Fig. 2. Images and cross-sectional images of hydrated matrices of tablets A–F after different time intervals of contact with buffer pH 3. Tablets were always placed with the HPMC layer on top and the KSR layer as bottom side. Purple (dark grey or black) domains indicate a $\text{pH} > 5$, yellow (light grey) domains indicate a $\text{pH} < 4.5$. The dry core appeared white. (For interpretation of the references to colour in this figure legend, the reader is referred to the web version of the article.)

2.7. Monitoring of hydration behaviour by means of NMR benchtop imaging

NMR imaging experiments were performed on a BT-MRI spectrometer working at a frequency of 20 MHz and using a static magnetic field (B_0) of 0.5 T (Maran DRX2, Oxford Instruments Molecular Biotech, Oxfordshire, UK). A standard spin-echo sequence was used with an echo time of 9.8 ms and a repetition time of 300 ms leading to an acquisition time of about 5 min for each image. Sixteen scans were accumulated to obtain 64×64 pixel images with a field of view of 4 cm^2 , which led to an in-plane resolution of $312.5 \mu\text{m}$. 2- and 3-layer tablets were placed in a USP paddle dissolution apparatus with 900 ml of buffer pH 3 of 37°C , stirred at 50 rpm, or in a beaker with 100 ml of same buffer at room temperature without stirring. The tablets were removed for MRI measurements after predefined time intervals and transferred to a sample holder. T_1 -weighted MRI images were measured after 10 min, 30 min, 1, 2, 3, 4 and 6 h of contact with buffer. Experiments were performed in triplicate. MRI intensity profiles of resulting images were investigated using Oxford Instruments RImageJ VO.NIX as plug-in for Image J.

3. Results

3.1. Microacidity measurements using a pH indicator dye

The microenvironmental pH of hydrating multi-layer tablets was visualised using the pH indicator bromocresol purple with a transition pH range of 5.2–6.8 and a colour change from yellow to purple. This dye was used to differentiate between tablet layers which assumed the pH of the surrounding buffer and areas with incorporated IBS ($\text{Na}_2\text{HPO}_4/\text{citric acid}$). The tablet layers with incorporated IBS were supposed to generate a pH_M of around 6 upon hydration while the pH of the surrounding buffer was 3 which enabled the monitoring of different colours depending on presence or absence of IBS. In addition, the colour change from yellow to purple could be easily monitored. Photographs of tablets A–F as whole and cross-sectioned after defined time intervals of contact with buffer are shown in Fig. 2. After 10 min of buffer contact, a differentiation between formulations A, B and C and D, E and F is easily possible. The HPMC-P and KSR-P layer of tablets A and D turned purple/blue immediately after contact with buffer, indicating a pH above 5. This finding corresponded to the expectation because the IBS was incorporated into both layers. The pH_M of

the exterior region of the KSR-P layer changed to yellow after 2 h whereas the HPMC-P layer appeared mainly purple over more than 4 h. The HPMC layer of tablets B and E (without IBS) turned yellow after contact with buffer. In the case of tablet B, the HPMC layer changed into purple, indicating a pH_M above 5, after 30–60 min of buffer contact. In contrast, the HPMC layer of tablet E maintained a yellow/orange colour over the analysed time interval of 6 h. The KSR layer of tablets C and F (without IBS) turned yellow after contact with buffer. No obvious change in colour could be observed over the analysed time.

3.2. Microacidity measurements using multispectral fluorescence imaging

Multispectral fluorescence imaging of 2-layer tablets was accomplished to analyse the pH_M of the tablet surface by means of a hydrophilic fluorescence dye. The emission spectrum of this dye undergoes a pH-dependent wave length shift (Fig. 3(a)). pH_M values could be calculated independently from the intensities for a pH range from pH 5 to 8 using a calibration curve (Fig. 3(b); Schädlich et al., 2009). Pseudo-coloured fluorescence images and corresponding pH_M values of both tablet layers of tablets A, B and C are illustrated in Fig. 4. The pH_M of both layers of tablet A showed values between pH 6.5 and 7.5 over more than 6 h. Higher pH_M values were detected within the HPMC-P layer compared to the KSR-P layer. The pH_M of the HPMC layer of tablet B increased from a predominantly acidic environment below the dye detection limit of pH 5 to values above pH 6 after about 3 h of contact with buffer (Fig. 4(B)). The pH_M shifting was delayed in comparison with the pH indicator results. This observation can be explained by the hindered hydration of the tablets from only two dimensions (see Section 2.4). The pH_M of the KSR layer of tablet C remained below pH 5 over more than 6 h (Fig. 4(C)).

3.3. Microacidity measurements using spatial spectral EPR imaging

EPR imaging provides the possibility to obtain spatial information about the pH_M within the tablets non-invasively. For the investigation of the pH_M by EPR imaging, the stable nitroxide radical 4-Amino-2,2,5,5-tetra-methyl-3-imidazoline-1-oxyl (AT) was used as pH-sensitive spin probe. Protonation of pH-sensitive spin probes leads to changes in the spin density of the nitroxide group (Fig. 5(b)) and therewith associated changes in the EPR spectra

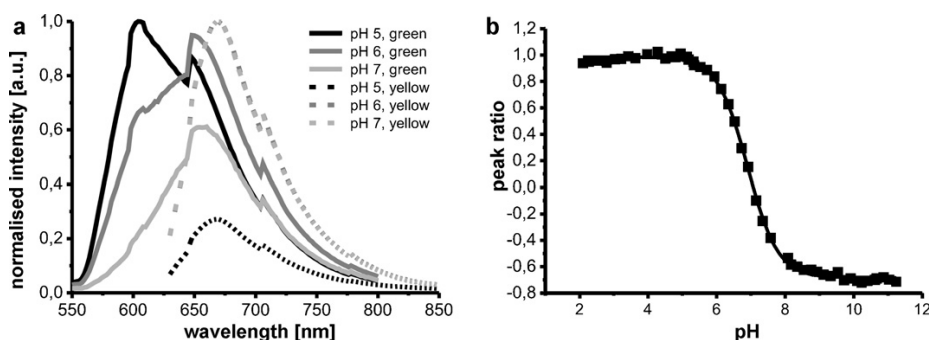


Fig. 3. (a) pH-dependent wave length shift of the emission spectrum of the fluorescence dye Carboxy SNARF[®]-1. A green and a yellow filter set were used. (b) pH sensitivity of the peak ratio of Carboxy SNARF[®]-1.

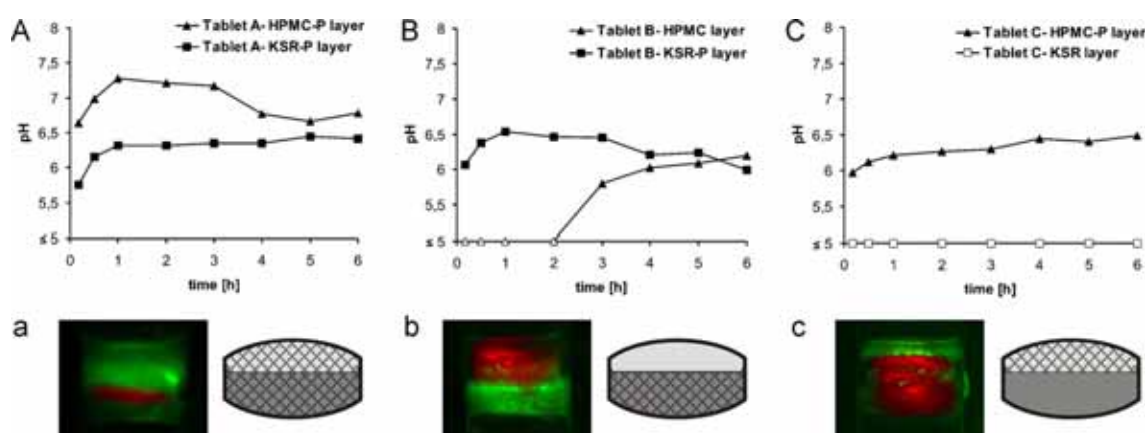


Fig. 4. (A–C) Mean pH_M values of the surface of both layers of tablets A, B and C from one dimension at different time intervals of contact with buffer pH 3. No values could be determined for areas with a pH < 5 (empty symbols). (a–c) Pseudo-coloured fluorescence images and corresponding schemata of tablets A, B and C after 30 min of buffer contact, red (dark grey) domains symbolise dry and acidic regions (pH < 5), green (light grey) domains symbolise a nearly neutral pH_M (pH > 6). (For interpretation of the references to colour in this figure legend, the reader is referred to the web version of the article.)

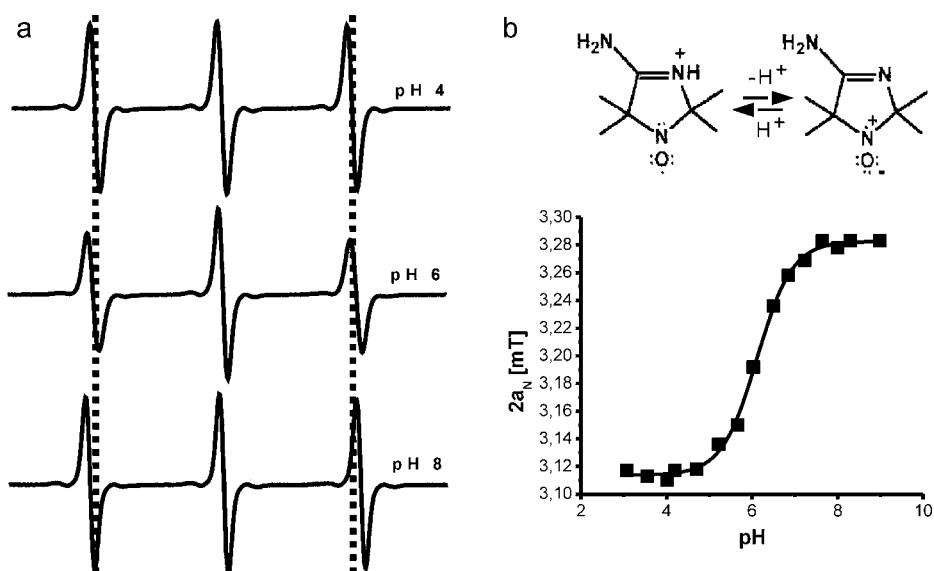


Fig. 5. (a) EPR spectra (first derivatives) of the spin probe 4-Amino-2,2,5,5-tetra-methyl-3-imidazoline-1-oxyl (AT) at different pH values. The dashed line symbolises 2a_N (a_N = the hyperfine splitting constant) for the spectrum at pH 4. Note that the distance between the first and the third amplitude is larger for the nonprotonated form (pH 8). (b) Principle of pH sensitivity and calibration curve of AT.

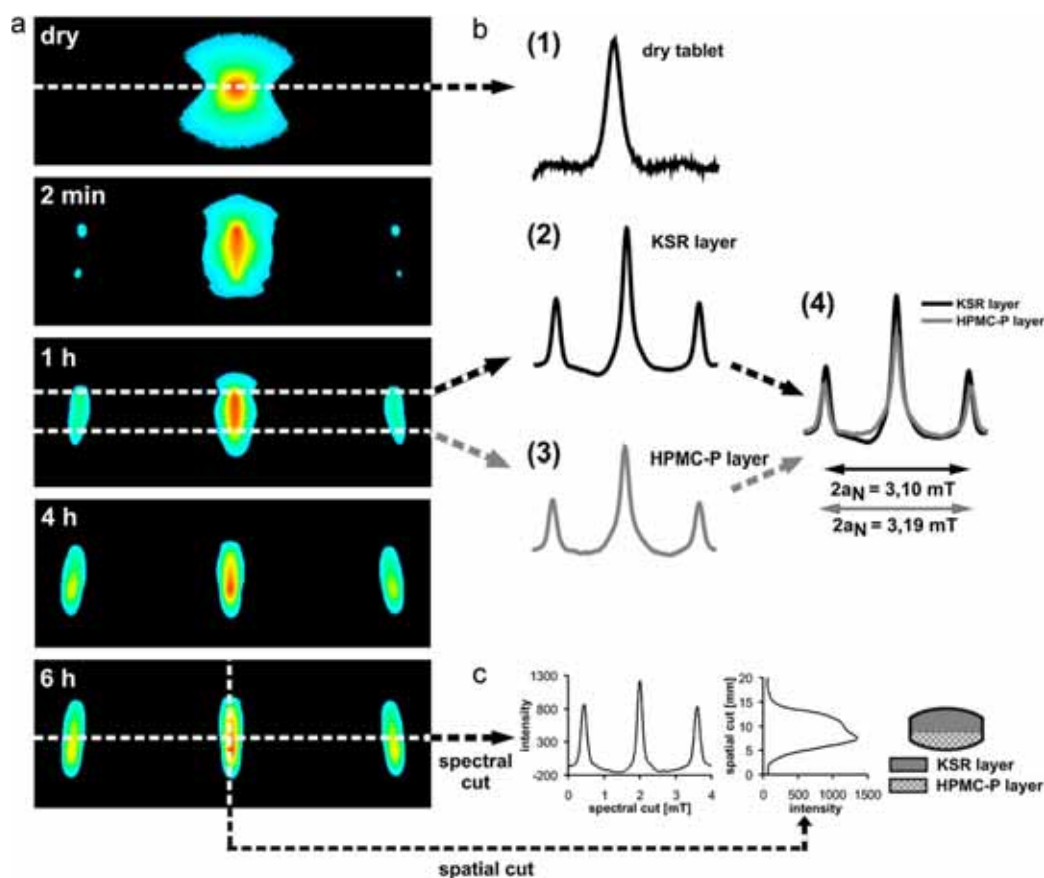


Fig. 6. (a) EPR images of AT-containing tablet C at different time intervals of contact with buffer pH 3. (b) EPR spectra which were extracted from the images of: (1) the dry tablet, (2) a region within KSR-layer after 1 h of buffer contact, (3) a region within HPMC-P-layer of the same image, (4) relation of spectra (2) and (3) with specified $2a_N$. (c) Spatial and spectral cut of tablet C after 6 h of buffer contact.

depending on pH (Fig. 5(a); Khramtsov et al., 1982). In particular, the distance of the first to the third peak ($2a_N$, where a_N is the isotropic hyperfine splitting constant) changes with changing pH of the surrounding buffer. Thus, a quantification of pH is possible by means of a calibration curve of $2a_N$ against buffer pH (Kempe et al., 2010). The pH dependency of the EPR signal of the spin probe AT follows a sigmoid dependence (Fig. 5(b)). Therefore, the pH_M calculation is only possible in a limited pH range of about ± 1.5 pH units depending of the pK_a of the spin probe (pK_a of AT is 6.1). Other spin probes having different pK_a values can be used to analyse different pH ranges.

Fig. 6(a) shows characteristic EPR images of tablet C at different time points of contact with buffer. The horizontal scale symbolises the spectral resolution (3 peaks of mobile AT) while the upright scale characterises the spatial resolution from the top to the bottom of the tablet (Fig. 6(c)). The dry tablet shows only one central peak of the immobile spin probe. Contact with buffer led to an increase in mobility of AT in the hydrated regions, visible through the appearance of the outer isotropic hyperfine splitting (Lurie and Mäder, 2005). The proportion of mobile to immobile spin probe increased steadily with time, detecting the liquid penetration to inner tablet regions which can be observed by the increase of intensity of the isotropic hyperfine splitting. It was also possible to follow the swelling process of the tablets because of the increase in spatial signal size of the images over time. The signals indicate a pH gradient within the wet tablet which is visible by the changing distance from first to third peak (both sloped outwards). EPR spec-

tra were extracted out of the horizontal layers of the presented images. Fig. 6(b) shows typical EPR spectra of: (1) a dry tablet; (2) the KSR layer after 1 h of buffer contact and (3) the HPMC-P layer of the same EPR image. By comparison of spectra (2) and (3), a changing distance of $2a_N$ can be found (4). $2a_N$ of spectrum 2 (KSR layer) underlay the calculable range, indicating a pH_M below 4.5. The calculated pH value of spectrum 3 (HPMC layer) was 6.03 which can be explained by the presence of IBS within this layer.

Spatial resolved pH_M values extracted from the EPR images of tablets A, B and C at different time intervals of buffer contact are presented in Fig. 7. The pH_M of whole tablet A was found to be around pH 6 for over 6 h (Fig. 7(A)). The acidic pH_M of the HPMC layer of tablet B increased quite fast to more neutral values above pH 6 (Fig. 7(B)) while the predominantly acidic pH_M of the KSR layer of tablet C changed only marginally in the centre region of the tablet (Fig. 7(C)). EPR imaging experiments of tablets A–F were repeated using a citric acid/phosphate buffer of pH 5.5 to gain information of the influence of the pH of the surrounding buffer on the pH_M . Similar results concerning the formation of pH_M gradients within tablets over time of buffer contact were obtained. Fig. 7(C2) shows the pH_M gradients within tablet C during contact with buffer pH 5.5. Interestingly, the pH_M of the KSR layer was below the pH of the surrounding buffer up to 1 h of buffer contact. A 10% Kollidon SR suspension in water generates a pH of about 4.6. Thus, Kollidon SR could cause the more acidic pH_M . After 1 h, the KSR layer assumed the pH of the surrounding buffer. The pH_M increased to values above

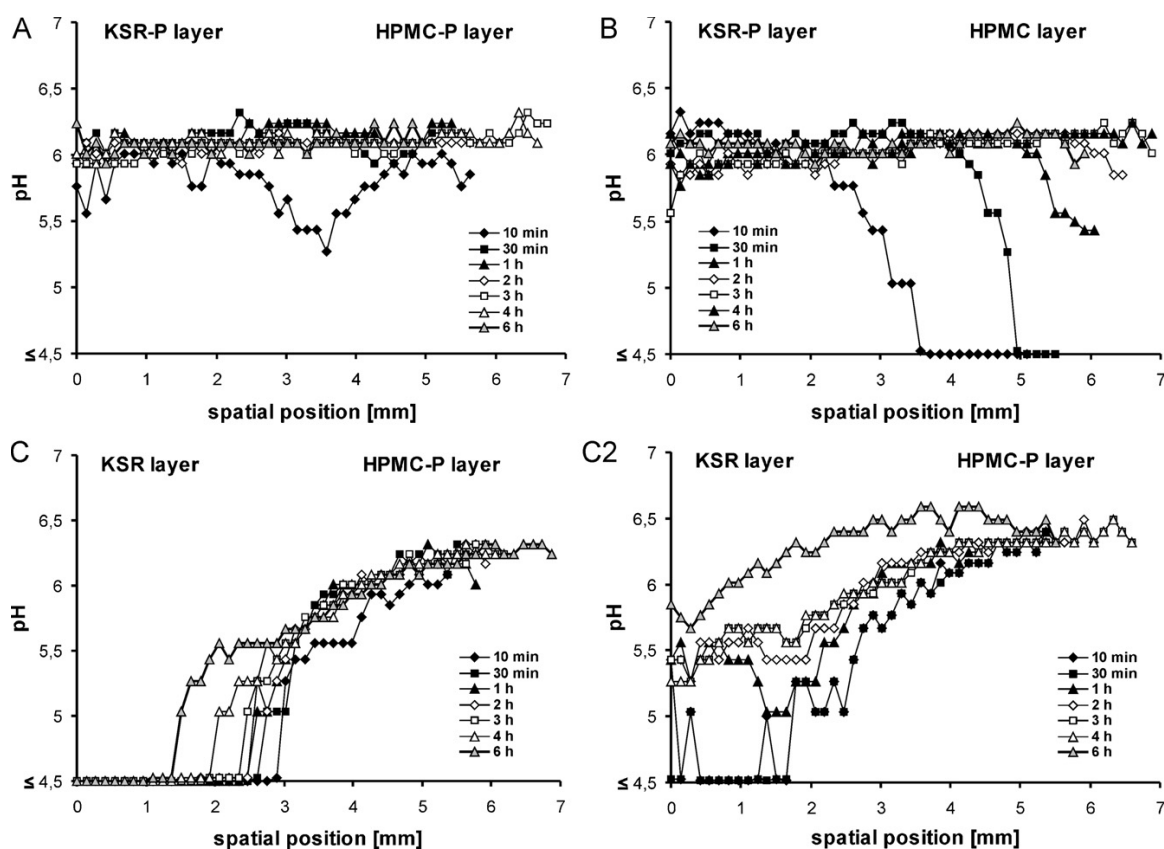


Fig. 7. (A–C2) pH_M averages within tablets A, B and C calculated from EPR images which were generated at different time intervals of contact with buffer pH 3. A buffer of pH 5.5 was used in the case of (C2). No values could be determined for areas with a $pH_M \leq 4.5$.

pH 6 after 6 h of buffer contact, possibly caused by the penetration of HPMC-P gel of low viscosity.

3-Layer tablets with an additional inter layer were analysed subsequently. The inter layer was added to enhance the integrity of both layers as well as to decrease diffusion processes between the layers. Fig. 8 demonstrates the differences in the EPR images of a 2- and a 3-layer tablet. The image of the 2-layer tablet C shows one homogeneous central signal. The central signal of the image of the 3-layer tablet F shows two separate areas of high intensity (red colour/dark grey). This difference is also obvious in the intensity profiles I in Fig. 8(b). The signal interruption of I_2 was caused by the lipophilic inter layer without spin probe. The transition of HPMC-P to KSR layer could be considerably monitored within the outer signals of image F because of a visible change of the distance of the first to the third peak ($2a_N$). Intensity profiles II and III illustrate a gradient within the right signal which is sloped outwards, thus indicating a pH_M gradient within the tablets.

pH_M profiles of tablets D–F over 6 h of buffer contact are presented in Fig. 9(D–F). Tablet D shows similar results like tablet A. The pH_M of the HPMC-P and the KSR-P layer lay around pH 6 over the analysed time interval. The HPMC layer of tablet E maintained an acidic pH_M over 6 h, which was different compared to tablet B. The inter layer seemed to hinder the approximation of pH_M of both layers. The protective character of the inter layer became also apparent in the case of tablet F. A sharp increase of the pH_M separates the acidic values of the KSR layer from the nearly neutral values of the HPMC-P layer over more than 6 h of buffer contact. The slight displacement over time may be caused by the swelling of the KSR layer.

3.4. Influence of the microenvironmental pH on the drug release

Dissolution studies of two model drugs were carried out to investigate the influence of the pH_M on the drug release. The anti-diabetic drug Metformin-HCl was used as freely soluble model drug showing pH independent release behaviour. Primarily, the drug release from 2-layer tablets was analysed. Unfortunately, these tablets could not withstand the release conditions and both tablet layers separated after about 2 h of dissolution testing. The layer separation led to an increase in dissolution rate of Metformin-HCl caused by the increased diffusion area (Fig. 10(a)). An additional inter layer of glycerol monostearate could considerably enhance the integrity of the tablets and prevent the separation of both tablet layers over the analysed time interval. Fig. 10(b) demonstrates the release behaviour of Metformin-HCl from 3-layer tablet formulations E and F. The IBS was present in the KSR-P layer of tablet E; while none was present in the KSR layer of tablet F. As expected, no influence of the pH_M on the drug release of Metformin-HCl could be found.

In contrast, NSAID Ketoprofen was analysed as model drug showing a pH dependent solubility. Ketoprofen is very slightly soluble at acidic pH (0.28 mg/ml at pH 4) and slightly soluble at pH 6.0 (3.68 mg/ml) (Sheng et al., 2006). The solubility increases with increasing pH because of the cumulative deprotonation of the carboxyl group (pK_a of 4.76). Fig. 10(c) demonstrates the dissolution profiles of Ketoprofen from 3-layer tablets E and F. Tablet formulation E enhanced the drug release considerably in comparison to tablet formulation F. The drug containing KSR-P layer of tablet E generated a pH_M of around 6, thus, leading to a higher solubility of

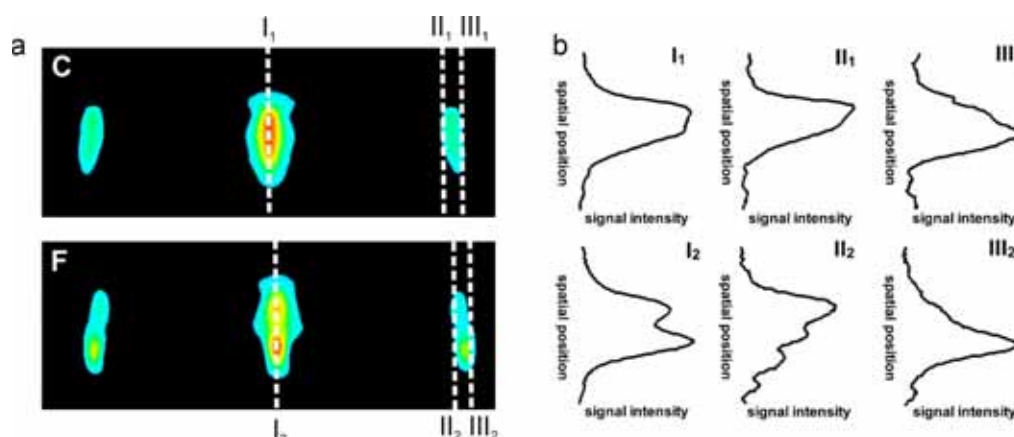


Fig. 8. (a) EPR images of tablets after 1 h of contact with buffer pH 3, the dotted lines show the position of the intensity profiles displayed in (b). Image C: 2-layer tablet C. Image F: 3-layer tablet F. (b) intensity profiles of the EPR signal of: (I) the central peak; (II) the left region of the right peak; (III) the right region of the right peak.

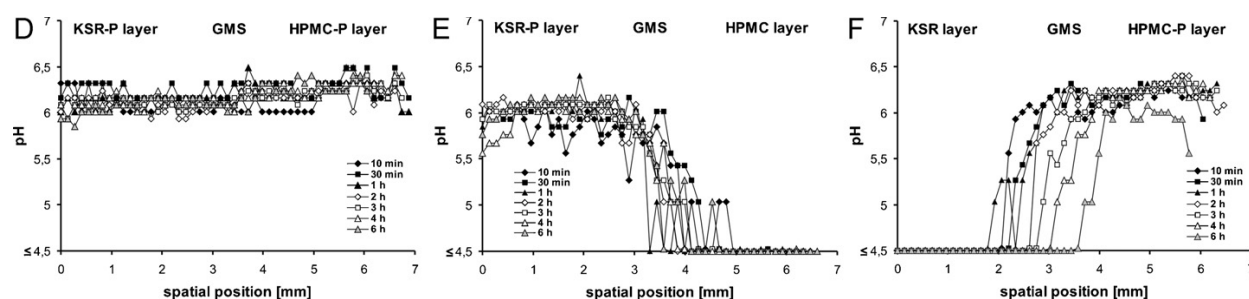


Fig. 9. (D–F) pH_M averages within tablets D, E and F calculated from EPR images which were generated at different time intervals of contact with buffer pH 3. No values could be determined for areas with a $pH_M \leq 4.5$.

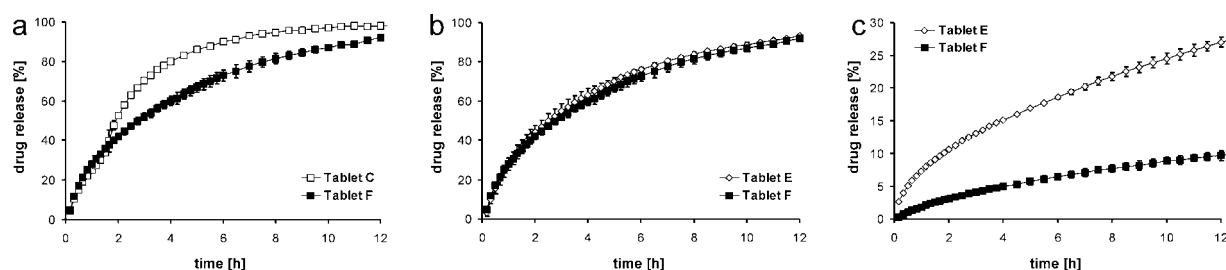


Fig. 10. Drug release in buffer pH 3. (a) Metformin-HCl release from 2-layer tablet C and 3-layer tablet F. (b) Metformin-HCl release from 3-layer tablets E and F. (c) Ketoprofen release from 3-layer tablets E and F.

Ketoprofen and therefore to an increase in drug release. The formulations were not further optimised regarding drug release, although even a drug release of around 30% over 12 h is quite low. However, the purpose of this investigation was not to develop an optimised formulation but to show the influence and importance of the pH_M within tablets on the drug release, especially for ionisable drugs.

3.5. Monitoring of hydration behaviour by means of 1H NMR benchtop imaging

Fig. 11 demonstrates the schematic process of tablet hydration of both tablet constitutions which could be monitored using benchtop MRI equipment over time of buffer contact. No considerable differences could be found between tablet formulations A, B and C (data not shown). Therefore, only 2-layer tablets C and 3-layer tablets F were further investigated. The hydration of 2-layer tablets

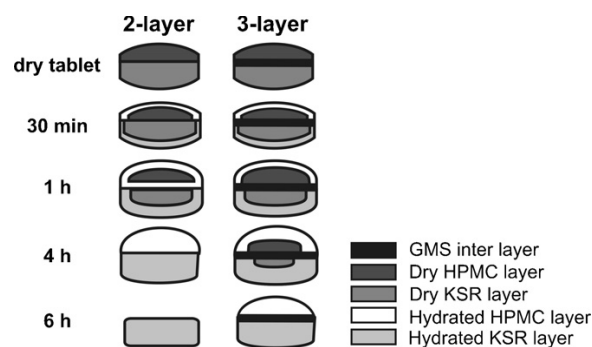


Fig. 11. Schematic process of tablet hydration of a 2- and a 3-layer tablet at different time intervals of contact with buffer.

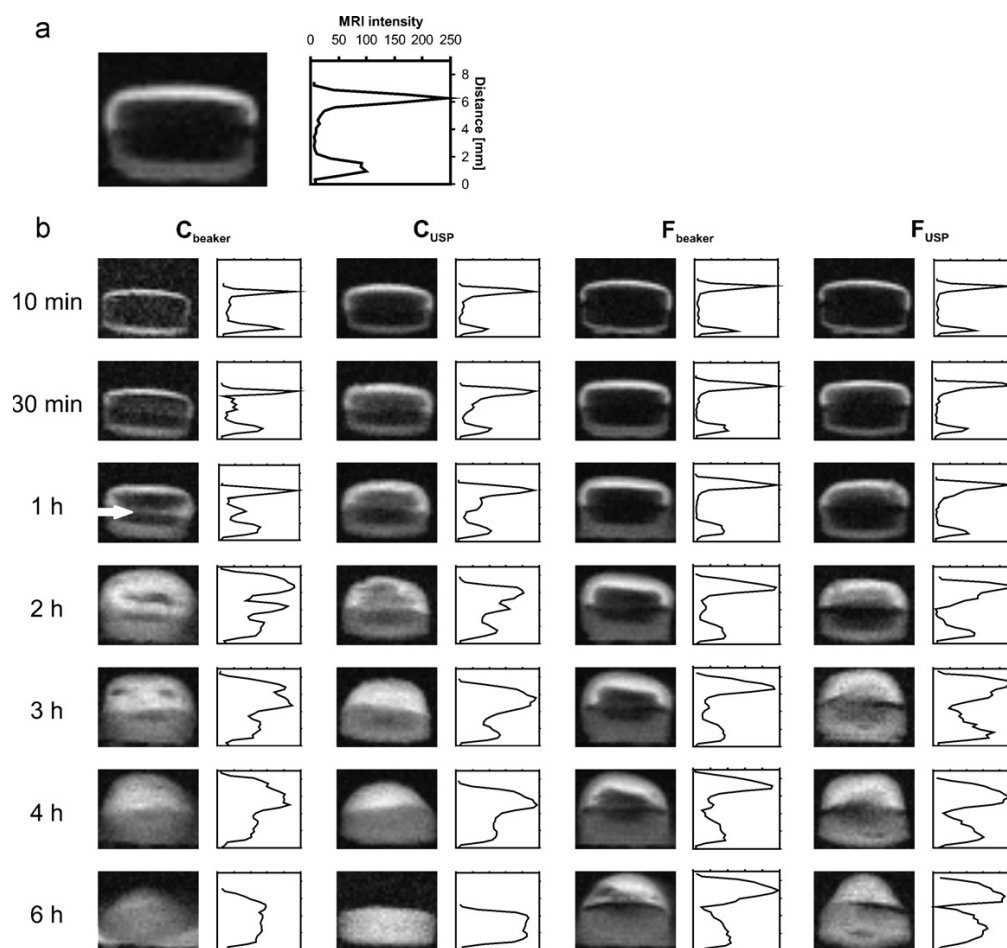


Fig. 12. (a) ^1H NMR benchtop magnetic resonance image and corresponding signal intensity profile of tablet preparation F after 30 min of contact with buffer, exemplified for scale labelling of (b). (b) ^1H NMR benchtop magnetic resonance images and corresponding signal intensity profiles of tablet preparations at different time intervals of contact with buffer. C_{beaker}: 2-layer tablet C, hydration in unstirred beaker. C_{USP}: 2-layer tablet C, hydration in USP paddle dissolution apparatus at 50 rpm. F_{beaker}: 3-layer tablet F, hydration in unstirred beaker. F_{USP}: 3-layer tablet F, hydration in USP paddle dissolution apparatus at 50 rpm. The arrow indicates the visible water penetration between both layers of tablet C.

started at the edges of the tablets but continued between the two layers, leading to a separation over time of hydration. Furthermore, diffusion processes between the layers could be facilitated. The swelling of the hydrated regions led to an increase in size. The tablets were completely hydrated after about 4 h of buffer contact. After 6 h, both layers were often separated. The additional inter layer of the 3-layer tablets prevented the penetration of water between the Kollidon SR and the HPMC layer. Therefore, the hydration process was slower because it continued only from the edges of the tablets to the inner regions. A dry core was existent even after 4 h of buffer contact. The 3-layer tablets remained complete over more than 6 h of hydration.

Characteristic T_1 -weighted BT-MRI images with corresponding intensity profiles of 2- and 3-layer tablets over time of buffer contact are presented in Fig. 12. Dark areas within the tablets refer to low spin densities and/or short relaxation times, which are related to dry parts of the tablets. Hydrated areas appear bright because of the water penetration and therewith associated increase in spin density. Relaxation times in the range of 10 up to hundred milliseconds give the brightest contrast under our measurement conditions (T_1 weighted). The HPMC layer appears brighter than the Kollidon SR layer. HPMC forms a gel upon hydration. The water inside the

gel layer was not as flexible as in the pores of the Kollidon SR matrix leading to shorter T_1 relaxation times and a brighter signal which could also be confirmed by NMR relaxometry (data not shown). A swelling of the HPMC and Kollidon SR layer could be monitored by increase in size of the tablets. The different tablet formulations were exposed to two different hydration settings. Tablets exposed to USP dissolution conditions showed a faster water penetration into and erosion of the HPMC layer compared to the unstirred tablets, visible by a faster decrease in size. Water penetration between both layers of the 2-layer tablet C could be monitored after 30 min of buffer contact independent from used hydration setting which is also illustrated in the corresponding MRI intensity profiles. After 1 h, an additional central peak could be monitored within the intensity profiles (Fig. 12(b); C, 1 h). In contrast, the hydration of 3-layer tablets F proceeded only from the edges of the tablets caused by the aforementioned interference of the inter layer. The inter layer is clearly visible as black region between the HPMC and the KSR layer over the analysed time interval of 6 h. Because of its lipophilic character, almost no water penetrated into this region leading to low spin density and a black colour. The MRI intensity profiles illustrate the low signal intensity between the HPMC and the KSR layer even after 6 h of contact with buffer (Fig. 12(b); F, 6 h).

4. Discussion

The purpose of present study was the detection of pH_M gradients within multi-layer tablets. Different techniques were investigated for comparison purposes, all leading to similar results. A pH indicator dye was incorporated into tablets A–F, which allowed the differentiation between the tablet formulations because of their differences in local pH and therewith associated colour changes. Furthermore, it was possible to monitor the shifting of pH_M within the tablet layers over time of buffer contact and to observe differences in the pH_M shifting of 2- and 3-layer tablets. Nevertheless, this technique allowed only a very rough determination of the pH_M . It was rather difficult to relate a specified pH value to the colour grading of the indicator. Colours indicating same pH appeared different in both matrix forming excipients (HPMC and KSR). In addition, to investigate the pH_M in the interior of the tablet, the tablet had to be cut. It was therefore not possible to analyse the pH_M of one tablet continuously.

Fluorescence imaging gave the opportunity to calculate an average pH_M of an estimated domain of each tablet layer using a fluorescence dye with pH dependent changes in the emission spectra. Similar pH gradients were detected compared to the results of the aforementioned method. However, a different hydration setting had to be used to allow a constant measuring area which changed and delayed the hydration process and made comparison with other results rather difficult. Higher pH_M values were detected within the HPMC-P layer compared to the KSR-P layer of tablet A (same amount of IBS in both layers). The usage of different excipients could have an impact on the emission spectrum. The influence of the nature of excipient on the pH_M calculation was therefore analysed by fluorescence imaging. Kollidon SR and HPMC showed no clear trend to enhance or decrease calculated pH_M values (data not shown). A 10% Kollidon SR suspension in water generates a pH around 4.6 which also influences the resulting pH_M . Furthermore, the photographs of pH-indicator containing tablets showed a yellow discolouration of the surface of the previously blue KSR-P layer after 1–2 h (Fig. 2). In contrast, the colour of the HPMC-P layer changed only marginally. With fluorescence imaging, it was only possible to analyse the pH_M of the surface of the tablets because of the limited penetration depth of the excitation and emission light. The pH_M of the surface of the tablet could differ from those of the inner regions which can also contribute to the monitored differences.

Therefore, EPR imaging was accomplished to determine the spatial pH_M distribution of the tablets non-invasively. EPR imaging provides the possibility to calculate the average pH_M of hydrated inner and outer regions of different cylindrical layers of the tablet giving a spatial pH_M resolution from top to the bottom of the tablet. Although the analysis with this technique is more time consuming, it gave unique information about the internal pH within analysed tablets and made a continuous measurement of one tablet over time of hydration possible. Furthermore, no influence of the nature of surrounding matrix material on the resulting $2a_N$ values could be detected (data not shown). However, the pH_M calculation is only possible in a limited pH interval of about ± 1.5 pH units depending of the pK_a of the spin probe (pK_a of AT is 6.1). Therefore, no pH_M values could be calculated in tablet regions showing a pH_M below 4.5. It is possible to investigate the pH_M within more acidic regions of the tablets using a spin probe with a lower pK_a .

The pH of the buffer strongly influenced the internal pH of tablet layers without IBS. Almost no influence could be monitored in the case of tablet layers with IBS (Fig. 7(C2)). The HPMC layer of tablet B (without IBS) showed an acidic pH_M after contact with buffer but started to change to nearly neutral values after 30 min. After 2 h, the complete HPMC layer showed a pH around 6 (Fig. 7(B)). A possible reason could be the migration of IBS out of the KSR-P layer into the

HPMC layer. In contrast, the HPMC layer of tablet E remained acidic over 6 h of buffer contact (Fig. 9(E)). The migration of IBS seems to be hindered by the lipophilic inter layer. In the case of the KSR layer of 2- and 3-layer tablet C and F (without IBS), an obvious pH_M gradient over more than 6 h of buffer contact was determined. Especially in the case of tablet F, the pH_M of the KSR layer showed an acidic $pH \leq 4.5$ over the analysed time interval of 6 h, confirming the protective character of the inter layer (Fig. 9(F)). This finding could also be valuable to separate drugs with different pH stability optima by the usage of multi-layer tablets with an additional lipophilic inter layer. However, the pH_M of the KSR layer of tablet C increased only marginally in the centre region of the tablet as well, which was different from the behaviour of the HPMC layer of tablet B. The different behaviour of both matrix-forming excipients might possibly be caused by a faster water exchange within the KSR layer in comparison to the HPMC layer. Furthermore, the acidic behaviour of Kollidon SR seems to have an influence on the pH_M generation as well.

Dissolution studies were carried out to analyse the influence of the pH_M on the drug release. Two model drugs were incorporated into the KSR/KSR-P layer of tablet E/F (with and without IBS). Metformin-HCl shows a pH independent solubility. Therefore, both formulations showed same drug release (Fig. 10(b)). In contrast, the release of Ketoprofen could be modified by the incorporation of the IBS. Ketoprofen shows a pH dependent solubility with an improved solubility under neutral conditions (see Section 3.4). Therefore, the drug release of tablet formulation E (with IBS) was faster compared to formulation F (without IBS) (Fig. 10(c)). These finding is in agreement with literature data where the drug release of weak acids could be improved by the incorporation of alkaline excipients (Doherty and York, 1989; Riis et al., 2007; Tran et al., 2008). Further formulation optimisation would be needed for a reasonable drug release over 12 h. This issue was beyond the scope of this work as it was intended to keep the formulation of the layers constant for comparability purposes.

Benchtom NMR imaging was accomplished to further analyse the differences in the hydration behaviour of 2- and 3-layer tablets. The MRI signal of the HPMC layer appeared brighter compared to the signal of the KSR layer. The water inside the gel layer of HPMC is not as flexible as in the pores of the KSR matrix leading to a shorter T_1 relaxation time and a brighter signal. This issue could also have an influence on the different behaviour regarding the migration of IBS. Besides, it could be detected that water penetrated between the two layers of the 2-layer tablets (Fig. 12(C)) which could enable a fast migration of IBS from the KSR-P to the HPMC layer of tablet B. Furthermore, a separation of both layers could be facilitated. The water penetration could be prevented by an additional lipophilic inter layer which improved the integrity of the tablets and possibly hindered the migration process of the IBS (Fig. 12(F)). In addition, 2- and 3-layer tablets were exposed to two different hydration settings. Tablets exposed to USP dissolution conditions showed a faster water penetration into and erosion of the HPMC layer compared to the unstirred tablets (Fig. 12). These findings are consistent with previous work, showing the dependence of erosion and hydration processes of hydrogel-forming HPMC on mechanical stress (Costa and Lobo, 2001; Kavanagh and Corrigan, 2004). Further studies have to be carried out to investigate, if mechanical stress could also change the migration behaviour of the IBS.

In conclusion, pH_M gradients within multi-layer tablets could be analysed by 3 different techniques, in particular, a pH indicator dye, fluorescence imaging and EPR imaging. It was possible to gain information about the pH_M with all applied techniques. The qualitative results were similar but the informative value showed major differences. The incorporation of a pH indicator dye turned out to be a simple, fast and inexpensive method to get an overview over proceeding processes. However, no precise pH_M determina-

tion was possible and the inner tablet regions could be analysed only invasively. Fluorescence imaging produced calculable results of the pH_M of the tablet surface. A spatial distribution of the surface pH_M could be provided. However, a different hydration setting had to be used, excipient interactions were hard to predict and the inner regions of the tablet can be analysed only by cutting the tablet. EPR imaging proved to be a powerful tool for the determination of spatial pH_M information non-invasively. However, it should be emphasised that the resulting pH_M describe an average pH_M value of a thin tablet layer, possibly forming a pH_M gradient inside this layer with different pH_M values in the outer regions compared to the centre of the tablet. Furthermore, it is a time consuming method which requires expensive equipment. Nevertheless, because of its superior advantages, EPR imaging was used as method of choice for further analysis. The influence of different variables on the pH_M was investigated. The incorporation of an IBS strongly influenced the pH_M as well as the nature of used matrix forming excipient. Kollidon SR generated a more acidic microenvironment compared to HPMC, which was obvious in particular when buffer pH 5.5 was used where the pH_M of the KSR layer underlay the buffer pH. The pH_M of the KSR layer maintained acidic over the analysed time interval. Otherwise, the HPMC layer was able to turn primary acidic pH_M to more neutral values although the acidic properties of the surrounding buffer which may be caused by the migration of IBS from the KSR-P layer. The variation of the buffer pH had an influence on the pH_M especially within tablet layers without IBS. An additional lipophilic inter layer strongly improved the integrity of both layers. Furthermore, it acted as pH neutral region which could decrease diffusion processes between the layers and therefore influence the pH gradient processing. BT-MRI was accomplished to gain a deeper insight on the differences of proceeding processes during hydration of 2- and 3-layer tablets. The protective character of the inter layer was confirmed which could prevent water penetration between the HPMC and the KSR layer, leading to the aforementioned advantages. Mechanical stress influenced the hydration process as well, which was monitored using different hydration settings. Moreover, an influence of the pH_M on the drug release of the weakly acidic drug Ketoprofen could be demonstrated. In contrast, the drug release of Metformin-HCl, showing pH independent solubility, was not influenced by varied pH_M , as expected.

Acknowledgements

The authors would like to thank Dr. Hendrik Metz for his support concerning EPR and MRI measurements and valuable scientific discussions.

References

- Adhikary, A., Vavia, P.R., 2008. Bioadhesive ranitidine hydrochloride for gastroretention with controlled microenvironmental pH. *Drug Dev. Ind. Pharm.* 34, 860–869.
- Akiyama, Y., Yoshioka, M., Horibe, H., Hirai, S., Kitamori, N., Toguchi, H., 1994. pH-independent controlled-release microspheres using polyglycerol ester-fatty acids. *J. Pharm. Sci.* 83, 1600–1607.
- Badawy, S.I., Hussain, M.A., 2007. Microenvironmental pH modulation in solid dosage forms. *J. Pharm. Sci.* 96, 948–959.
- BASF AG, 1999. Technical Information for Kollidon SR. Ludwigshafen, Germany.
- Brunner, A., Mäder, K., Göpferich, A., 1999. The microenvironment inside biodegradable microspheres: changes in pH and osmotic pressure. *Pharm. Res.* 16, 852–858.
- Ching, A.L., Liew, C.V., Chan, L.W., Heng, P.V.S., 2008. Modifying matrix microenvironmental pH to achieve sustained drug release from highly laminating alginate matrices. *Eur. J. Pharm. Sci.* 33, 361–370.
- Cope, S.J., Hibberd, S., Whetstone, J., MacRae, R.J., Melia, C.D., 2002. Measurement and mapping of pH in hydrating pharmaceutical pellets using confocal laser scanning microscopy. *Pharm. Res.* 19, 1554–1563.
- Costa, P., Lobo, J.M.S., 2001. Influence of dissolution medium agitation on release profiles of sustained-release tablets. *Drug Dev. Ind. Pharm.* 27, 811–817.

- Doherty, C., York, P., 1989. Microenvironmental pH control of drug dissolution. *Int. J. Pharm.* 50, 223–232.
- Gibaldi, M., 1984. *Biopharmaceutics and Clinical Pharmacokinetics*. Lea and Febiger, Philadelphia.
- Glombitza, B.W., Schmidt, P.C., 1995. Surface acidity of solid pharmaceutical excipients. Part 2. Effect of the surface acidity on the decomposition rate of acetylsalicylic acid. *Eur. J. Pharm. Biopharm.* 41, 114–119.
- Glombitza, B.W., Oelkrug, D., Schmidt, P.C., 1994. Surface acidity of solid pharmaceutical excipients. Part 1. Determination of the surface acidity. *Eur. J. Pharm. Biopharm.* 40, 289–293.
- Grundy, J.S., Foster, R.T., 1996. The nifedipine gastrointestinal therapeutic system (GITS). Evaluation of pharmaceutical, pharmacokinetic and pharmacological properties. *Clin. Pharmacokinet.* 30, 28–51.
- Gutsche, S., Krause, M., Kranz, H., 2008. Strategies to overcome pH-dependent solubility of weakly basic drugs by using different types of alginates. *Drug Dev. Ind. Pharm.* 34, 1277–1284.
- Ingani, H.M., Timmermans, J., Möes, A.J., 1987. Conception and in vivo investigation of peroral sustained release floating dosage forms with enhanced gastrointestinal transit. *Int. J. Pharm.* 35, 157–164.
- Jantratid, E., Janssen, N., Reppas, C., Dressman, J.B., 2008. Dissolution media simulating conditions in the proximal human gastrointestinal tract: an update. *Pharm. Res.* 25, 1663–1676.
- Kavanagh, N., Corrigan, O.I., 2004. Swelling and erosion properties of hydroxypropylmethylcellulose (hypromellose) matrices—influence of agitation rate and dissolution medium composition. *Int. J. Pharm.* 279, 141–152.
- Kempe, S., Metz, H., Mäder, K., 2010. Application of Electron Paramagnetic Resonance (EPR) spectroscopy and imaging in drug delivery research – chances and challenges. *Eur. J. Pharm. Biopharm.* 74, 55–66.
- Khramtsov, V.V., Marsh, D., Weiner, L., Grigoriev, I.A., Volodarsky, L.B., 1982. Proton exchange in stable nitroxyl radicals. EPR study of the pH of aqueous solutions. *Chem. Phys. Lett.* 91, 69–72.
- Li, L., Schwendeman, S.P., 2005. Mapping neutral microclimate pH in PLGA microspheres. *J. Control. Release* 101, 163–173.
- Lurie, D., Mäder, K., 2005. Monitoring drug delivery processes by EPR and related techniques – principles and applications. *Adv. Drug Deliv. Rev.* 57, 1171–1190.
- Mäder, K., Bacic, G., Domb, A., Elmalak, O., Langer, R., Swartz, H.M., 1997. Non invasive in vivo monitoring of drug release and polymer erosion from biodegradable polymers by EPR spectroscopy and NMR imaging. *J. Pharm. Sci.* 86, 126–134.
- Malaterre, V., Metz, H., Ogorka, J., Gurny, R., Loggia, N., Mäder, K., 2009. Benchtop-magnetic resonance imaging (BT-MRI) characterization of push-pull osmotic controlled release systems. *J. Control. Release* 133, 31–36.
- Metz, H., Mäder, K., 2008. Benchtop-NMR and MRI – a new analytical tool in drug delivery research. *Int. J. Pharm.* 364, 170–175.
- Metz, H., Bar-Shalom, D., Mäder, K., 2007. Detailed monitoring of the release mechanism from Egalet tablets by ESR and NMR imaging. In: 33rd CRS Annual Meeting, poster.
- Nott, K., 2010. Magnetic resonance imaging of tablet dissolution. *Eur. J. Pharm. Biopharm.* 74, 78–83.
- Pudipeddi, M., Zannou, E.A., Vasanthavada, M., Dontabhaktuni, A., Royce, A.E., Joshi, Y.M., Serajuddin, A.T.M., 2008. Measurement of surface pH of pharmaceutical solids: a critical evaluation of indicator dye-sorption method and its comparison with slurry pH method. *J. Pharm. Sci.* 97, 1831–1842.
- Rahman, Z., Ali, M., Khar, R.K., 2006. Design and evaluation of bilayer floating tablets of captopril. *Acta Pharm.* 56, 49–57.
- Richardson, J.C., Bowtell, R.W., Mäder, K., Melia, C.D., 2005. Pharmaceutical applications of magnetic resonance imaging (MRI). *Adv. Drug Deliv. Rev.* 57, 1191–1209.
- Riis, T., Bauer-Brandl, A., Wagner, T., Kranz, H., 2007. pH-independent drug release of an extremely poorly soluble weakly acidic drug from multiparticulate extended release formulations. *Eur. J. Pharm. Biopharm.* 65, 78–84.
- Schädlich, A., Ullrich, S., Mäder, K., 2009. In vivo pH measurements of in situ forming sucrose ester implants using multispectral fluorescence imaging. In: Poster, 36th Annual Meeting and Exposition of the Controlled Release Society, Copenhagen.
- Scheef, C.A., Oelkrug, D., Schmidt, P.C., 1998. Surface acidity of solid pharmaceutical excipients. III. Excipients for solid dosage forms. *Eur. J. Pharm. Biopharm.* 46, 209–213.
- Sheng, J.J., Kasim, N.A., Chandrasekharan, R., Amidon, G.L., 2006. Solubilization and dissolution of insoluble weak acid, ketoprofen: effects of pH combined with surfactant. *Eur. J. Pharm. Sci.* 29, 306–314.
- Siepe, S., Lueckel, B., Kramer, A., Ries, A., Gurny, R., 2006. Strategies for the design of hydrophilic matrix tablets with controlled microenvironmental pH. *Int. J. Pharm.* 316, 14–20.
- Streubel, A., Siepmann, J., Dashevsky, A., Bodmeier, R., 2000. pH-independent release of a weakly basic drug from water-insoluble and -soluble matrix tablets. *J. Control. Release* 67, 101–110.
- Strübing, S., Abboud, T., Contri, R.V., Metz, H., Mäder, K., 2008a. New insights on Polyvinylacetate based coated floating tablets: characterisation of hydration and CO₂ generation by benchtop MRI and its relation to drug release and floating strength. *Eur. J. Pharm. Biopharm.* 69, 708–717.
- Strübing, S., Metz, H., Mäder, K., 2008b. Characterization of polyvinyl acetate based floating matrix tablets. *J. Control. Release* 126, 149–155.
- Tatavarti, A.S., Hoag, S.W., 2006. Microenvironmental pH modulation based release enhancement of a weakly basic drug from hydrophilic matrices. *J. Pharm. Sci.* 95, 1459–1468.

- Tatavarti, A.S., Mehta, K.A., Augsburg, L.L., Hoag, S.W., 2004. Influence of methacrylic and acrylic acid polymers on the release performance of weakly basic drugs from sustained release hydrophilic matrices. *J. Pharm. Sci.* 93, 2319–2331.
- Thoma, K., Zimmer, T., 1990. Retardation of weakly basic drugs with diffusion tablets. *Int. J. Pharm.* 58, 197–202.
- Tran, P.H.L., Tran, H.T.T., Lee, B.-J., 2008. Modulation of microenvironmental pH and crystallinity of ionizable telmisartan using alkalizers in solid dispersions for controlled release. *J. Control. Release* 129, 59–65.
- Varma, M.V.S., Kaushal, A.M., Garg, S., 2005. Influence of micro-environmental pH on the gel layer behavior and release of a basic drug from various hydrophilic matrices. *J. Control. Release* 103, 499–510.
- Wei, Z., Yu, Z., Bi, D., 2001. Design and evaluation of a two-layer floating tablet for gastric retention using cisapride as a model drug. *Drug Dev. Ind. Pharm.* 27, 469–474.
- Zinchuck, A.V., Hancock, B.C., Shalaev, E.Y., Reddy, R.D., Govindarajan, R., Novak, E., 2005. The influence of measurement conditions on the Hammett acidity function of solid pharmaceutical excipients. *Eur. J. Pharm. Biopharm.* 61, 158–170.

Annex

<i>Acknowledgements</i>	<i>I</i>
<i>Publication list</i>	<i>III</i>
<i>Curriculum vitae</i>	<i>VII</i>
<i>Declaration of the self-contribution of research articles</i>	<i>VIII</i>
<i>Selbstständigkeitserklärung</i>	<i>XI</i>

Acknowledgements

First and foremost, with a deep sense of respect and heartfelt gratitude I would like to extend my unreserved indebtedness to my supervisor, Prof. Dr. habil. Karsten Mäder, head of the Pharmaceutical Technology Group within the Department of Pharmaceutical Technology and Biopharmaceutics at the Martin Luther University of Halle-Wittenberg in Germany. I want to thank him for the opportunity to join his research group and for the suggestion of the very interesting topic of my PhD work. Furthermore I would like to thank him for all kinds of scientific discussions, questions and inspirations while providing me freedom immersing into the fluorescence imaging research.

Secondly, I am very grateful to Associate Prof. Dr. Judith Kuntsche for her contribution to the particle size measurements, for the fruitful discussions and for her help in revising many of my published manuscripts. Thirdly, I would like to thank Dr. Thomas Müller and Dr. Henrike Caysa for the very fruitful cooperation in supporting the nanocarrier *in vivo* experiments and in giving me valuable technical and anatomical tips. Their expert knowledge of the xenograft cancer models was the basis for a couple of experiments. Very special thanks go to Dr. Sabine Kempe for her support in performing the pH measurements, for the many fruitful discussions during the last years and for revising this doctoral thesis. I am also very thankful to Friederike Eisenächer and Dr. Wolfgang Schmid for the opportunity of performing *in vitro* experiments together.

Special thanks go to Prof. Dr. habil. Achim Göpferich and his working group, in particular to Dr. Cornelia Rose for the PEG-PLA polymer synthesis, the nanoparticle preparation and their pre-characterization. My enormous thanks go also to Prof. Dr. habil. Jörg Kreßler and his working group in particular to Dr. Regina Schöps, Dr. Elkin Amado, Dr. Yanjiao Jiang and Toufik Naolou for their contribution to the PVA experiments and for the informative dialogues.

Prof. Dr. habil. Thomas Groth, Dr. Jürgen Vogel and Marcus Niepel are acknowledged for supporting me by conducting the confocal microscopy experiments. I would also like to thank Dr. Gerd Hause for his support in performing frozen section slides and TEM test measurements.

Furthermore, my thanks go to Dr. Hendrik Metz, Dr. Alexander Lochmann, Dr. Jun Li and Frederike Tenambergen for their help and cooperation. I thank Dieter Reese und his marvellous team, Ute Mentzel, Kerstin Schwarz and Sigrid Todte for their great help to me during the daily scientific life and I want to cordially thank them for their kindness and their helpfulness. I also would like to appreciate Martina Henicke and Constanze Gottschalk for their treasured support with the animal care.

I would like to extend my thanks and appreciation to all my colleagues for the great time. I will miss the kind and hearty atmosphere and the interesting discussions most notably during the lunchtime. Here, I would like to acknowledge in particular Dr. Sandra Klein and Dr. Sandra Strübing as well as Dr. Johannes Oidtmann, Dr. Sebastian Ullrich and Stefan Hoffmann.

Svetlana Orlova-Sitova from Fresenius Kabi, Germany is acknowledged for reviewing the PhD thesis. The Federal State of Saxonia Anhalt (FKZ 3646A/0907) and the Deutsche Forschungsgemeinschaft (MA 1648/7-1, LSM: INST 271/250-1) are gratefully acknowledged for partly supporting some of the *in vivo* studies and *ex vivo* characterizations.

I wish to pay my gratitude to my parents for their positive support during the past years. My heartfelt gratitude goes also to my sister and to all of my friends for their support and patience.

Last but not least I wish to thank my wife Annekatrin for appreciating my work and giving me strength and motivation to get this work done.

Publication list

Research articles (published or under peer review)

(a) Investigation of the *in vivo* fate of a water soluble polymer

- (I) **Schädlich, A.**, Naolou, T., Amado, E., Schöps, R., Kressler, J., Mäder, K., (2011) Noninvasive *in vivo* monitoring of the biofate of 195 kDa poly(vinyl alcohol) by multispectral fluorescence imaging. *Biomacromolecules* 12 (10): 3674-3683.
- (II) Jiang, Y., **Schädlich, A.**, Amado, E., Weis, C., Odermatt, E., Mäder, K., Kressler, J., (2010) In-vivo studies on *intraperitoneally* administrated poly(vinyl alcohol). *Journal of Biomedical Materials Research Part B-Applied Biomaterials* 93B (1): 275-284.
- (III) **Schädlich, A.**, Jiang, Y., Kressler, J., Mäder, K., (2010) Tracking the *in vivo* fate of high molar mass poly(vinyl alcohol) using multispectral fluorescence *in vivo* imaging. *Scientifically Speaking News (Controlled Release Society)* 27 (2): 15-16. **(Cover Story)**

(b) Characterization of nanocarriers and their potential usage in cancer therapy

- (IV) **Schädlich, A.**, Rose, C., Kuntsche, J., Caysa, H., Mueller, T., Göpferich, A., Mäder, K., (2011) How stealthy are PEG-PLA nanoparticles? An NIR *in vivo* study combined with detailed size measurements. *Pharmaceutical Research* 28: 1995-2007.
- (V) **Schädlich, A.**, Caysa, H., Mueller, T., Tenambergen, F., Rose, C., Göpferich, A., Kuntsche, J., Mäder, K., (2011) Tumor accumulation of NIR fluorescent PEG PLA nanoparticles: impact of particle size and human xenograft tumor model. *ACS Nano* 5 (11): 8710-8720.

(VI) Schädlich, A., Hoffmann, S., Mueller, T., Caysa, H., Rose, C., Göpferich, A., Li, J., Kuntsche, J., Mäder, K., (2012) Accumulation of nanocarriers in the ovary: A neglected toxicity risk? *Journal of Controlled Release* 160 (1): 105-112. **(Cover Story)**

(c) Characterization of *in situ* forming implants for potential controlled API release

(VII) Schädlich, A., Kempe, S., Mäder, K., (2013) Long-term *in vivo* pH measurements of *in situ* forming PLGA implants using multispectral fluorescence imaging. Submitted to *Journal of Controlled Release*. **(under peer-review)**

(d) Investigating alternative application fields of fluorescence imaging

(VIII) Eisenächer, F., **Schädlich, A.**, Mäder, K., (2011) Monitoring of internal pH gradients within multi-layer tablets by optical methods and EPR imaging. *International Journal of Pharmaceutics* 417 (1-2): 204-215.

Research articles (in preparation)

(d) Investigating alternative application fields of fluorescence imaging

(IX) Li, J., **Schädlich, A.**, Hause, G., Vogel, J., Kuntsche, J., Groth, T., Mäder, K., Pre-clinical *in vivo* studies of oily core PEG-PLGA nanocapsules using fluorescence imaging. **(in preparation)**

(X) Lochmann, A., **Schädlich, A.**, Nitzsche, H., Metz, H., Schön, I., Schwarz, E., Mäder, K., Quantitative monitoring of the *in vivo* efficiency of rhBMP-2 loaded PLGA and PEG-PLGA microparticles by means of optical imaging, CT and BT-MRI. **(in preparation)**

Conference contributions (selection)

(a) Investigation of the *in vivo* fate of a water soluble polymer

1. **Schädlich, A.**, Jiang, Y., Kressler, J., Mäder, K., (2009) Multispectral *in vivo* imaging of fluorescence labeled poly(vinyl alcohol). CRS Meeting, Copenhagen
2. **Schädlich, A.**, Jiang, Y., Kressler, J., Mäder, K., (2009) Tracking the fate of fluorescence labeled poly(vinyl alcohol) a multispectral *in vivo* analysis. CRS Annual Meeting, Halle

(b) Characterization of nanocarriers and their potential usage in cancer therapy

3. **Schädlich, A.**, Hoffmann, S., Mueller, T. Caysa, H. Mäder, K., (2012) Is the accumulation of nanocarriers in the ovary a common phenomenon? 76th Prague Meeting on Macromolecules: Polymers in Medicine, Prague
4. **Schädlich, A.**, Rose, C., Kuntsche, J., Caysa, H., Mueller, T., Göpferich, A., Mäder, K., (2010) *In vivo* and *ex vivo* studies of PEG - PLA block copolymer nanoparticles for tumor visualisation and treatment. DPhG Jahrestagung, Braunschweig (Lesmüller Poster Award)
5. **Schädlich, A.**, Rose, C., Kuntsche, J., Mueller, T., Göpferich, A., Mäder, K., (2010) *In vivo* studies of PEG - PLA block copolymer nanoparticles for the visualisation of colon carcinoma. 8th International Symposium on Polymer Therapeutics, Valencia
6. **Schädlich, A.**, Rose, C., Kuntsche, J., Mueller, T., Göpferich, A., Mäder, K., (2010) *In vivo* fate and tumor targeting studies of new synthesized PEG – PLA block copolymer nanoparticles using non invasive fluorescence imaging. 7th APV World Meeting, Malta

(c) Characterization of *in situ* forming implants for potential controlled API release

7. **Schädlich, A.**, Kempe, S., Ullrich, S., Mäder, K., (2010) *In vitro* and *in vivo* pH measurement studies of *in situ* forming sucrose ester and PLGA implants using EPR spectroscopy and fluorescence imaging. 7th APV World Meeting, Malta

(d) Investigating alternative application fields of fluorescence imaging

8. Hoffmann, S., **Schädlich, A.**, Caysa, H., Müller, T. and Mäder, K., (2011) HES 450 as potential drug delivery system for passive tumor targeting: An *in vivo* study in nude mice using near infrared optical imaging. European Summerschool in Nanomedicine, Wittenberg
9. Hoffmann, S., **Schädlich, A.**, Caysa, H., Mäder, K., (2010) *In vivo* characterisation of high molecular weight hydroxyethyl starch using noninvasive fluorescence imaging. 8th International Symposium on Polymer Therapeutics: From Laboratory to Clinical Practice, Valencia (Spain)
10. Hoffmann, S., **Schädlich, A.**, Caysa, H. and Mäder, K., (2010) Plasma volume expanders as potential drug delivery systems – An *in vivo* study utilising noninvasive near infrared fluorescence optical imaging. DPhG Jahrestagung Braunschweig
11. Eisenächer, F., **Schädlich, A.**, Mäder, K., (2010) Microacidity measurements of 2-layer tablets using multispectral fluorescence imaging and electron paramagnetic resonance. 7th APV World Meeting, Malta
12. **Schädlich, A.**, Ullrich, S., Mäder, K., (2009) *In vivo* pH measurements of *in situ* forming sucrose ester implants using multispectral fluorescence imaging. CRS Meeting, Copenhagen
13. **Schädlich, A.**, Ullrich, S., Mäder, K., (2008) Multispectral fluorescence *in vivo* imaging of *in situ* forming sucrose ester implants. CRS Annual Meeting, Braunschweig
14. **Schädlich, A.**, Ullrich, S., Mäder, K., (2008) In situ forming sucrose ester implants: Preparation and *in vivo* characterisation by multispectral fluorescence *in vivo* imaging. 6th APV World Meeting, Barcelona
15. **Schädlich, A.**, Ullrich, S., Mäder, K., (2007) *In vivo* imaging of Nile red incorporated sucrose ester nanodispersions. Summer School in Nanomedicine, Cardiff

Curriculum vitae

Personal details

Name: Andreas Schädlich
Born: 16. May 1980 in Schlema, Germany
Nationality: German
Academic degree: Dipl. Pharm., 'Apotheker'

Work experience

since 11/2011 (Junior) GMP-Compliance Manager
Fresenius Kabi Deutschland GmbH, Germany

02/2007 – 06/2011 Research and teaching assistant (Pharmaceutical Technology)
Institute of Pharmacy, Martin Luther University Halle-Wittenberg

05/2006 – 11/2006 Pharmacist in training
Apotheke im Neustadt-Centrum, Halle (Saale)

11/2005 – 04/2006 Pharmacist in training (Pharmaceutical Technology)
Institute of Pharmacy, Martin Luther University Halle-Wittenberg

Education

12/2006 – 11/2009 Master of Business Administration (MBA) student
Health Care Management, University of Bayreuth

12/2006 – 10/2011 PhD Student in the group of Prof. Dr. habil. Karsten Mäder
Institute of Pharmacy, Martin Luther University Halle-Wittenberg

12/2006 3rd State examination and registration as German pharmacist
'Apotheker'

11/2005 – 04/2006 Diploma student in the group of Prof. Dr. habil. Karsten Mäder
Institute of Pharmacy, Martin Luther University Halle-Wittenberg
'Development and characterization of solid lipid formulations for a
poorly soluble drug based on Sucrose Ester'
(Industrial Cooperation)

2001 – 2005 Pharmacy student
Institute of Pharmacy, Martin Luther University Halle-Wittenberg

2000 – 2001 Civil service, Schneeberg

1992 – 1999 Johann-Gottfried Herder High School, Schneeberg

Halle (Saale), den 24. September 2013

sgd. A. Schädlich

Dipl. Pharm. Andreas Schädlich

Declaration of the self-contribution of research articles

The cumulative doctoral thesis is compiled with several research articles published or in peer-review. Most of the research work in the thesis was carried out by myself independently in the Pharmaceutical Technology Group at the Martin Luther University under the supervision of Prof. Dr. habil. K. Mäder. His contribution to the publications includes the strategic planning of the experiments and also the final review of the articles. In addition Prof. Dr. habil. K. Mäder supported the published research work in many scientific discussions, questions and inspirations.

(a) Investigation of the *in vivo* fate of a water soluble polymer

- (I) **Schädlich, A.**, Naolou, T., Amado, E., Schöps, R., Kressler, J., Mäder, K., (2011) Noninvasive *in vivo* monitoring of the biofate of 195 kDa poly(vinyl alcohol) by multispectral fluorescence imaging. *Biomacromolecules* 12 (10): 3674-3683.

My contribution was about 65 %. I have planned and performed all *in vivo* and *ex vivo* experiments. Prof. Dr. habil. J. Kressler has supervised his Mr. T. Naolou and Dr. E. Amado who have performed the labeling and Dr. R. Schöps in performing *in vitro* filtration experiments.

I drafted the manuscript and completed the publication after discussing it with the co-authors.

- (II) Jiang, Y., **Schädlich, A.**, Amado, E., Weis, C., Odermatt, E., Mäder, K., Kressler, J., (2010) In-vivo studies on *intraperitoneally* administrated poly(vinyl alcohol). *Journal of Biomedical Materials Research Part B-Applied Biomaterials* 93B (1): 275-284.

My contribution was about 25 %. I made all *in vivo* and *ex vivo* fluorescence imaging experiments and I have written the related paragraphs in the manuscript.

- (III) **Schädlich, A.**, Jiang, Y., Kressler, J., Mäder, K., (2010) Tracking the *in vivo* fate of high molar mass poly(vinyl alcohol) using multispectral fluorescence *in vivo* imaging. Scientifically Speaking News (Controlled Release Society) 27 (2): 15-16. **(Cover Story)**

My contribution was about 70 %. I made all *in vivo* and *ex vivo* fluorescence imaging experiments and I have written the manuscript.

(b) Characterization of nanocarriers and their potential usage in cancer therapy

- (IV) **Schädlich, A.**, Rose, C., Kuntsche, J., Caysa, H., Mueller, T., Göpferich, A., Mäder, K., (2011) How stealthy are PEG-PLA nanoparticles? An NIR *in vivo* study combined with detailed size measurements. Pharmaceutical Research 28: 1995-2007.

- (V) **Schädlich, A.**, Caysa, H., Mueller, T., Tenambergen, F., Rose, C., Göpferich, A., Kuntsche, J., Mäder, K., (2011) Tumor accumulation of NIR fluorescent PEG PLA nanoparticles: impact of particle size and human xenograft tumor model. ACS Nano 5 (11): 8710-8720.

My contribution to both papers was about 70 % respectively. All biodistribution studies and the writing of the manuscripts were carried out by myself. The preparation of the nanoparticles was performed by Dr. C. Rose, member of Prof. Dr. A. Göpferich's group at the University of Regensburg. Associate Prof. Dr. J. Kuntsche carried out the particle size measurements and mainly reviewed the article.s F. Tenambergen also supported the particle size measurements. Dr. H. Caysa and her group leader Dr. T. Müller have supported the *in vivo* experiments while providing the xenograft tumor model, performing the nanoparticle injections and supporting the cell experiments.

(VI) Schädlich, A., Hoffmann, S., Mueller, T., Caysa, H., Rose, C., Göpferich, A., Li, J., Kuntsche, J., Mäder, K., (2012) Accumulation of nanocarriers in the ovary: A neglected toxicity risk? *Journal of Controlled Release* 160 (1): 105-112. **(Cover Story)**

My contribution was about 80 %. All studies were mainly performed by myself. I have written the manuscript and completed it after discussing the paper with the co-authors. S. Hoffmann, Dr. H. Caysa and Dr. T. Müller have partly supported the *in vivo* experiments. The preparation of the nanoparticles/nanocapsules was performed by Dr. C. Rose and Dr. J. Li. Associate Prof. Dr. J. Kuntsche carried out the particle size measurements and reviewed the article. Prof. Dr. A. Göpferich supervised the nanoparticle preparation and reviewed the manuscript.

(c) Characterization of *in situ* forming implants for potential controlled API release

(VII) Schädlich, A., Kempe, S., Mäder, K., (2013) Long-term *in vivo* pH measurements of *in situ* forming PLGA implants using multispectral fluorescence imaging. Submitted to *Journal of Controlled Release* **(under peer-review)**

My contribution was about 75 %. All fluorescence imaging as well as the writing of the manuscript was performed by myself. Dr. S. Kempe from the same group has carried out the EPR experiments and has revised the manuscript.

(d) Investigating alternative application fields of fluorescence imaging

(VIII) Eisenächer, F., Schädlich, A., Mäder, K., (2011) Monitoring of internal pH gradients within multi-layer tablets by optical methods and EPR imaging. *International Journal of Pharmaceutics* 417 (1-2): 204-215.

My contribution was about 30 %. I have performed the fluorescence pH measurements and have written the related paragraphs in the manuscript.

Halle (Saale), den 24. September 2013

sgd. A. Schädlich

sgd. Karsten Mäder

Dipl. Pharm. Andreas Schädlich

Prof. Dr. habil. Karsten Mäder
(Co-Author)

Selbstständigkeitserklärung

Hiermit erkläre ich gemäß § 5 der Promotionsordnung der Naturwissenschaftlichen Fakultät I der Martin-Luther-Universität Halle-Wittenberg, dass ich die Ergebnisse der vorliegenden kumulativen Dissertationsarbeit

Pre-clinical *in vivo* studies of parenteral drug delivery systems
using non-invasive multispectral fluorescence imaging

am Institut für Pharmazie im Institutsbereich Pharmazeutische Technologie und Biopharmazie der Martin-Luther-Universität Halle-Wittenberg unter Anleitung von Herrn Professor Dr. rer. nat. habil. Karsten Mäder selbstständig erarbeitet und die Dissertation ohne fremde Hilfe verfasst habe.

Ferner erkläre ich, dass ich keine anderen als die von mir angegebenen Quellen oder Hilfsmittel benutzt habe und die den verwendeten Werken wörtlich- oder inhaltlich entnommenen Stellen als solche kenntlich gemacht habe.

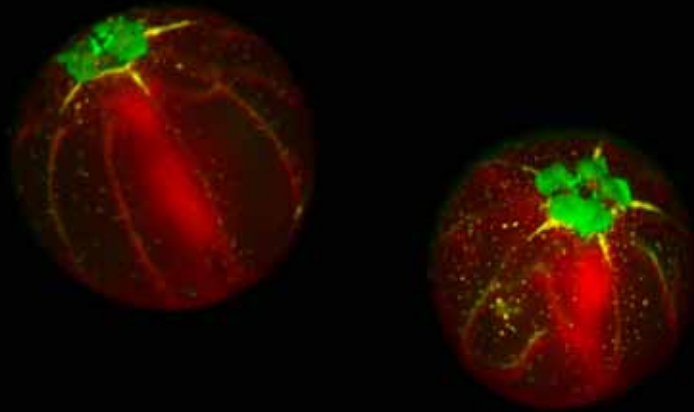
Weiterhin erkläre ich, dass ich mich mit der vorliegenden Dissertationsarbeit erstmals um die Erlangung eines Doktorgrades bewerbe.

Halle (Saale), den 24. September 2013

sgd. A. Schädlich

Dipl. Pharm. Andreas Schädlich

DAS SCHÖNSTE, WAS WIR ENTDECKEN KÖNNEN,
IST DAS GEHEIMNISVOLLE.



THE MOST BEAUTIFUL THING WE CAN EXPERIENCE IS THE MYSTERIOUS.
IT IS THE SOURCE OF ALL TRUE ART AND ALL SCIENCE.
HE TO WHOM THIS EMOTION IS A STRANGER, WHO CAN NO LONGER PAUSE
TO WONDER AND STAND RAPT IN AWE, IS AS GOOD AS DEAD: HIS EYES ARE CLOSED.

ALBERT EINSTEIN (1879 - 1955)

Cover picture: Unmixed fluorescence image of a female mouse 24 hours after *i.p.* injection of PVA. The incremental jet color image represent the threshold fluorescence PVA-TMR signal.

Reprinted and adapted from Scientifically Speaking News (Controlled Release Society) 27 (2), Cover page, Tracking the *in vivo* fate of high molar mass poly(vinyl alcohol) using multispectral fluorescence *in vivo* imaging., Andreas Schädlich, Yanjiao Jiang, Jörg Kressler and Karsten Mäder,

© Copyright 2010, with permission from Controlled Release Society.

Back: Unmixed fluorescence image of red currants